NUMERICAL STUDY OF PILE CAPACITY CONSIDERING INSTALLATION AND NEGATIVE SKIN FRICTION EFFECTS

SUN JIE

NATIONAL UNIVERSITY OF SINGAPORE

2012

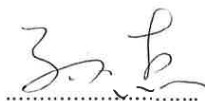# NUMERICAL STUDY OF PILE CAPACITY CONSIDERING INSTALLATION AND NEGATIVE SKIN FRICTION EFFECTS

SUN JIE

(BEng,MEng, Southeast University)

A THESIS SUBMITTED
FOR THE DEGREE OF DOCTOR OF PHILOSOPHY
DEPARTMENT OF CIVIL AND ENVIRONMENTAL
ENGINEERING
NATIONAL UNIVERSITY OF SINGAPORE
2012

DECLARATION

I hereby declare that, except where specific reference is made to the work of others, the contents of this dissertation are original and have not been submitted in whole or in part for consideration for any other degree or qualification to this or any other university.

Jie SUN
Dec 2012

SUMMARY

The accurate estimation of the pile axial capacity is a very difficult task until present time, especially for displacement piles. Over the years, the development of numerical modeling of displacement piles is still quite behind practice. There is therefore a clear need for the numerical prediction of pile behavior. This thesis is dedicated to address same factors in numerical modeling of single pile behavior and the change of soil stress state during installation and subsequent loading, in order to improve the accuracy of the design of single axially loaded pile.

Firstly, the effects of different constitutive soil models on modeling pile behavior were investigated. The Hardening Soil model could simulate more realistic soil behavior. The soil element close to the pile has complex stress history during the pile installation and these stress change significantly affect the pile bearing capacity. Hence, the Hardening Soil model is superior to the Mohr-Coulomb model for modeling displacement pile.

The improved numerical procedure that simulates installation effects based on simple cavity expansion theory was proposed. The spherical cavity expansion is applied to the soil cluster below the pile tip instead of the vertical prescribed displacement; and the horizontal prescribed displacement is applied at the interface between pile and soil along the shaft. This proposed numerical procedure provides better prediction of total shaft friction and end bearing capacity than using the combination of applying horizontal prescribed displacement to the pile shaft and applying vertical prescribed displacement to pile tip, compared to existing pile model tests.

A series of full scale pile load tests were conducted at Tuas View. Three spun piles

were installed in similar soil condition under different Jack-in forces. It was shown that the different Jack-in force did not affect the shaft friction significantly and the difference in behaviors between test piles is mainly caused by the difference in the toe stiffness response. The larger the jack-in force, the larger the stiffening effect, which is due mainly to the increase in volumetric compression of the bulb of soil below the toe of the piles. The test results provide support for the proposed numerical procedure using spherical cavity expansion to pile toe to model installation effect and also provide some independent data that validated the general applicability of the proposed numerical procedure for simulation of installation effects of displacement piles.

A detailed numerical study was carried out to study the effect of negative skin friction on pile behavior and also to verify the Unified Design Method for pile foundations. It was found that the pile behavior obtained from finite element method shows good agreement with the Unified Design Method's principle and concept. The numerical study also showed that skin friction is usually not fully mobilized near the neutral point. Therefore, the Unified Design Method with proper consideration of partial degree of mobilization of NSF near the NP may give more economical design of piles subjected to NSF, especially for those cases with large L/d ratio and small magnitude of ground settlement and the pile-soil stiffness ratio K.

Keywords: Finite Element Method, Full Scale Test; Negative Skin Friction, Ultimate Bearing Capacity; Jack-In Pile

ACKNOWLEDGEMENTS

CONTENTS

LIST OF FIGURES

LIST OF TABLES

NOTATION

Roman

a	Current radius of the spherical cavity
a_o	Initial radius of the spherical cavity
c_u	Undrained shear strength of clay
d	Diameter of pile
e_{int}	Initial void ratio
e_{max}	Maximum void ratio
m	Stress dependent stiffness according to a power law
p_0	In situ mean effective stress
p'_c	Pre-consolidation stress
p_{limit}	Cavity limit pressure
p^{ref}	Reference pressure
q	Deviator stress
q_a	Asymptotic value of the shear strength
q_b	Ultimate end bearing resistance
q_c	CPT total cone resistance
q_E	CPT effective cone resistance
q_f	Ultimate deviatoric stress
s_f	Final sensitivity of the structure clay
s_o	Initial sensitivity of the structure clay
A_c	Cross section of pile
D_{cone}	Diameter of cone penetrometer
E_{50}	Secant modulus at 50% strength
E_{50}^{ref}	Secant modulus at 50% strength at p^{ref}
E_{oed}^{ref}	Modulus at 50% strength at p^{ref}
E_{ur}^{ref}	Triaxial unloading modulus at p^{ref}
E^{PMT}	Loading modulus from pressuremeter test
E_{ur}^{PMT}	Unloading modulus from pressuremeter test
E_s	Secant modulus of concrete
E_{s1}	Young's modulus of soft layer clay
E_{s2}	Young's modulus of stiff layer clay
EA	Axial stiffness of pile
F_{base}	Base capacity
F_{shaft}	Shaft capacity
F_{total}	Total capacity
G	Shear modulus
G_o	Small strain in-situ stiffness
K	Pile-soil stiffness ratio
K_o	Lateral stress coefficient
K_o^{nc}	Lateral stress coefficient for NC soil
K_p	Passive lateral stress coefficient

L	Length of the pile
I_r	Rigidity index
N_c	Bearing capacity factor in clay
N_q	Bearing capacity factor in sand
Pa	Atmospheric pressure
$P_{n,mob}$	Mobilized maximum dragload at neutral point
$P_{n,\beta}$	Calculated maximum dragload at neutral point based on β method
Q_{allow}	Allowable axial load capacity of the pile
Q_{ult}	Geotechnical axial load capacity of the pile
R_{inter}	Interface strength reduction factor
S_0	Ground settlement
Z_n	Depth of neutral point

Greek

α	Total stress parameter for shaft friction
β	Effective stress parameter for shaft friction
δ	Pile-Soil interface friction angle
ε_1	Axial strain
ε_v	Volumetric strain
ϕ_i	Effective friction angle of interface element
γ_{sat}	Saturated unit weight
γ'	Effective unit weight
η	Degree of mobilization of NSF
ν	Poisson ratio of soil
λ^*	Slope of isotropic compression line in p'-v space
κ^*	Slope of swelling line in p'-v space
φ'	Soil effective friction angle
φ_c	Critical state friction angle
σ_1'	Major effective principle stress
σ_3'	Minor effective principle stress
σ_h'	Normal effective stress on the pile shaft
σ_{vo}'	Effective overburden stress
σ_{vo}	Total overburden stress
τ_s	Ultimate unit shaft friction
ψ	Dilatancy angle
ψ_m	Mobilized dilatancy angle
Δu_x	Prescribed horizontal displacement
Δu_y	Prescribed vertical displacement
$\Delta \varepsilon_v$	Prescribed volumetric strain

ABBREVIATIONS

ALE	**A**rbitrary **L**agrangian-**E**ulerian
API	**A**merican **P**etroleum **I**nstitute
CFA	**C**ontinuous **F**ight **A**uger
CD	**C**onsolidation **D**rained
CIU	**I**sotropic **C**onsolidation **U**ndrained
CPT	**C**one **P**enetration **T**est
CPTU	**C**one **P**enetration **T**est with Piezocone
COV	**C**oefficient **O**f **V**ariation
ESP	**E**ffective **S**tress **P**ath
FEM	**F**inite **E**lement **M**ethod
HYP	**Hyp**oplastic model
ICP	**I**mperial **C**ollege **P**ile
MC	**M**ohr- **C**oulomb model
HS	**H**ardening **S**oil model
NCL	**N**ormal **C**ompression **L**ine
NGI	**N**orwegian **G**eotechnical **I**nstitute
NISRE	**N**ormalized **I**ncremental **S**tress **R**esponse **E**nvelope
NSF	**N**egative **S**kin **F**riction
NP	**N**eutral **P**oint
OCR	**O**ver **C**onsolidation **R**atio
PDA	**P**ile **D**riving **A**nalyzer
PHC	**P**restressed **H**igh-strength **C**oncrete
PMT	**P**ressuremeter **T**est
UDM	**U**nified **D**esign **M**ethod
SBS	**S**tate **B**oundary **S**urface
SDCM	**S**tiffened **D**eep **C**ement **M**ixing
SPT	**S**tandard **P**enetration **T**est

CHAPTER 1 INTRODUCTION

1.1 BACKGROUND

The use of piles is one of the earliest examples of the art and science of a civil engineer to overcome the difficulties of founding on soft soils. In China, timber piling was used by the builder of the Han Dynasty (200BC to AD 200). Although, the pile has been used since ancient times and there is an enormous amounts of research that has been carried out to gain better understanding of pile behavior and the factors which govern this behavior. Continuous improvement and technological advances have been made in construction and testing of piles, and analysis method to make the economics of deep foundations more attractive. However, "we may never be able to estimate axial pile capacity in many soil types more accurately than about 30%" (Randolph, 2003). In addition, the effects of various methods of pile installation on the bearing capacity and deformation characteristics cannot be calculated by strict application of soil or rock mechanics theory (Tomlinson and Woodward, 2008). As a result, for current design, larger safety factors are used to allow for uncertainty in pile performance.

An international pile prediction event on pile capacity and pile load-movement

response to axial loading was held at Portugal in 2003(Santos, Duarte et al. 2005).

Three different kinds of piles were executed: bored piles, continuous flight auger

(CFA) piles and driven piles. A total of 32 persons from 17 countries submitted

predictions before static loading tests were performed. The extensive in-situ and

laboratory investigations of the experimental site were undertaken which allowed a

confident and flexible choice for input parameters for pile prediction event. However,

the predictions presented in Figure. 1.1 are very scattered demonstrating that the

accurate estimation of pile axial capacity is still a very difficult task, even if the soils

around pile have been fully and carefully investigated. The majority of the predictors

overestimated the bearing capacity of the bored piles and CFA piles, while they

underestimated the bearing capacity of the driven piles. Similar scatter were found in

the pile prediction event at the 2002 ASCE GeoInstitue's Deep Foundation Conference

(Fellenius, Hussein et al. 2004), presented in Fig. 1.2. Furthermore, the long term

capacity of the pile is a function of the re-consolidation process modifying the

effective stresses after the pile installation, especially for displacement piles (driven

piles and Jack-in piles). The process of installation of displacement pile is usually

undrained and the surrounding soils immediately around the pile shaft and base are

subject to very high stresses that would produce excess pore pressures, as the soils

shear and deform around the pile. When the pile is driven or jacked into the

consolidating ground, the situation becomes even more complicated. The negative skin

friction (NSF) will occur when the soil around the pile shaft settle more than that of

pile itself. However, to date the complex mechanism of NSF on the pile is still not

well understood. Therefore, there is need to investigate further the behavior of single

pile under axially load condition.

The finite element method (FEM) is widely used for geotechnical problems recently

with the rapid development of hardware and software of the computer (Wehnert 2006).

Since FEM takes the complex soil condition as well as complex soil-structure

interaction into account, it is widely used in the scenarios that have complex load

combinations and strong interaction with neighboring structures, in order to reach an

optimal and economical design. Moreover, with the developments of advanced and

sophisticated constitutive models, the complex soil behavior which is non-linear and

time-dependent can be simulated, making the FEM calculations more accurate and

reliable.

1.2 RESEARCH OBJECTIVES AND SCOPE

The goal of this thesis is to improve the accuracy of the design of single axially load

pile by using FEM. In a nutshell, it tackles the prediction by developing a numerical

model that includes the effects of installation method, using a commercially available

FEM package, PLAXIS (Brinkgreve *et al.*, 2009). Such a model could predict a

reasonable stress field after installation, and provide a reasonable prediction of bearing

capacity with time. The numerical model could give a reasonable estimation of the

distribution of shaft resistance and end bearing, as well as the load-settlement behavior

of the pile type to be studied. Factors affecting the behavior of axially loaded pile,

including constitutive soil models, installation method (particular attention is given to Jack-in method), negative skin friction and interface, are investigated by using PLAXIS and the FEM results are validated with laboratory tests and full scale pile load tests.

In particular, the objectives in this thesis are:

1) To investigate the effects of different constitutive soil models (Mohr-Coulomb model, Hardening Soil model and Hypoplastic model) on modeling pile behaviors. This involves proper calibration of the constitutive model for determination of input parameters of constitutive soil models from in-situ and laboratory tests, and the validation of the applicability of the constitutive soil model for single pile response in FEM.

2) To develop an improved numerical procedure that simulates installation effects based on cavity expansion theory for pile shaft and end bearing resistance.

3) To conduct a series of full-scale pile load tests and back-analyses of the tests' results and to validate the installation effects by the modeling proposed above.

4) To study the effects of negative skin friction on pile behavior numerically and verify the Unified Pile Design Method for pile foundations based on existing case history. This aids in better understanding on design for negative skin friction in pile.

1.3 ORGNIZATION OF THESIS

This thesis comprises seven Chapters.

Chapter 2 reviews the literature relating to axially-loaded piles. Firstly, previous works on the mechanics of pile behavior were highlighted. This is further divided into two parts: field and lab test as well as numerical study. Secondly, state of the art design methods for axial pile capacity were also examined. Links were drawn between the complex yet frequently contradictory behavioral observations, and the inadequacy of numerical simulation and current design methods.

Chapter 3 describes the constitutive models (Mohr-Coulomb model, Hardening Soil model and Hypoplastic model) that were used in this research. Firstly, the background of constitutive models and the determinations of input parameters of constitutive soil models from in-situ and laboratory tests were presented. Then, the evaluations of different constitutive models behavior on single element test and modeling pile behavior were presented. Finally, applications of Hypoplastic model to simulate the hysteresis behavior of pile under axial cyclic load and the strain softening of soil-pile interface behavior were demonstrated.

Chapter 4 presents the development of a new improved numerical procedure for modeling installation effects in displacement pile, and compares its performance to previous methods using centrifuge pile load tests and field pile load tests' data. Firstly

a review of the modeling bored pile showed the importance of interface elements and

mesh design in computing load capacity of the pile. Secondly, previous method of

modeling displacement pile installation effect was reviewed and the problem of their

procedure was investigated. Finally, the improved numerical procedure was proposed

to give better agreement with laboratory and field tests' results.

Chapter 5 describes the full-scale field pile load testing program conducted in Jurong

sedimentary soils in Singapore and extensive in-situ and laboratory investigations of

the experimental site. The analyses of the pile load tests results were presented.

Comparisons were made between tests' results and FEM model predictions using the

proposed numerical procedure described in Chapter 4.

Chapter 6 describes the effects of negative skin friction on pile behavior with time and

presents the verification of the Unified Pile Design Method through analysis of well-

documented case studies. Recommendation for rational consideration of NSF in pile

design was made.

Chapter 7 summarizes the conclusions from this research and makes some

recommendations for future research.
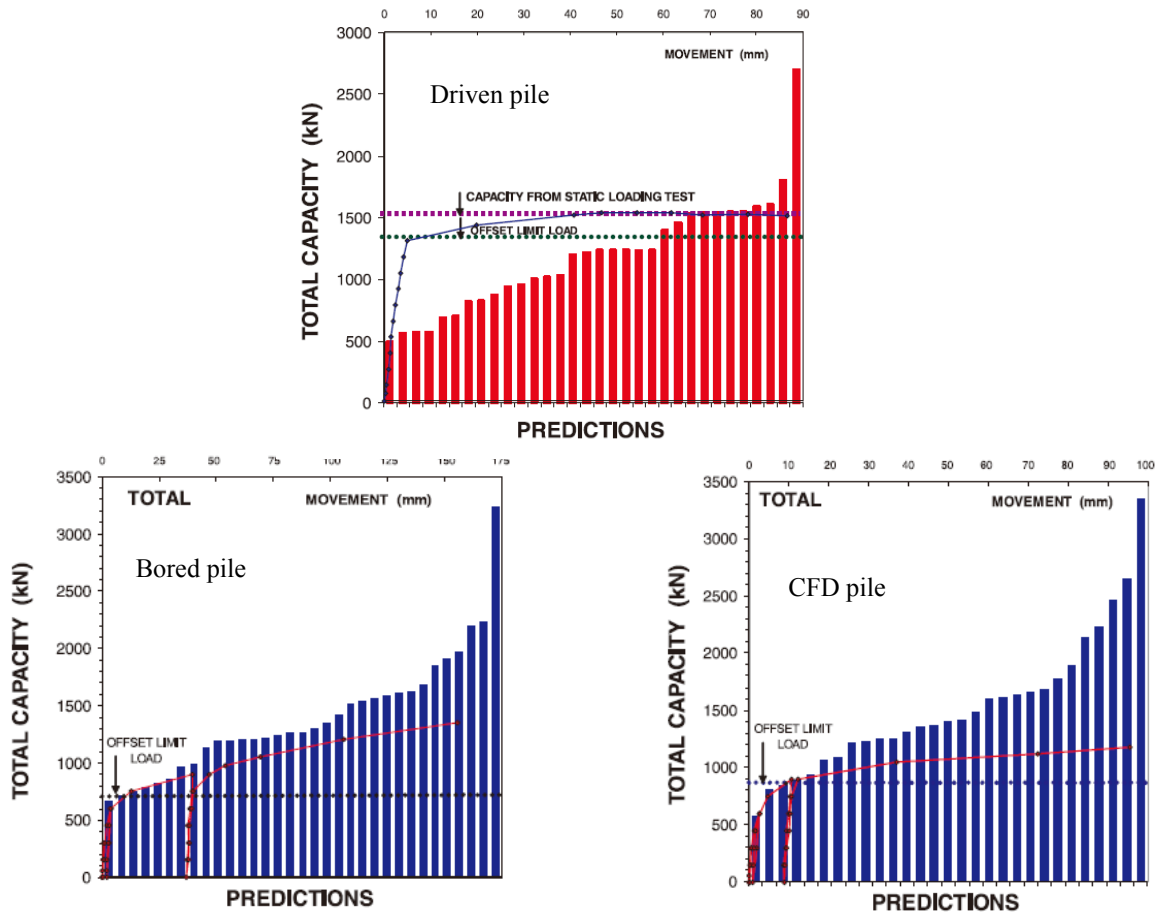
Figure 1-1 Total capacities predicted for different piles (Fellenius, Santos et al. 2007).
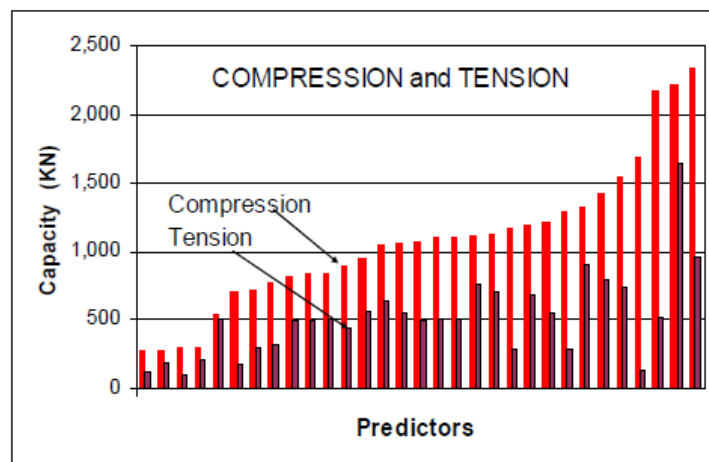
Figure 1-2 Total capacities predicted for test piles (Fellenius, Hussein et al. 2004).

CHAPTER 2 LITERATURE REVIEW

2.1 INTRODUCTION

2.1.1 Previous research on piles

Pile is one of the oldest topics in geotechnical engineering and rational design methods based on soil mechanics principles were established over 50 years ago. A great volume of field experience and empirical data on the performance of pile foundations have been published and an enormous amount of researches have been carried out after that.

However, the prediction of piles bearing capacity is a very complex problem which is partially based on theoretical concepts derived from the sciences of soil mechanics, but is mainly based on empirical methods obtained from field experience until the present time and is arguably the area of the greatest uncertainly in foundation design (Randolph *et al.,* 1994).

2.1.2 Complexity of pile behavior

The conditions which give the bearing capacity of pile foundation are significantly different from the shallow spread foundations (Tomlinson and Woodward, 2008). In the latter case, virtually the whole mass of soil influenced by the applied load

remained undisturbed and unaffected by the construction operations (Figure 2.1a). Thus, the bearing capacity of shallow spread foundations can be predicted from the knowledge of the physical characteristics of the undisturbed soil. While the soil in contact with the pile face is completely disturbed by the type of methods of installation (Figure 2.1b) and the soil under the tip of the piles is compressed to an extent which significantly affect its end-bearing capacity. As a result, the behavior of piles is influenced profoundly by the method used to install the piles and cannot be predicted solely from the physical properties of the piles and the undisturbed soil.

Furthermore, the process of installation of displacement piles will make the problem more complicated as compared to the non-displacement piles. During the installation of a displacement pile, large deformation will be made. This change the stresses and the strains within the deforming soil varying from the in situ stress level and zero strain to tens of MPa stress and of the order of 100% strain respectively (Mair, 1993). In addition, the stiffness and the strength of soil around the pile may change over periods of days, months or years after pile installation. These changes may be due to pore pressure dissipation (Randolph & Worth, 1979), soil ageing (Ng *et al.*, 1998) and creep (White *et al.*, 2005). When the settlement of the soil by the consolidation is larger than that of the pile carrying an axial load from superstructure, the soil will drag down the pile. As a result, negative skin friction will occur. Piles are usually installed to transfer loads through soft or loose soil layers to stiffer soil, NSF will always develop along the pile and accumulate over time to cause drag load due to soil

reconsolidation after pile had been driven or jacked-in(Fellenius 2006). However, the complex mechanism of NSF on piles is still not clearly understood and quite substantial misconceptions and confusions still prevail among engineers when it comes to the design of the pile subjected to NSF.

The complexity of pile behavior makes accurate prediction of pile axial capacity to be very a difficult task, as demonstrated in Chapter 1. A wide range of predictions for axial capacity can be produced by current design method. Prediction of the performance cannot be wholly based on empirical method. It should be derived from an understanding of the underlying mechanics of pile behavior and the influence of the installation procedure. Therefore, this literature review concentrates on experimental and numerical studies of the soil behavior during and after the pile installation as well as the assumptions and input parameters required by current design methods. As a particular topic of interest, only displacement piles will be examined in detail.

2.2 EXPERIMENTS ON SINGLE PILES

In order to validate the numerical results and develop reliable and broadly applicable design method, clear existing experimental evidence should be tested first. It is suggested that carefully designed field tests with highly sensitive instrumented pile provide the key to understanding the mechanisms that govern pile behavior and establishing well-based design criteria. In addition, well-designed laboratory

experiments also play an important role, especially centrifuge tests. This section will highlight insight into the change of the soil stresses after pile installation (section 2.2.1-2.2.2) as well as understanding of the mechanism of NSF on piles from the field tests (section 2.2.3).

2.2.1 Study of stress distribution along single pile in sands

The measurement of the shaft friction and radial effective stress in sands acting at a number of levels along pile shaft in the field was reported by Lehane *et al* (1993). The instrumented piles were installed by fast-jacking. Radial effective stress measured at fixed depths in soil profile during the installation reported by Lehane *et al* (1993) shows that it reduces as the relative depth of the pile tip (h/R) increases (Figure 2.4), which means the radial effective stress at a given depth decreases gradually as the pile toe penetrates deeper past that depth. The same tendency was found in the change of local shear stress along pile shaft during the installation (Figure 2.5). This feature is known as "friction fatigue" observed by Heerema (1980) or "h/R effect" observed by Bond & Jardine (1991). As can be seen in Figure 2.4, the radial effective stress increases with depth along the pile shaft after the installation.

The distribution of shaft friction was also measured during load testing by Lehane *et al* (1993). The data presented by Lehane *et al* (1993) showed that the highest stresses are mobilized near the pile tip. This profile is different from that reported by Vesic (1970).

Vesic postulated that the local shear stress diminished with depth below a certain level (Figure 2.6). However, it has been questioned critically by a number of authors subsequently. Kulhawy (1984) argued that the trend of the field tests reported by Vesic could be explained by reductions in Ko due to over consolidation ratio (OCR) declining with depth. Fellenius & Altaee (1995) suggested that residual loads may lead to Vesic false conclusion that the maximum value of unit shaft friction occurs some distance above the pile tip.

Tomlinson (2001) presented data from load testing of a 762 mm diameter open-end tubular pile embedded in loose to medium dense micaceous silt at a site of the Jamuna River Bridge in Bangladesh (Figure 2.7). The "friction fatigue" or "h/R effect" was observed and the shaft friction is concentrated very close to pile tip and decays rapidly along the shaft.

A series of model pile tests were conducted in the centrifuge by Nicola *et al* (1999). The model piles were driven by a miniature pile driving actuator into silica flour of varying densities. The shaft friction distribution was measured during load testing. The analysis of the load test revealed that the shaft friction increased approximately linearly with depth at a low rate, but with a marked increase close to the pile tip (Figure 2.8). The "friction fatigue" or "h/R effect" was also observed. It was found that shaft friction degradation occurred when unload-reload loop occurred during the installation (Figure 2.9).

12

Nicola *et al* (1999)'s measured shaft friction distribution is comparable with the design approach proposed by Randolph *et al* (1994). This design approach which is considered "friction fatigue" or "h/R" effect will be discussed in section 2.4.2.2.

The measurements of horizontal stress acting on the pile during installation and subsequent cyclic loading in the drum centrifuge tests were reported by White *&* Lehane (2004). The model piles were installed by three methods: monotonic installation, jacked installation and 'pseudo-dynamic' installation. The difference between these three methods is monotonic installation does not comprise cyclic loading, while 'pseudo-dynamic' installation comprise twice as much cyclic loads as jacked installation does.

The observations of horizontal stress during the installation reported by White *&* Lehane (2004) show that no friction fatigue was found during monotonic installation (Figure 2.10) while cyclic installation methods (jacked installation and 'pseudo-dynamic' installation) have been reported to cause the significant degradation of shaft friction (Figure 2.11). Furthermore, reducing the cycling in installation will reduce the degradation of shaft friction. As a result, modern installation techniques of pile jacking may yield higher shaft friction than conventional dynamic installation methods. This is in agreement with those proposed by Chow (1997).

2.2.2 Study of stress distribution along single pile in clays

The extensive research programme undertaken at Imperial College using a heavily instrumented 7m pile is reported by Bond *et al* (1991); Lehane *et al* (1994a) and Lehane *et al* (1994b). The instrumented piles were jacked into three different clay sites and the radial effective stress and the shear stress were measured at a number of locations along the pile shaft during installation, stress equalization, and load testing. The three sites comprise heavily over-consolidated clay (London), stiff glacial clay (Cowden), and lightly over-consolidated soft marine clay (Bothkennar). The key observations relating to the mechanism of shaft friction were as follows.

Firstly, the "*h/R*" effect was found in all soil sites during the installation stage. Figure 2.13 shows that the radial total stresses acting at fixed depths reduce as the pile penetrates to deeper levels. The rates of stress reduction depend on the soil type. Secondly, pore pressures rise to reach maxima shortly after installation, and then reduce monotonically to ambient values during equalization (Figure 2.14). While the radial total stresses reduce throughout equalization (Figure 2.15). The radial total stresses and pore pressure changes during equalization led to the variations of the radial effective stresses with time shown in Figure 2.16. Radial effective stresses show temporary minima shortly after installation. These were most pronounced in stiff clay at Cowden. Thus the short-term minimum capacity of pile would result if load testing was done after short time from installation. The occurrence of a temporary dip in capacity has important implications for large diameter piles, as the rate of equalization

varies in inverse proportion to the square of diameter. Furthermore, if the bearing capacity of the displacement pile is to confirm the design calculations by short-term load test, then it should allow the safety factor for any reduction in bearing capacity with time. Finally, the increment of the radial effective stress depends on the over-consolidation ratio (OCR) of clay. As can be seen in Figure 2.16, the radial effective stress (σ'_{rc}) after equalization is three times those measured just after installation (σ'_{ri}) at Bothkennar (OCR=1.5). However, at Cowden (OCR=6), σ'_{rc} is comparable to σ'_{ri}, and in the London clay (OCR=30), σ'_{rc} is less than σ'_{ri}. In addition, the equalized radial stress ratios depend primarily on the OCR and sensitivity of the clay and reduce as h/R increases.

Based on this series of field researches performed by Imperial College, Jardine and Chow (1996, 2005) proposed a new design approach for calculating the axial capacity of displacement pile. The resulting design equations are shown below (Equation 2.1-2.5).

$$\tau_f = \sigma'_{rf} \tan \delta_f = (K_f / K_c)\sigma'_{rc} \tan \delta_f \qquad (2.1)$$

$$\sigma'_{rc} = K_c \sigma'_{vo} \qquad (2.2)$$

$$K_c = [2.2 + 0.016 OCR - 0.870\Delta I_{vy}]OCR^{0.42}(h/R)^{-0.20} \qquad (2.3)$$

$$\Delta I_{vy} = \log_{10} S_t \qquad (2.4)$$

$$K_f / K_c = 0.8 \qquad (2.5)$$

The notations are as follows:

τ_f Peak local shear stress

δ_f Interface friction angle at failure

σ'_{rf} Radial effective stress at failure

σ'_{rc} Radial effective stress at end of equalization

σ'_{vo} Free-field vertical effective stress

OCR Over consolidation ratio

ΔI_{vy} Relative void index at yield

h Distance above the pile tip

R Pile radius

K_c Coefficient of radial effective stress for shaft at end of equalization

K_f Coefficient of radial effective stress for shaft at failure

Pile capacity increases with time after installation is known as pile set-up. The series pile tests reported by Komurka (2004) demonstrates unit set-up distribution characterization and depth-variable penetration resistance criteria development.

The five pipe piles were driven in the Menomonee River Valley in Milwaukee. The Pile Driving Analyzer (PDA) tests were conducted at end of initial drive (EOID) and 69 to 70 days after EIOD. The results were shown in Figure 2.16. As can be seen, the set-up can account for a significant portion of long-term pile capacity. Piles exhibiting different driving behavior can exhibit similar set-up distributions. Komurka and

Wagner (2003) suggested that initial-drive dynamic monitoring results, combined with set-up distributions, can be used to predict pile's long-term capacity as functions of depth (Figure 2.17). Therefore, set-up effect can be considered in pile design.

2.2.3 Study of negative skin friction along single pile in clays

Since the beginning of 20th century, especially after the 1960s, plenty of researches include full-scale long-term field tests have been conducted to study the magnitude and development of NSF due to soil settling around the piles. One of major references and the pioneering papers is a well-documented case history presented by Endo et al.(1969).

Five strain-gages instrumented steel pipe piles (4 closed-toe and 1 open-toe piles) were driven during May-June 1964. Seven settlement gages and seven piezometers were also installed in the soil near the piles. The consolidation of the soil is due to ongoing pumping of water from the sand layer below 43m depth. Figure 2.18 shows the axial force distribution on pile and the pile movement and soil settlement change with time (672 days) for both open-toe and closed-toe piles. From Figure 2.18, Endo et al. concluded that the neutral plane (NP) is the location of the force equilibrium in pile as well as the location where there is no relative movement between the pile and the soil, supported by Bozozuk (1972) and Indraratna et al. (1992) from their own field tests. Another important feature is that the axial forces increase with depth and that the NSF

in the upper portion of the pile does not increase with the settlement of the soil. Figure 2.19 shows the pore pressure distribution change with time. As can be seen, the pore pressure did not change much during the last few years (Oct 1964 to Apr 1966) in the upper portion of the pile which indicted the effective stress did not change much during that time in that zone. Based on this, Fellenius (2009) remarked that the shear force (or NSF) are proportional to the effective stress and its development with time and they are independent of the magnitude of the settlement and he supported his conclusion by fitting an effective stress analysis to the load distribution data points of two-year measurements of Apr 1966 and also to other well-documented case histories (Bejrrum and Johannessen (1965), Bozozuk (1972), Clemente (1981) and Leung et al. (1991), Indraratna et al. (1992)). In addition , by revisiting these case histories , Fellenius (2006) found that the length of zone of transition from NSF to positive skin friction is a function of the magnitude of the movement between the pile surface and the soil. Small relative movement will result in a long transition zone and large relative movement will result in a short transition zone. Moreover, the temporary load (like live load) does not contribute to the load at NP, thus the drag load and live load should not be considered at the same time. This concept is supported by Bozozuk (1981). Based on these generally applicable conclusions which are very important for design of pile foundations from many reported full-scale tests, Fellenius has over years developed a new unified design method which was summarized in three steps (Fellenius 1988; Fellenius 1997; Fellenius 2004):

1. Allowable load (dead load plus live load) is equal to the pile capacity divided by

the factor of safety.

2. The load (dead load plus drag load) at the NP must be smaller than the axial

    structural strength of the pile divided by the factor of safety (or by a similar

    approach to the allowable structural load).

3. The settlement calculated at pile toe level or at the NP must be smaller than the

    maximum tolerable value.

More details of the unified design method will be discussed in section 2.4.3.

2.3 NUMERICAL STUDIES ON SINGLE PILES

2.3.1 Modeling of non-displacement pile

The soil around pile is completely disturbed by pile installation. However, the change

of in-situ stress state next to the pile shaft is only marginal while installing a non-

displacement pile with casing (Katzenbach, Arslan et al. 1995). As a result, the pile is

normally modeled as a cluster of volume elements having the dimensions and location

of the pile installed at depth. The numerical approaches differ from each other mainly

in the way the soil was modeled. The back analysis of a pile load test in stiff clay was

presented by Wehnert & Vermeer (2004) using three different models to describe the

soil behavior. They are the elastic-plastic Mohr-Coulomb model (MC), the Soft-Soil

model (SS), which is based on the modified Cam-Clay model, and the advanced

Hardening-Soil model (HS) in the commercially available FEM package, PLAXIS.

Three key findings can be drawn from their study:

Firstly, the importance of the interface elements was demonstrated. The calculation of shaft resistance is heavily mesh-dependent without interface elements (Figure 2.20). For base resistance, at least two or three elements are need at the pile tip to get rid of the mesh dependency. Secondly, for base resistance, the difference between computational results using different soil models appeared to be remarkably small (Figure 2.20). Wehnert & Vermeer (2004) suggested that the choice of the constitutive model is not important for the base bearing resistance; the more significant thing for modeling of the base bearing resistance is the right choice of the soil stiffness. As can be seen in Figure 2.21, the results for the shaft friction depend significantly on the choice of the constitutive model. For small displacement, the MC and the SS model lead to the same curve and behave stiffer than the HS model, while the HS model gives the largest peak value. Finally, comparing the results of the three models with the results of pile load test, Wehnert & Vermeer (2004) suggested that the HS model would be the best (Figure 2.22). This is supported by Li (2004). Similar numerical procedure was adopted by Li (2004) for the study of kentledge effect on modeling bored piles. As can be seen in Figure 2.23, the back analyzed load settlement curves using the HS model give a better match than those using the MC model, especially on residual settlement. The measured residual settlement was 11mm after unloading from 26400kN ($2 \times W.L.$) and 23mm after unloading from 39600kN ($3 \times W.L.$), while the corresponding calculated settlement was 9.3mm and 25mm respectively when the HS

model is used. However, the corresponding calculated settlement was 0.8mm and

13.9mm respectively when the MC model is used. This is because the MC model only

has one stiffness parameter 'E_{50}', so it cannot capture the unloading behavior while

the stiffness in the HS model distinguishes between 'primary loading', 'unloading' or

'reloading'. The difference between the MC model and the HS model will be

discussed in section 3.3.1.

2.3.2 Modeling of displacement pile

As mentioned in section 2.1, the process of installation of displacement piles will

significantly change the stress and strain state of deforming soil around piles compared

with non-displacement piles. Numerical modeling of displacement pile installation

effects becomes a difficult task and a lot of numerical studies have been carried out.

A numerical model which simulates the penetration of a displacement pile into

homogenous sand by three different installation methods: Jack-in method, driving and

vibratory driving method was present by Mahutka *et al* (2006). The solution of the

boundary value problem is computed numerically with the commercial code

ABAQUS. The constitutive equation of hypoplasticity is used to model sand. A

kinematic contact formulation in combination with the Coulomb friction model is used

for contact between pile and soil.

Here, only the results of Jack-in pile that are of our major concern are presented (Figure 2.24 and 2.25):

- Pile penetration in loose sand causes settlement at ground close to pile, the further the pile penetrates, and the greater is the surface area that is affected by settlements. While for dense sand the penetration process causes heave initially then the heave finally turns into settlements as pile penetrates further.

- After installation, the radial stresses around pile for both loose and dense sand increase and exceed the Ko state. Furthermore, very high radial stress can be observed at the pile tip. Mahutka *et al* (2006) explained that can be caused by the radial spreading of the stressed below the pile tip.

Mahutka *et al*'s model can give reasonable stress and strain field after installation. However, Mahutka *et al* (2006) did not compare their numerical results with any field tests or laboratory tests. There are no attempts to simulate the subsequent pile load test. Thus, bearing capacity of the displacement pile is not calculated.

The numerical studies presented by Berg (1994), Susila et al., (2003), Sheng et al., (2005), Dijkstra *et al.,* (2006), Anaraki (2008), Dijkstra *et al.,*(2011) could be classified under the Arbitrary Lagrangian-Eulerian (ALE) approach. In an ALE approach the material displacements are uncoupled from the nodal point displacements. Element shapes can be independently optimized from deformations,

therefore no mesh distortions will occur. As early works in this area, the ALE method

was successfully implemented to simulation a cone penetration test (Berg, 1994). The

cone or pile is modeled as a fixed boundary and interface friction is taken into account

between the soil and the boundary. The penetration process itself is initiated by

applying incremental material displacements at lower boundary of the mesh. The soil

is pushed along the cone or pile, instead of it being pushed into the soil. The Drucker-

Prager constitutive model was used for the majority of the calculations and it was

found that it is difficult to obtain stable solutions for the Mohr-Coulomb model. Later,

similar calculations were made with ABAQUS for cone penetration in sand and clay

(Susila et al., 2003; Sheng et al., 2005). Numerical frameworks capable of large

deformation are readily available. However, these frameworks often lack advanced

constitutive models. Dijkstra *et al.,*(2011) also pointed out that previous fixed pile

approach requires somewhat unrealistic boundary conditions, i.e. pre-embedment of

the pile in the geometry, a initially constant stress field in the entire domain and a

counter-acting force on the top boundary. The results for the pile installation are only

reliable at full penetration, as at that stage the flow becomes stationary. In order to

overcome these limitations, Dijkstra *et al.,*(2011) introduced simulations combining

large deformations and advanced constitutive modeling by the moving pile approach,

which is a stepwise penetration of the pile into the soil. The soil is modeled by the

Hypoplastic model and only sandy soil is considered. It was found that the change of

effective stress below the pile base and the change of porosity near the pile shaft were

reasonably simulated by using the moving pile approach combined with the

Hypoplasicity model, although the difference between the calculation and the experimental results is obvious. The similar results were reported by Anaraki (2008) using the Hypoplastic model. He compared his computed results to centrifuge tests (Dijkstra et al., 2006b) shown in Figure 2.26. As can be seen, the effective stress below the pile base from the ALE approach is larger than that from centrifuge tests.

The bearing capacity of the displacement pile after installation computed by Dijkstra *et al.,* (2006a) was compared to centrifuge tests' results (Allard, 1996). The calculated end bearing capacity is approximately 97% of the experimentally observed value while the total shaft capacity overestimates the experimental results by 78%.

Besides modeling the pile installation process, some researchers try to use some simple techniques like prescribing boundary conditions at pile-soil interface to model the installation effects (Baars and Niekerk (1999), Broere & van Tol (2006) and Said et al., (2008)). The idea of using prescribing boundary conditions was first introduced by Baars and Niekerk (1999). Broere & van Tol (2006) and Said et al., (2008) also used this simple technique to model installation effects of the displacement pile. Broere & van Tol (2006) compared the computational results of total capacity and shaft friction with the results of two centrifuge tests (Figure 2.27). It is shown that modeling the installation effects is possible by increasing the volume of the pile cluster by volumetric expansion ($\Delta \varepsilon_v$) or prescribing displacements (Δu_x and Δu_y) at the pile-soil interface. This simple technique can be used to obtain an acceptable prediction of

the bearing capacity of a displacement piles in sand. However, the normal stresses along pile shaft after pile installation and shaft friction at failure (Figure 2.28) differ from observations by many authors (e.g., Lehane *et al*, 1993; De Nicola *et al*, 1999; White & Lehane, 2004; Tomlinson, 2001). Broere & van Tol (2006) did not give explanation, thus not all details are fully captured.

2.3.3 Summary

In summary, the recent developments of numerical modeling of displacement piles are still behind practice. The installation of Jack-in piles involved the quasi-static insertion of a solid cylindrical or square pile into the ground by means of large hydraulic pressures. During the installation, the soil around the pile is pushed away and compacted while the stresses surrounding the pile are significantly increased. These complicate the problem greatly. Pervious numerical studies indicate the need for improvements. The installation process can not be modeled in regular Finite Element environment due to mesh distortion. The ALE numerical scheme is well suited to large strains analysis and has been successfully implemented in installation process of displacement piles. The ALE framework combined with advance constitutive soil model is capable of modeling reasonable stress and density response during the pile installation (Dijkstra *et al.,* 2011). However, the bearing capacity of displacement piles derived from ALE is grossly overestimated, compared to experimental results. In addition, the ALE approach is difficult to use and is costly in terms of calculation time

compared to regular Finite Element Analysis. As a result, these would make the ALE approach hardly applicable to practical engineering design. The simple technique, prescribing boundary conditions at pile-soil interface, gives a possible tool to modeling installation effect of displacement pile in regular Finite Element environment. This technique could give the reasonable bearing capacity of the displacement pile when properly calibrated, although not all details are fully captured.

2.4 ANALYSES AND PILE DESIGN

The above reviews have examined experimental data of the behavior of piles and the numerical studies on the single pile. In order to compare these with current design practice, a brief review of the wide variety of current techniques is presented below.

2.4.1 Prediction of base capacity

2.4.1.1 Bearing capacity theory

The bearing capacity based on the plasticity approach is first developed by Prandtl (1921) is widely used in practice primarily to predict pile base capacity because of its relative simplicity and general acceptance by engineers. The ultimate end bearing resistance q_b is given by:

$$q_b = N_q \sigma'_{vo} \quad \text{in sand} \tag{2.7}$$

$$q_b = N_c c_u \quad \text{in clay} \tag{2.8}$$

where N_q and N_c are the dimensionless bearing capacity factors in sand and in clay

respectively, σ'_{vo} is the effective overburden stress at pile base level and c_u is the undrained shear strength of clay.

Over the years, a large variety of formulations for N_q have been published and a wide number of correlations proposed to link friction angle φ and N_q (Figure 2.29). These correlations show a significant variation in predicted base capacity. Furthermore, N_q is not a function of friction angle, φ only. Gupta (2002) demonstrated that the rigidity index $I_r = 2G / q_f$ also has significant effect on N_q. In order to combine the effects of φ and I_r, the semi-analytical models for deep bearing failure were developed. The most promising approach appears to be through an analogy with spherical cavity expansion that has been widely used which will be discussed later.

The bearing capacity factor N_c is commonly taken as 9. However, the recent research demonstrates that the $q_b = N_c C_u$ is far from ideal (Jardine *et al.*, 2005). No unique N_c value was found to apply and values far above 9 were developed in many close-end pile tests.

2.4.1.2 Cavity expansion theory

Ladanyi (1961) suggested that the deformation bulb beneath a loaded pile tip strongly resembles that for a spherical cavity expanded in an infinite medium. A similar observation was found by Yasufuku & Hyde (1995) and Yasufuku *et al.* (2001).

Therefore, Cavity expansion theory offers an alternative design approach for base

capacity. The base capacity is related the limit pressure inside the cavity based on

semi-empirical relationships, as shown in Figure 2.30.

The design approach proposed by Randolph *et al.* (1994) used spherical cavity

expansion theory to predict base resistance in sand. It is proposed that the cavity

expansion analysis of Carter *et al.* (1986) or Yu & Houlsby (1991) can be used to

evaluate the cavity limit pressure $p_{\lim it}$. These solutions are based on elastic-perfect

plastic soil model with Mohr-Coulomb failure criterion and a constant rate of dilation.

From vertical force equilibrium of soil wedge in Figure 2.30, the following

relationship between q_b and $p_{\lim it}$ is obtained:

$$q_b = p_{\lim it}(1 + \tan\alpha \cdot \tan\varphi) \tag{2.9}$$

where φ is the soil friction angle and α may be taken as $45 + \varphi/2$ for the soil wedge

under pile or is equal to $60°$ for a standard cone penetrometer.

The predicted base resistance in clay was first proposed by Gibson (1950), also using

spherical cavity expansion theory. Figure 2.31 (b) shows analogies between $p_{\lim it}$ and

q_b. Based on the vertical force equilibrium of soil wedge in Figure, q_b is given by:

$$q_b = p_{\lim it} + \alpha \cdot c_u \tag{2.10}$$

Cavity expansion theory, unlike bearing capacity theory, can take account both elastic

and plastic deformations, and also consider the influence of penetration process on

initial stress state and effects of stress rotations that occur around the cone tip in an approximate manner (Yu and Mitchell, 1998). However, in design, the use of a spherical cavity expansion method suffers the disadvantage of requiring a relatively large number of input parameters. The predicted cavity pressure is strongly dependent on the angle of dilation (Yu & Houlsby, 1991). Therefore, it is important to evaluate this parameter precisely. An accurate estimation of this parameter is difficult in practice since it varies significantly with stress state and strain level.

2.4.1.3 Correlations with Cone Penetration Test (CPT) and Piezocone (CPTU) data

The CPT test produces direct measurements of in-situ resistance under conditions that resemble closely those at a pile tip. The similar contained failure system and boundary conditions allow the CPT data to be used directly, without having to decouple the full set of complex soil parameters.

Correlations with the CPT data often take the following form:

$$q_b = \alpha \cdot q_c \qquad\qquad (2.11)$$

where α is an empirical coefficient and q_c is the total cone resistance

q_c is usually the averaged value over a vertical range to account the effect of local heterogeneities. A simple arithmetic average of q_c over a vertical range of +/-1.5D is widely used to derive q_c (Bustamante & Gianeselli, 1982; Randolph, 2003; Jardine *et*

29

al., 2005; White & Bolton, 2005).

A number of authors have proposed that α is less than unity. The factors influence the reduction factor are summarized by White (2002) and illustrated schematically in Figure 2.42. The most important reduction factors considered in design are due to partial mobilization and pile diameter.

The reduction factor due to partial mobilization is first considered by Fleming (1992) who proposed a hyperbolic relationship for bored piles, then further developed by Lee & Sagado (1999). They predicted that if piles were pushed down to a condition of continued penetration at constant load, the base resistance q_b would equal q_c.

The reduction factor due to pile diameter is studied by Chow (1997) based on a database of high-quality pile load test in sand. The q_c is obtained by averaging over +/-1.5D relative to the pile base, and q_b is that mobilized at a pile base displacement of 0.1D. The design curve proposed by Jardine & Chow (1996, 2005) is expressed as:

$$q_b = [1 - 0.5 \cdot \log(\frac{D}{D_{cone}})]q_c \qquad (2.12)$$

where D_{cone} =0.036m and lower limit of $q_b = 0.3q_c$ is suggest for piles with D>0.9m

This finding is evidenced by Eslami and Fellenius (1997). They concluded that the larger the pile diameter, the larger the movement required to mobilized the toe resistance.

The installation method also affects the α value. The α value is normally lower for non-displacement piles than that for displacement piles in the same type soil. For displacement piles, Jack-in piles, compared to driven pile, exhibit a stiffer base response and a greater base capacity if defined by settlement criterion. This is due to the stiffening effect of the final jacking stroke and the resulting residual base load. Thus for closed-end driven pile in sand, the UWA-05 design method recommends a value of $\alpha = 0.6$ in Equation 2.5 (Lehane *et al.,* 2005). For closed-end Jack-in piles, White & Bolton (2005) and Xu & Lehane (2005) found $\alpha \approx 0.9$ for a database of load tests based on settlement criterion of D/10.

The piezocone, which is a cone penetrometer equipped with a gage measuring the pore pressure at the cone immediately behind the cone, is a considerable advancement on static cone. In this test, q_c can be corrected for pore pressure and adjusted to "effective" stress, q_E. Eslami and Fellenius (1997) pointed out that the soil is governed by effective stress and Eq. 2.11 employs total stress value. Thus they proposed Eslami and Fellenius method which is based on effective stress, expressed:

$$q_b = C_t \cdot q_E \tag{2.13}$$

where C_t is the toe correlation coefficient

2.4.2 Prediction of shaft capacity

2.4.2.1 Total stress analysis for piles in clay

One of the traditional methods of estimating the ultimate unit shaft friction, τ_s, involves the use of the total stress method for piles in clay soils. This method relates τ_s relates to the undrained shear strength c_u as:

$$\tau_s = \alpha \cdot c_u \tag{2.14}$$

Usually α is less than unity and depends on the surrounding soil. The American Petroleum Institute (API, 1993) guidelines, based on total stress method, proposed estimating the shaft friction in clay from the following two equations:

$$\tau_s = 0.5\psi^{-0.5} \cdot c_u \quad \psi \leq 1, \ 0.5\psi^{-0.5} \leq 1 \tag{2.15}$$

$$\tau_s = 0.5\psi^{-0.25} \cdot c_u \quad \psi > 1 \tag{2.16}$$

where $\psi = \dfrac{c_u}{\sigma'_{vo}}$, σ'_{vo} is the effective overburden stress of soil

Karlsrud *et al.* (1992,2005) found the API (1993) does not predict the low shaft friction values measured in NC clays of low plasticity (Figure 2.32).Therefore, Karlsrud *et al.* proposed a modification of total stress method (NGI-99), that leads to a better agreement between calculated and measured capacities. The comparison between API-93 and NGI-99 is shown in Figure 2.33.

The enduring popularity of total stress method is due to its simplicity and low cost of

obtaining the undrained shear strength. However, this method should be used with caution, since the load transfer between a pile and the soil is governed by effective stress. Investigations on instrumented piles in clay (e.g., Bjerrum et al. 1965; 1969, Endo et al. 1969, Burland 1973, Konrad and Roy 1987, Bond and Jardine 1995, Fellenius 2008) have established that the pile resistance is proportional to the effective overburden stress in clay. Moreover, Fellenius (2008) commented that the total stress method is useful for the engineer working in a known soil, but it do not correlate consistently to pile unit shaft resistance in general.

2.4.2.2 Effective stress analysis in sands and clays

It is well accepted that the pile resistance is proportional to the effective overburden stress in sand. This phenomenon has also been found in clay, as mentioned in previous section. Based on this, the effective stress method (commonly termed as β method today) is first introduced by Bjerrum (1969) and shown in following equation:

$$\tau_s = \beta \cdot \sigma'_{vo} \tag{2.17}$$

Over the years, various refinements to Eq. 2.17 have been proposed. The API (1993) method, for example, defines:

$$\tau_s = K_s \tan \delta \cdot \sigma'_{vo} = \beta \cdot \sigma'_{vo} \tag{2.18}$$

where K_s =lateral stress coefficient; δ =pile-soil interface friction angle;

Since it is recognized that the friction fatigue does exist, new design methods have been proposed to capture the influence of h/R effect on K_s. Randolph *et al.* (1994) proposed design approach which suggests an exponential variation of radial stress along pile shaft in sand of the form

$$K_s = K_{min} + (K_{max} - K_{min})e^{-\mu h/D} \tag{2.19}$$

where K_{max} may be taken as a proportion of the normalized q_c, typically 1-2% of q_c / σ'_{vo}, K_{min} can be linked to the K_a, μ controls the rate of exponential decay.

Based on IC (Imperial College) field studies and database of high-quality pile load tests, Jardine and Chow (1996) have related K_s to q_c, "h/R" effect and dilatant increase in normal stress during pile loading and proposed a design method for displacement piles. The resulting design equations for driven pile in sand are shown below. The equations for pile in clay are discussed in detail in Section 2.2.2.1.

$$\tau_s = \sigma'_{rf} \tan \delta_f = (\sigma'_{rc} + \Delta\sigma'_r) \tan \delta_f \tag{2.20}$$

$$\sigma'_{rc} = 0.029 \cdot q_c (\sigma'_{vo} / P_a)^{0.13} \cdot (h / R)^{-0.38} \tag{2.21}$$

$$\Delta\sigma'_r = 2G \cdot \delta h / R \tag{2.22}$$

where σ'_{rf} is the local radial effective stress at failure, σ'_{rc} is the local radial effective stress after installation, P_a is the atmospheric pressure, $\Delta\sigma'_r$ is the dilatant increase in local radial effective stress during loading and δ_h is the pile roughness, equals to 0.02mm for lightly rusted steel pile.

A slightly modified form of Eq. 2.21 was suggested by Lehane et al. (2005). The shaft friction was calculated as:

$$\tau_s = 0.03 q_c \left(\frac{h}{d}\right)^{-0.5} \tan \delta \quad \text{for driven pile} \tag{2.23}$$

$$\tau_s = 0.03 q_c \left(\frac{h}{d}\right)^{-0.3} \tan \delta \quad \text{for jack-in pile} \tag{2.24}$$

Current prediction methods (Randolph *et al.,* 1994; Jardine and Chow, 2005; Lehane et al., 2005) accounting for friction fatigue can match more closely distribution of shaft friction observed during instrumented pile tests. However, Fellenius (2008) commented that not all parameters for Randolph *et al.,* (1994) and Jardine and Chow (2005)'s methods are determined for a routine design case and when they are, they vary considerably depending on natural variation and methods of determining them. Therefore, once the potential ranges of each parameter are considered, for any specific case, the results from their methods will range from the very small to very large variations in predictions.

2.4.3 Design method for NSF in piles

Although the NSF has been recognized since beginning of 20th century, the mechanism of NSF is still not fully understood by many engineers in practice. A number of fundamental issues have not been resolved yet. For example, in some text books, the NSF is been treated as "additional loads on the pile. The net effect is that the pile load

capacity is reduced and pile settlement increases. The allowable load capacity is given

as:"

$$Q_{allow} = \frac{Q_{ult} - Q_{neg}}{F_s} - Q_{neg} \qquad (2.25)$$

where Q_{ult} is geotechnical axial load capacity of the pile

Some design codes such as the "EuroCode 7" by the European Community and the

"Singapore Standard: Code of Practice for Foundations"(CP4) by Building and

Construction Standards Committee of Singapore (2003) have adopted this concept.

However, Fellenius (1997) and Poulos (1997) clearly stated that NSF or dragload do

not diminish geotechnical axial load capacity of the pile and these recommendations

on how to consider NSF in pile are not correct. Based on many years' observations

from field tests, Fellenius (1998, 2004) further deemed that "The dragload is of

concern only for the pile structural strength and the designer must ensure the load can

be accommodated without the pile experiencing structural distress. The dragload must

not be added to the loads from the structure when checking that the design load does

not exceed the allowable load. Neither should the capacity value be reduced by the

dragload. Treating the dragload as a load similar to the loads from the structure is a

very costly error.". Based on Fellenius "Unified Design Method" (UDM), the allowed

load can be determined by geotechnical axial load capacity of the pile divided by an

appropriate factor of safety. For example, if the Q_{ult} is 1400 kN established from static

loading test, dragload is established to 300 kN and factor of safety is 2.0. The factored

dead and live load is 700 kN in total. Then using Fellenius's concept, $Q_{allow} = 700\,\text{kN}$

while based on "EuroCode 7" or "CP4", $Q_{allow} = 250\,\text{kN}$ which means the length of pile will be significantly increased and number of the piles will also be considerably increased to meet the design requirement. Moreover, Fellenius's "Unified Design Method" is based on the interaction between forces and movements and considered capacity, dragload and settlement, which are three major aspects in design of a pile foundation. The principles of the mechanism are illustrated in Figure 2.34. The "Unified Design Method" has been adopted by some foundation design codes such as the "Canadian Building Code and Highway Design Code" (1992), "Civil Design Criteria for Road and Rail Transit System" by Land Transport Authority of Singapore (2002), the "Australian Piling Standard" (1995) and "Pile Design and Construction" by Geotechnical Engineering Office of Hong Kong (2006). The Unified Pile Design Analysis can be conducted in an iterative procedure suggested by Fellenius (2011) and summarized as:

1. Calculate and plot the distribution of the shaft resistance and determine toe resistance and toe movement curve.

2. Calculate and plot the distribution of soil settlement developing after the sustained load has been place on the pile.

3. Assume a location of the NP and use the toe resistance relation (determined in step 1) to determine the additional toe force that fit the NP location as force equilibrium and the toe movement that will fit the NP as settlement equilibrium.

4. Repeat step 3 as necessary with a new NP until the determined toe force and net toe movement (toe penetration) agree with that corresponding to toe resistance

relation (determined in step 1).

However, the transition zone for skin friction is not considered in the iterative procedure and fully mobilized skin friction is assumed. This postulation will considerably overestimate the dragload when the settlement of soil is small. The factors which affect the transition zone have not been fully investigated in the method. In addition, the universal applicability of "Unified Design Method" has actually not been tested rigorously by all kinds of piling condition. Evidently more studies need to be conducted to verify and improve Fellenius' "Unified Design Method".

2.4 SUMMARY

This review of previous piling researches can be summarized as follows:

- Recent field tests and centrifuge tests have revealed a number of features of displacement pile behavior, particularly in relation to "h/R" effect during the installation stage, the distribution of shaft friction, and changes in total stress and excess pore pressure throughout equalization within and around displacement pile in clay. In practice, ICP (Imperial College Pile) design method (Jardine *et al.,* 2005) based on high quality load test database offers improved prediction of capacity of driven pile in both sand and clay.

- Generally applicable conclusions which are very important for design of pile

foundations were found from many well-documented cases. The Neutral Plane, NP is the location of the force equilibrium in pile as well as the location where there is no relative movement between the pile and the soil. Negative Skin Friction, NSF or dragload do not act like an applied load from the superstructure. It involves a complex pile-soil interaction and is a function of the relative pile-soil displacement.

- The installation of Jack-in piles causes the soil around the pile to be pushed away radially which leads to significant increase in the stresses of the soil surrounding the pile. These large changes in shear strains and stresses complicate the problem. The complexity of the problem and their interaction explain why little or no progress has been made up to now in modeling of displacement piles in FEM analysis (Broere & Van Tol, 2006) and evidently more studies need to be conducted for further improvements.

- The prediction of base resistance remains highly empirical. Similar failure system and boundary conditions of piles and CPT allow the CPT data to be used directly. However, reduction factors should be considered in using cone data to predict pile capacity, especially reduction factors due to partial mobilization and due to pile diameter in sand.

- The pile shaft resistance is proportional to the effective overburden stress. New design methods (Randolph *et al.,* 1994; Jardine and Chow 2005) which are based on effective stress method considered the friction fatigue effect on shaft friction capacity and can predict good results of shaft friction at field scale.

However, their methods are difficulty to apply to engineering design as installation methods strongly influence the rate of decay.

- Additional uncertainty in the prediction and measurement of pile capacity arises from NSF. Many engineers and some design codes still treat NSF or dragload as another load and lump it together with the dead and live loads. This wrong concept usually makes for costly design. Fellenius's "Unified Design Method" corrects the misconceptions and considered capacity, dragload and settlement together. However, more studies still need to be conducted to verify and improve Fellenius' "Unified Pile Design Method".

In summary, although, enormous research has been performed, the accurate estimation of the pile axial capacity is still a very difficult task. The numerical studies on prediction of pile behavior need to be improved to get a good picture on change of soil stress state during installation and subsequent loading, which will influence the pile behavior, in order to improve the accuracy of the design of single axially loaded pile.
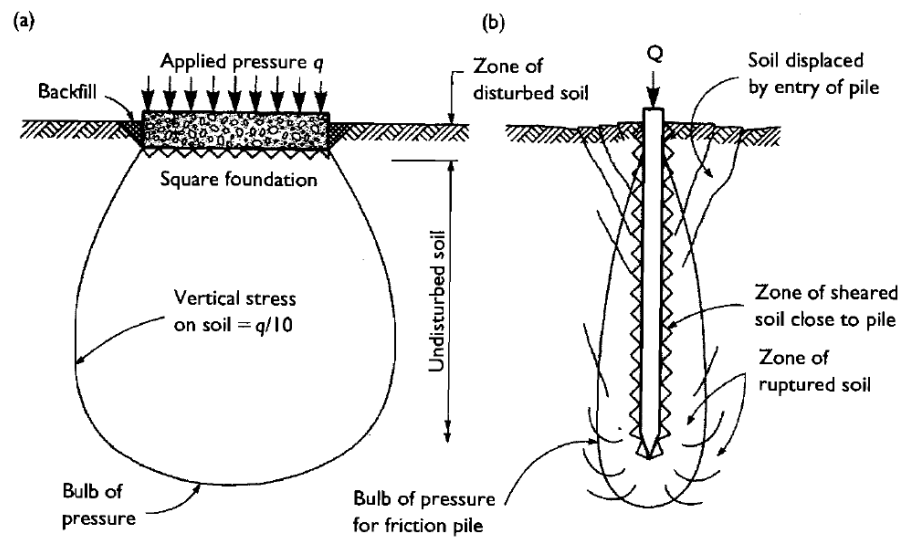
Figure 2-1 Comparison of pressure distribution and soil disturbance beneath spread and piled foundations (a) Spread foundation (b) Single pile (Tomlinson *et al.*, 2008).
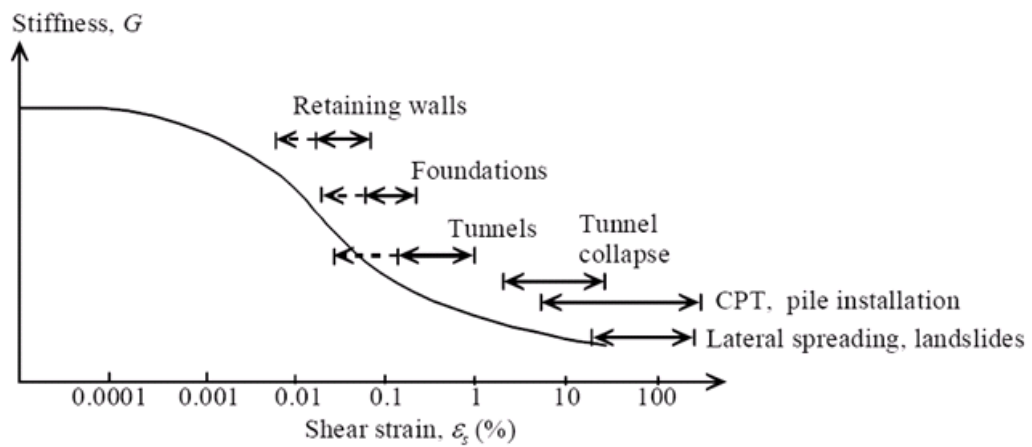
Figure 2-2 Strain levels in the geotechnical world (after Mair, 1993).
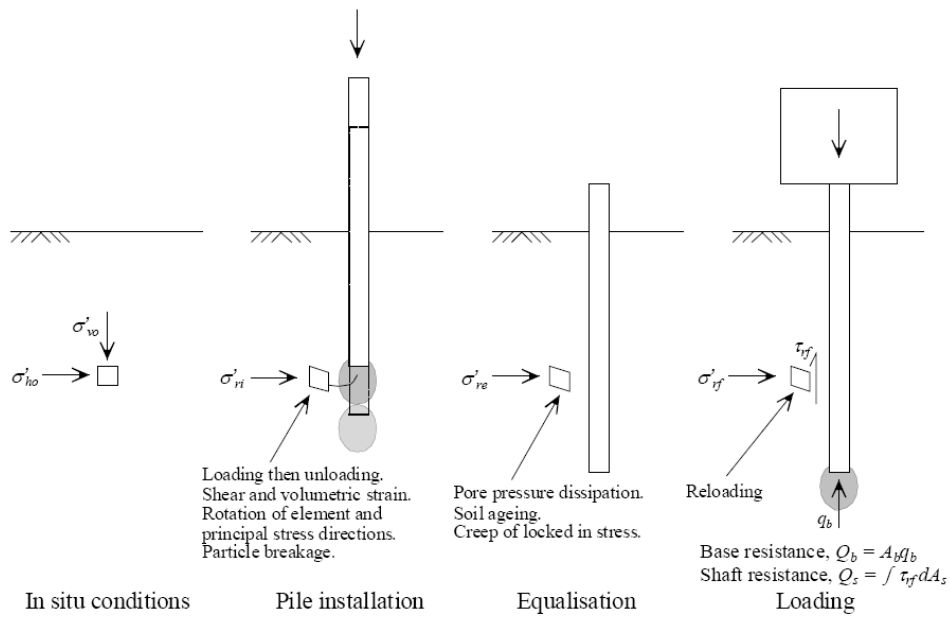
Figure 2-3 Stress history of a soil element close to displacement pile (White, 2002).
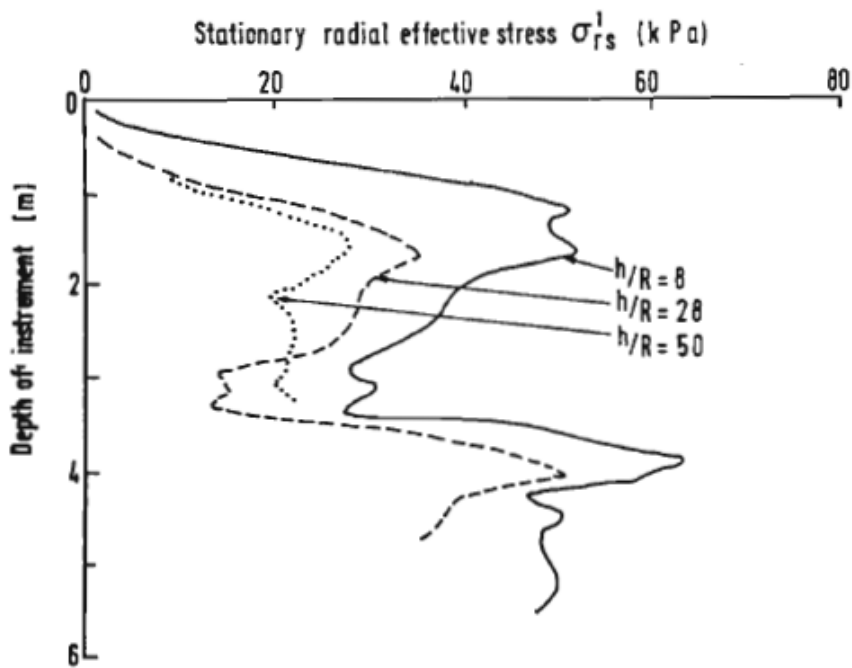
Figure 2-4 Radial effective stress during installation (Lehane *et al*, 1993).
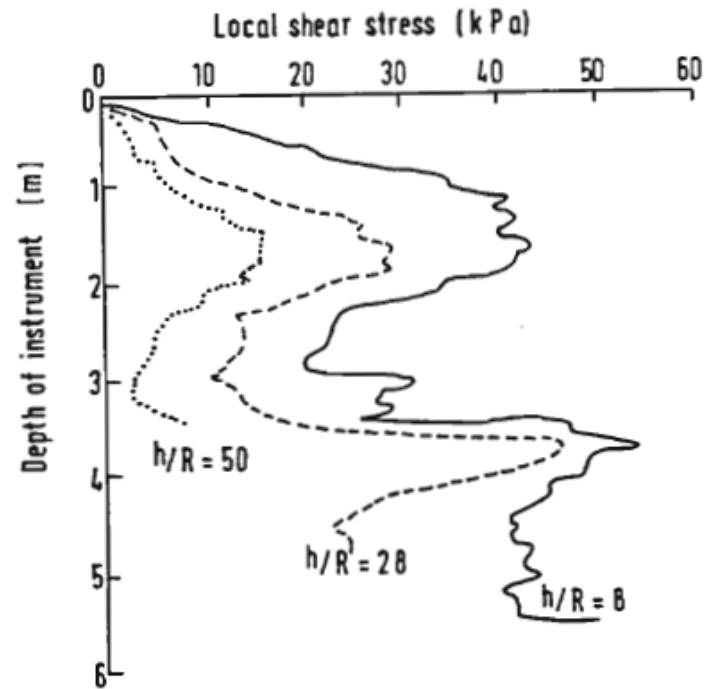
Figure 2-5 Local shear stress during installation (Lehane *et al*, 1993).
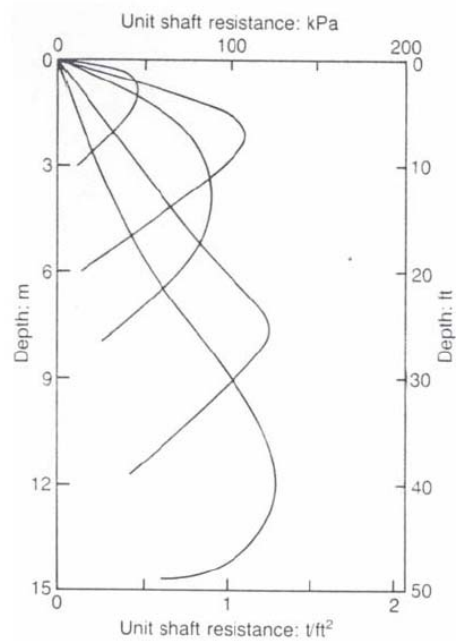
Figure 2-6 Measurement of shaft friction distribution (Vesic, 1970).
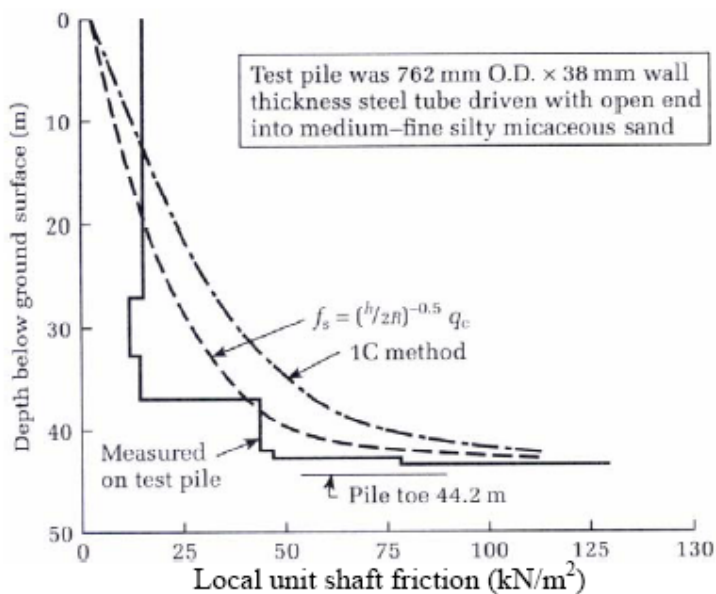
Figure 2-7 Field measurement of shaft friction distribution (Tomlinson, 2001).
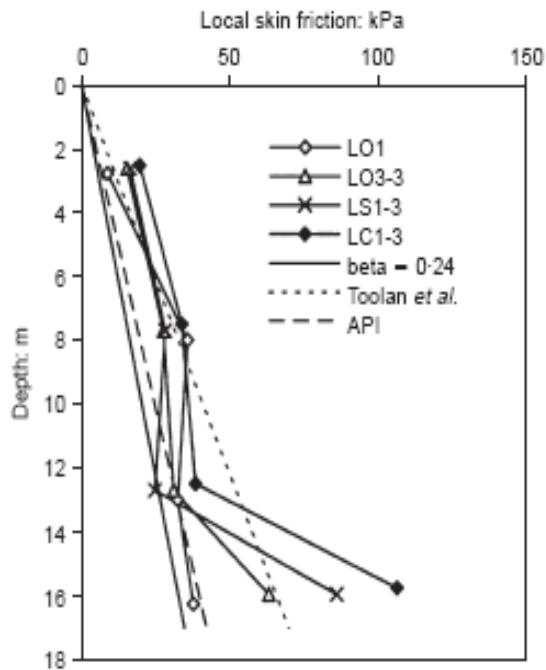
Figure 2-8 Measurement of shaft friction distribution on centrifuge model piles (De Nicola, 1996).
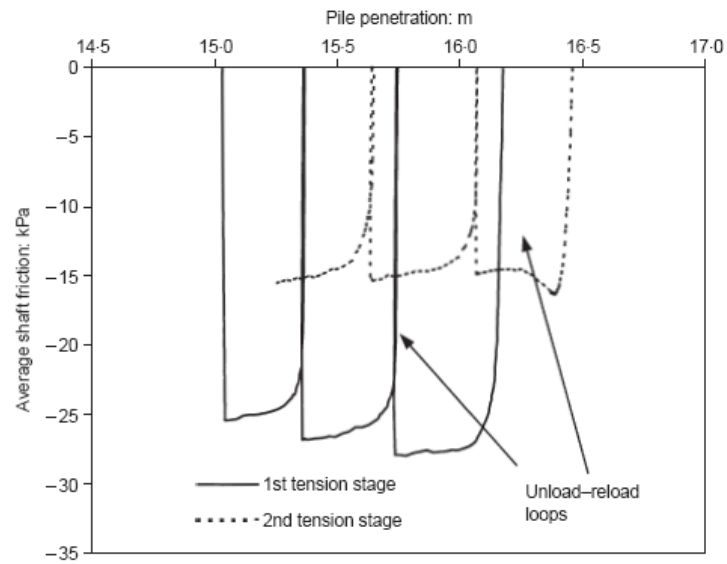
Figure 2-9 Shaft friction degradation due to unload-reload loops (De Nicola and Randolph, 1999).
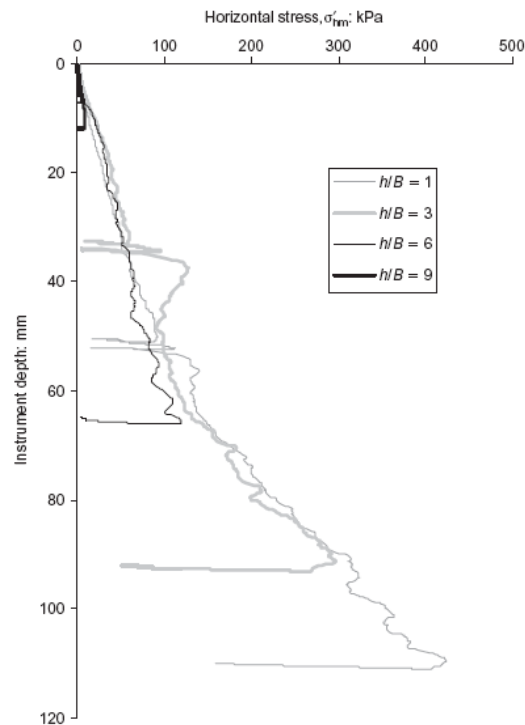
Figure 2-10 Horizontal stress measurements during monotonic installation (White & Lehane, 2004).
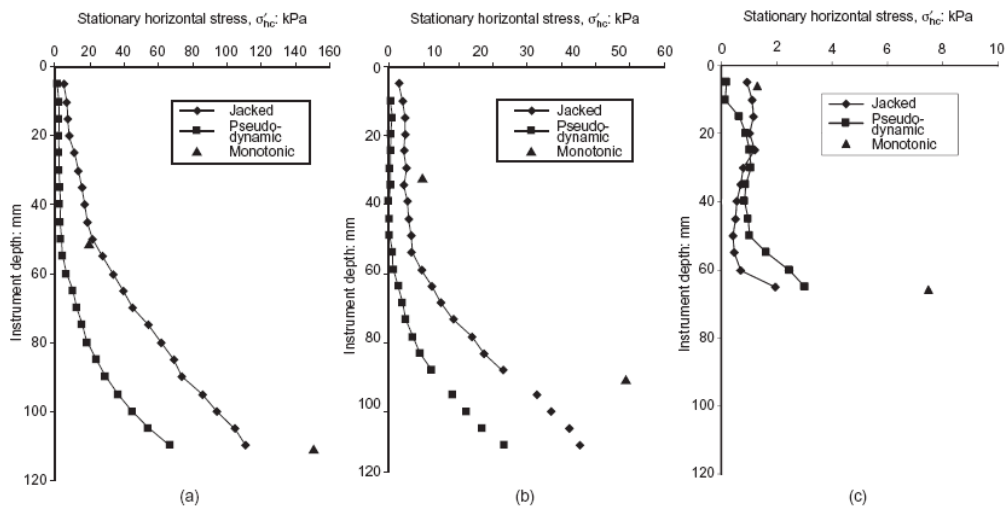
Figure 2-11 Variation of stationary horizontal stress with different installation method, (a) h/R=1, (b) h/R=3 and (c) h/R=6 (White & Lehane, 2004).

$$U_d = \left(\frac{u_{max} - u}{u_{max} - u_o} \right)$$
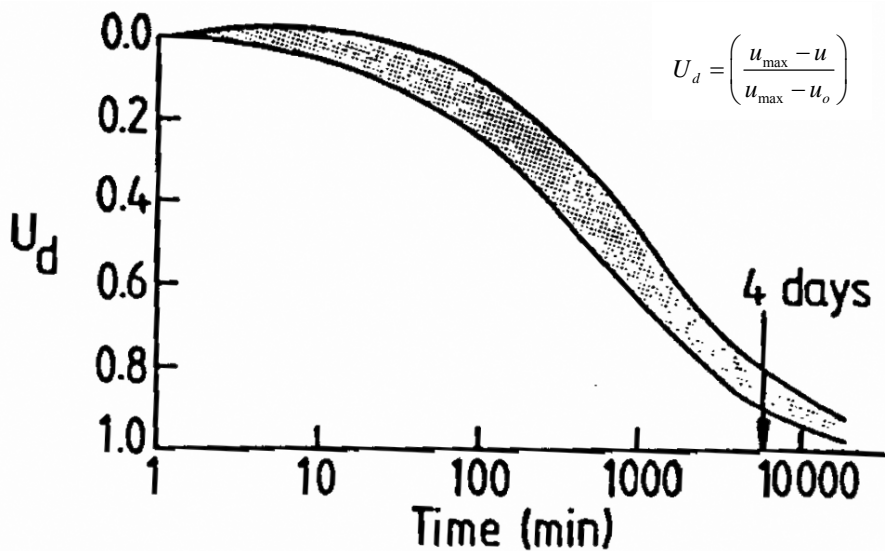
Figure 2-12 Equalization pore pressure measurements (Lehane & Jardine, 1994).
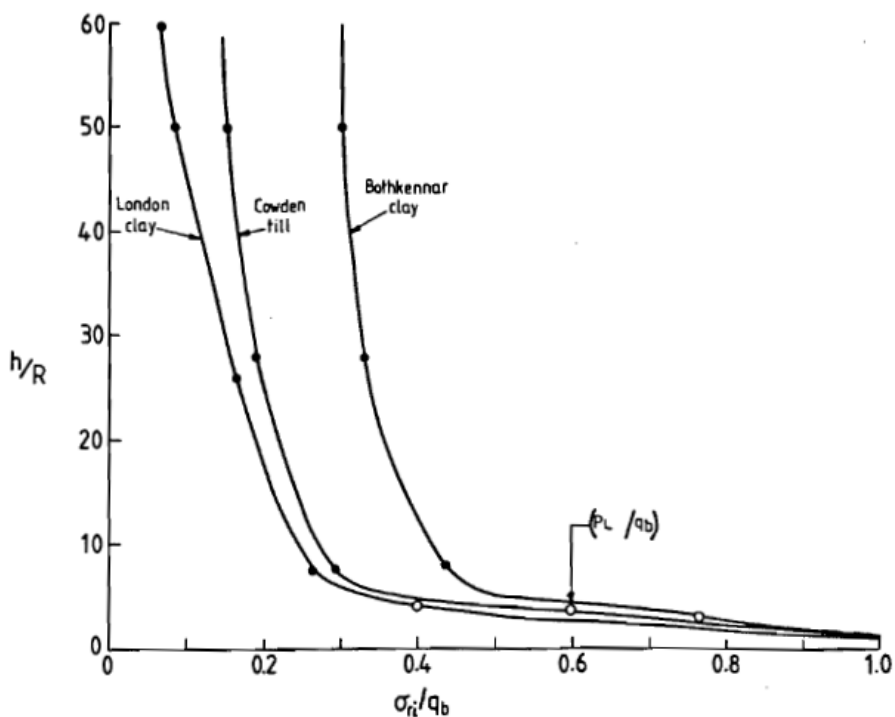
Figure 2-13 Normalized installation radial total stresses (Lehane & Jardine, 1994).

$$\frac{H}{H_i} = \left(\frac{\sigma_r - u_o}{\sigma_{ri} - u_o} \right)$$
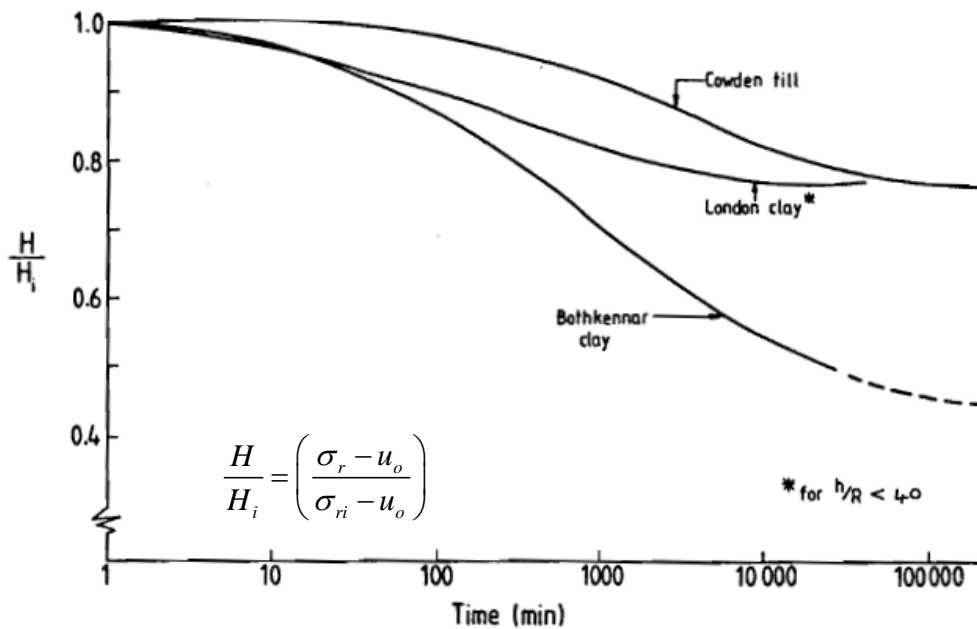
Figure 2-14 Relative reductions in radial total stress during equalization (Lehane & Jardine, 1994).
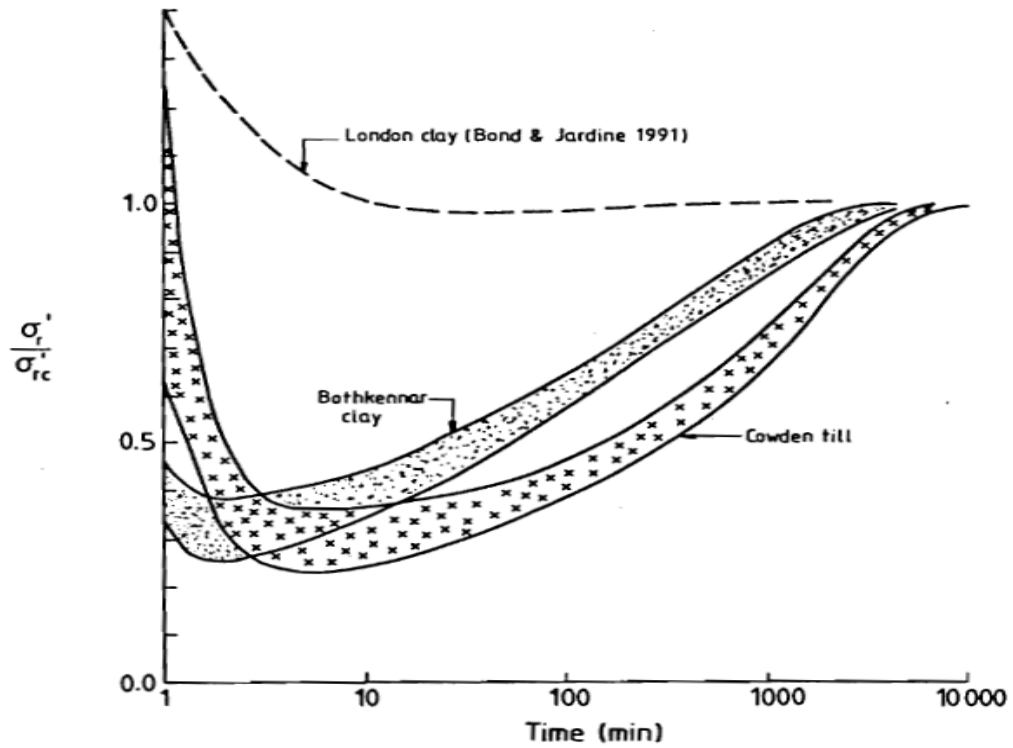
Figure 2-15 Normalized variations of radial effective stress during equalization (Lehane & Jardine, 1994).
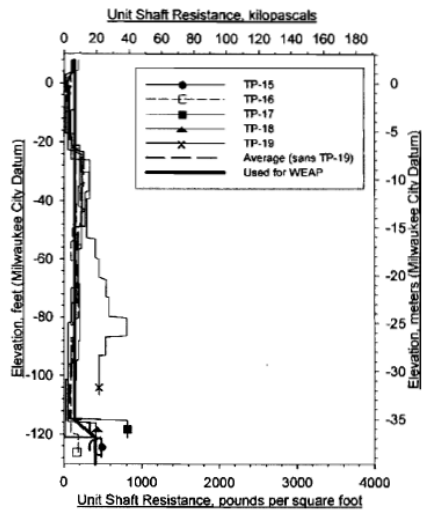
(a) EOID
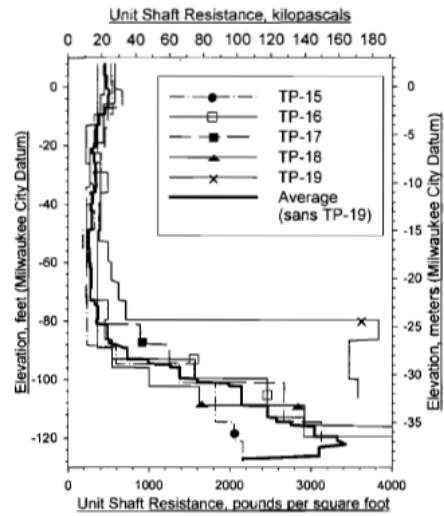
(b) After EOID
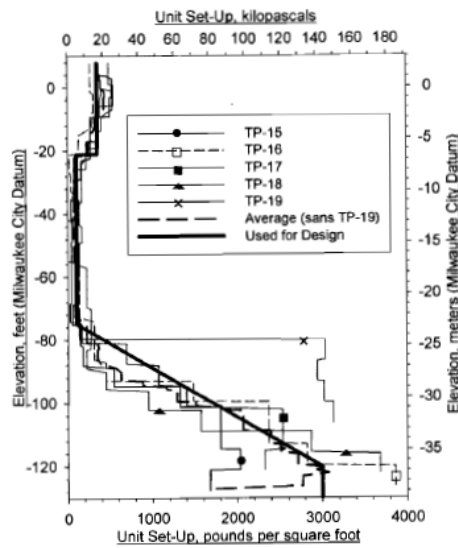
(c) Set-up

Figure 2-16 CAPWAP unit shaft resistance distribution (Komurka, 2003).
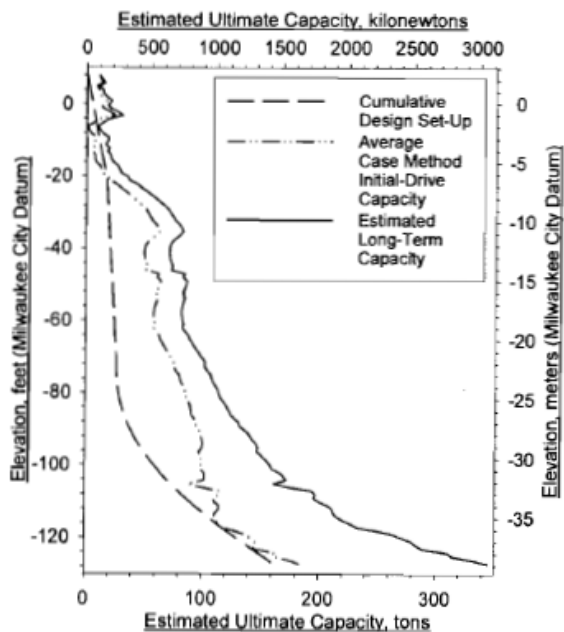
Figure 2-17 Estimated ultimate capacity vs. elevation (Komurka, 2003).
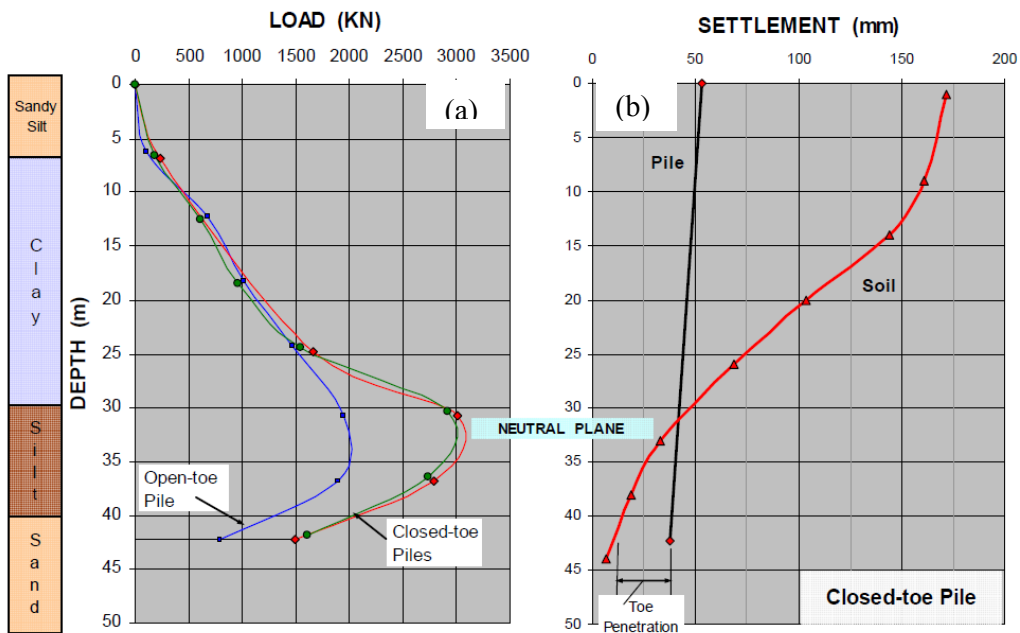
Figure 2-18 (a) Distribution of load in the pile; and (b) Distribution of soil and pile settlement 672days after start of monitoring (Fellenius, 2006).
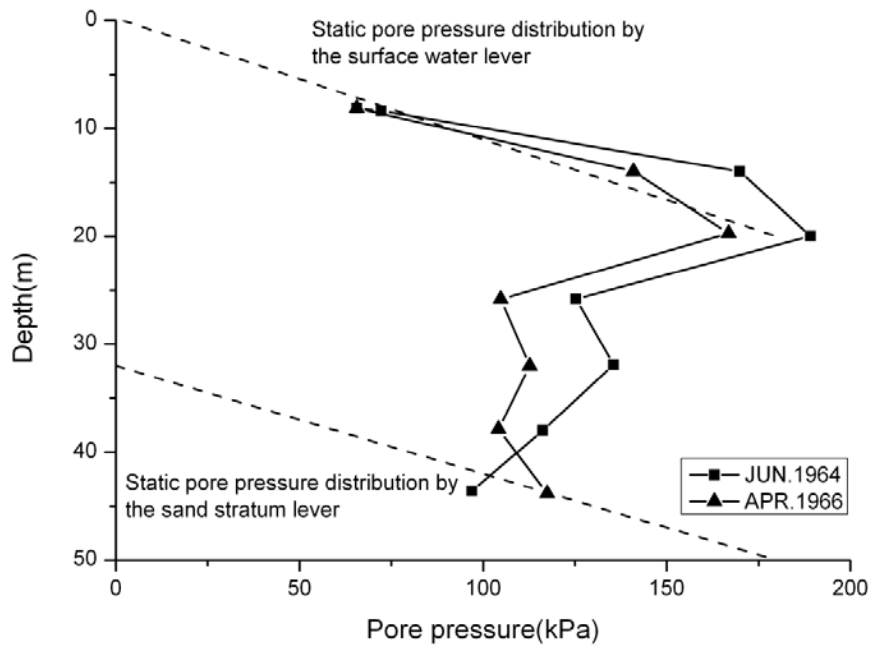
Figure 2-19 The measured distribution of pore pressure at start of monitoring and two years later (Data from Endo et al., 1969).
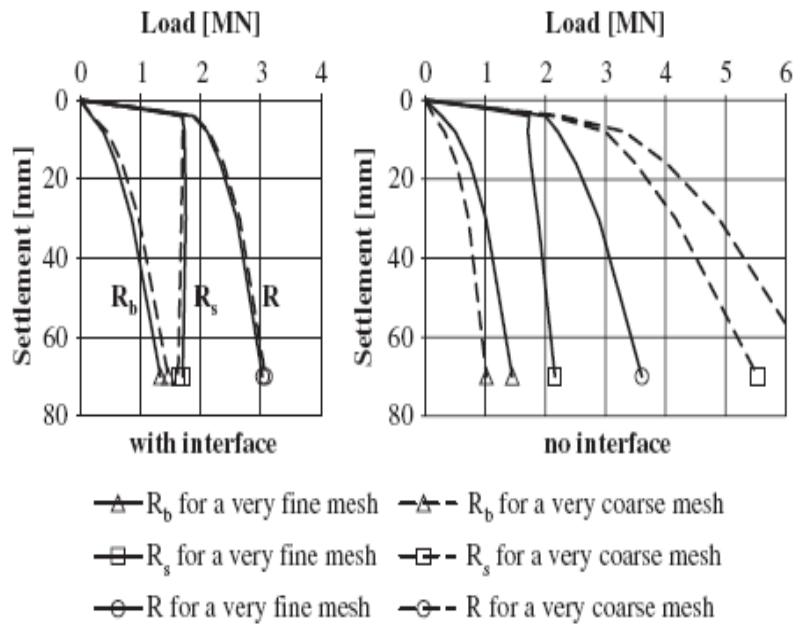
(a) MC model
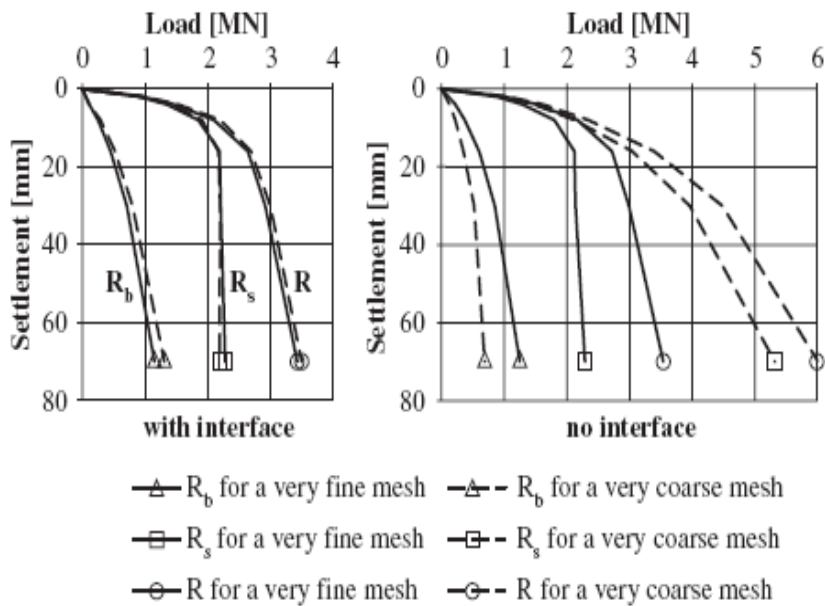
(b) HS model

Figure 2-20 Mesh dependency with interface elements and without interface elements (Wehnert and Vermeer, 2004).
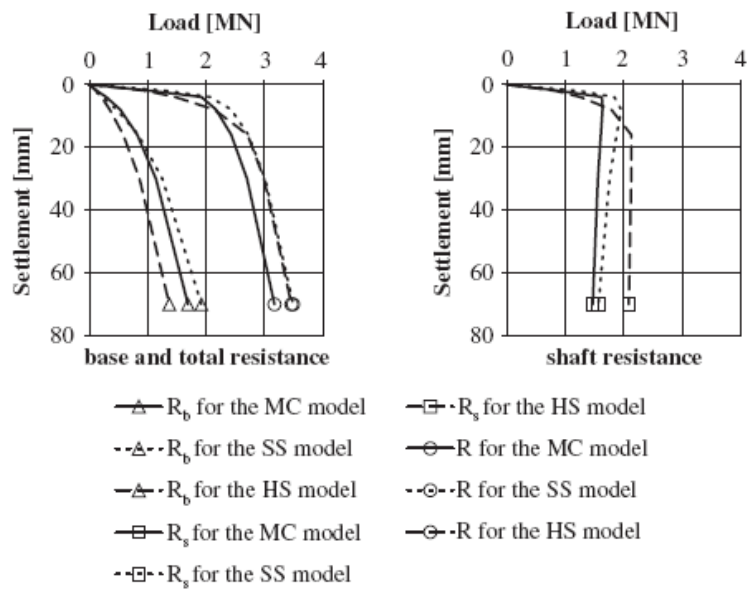
Figure 2-21 Base resistance R_b, shaft resistance R_s, and total resistance R for the MC, the SS and the HS models (Wehnert and Vermeer, 2004).

52
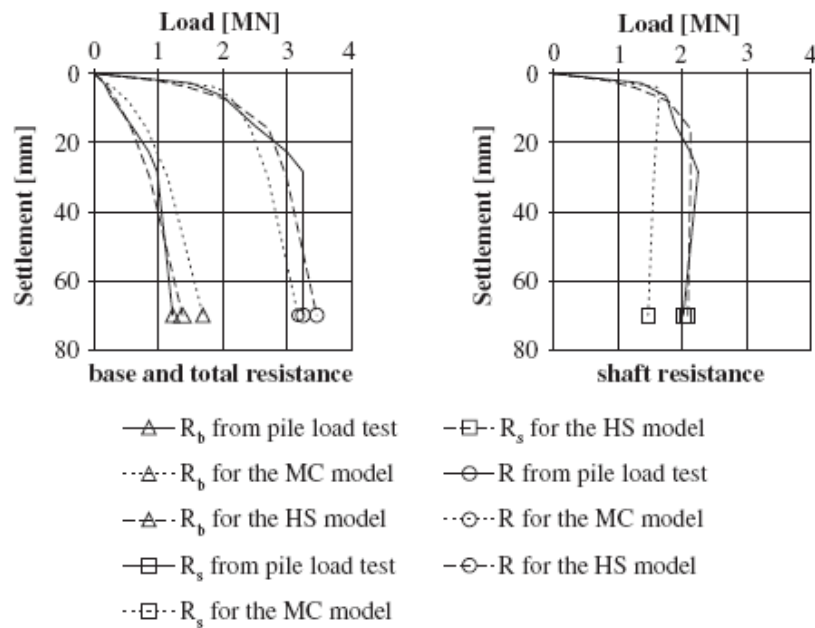
Figure 2-22 Results of the pile load test of the MC and the HS models for Base resistance R_b, shaft resistance R_s, and total resistance R, compared to pile load test(Wehnert and Vermeer, 2004).
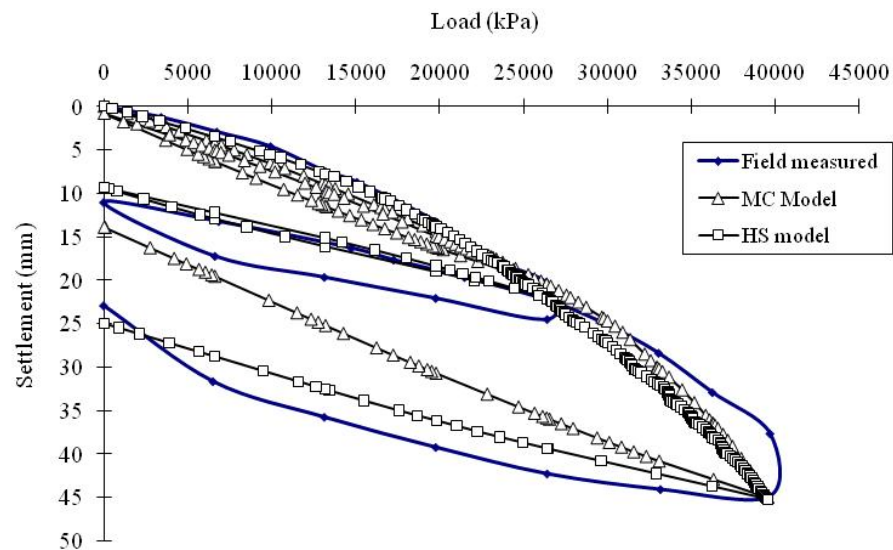
Figure 2-23 Results of the pile load test of the MC and the HS models, compared to pile load test (Li, 2004).
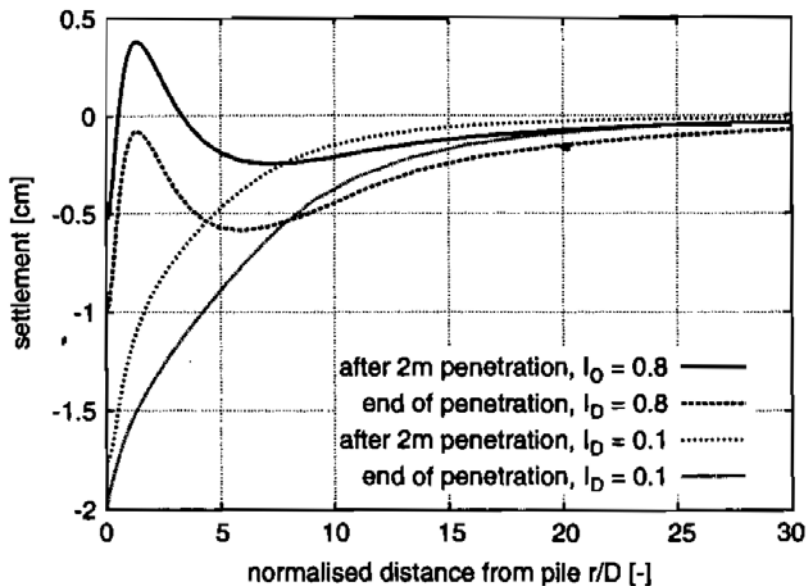
Figure 2-24 Vertical surface displacements during pile jacking for different penetration depths (Mahutka *et al.*, 2006).
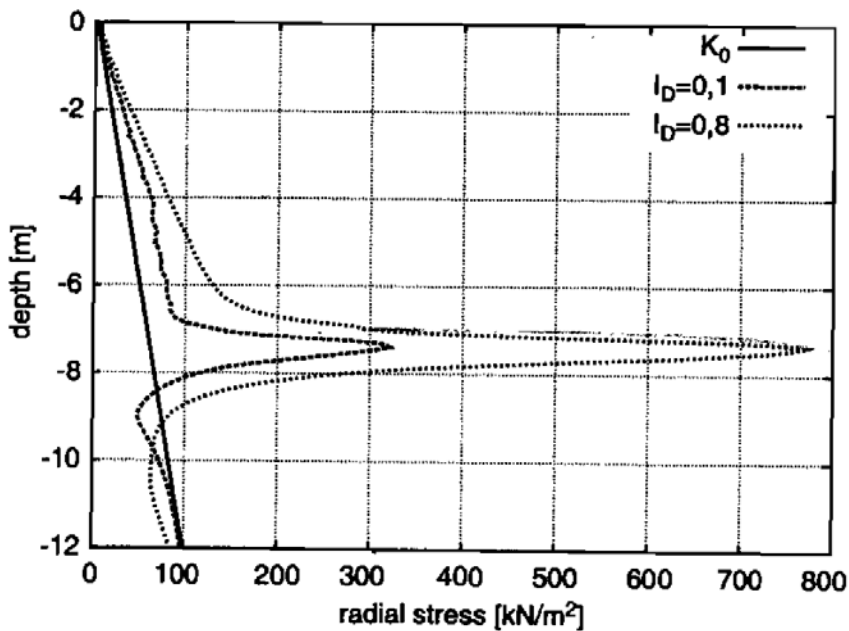
Figure 2-25 Lateral earth pressures after pile jacking along a vertical cross section at a distance 10cm from the pile shaft (Mahutka *et al.*, 2006).
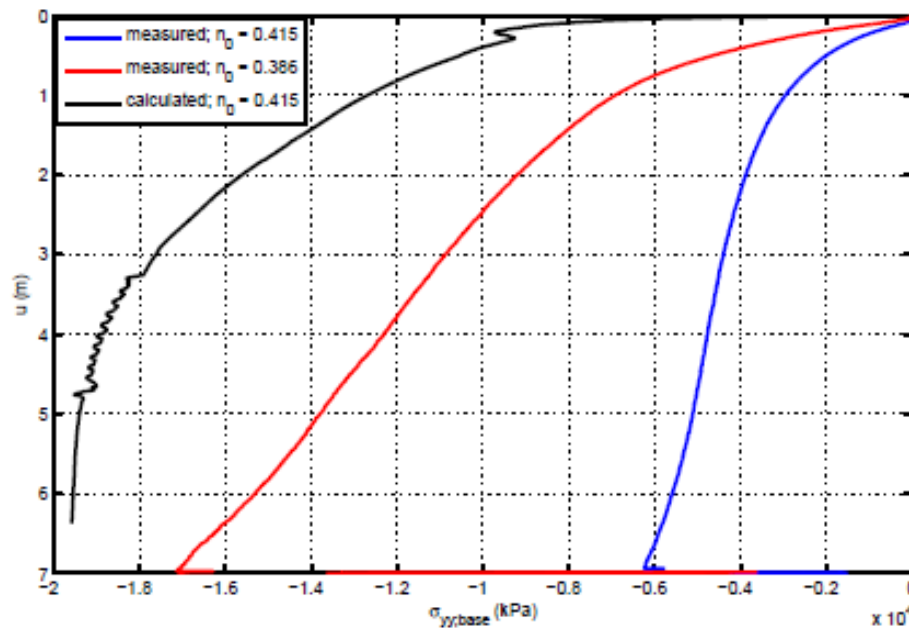
Figure 2-26 Numerical simulation of the bearing capacity of the displacement pile versus movement (Anaraki, 2008).
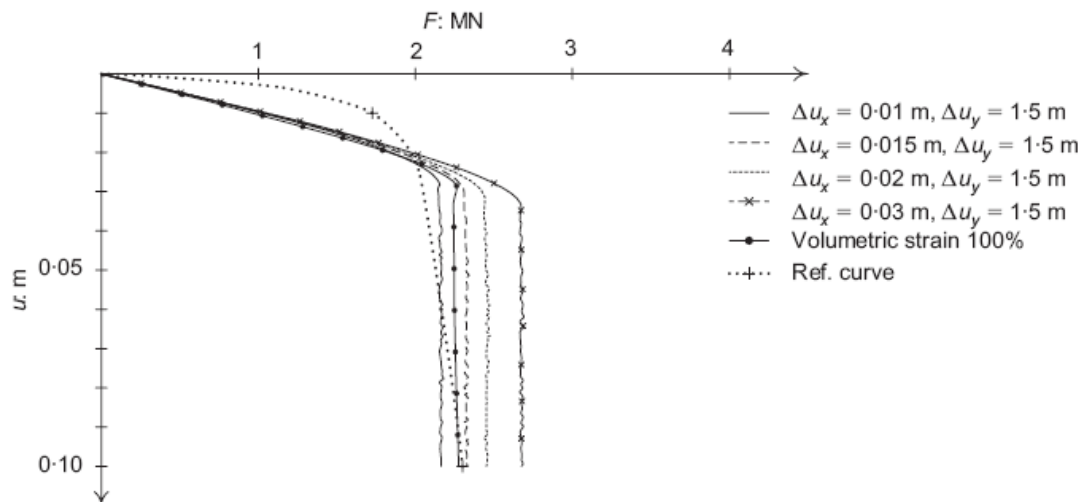
Figure 2-27 Load-settlement curves for meshes with an initial prescribed displacement at border of the pile volume, compared with the case of 100% initial volume strain (Broere & van Tol, 2006).
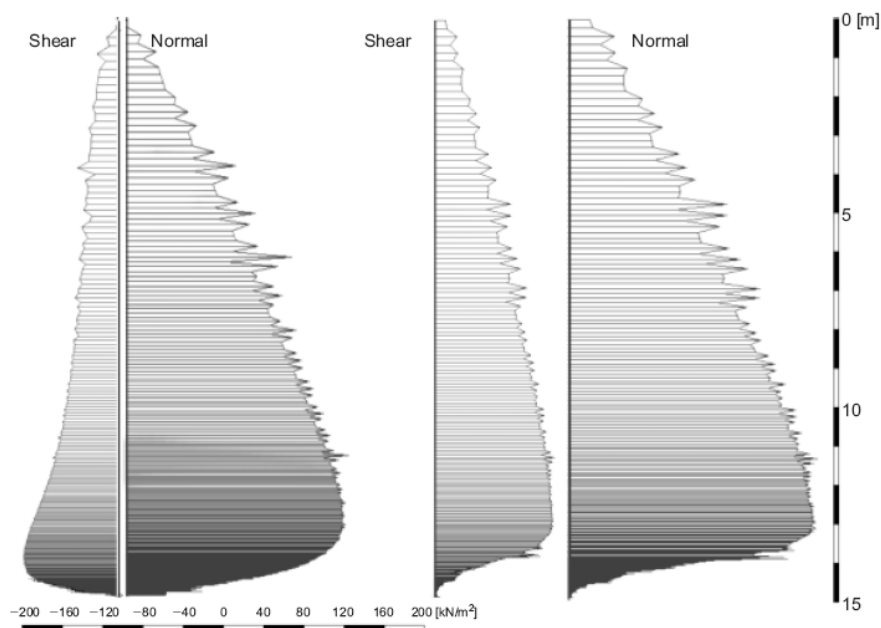
Figure 2-28 Normal and shear stresses in the pile-soil interface after pile installation (left) and at failure (right) (Broere & van Tol, 2006).
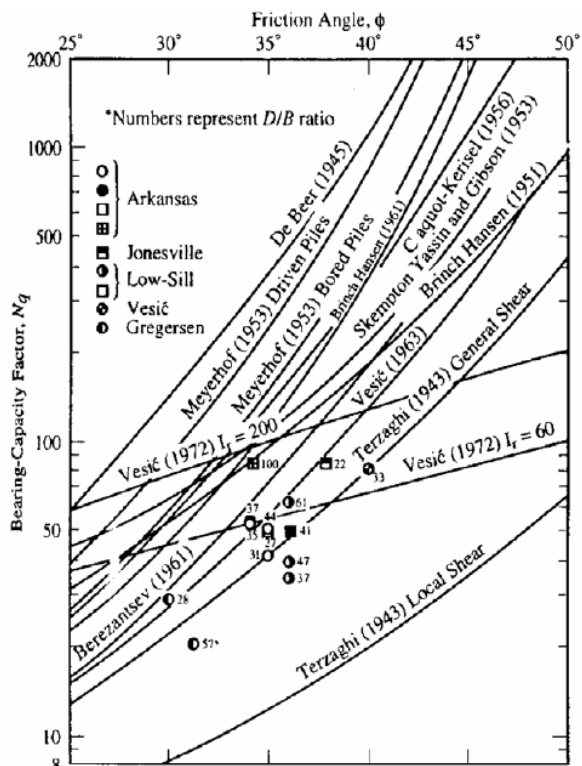
Figure 2-29 Bearing capacity factor N_q proposed by different authors (Coyle & Castello, 1981).

(a) Randolph *et al.* (1994)   (b) Gibson (1950)
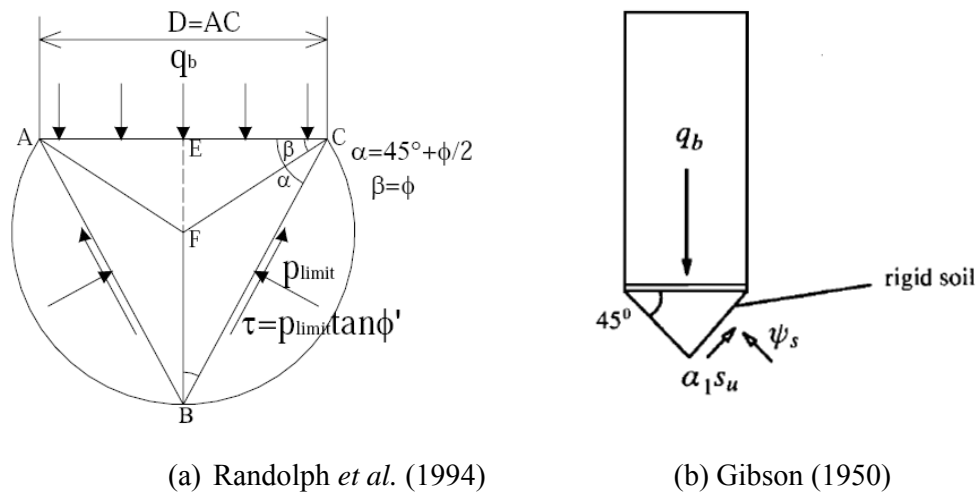
Figure 2-30 Assumed relationships between pile base resistance q_b and cavity limit pressure p_{limit} in (a) sand and (b) clay.
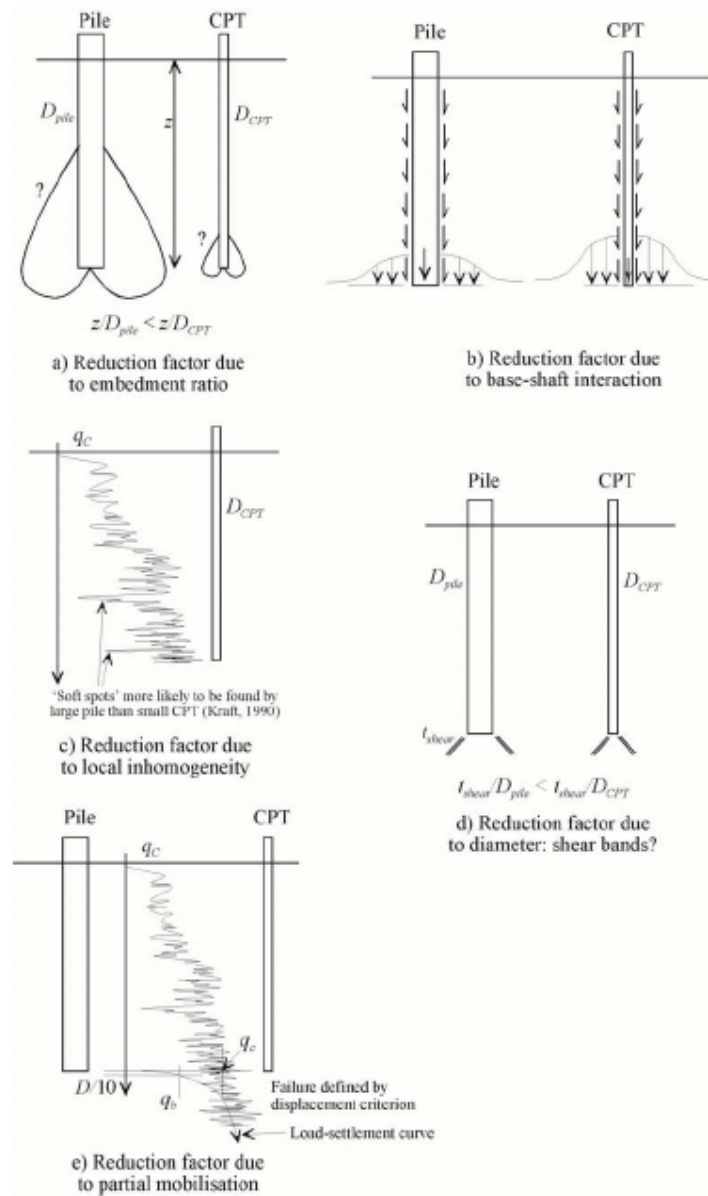
Figure 2-31 Factors influencing the reduction factor between CPT and base resistance (White, 2002).
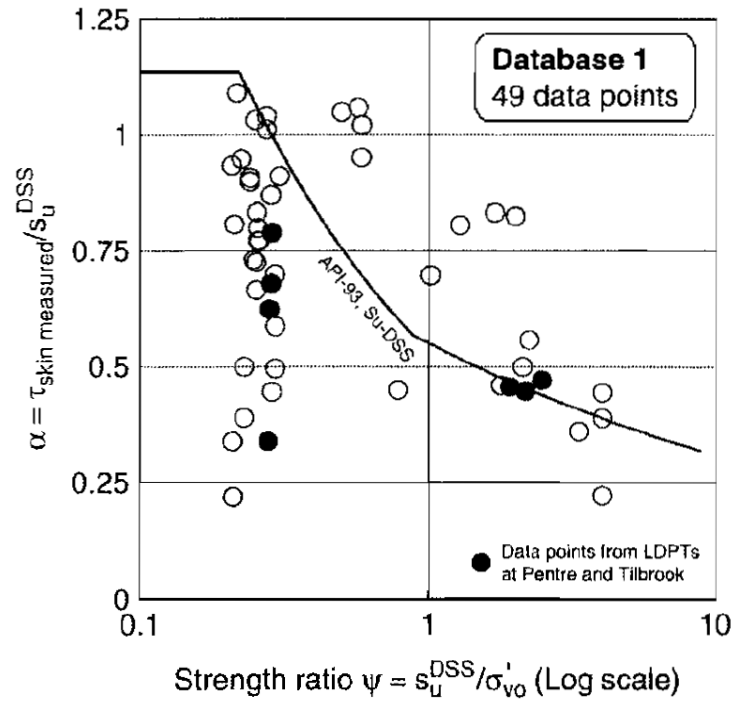
Figure 2-32 API (93) compared with field shaft friction measurement (Karlsrud *et al*, 2005).
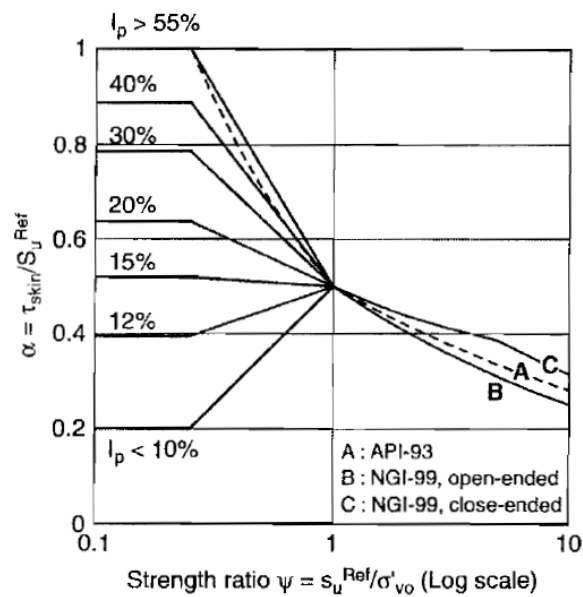
Figure 2-33 Comparison of between NGI-99 and API-93 (Karlsrud *et al*, 2005).
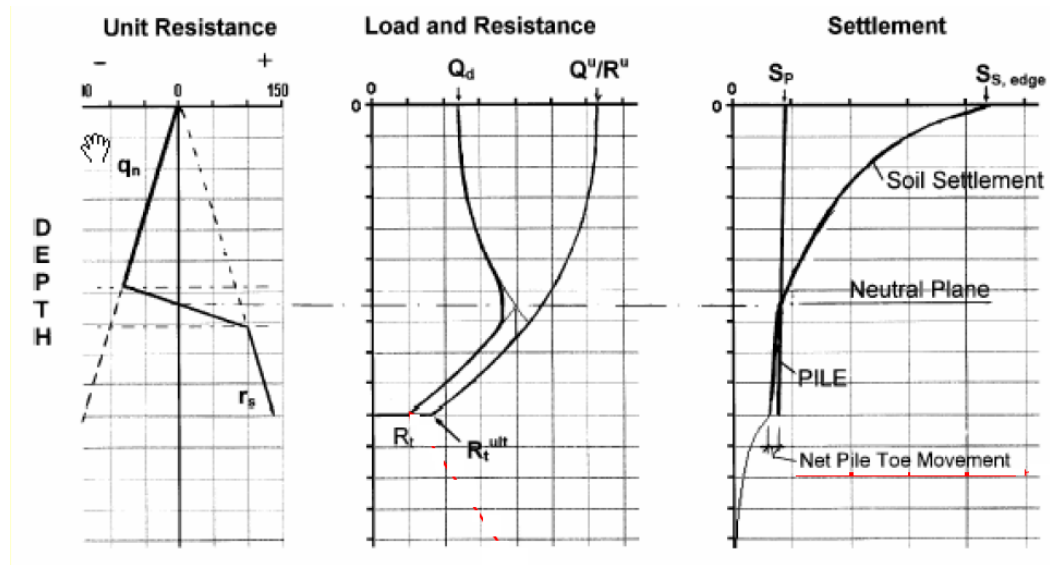
Figure 2-34 The principles of the mechanism of the Unified Pile Design method proposed by Fellenius (1997).

CHAPTER 3 CONSTITUTIVE MODEL

3.1 INTRODUCTION

Over the last fifty years, constitutive soil models have undergone considerable improvement and many advanced and sophisticated constitutive models have been proposed to simulate the complex soil behavior. Nowadays, users of any of the commercially available finite element packages, like PLAXIS, ABAQUS, can choose from several constitutive soil models, which were available only for researchers and specialists a few years ago. Potts *et al*.,(2002) stated that the correct selection of a soil model is important and designer should not use either a too simple model that does not consider the relevant features of the problem, or a too complex one, which could mask the main aspects of the solution and require the determination of obscure material properties. Therefore, this chapter will present some possible constitutive soil models used in this thesis.

Firstly, the backgrounds of the constitutive soil models (i.e., Mohr-Coulomb model, Hardening Soil model and Hypoplastic model) and the determination of input parameters for these models from in-situ and laboratory tests are presented. Thereafter,

evaluations of different constitutive models behavior on single element test and

modeling pile behavior are described. Finally, the application of Hypoplastic model to

soil-pile interface is presented.

3.2 CONSTITUTIVE MODEL

The selection of the presented constitutive soil models are within the scope of this

study. Only the isotropic behavior is considered in all the cases and the influence of

anisotropy is not been taken into account.

3.2.1 Mohr-Coulomb model

Mohr-Coulomb (MC) model is a linear elastic perfectly plastic model. It is one of the

first generation of soil models which cover the long period between the work of

Coulomb in 1773 and the rise and development of finite element method in 1960s. The

strain is decomposed into elastic and plastic part in MC model, like all the elasto-

plastic models:

$$\varepsilon = \varepsilon^e + \varepsilon^p \tag{3.1}$$

In order to evaluate whether plasticity occurs, a yield function, named f, is

introduced. The plastic yield coincides with the failure condition in the MC model.

Thus, the yield surface is fully defined by model parameters and not affected by

straining. Within the corresponding fixed yield surface in stress space the behavior is

purely elastic and all strains are reversible. The failure criterion of the MC model is

shown in Figure 3.1 which is governed by the cohesion c' and the effective friction angle φ', expressed as:

$$\tau_f = c' + \sigma_f \tan \varphi' \qquad (3.2)$$

The failure criterion can also be expressed in terms of effective principal stresses and Eq. 3.2 can be transformed into:

$$(\sigma_1' - \sigma_3') = (\sigma_1' + \sigma_3')\sin \varphi' + 2c'\cos \varphi' \qquad (3.3)$$

By rearranging the failure criterion in Eq.3.2, the yield function, f, can be obtained:

$$f = (\sigma_1' - \sigma_3') - (\sigma_1' + \sigma_3')\sin \varphi' - 2c'\cos \varphi' \qquad (3.4)$$

When yield condition is extended to general states of stress, the full MC yield criterion consists of six yield functions in effective principal stresses. These six yield functions together represent a hexagonal cone in effective principal stress space as shown in Figure 3.2. Stress state with $f > 0$ (Outside the cone) is not acceptable. $f = 0$ (On the cone), plasticity occurs. $f < 0$ (Inside the cone), the soil behaves linear elastic.

According to the classical theory of plasticity (Hill 1950), plastic strain rates are proportional to the derivative of the yield function with the respect to the stresses. However, this classic form of theory (so called associated plasticity) leads to overestimate of the plastic volumetric changes. Therefore, in addition to the yield function, f, a plastic potential function, g, is introduced. The plastic strain rates then are proportional to the derivative of the potential function. The plastic potential function, g, is defined as yield function in dependence of the effective principal

stresses and the dilatancy angle ψ rather than the effective friction angle φ', and is expressed as below:

$$g = (\sigma_1' - \sigma_3') - (\sigma_1' + \sigma_3')\sin\psi - 2c'\cos\psi \qquad (3.5)$$

In summary, the MC model is a simple elastoplastic model with fixed yield surface (no hardening or softening). Within the fixed yield surface, the behavior is purely elastic. The MC model requires five parameters: E, v, φ', c' and ψ, which are familiar to most geotechnical engineers and can be easily obtained from basic tests. This is why the MC model has enduring popularity and become a standard model in practice. However, such a fact does not imply anything about its suitability. Many limitations of the MC model can be found. For example, the fixed yield surface in effective principal stress space in the MC model means the model cannot capture the strain hardening or softening behavior which can be observed in most soils. The volume increase due to the dilatancy during plastic shearing is not limited which is also unrealistic for the real soil. Moreover, the MC model does not take into account the history of stress and strain. Consequently, it is not possible to distinguish between 'primary loading', 'unloading' and 'reloading' inside the yield surface. As a result, the calculation of bearing capacity of the displacement pile can be highly unrealistic. Although the MC model has many drawbacks, it can be used as the first model in FEM calculation to get better understanding of the problem and to verify results from FEM with Closed-form solutions before working with advanced soil models.

3.2.2 Hardening Soil model

The hardening soil (HS) model was developed by Schanz (1998) and Schanz et al. (1999) on the basis of the Double Hardening model by Vermeer (1978). In order to avoid some of the limitations of the MC model, the yield surface of the HS model is not fixed in effective principal stress space. It can expand due to plastic straining. Therefore, the HS model can simulate irreversible plastic strains due to primary compression in the oedometer loading and the isotropic loading (So-called compression hardening) and the irreversible plastic strains due to the primary deviatoric loading (So-called shear hardening). Other important features of the HS model are stress-dependent stiffness which stiffness is dependent on effective stress according to a power law and distinguishing between 'primary loading', 'unloading' or 'reloading' inside the yield surface.

3.2.2.1 Hyperbolic stress-strain relationship

In drained triaxial primary loading, the experimentally observed relationship between axial strain and deviatoric stress in soils can be well approximated by a hyperbolic function. This hyperbolic relationship for stress-strain was first formulated by Kondner and later used in well-known the Hyperbolic model (Duncan and Chang, 1970).

$$\varepsilon_1 = \frac{1}{2E_{50}} \frac{q}{1 - q/q_a} \tag{3.6}$$

where q_a is the asymptotic value of the shear strength and E_{50} is the secant modulus

at 50% strength.

The Eq.3.6 is illustrated in Figure 3.3. The q_a is linked with the ultimate deviatoric

stress, q_f, according to the following Equation:

$$q_a = \frac{q_f}{R_f} \tag{3.7}$$

The above relationship for q_f is derived from the MC failure criterion, defined as:

$$q_f = (c' \cot \varphi' - \sigma_3') \frac{2 \sin \varphi'}{1 - \sin \varphi'} \tag{3.8}$$

The ratio between q_a and q_f, R_f, is always less than one. Duncan and Chang, (1970)

found that R_f for different soils is between 0.75 and 1. Thus, $R_f = 0.9$ is suitable value

and it is employed for all following analyses in this thesis.

In contrast to primary deviatoric loading, unloading or reloading is modeled as pure

elastic behavior, followed the Hooke's law. The elastic unloading-reloading stiffness

E_{ur} relates elastic stress to elastic strain. Both E_{50} and E_{ur} are depended on effective

stress according to power law and defined as:

$$E_{50} = E_{50}^{ref} \left(\frac{c' \cos \varphi' + \sigma_3' \sin \varphi'}{c' \cos \varphi' + p^{ref} \sin \varphi'} \right)^m \tag{3.9}$$

$$E_{ur} = E_{ur}^{ref} \left(\frac{c' \cos \varphi' + \sigma_3' \sin \varphi'}{c' \cos \varphi' + p^{ref} \sin \varphi'} \right)^m \tag{3.10}$$

where E_{50}^{ref} and E_{ur}^{ref} are the reference stiffness corresponding to the reference

confining pressure p^{ref}.

3.2.2.2 Compression hardening of the HS model

In order to avoid the unbounded elastic compression strain, a cap type yield surface f^c, is introduced in the HS model (see Figure 3.4). This cap type yield surface describes the compression hardening under isotropic stress. For triaxial condition, f^c is defined as:

$$f^c = \frac{q^2}{\alpha^2} + p^2 - p_p^2 \qquad (3.11)$$

where $p = (\sigma_1' + \sigma_2' + \sigma_3')/3$ is mean effective stress, $q = \sigma_1' - \sigma_3'$ is deviatoric stress, α is a cap parameter, p_p is isotropic pre-consolidation stress.

Then the hardening law relation p_p to volumetric strain is defined as:

$$\varepsilon_v^{pc} = \frac{\beta}{1-m} \left(\frac{p_p}{p^{ref}} \right)^{1-m} \qquad (3.12)$$

The size and shape of the cap are determined by p_p and α respectively, as shown in Figure 3.4. Input data on initial p_p value is provided by means of the PLAXIS procedure for initial stresses. The cap yield surface expands as a function of p_p. The two parameters α and β in Eqs. 3.11 and 3.12 are internal model parameters which are calculated from the input parameters. α relates to K_o^{nc}, which is K_o-value for normal consolidation and β is primarily dependent on E_{oed}^{ref}, which is the tangent stiffness for primary oedometer loading. The plastic potential for the cap-type yield surface is chosen equal to its yield surface ($g^c = f^c$), so that plastic strain on the cap-type yield surface is associated. Thus:

$$\dot{\varepsilon}_v^{pc} = \lambda \frac{\partial f^c}{\partial \sigma '} \text{ and } \lambda = \frac{\beta}{2p}\left(\frac{p_p}{p^{ref}}\right)^m \frac{\dot{p}_p}{p^{ref}} \qquad (3.13)$$

Similar to stiffnesses E_{50} and E_{ur}, E_{oed} is also dependent on the effective stress according to power law, expressed:

$$E_{oed} = E_{oed}^{ref}\left(\frac{c'\cos\varphi' + \sigma_1'\sin\varphi'}{c'\cos\varphi' + p^{ref}\sin\varphi'}\right)^m \qquad (3.14)$$

It should be noted that in contrast to E_{50} and E_{ur}, E_{oed} is dependent on the major effective principle stress σ_1'.

3.2.2.3 Shear hardening of the HS model

With the cap yield surface f^c, the plastic volume strain due to isotropic compression is described. However, the plastic strain in the deviatoric stress cannot be modeled by f^c. As a result, a cone-type yield surface is introduced in the HS model to account for shear hardening, defined as:

$$f^s = \frac{1}{E_{50}}\frac{q}{1 - q/q_a} - \frac{2q}{E_{ur}} - \gamma^p \text{ and } \gamma^p = 2\varepsilon_1^p - \varepsilon_v^p \qquad (3.15)$$

γ^p is the hardening parameter. If the plastic volumetric stain is assumed relatively small compared to axial strain under triaxial condition, then it leads to the approximation $\gamma^p \approx 2\varepsilon_1^p$. For primary loading which implies the yield condition ($f^s = 0$), axial plastic strain can be determined from Eq. 3.16:

$$\varepsilon_1^p \approx \frac{1}{2}f^s = \frac{1}{2E_{50}}\frac{q}{1 - q/q_a} - \frac{q}{E_{ur}} \qquad (3.16)$$

Under primary loading, the elastic strains also develop. For drained triaxial condition, the elastic strains are given by:

$$\varepsilon_1^e = \frac{q}{E_{ur}} \qquad \varepsilon_2^e = \varepsilon_3^e = v_{ur}\frac{q}{E_{ur}} \tag{3.17}$$

Combining the elastic and the plastic portion of axial strain according to Eq. 3.16 and 3.17, the relationship for axial strain ε_1 is exactly the same as Eq.3.6.

Associated plasticity is an unrealistic assumption for most geotechnical materials. Thus, an additional plastic potential of the form:

$$g^s = (\sigma_1' - \sigma_3') - (\sigma_1' + \sigma_3')\sin\psi_m \tag{3.18}$$

is introduced. The mobilized dilatancy angle ψ_m in the above equation is defined according to Rowe's stress dilatancy theory:

$$\sin\psi_m = \frac{\sin\varphi_m' - \sin\varphi_{cv}}{1 - \sin\varphi_m'\sin\varphi_{cv}} \tag{3.19}$$

where φ_{cv} is the critical state friction angle and φ_m' is the mobilized friction angle, calculated as follows:

$$\sin\varphi_m' = \frac{\sigma_1' - \sigma_3'}{\sigma_1' + \sigma_3' - 2c'\cot\varphi'} \tag{3.20}$$

Finally, the required model parameters and main features of the HS model are summarized here. A total of eight input parameters are required. For strength parameters, φ', c' and ψ, same as the MC model. For stiffness, elastic parameters are used as E_{ur}^{ref} and v_{ur} for unloading or reloading condition. Secant stiffness parameter E_{50}^{ref} and tangent stiffness E_{oed}^{ref} are used for deviatoric loading and primary oedometer

loading respectively. The last parameter m, is the power for stress level dependency of stiffness. All eight parameters for the HS model have a clear geotechnical relevance and the determination of parameters will be discussed in section 3.3.1. The advantage of the HS model over the MC model is not only the use of a hyperbolic stress-strain relationship instead of a bi-linear relationship, but also controls of stress level dependency. The stiffness depends on the stress level. The two kinds of yield surfaces (f^c and f^s) enable the HS model to model the compression hardening and the shear hardening. Another feature of the HS model is the distinguishing between 'primary loading' and 'unloading'/'reloading' inside the yield surface. Although, the HS model can be treated as an advanced soil model, there still are a number of features of the real soil behavior that the model does not include. The major limitation is that the HS model does not account for strain softening behavior. In order to model more accurately the behavior of real soil, a more complex model is needed.

3.2.3 Hypoplastic model

Hypoplasticity is a particular class of incrementally non-linear constitutive models. In hypoplasticity, the strain rate is not decomposed into elastic and plastic components and the model do not use explicitly the notions of the yield surface and the plastic potential surface. These are the major differences from the elasto-plastic model, like the MC model and the HS model. The basic structure of the hypoplastic (HYP) model has been developed since 1980s (Gudehus and Kolymbas 1979). The constitutive

model was first primarily applied to granular materials and has been successfully used

in many geotechnical problems for sands in Europe. The progress of hypoplastic

models suitable for the description of fine grained soils has not been applied widely in

the past. Recently, rate-dependent hypoplastic models developed for clay have been

proposed (Masin 2005). Within this study, only the hypopastic model for clay is

selected.

3.2.3.1 Basic hypoplastic model for clay

A general form of the hypoplastic equation implementing the critical state concept was

proposed by Gudehus (1996), expressed as:

$$\dot{\sigma} = f_s L : D + f_s f_d N \| D \| \tag{3.21}$$

where $\dot{\sigma}$ is the objective stress ratio, D is the Euler's stretching tensor and L and N are

fourth- and second order constitutive tensors, respectively. f_s are f_d scalar factors

expressing the influence of stress level and density.

At the critical state, $\dot{\sigma} = 0$ and $f_d = 1$. Substituting these into Eq. 3.21 leads to the

following condition for the critical state:

$$\vec{D} = -L^{-1} : N = -B \tag{3.22}$$

Taking the norm of the both sides of Eq. 3.22, we obtain for the critical state：

$$\| B \| = 1 \tag{3.23}$$

Using above transformations, Niemunis (2002) proposed a simple rearrangement of

Eq. 3.21, which allows definition of critical state stress condition and flow rule. The

tensor N is now defined as:

$$N = L:(-Y\vec{m}) \tag{3.24}$$

Then the critical state locus is given by： $\|B\| = 1 = Y$ and the strain rate direction at the

limit state is given by: $\vec{D} = \vec{m}$. Y and $\vec{m}$ may be seen as equivalent of the yield surface

and the flow rule in elasto-plasticity respectively. Eq. 3.21 and 3.24 can be combined

to get:

$$\dot{\sigma} = f_s L:(D - f_d Y \vec{m} \| D \|) \tag{3.25}$$

Based on Eq.3.25, Masin(2005) developed a hypoplastic model for clay with

following properties:

1) The fourth-order constitutive tensors L is from model by Herle and Kolymbas

    (2004). The shear stiffness is controlled by the model parameter r.

2) The critical state $Y = 1$ is defined by Matsuoka-Nakai criterion which is controlled

    by the parameter φ_c (critical state friction angle) and flow rule $\vec{m}$ is defined as $-\vec{B}$

    from van Wolffersdorff model.

3) The scalar factor which expresses the influence of the mean stress, f_s, is

    calculated based on the formulation of the pre-defined isotropic normal

    compression line (NCL). The NCL is defined as: $\ln(1+e) = N - \lambda^* \ln p$, controlled

    by the model parameter N and λ^* (Figure 3.5).

4) The scalar factor which expresses the influence of density (Over-consolidation

    ratio), f_d, is defined as $f_d = 0$ for $p=0$; $f_d = 1$ at critical state and $f_d = const. > 1$ at

normally compression states. Beside N and λ^*, another model parameter κ^* is introduced to control f_d.

In summary, the model requires five parameters: $\varphi_c, N, \lambda^*, \kappa^*$ and r. φ_c is the critical state friction angle. N and λ^* control the position and slope of the isotropic NCL and κ^* controls the slope of the isotropic unloading line, shown in Figure 3.4. The positions of the isotropic NCL and the critical state line correspond to Modified Cam clay model. r controls the shear stiffness. The Basic Hypoplastic model is capable of predicting a wide range of aspects of fine grained soils behavior, demonstrated by Masin (2005). However, this Basic Hypoplastic model is more suitable to the reconstituted soil. When predicting the behavior of natural soil with structure, the modification needs to be added to the Basic Hypoplastic model. Moreover, the small-strain behavior of the soil cannot be captured by the Basic Hypoplastic model.

3.2.3.2 Enhanced hypoplastic model for structured clay

Natural (Undisturbed) soils have different structure compared to the reconstituted soils. The differences are mainly caused by the fabric and bonding inside the natural soils. Fabric is created during soil sedimentation and bonding is created during the subsequent diagenetical processes. The influence of structure in clays can be quantified by the different sizes of the state boundary surface (SBS) of the structured and reconstituted soils, demonstrated in Figure 3.6 by Cotecchia and Chandler (2000).

Based on concept of Cotecchia and Chandler's framework for behavior of structure clays, Masin developed an enhanced hypoplastic model which is modified from the Basic Hypoplastic model for structured clays (Masin 2007).

In the enhanced hypoplastic model, a new state variable is introduced to describe the effects of structure, namely the ratio of sizes of the SBSs of natural and reconstituted soils, referred to as "sensitivity" (s). s is measured along the constant volume sections through the SBSs, demonstrated in Figure 3.7. The Hvorslev equivalent pressure of the structured clays is calculated by sp_e^*. Then p_e^* in the expression of f_d is replaced by sp_e^*. By doing this, the SBS of nature clays is s times larger than the SBS of corresponding reconstituted clays. For most stiff clays, the sensitivity (s) is constant (So-called stable structure) (Ingram 2000). For another kind of soil, the sensitivity decreases with loading (So-called meta-stable structure). In order to predict the structure degradation, s is defined as (Masin 2007):

$$\dot{s} = -\frac{k}{\lambda^*}(s - s_f)\dot{\varepsilon}^d \qquad (3.26)$$

where k is a constitutive model parameter that controls the rate of the structure degradation and s_f is the final sensitivity, and $\dot{\varepsilon}^d$ is the damage strain rate, defined by:

$$\dot{\varepsilon}^d = \sqrt{\left(\dot{\varepsilon}_v\right)^2 + \frac{A}{1-A}\left(\dot{\varepsilon}_s\right)^2} \qquad (3.27)$$

where A is a additional model parameter that controls the relative importance of the volumetric $\dot{\varepsilon}_v$ and shear $\dot{\varepsilon}_s$ strains components.

k, A and s_f are new constitutive model parameters, introduced to the enhanced

hypoplastic model. The value of k is in the range $0 \leq k \leq 1$, suggested by Masin. Obviously, when $k = 0$, the model will predict the stable structure. The researches by Rouainia and Muir Wood (2000), Gajo and Muir Wood (2001), and Callisto and Rampello (2004) indicate that the value of A for most clays may be expected to be in the range $0 < A < 0.5$, and s_f for many soft clays equal to one.

By introducing the structure degradation, the enhanced hypoplastic model is capable of predicting the strain softening. The evaluation of this model and the application to simulate the softening behavior of pile-soil interface will be discussed in section 3.4.2 and 3.5 in details.

3.3 DETEMINATION OF MODEL PARAMETERS

Successful application of the constitutive model is not possible without a reliable procedure to obtain the model parameters. In this section, the determination of model parameters is presented. Particular attention is given to the HS model and the HYP model.

3.3.1 Parameters for the HS (Hardening Soil) model

As mentioned in section 3.2.2, there are eight input parameters required for the HS model, represent as strength and stiffness parameters. φ', c' and ψ are strength

properties. E_{ur}^{ref} , v_{ur} , E_{50}^{ref} , E_{oed}^{ref} .and m are stiffness properties.

φ',c' can be directly obtained from consolidated triaxial tests at different confining pressures. One can either plot the principal effective stress as Mohr stress circles in a $\sigma'-\tau$ diagram or plot the principal effective stress as a function of the axial strain ε_1 to determine φ',c' , suggested by Brinkgreve (2005). In the latter case, φ',c' are calculated by solving two equations with two unknowns, as demonstrated in Figure 3.8. The dilatancy angle ψ is relevant for dense sands or highly over-consolidated clays. For sand, ψ can be determined from the standard drained triaxial test, when plotting the volume strain ε_v as a function of ε_1 , shown in Figure 3.9. It should be noted that the dilatancy effect comes to an end when the soil reaches its critical state in reality. However, in the HS model, ψ is a model parameter which does not automatically consider the end of the dilatancy. Thus, when ψ is used, dilatancy cut-off function should be turned on. Additional parameters the initial void ratio, e_{init} , and the maximum void ratio, e_{max} , are needed as input. As soon as the volume change results in a state of e_{max} , ψ_{mob} is set back to zero.

Compared to strength properties, stiffness properties are more important in modeling pile behavior, especially for modeling of the base bearing resistance of the pile (Wehnert and Vermeer 2004). Reflecting the particular interest of this study, more attention is given to E_{ur}^{ref} and E_{50}^{ref} . E_{ur}^{ref} and E_{50}^{ref} have a clear physical meaning, as shown in Figure 3.4. However, this does not mean they can be easily selected. The

E_{ur}^{ref} and E_{50}^{ref} can be directly obtained from a standard consolidated drained (CD) triaxial test. While in reality E_{ur}^{ref} and E_{50}^{ref} are underestimated through standard CD triaxial test due to the effects of sampling disturbance. This effect becomes more significant when soils are stiffer. Piles are usually installed to transfer loads through soft or loose soil layers to stiffer soils. As a result, it is not suitable to use the standard CD triaxial test to determinate the value of E_{ur}^{ref} and E_{50}^{ref} for modeling pile. The effect of sampling disturbance can be reduced by using high quality sampling tube, like Japanese thin-walled piston sampling tube (JSSMFE 1977), and the CD triaxial test with external LVDT. However, these are not available in most projects.

The correct value of E_{ur}^{ref} and E_{50}^{ref} also can be obtained through the FE-simulation of the pressuremeter test which is best fitted to the field measurement. The FE-simulation of the pressuremeter test has been studied by several researchers (Schanz et al. 1999, Townsend et al. 2001 and Monnet 2007). The numerical procedure is briefly summarized here. The axisymmetric mesh and initial stress are generated first. Then in the first calculation step, the material of the pressuremeter cluster is removed and the horizontal distributed Load B is imposed on the boundary between the pressuremeter and the soil (Figure 3.10). The initial value of the Load B is set to the average initial horizontal stress along that boundary to make sure no deformation occurs before the pressuremeter test. The expansion of the pressuremeter is simulated by subsequently increased Load B according to the loading history in the field test. In order to allow discontinuity deformation and get rid of deformation constrains of Point A, two

interfaces are introduced (Figure 3.10). Extra geometry lines are created around

pressuremeter to locally generate a finer mesh. It should be noted that the calculation

requires large deformation and the updated mesh needs to be used. The pressure p

inside the pressuremeter has to be calculated according to Eq. 3.28,

$$p = \sum LoadB \frac{r_0}{r_0 + \Delta r} \qquad (3.28)$$

where r_o is the initial radius of the pressuremeter

This determination of E_{ur}^{ref} and E_{50}^{ref} based on pressuremeter test has been successfully

applied to one project in Singapore. In order to obtain correct stiffness parameters of

completely weathered Granite (G VI to G V soil), a total 17 CD triaxial tests and 23

pressuremeter tests have been conducted by SOIL IVESTIGATION PTE LTD. The

results of the field tests are summarized in Table 3.1 and Table 3.2 and shown in

Figure 3.11~3.14. E_{50} and E_{ur} in Figure 3.11 and 3.12 are calculated according to Eqs.

3.9 and 3.10. As can be seen from Figure 3.11 and 3.12, E_{50} and E_{ur} are approximately

constant after SPT-N=50. This indicates that E_{50} and E_{ur} obtained through the standard

CD triaxial test are unreliable for larger SPT-N value due to the significant sampling

disturbance. The elastic modulus E^{PMT} and E_{ur}^{PMT} obtained from the pressuremeter test

shows a more correct relationship between elastic modulus and SPT-N. The

pressuremeter test suffers fewer disturbances and reflects the correct value of soil

stiffness. A total of 12 pressuremeter tests with SPT-N value of the soil larger than 50

were selected for FE-simulation. E_{50}^{ref} and E_{ur}^{ref} are obtained from FE-simulation which

best fit tests measurements. The back-calculated results from FE-simulation are

plotted in Figure 3.11 and 3.12. Clearly, E_{50} and E_{ur} obtained from FE-simulation of

pressuremeter test provided a reasonable relationship with the value of SPT-N. By

using standard CD triaxial test, E_{50} and E_{ur} are seriously underestimated by

approximately 50% when the value of SPT-N increases from 50 to 100. Consequently,

this will cause significant overestimates of calculated deformations using FEM

models. Thus, the determination of E_{50}^{ref} and E_{ur}^{ref} through the FE-simulation of the

pressuremeter test is employed for all the following analyses. It should be noted that

there is wide range for E_{50}^{ref} and E_{ur}^{ref} in the soil SPT-N=100. It is because that actually

the soil may have N-value greater than 100, but the SPT test did not continue beyond

100 blows.

Table 3-1 Summary of CD triaxial test

Borehole	Depth(m)	Soil Type	SPT-N	c' (kPa)	φ' (Deg)	E_{50}^{ref} (kPa)*	E_{ur}^{ref} (kPa)*
AB-16	25.0-26.0	GV	17	17	33	10200	106000
AB-16	33.0-34.0	GV	50	40	28	15000	96000
AB-17	25.0-26.0	GV	35	16	32	9565	124340
AB-17	33.0-34.0	GV	50	30	33	14818	99280
AB-18	25.0-25.3	GV	50	27	32	14513	85920
AB-18	33.0-34.0	GV	100	26	37	11835	103000
AB-19	20.5-25.5	GV	15	21	35	21500	167100
AB-20	25.0-26.0	GV	35	26	29	6657	113200
AB-20	33.0-34.0	GV	100	19	35	21000	63000
AB-21	33.0-34.0	GV	100	30	32	14000	110600
AB-23	37.5-38.5	GV	100	29	28	14500	75400
AB-24	18.0-19.0	GV	20	25	32	10600	78400
AB-25	18.0-18.3	GV	22	16	36	12300	84870
AB-25	25.0-26.0	GV	30	16	32	7100	56100
AB-27	18.0-18.5	GVI	12	4	36	7800	61620
AB-27	33.0-34.0	GV	75	20	34	8300	116200
AB-29	18.0-18.5	GVI	14	21	34	7200	93600

* E_{50}^{ref} and E_{ur}^{ref} are determined as $p^{ref} = 100kPa$.

Table 3-2 Summary of pressuremeter test

Borehole	Depth(m)	Soil Type	SPT-N	E^{PMT} (kPa)	E_{ur}^{PMT} (kPa)
AB-16	20.0	G V	40	30409	96578
AB-16	35.0	G V	50	21611	130090
AB-16	11.0	G V	100	43442	261478
AB-16	26.5	G V	100	31443	184738
AB-17	10.5	G VI	7	3983	83720
AB-17	26.5	G V	33	13689	75475
AB-17	35.0	G V	51	21241	184548
AB-18	26.5	G V	20	29864	90567
AB-18	20.5	G V	21	11078	75311
AB-18	35.0	G V	100	33554	250171
AB-19	10.5	G VI	8	7174	29356
AB-19	20.0	G V	15	22291	100741
AB-19	26.0	G V	16	15267	75233
AB-19	35.0	G V	70	30237	172248
AB-20	35.0	G V	100	36688	425273
AB-21	10.5	G V	35	50865	264941
AB-21	20.0	G V	100	42397	251624
AB-21	26.5	G V	50	14463	193745
AB-21	35.0	G V	100	52870	341416
AB-25	11.0	G V	10	11579	57822
AB-27	11.5	G VI	16	8290	87541
AB-27	16.5	G VI	12	12185	93847
AB-27	26.5	G V	48	22633	137105
AB-27	35.0	G V	70	35733	301983

3.3.2 Parameters for the HYP model

There are total five parameters for basic HY model: φ_c, N, λ^*, κ^* and r. The parameter φ_c is the critical state friction angle. It can be found using a linear regression through the critical state points from the triaxial test. N and λ^* control the isotropic normal compression line in the $\ln p$ vs. $\ln(1+e)$ space. These parameters can be determined from isotropic compression test, as shown in Figure 3.5. It should be noted that in the

case of stiff clay (stable structure), N should be found using isotropic compression test on natural soil. κ^* controls the unloading line of isotropic compression test and non-linear behavior inside SBS. Thus, κ^* should not be direct measurement of the slope of loading/unloading line. It should be calibrated by the parametric study by simulation of the isotropic test. The parameter r controls the shear module. As suggested by Masin (2005), the parameter r can be calibrated by a parametric study, demonstrated in Figure 3.8.

As mentioned in section 3.2.3.2, k, A and s_f are additional constitutive model parameters for the enhanced hypoplastic model. The parameter k controls the rate of the structure degradation. It can be calibrated by simulation of isotropic or oedometric compression test. If isotropic compression test is used, k will be calibrated independently of parameter A. The parameter A controls the relative importance of the volumetric $\dot{\varepsilon}_v$ and shear $\dot{\varepsilon}_s$ components. A is calibrated with the already known value of k using simulation of triaxial shear test.

3.4 EVALUATION OF MODEL PREDICTIONS

3.4.1 Evaluation of the MC and the HS model

To evaluate the performance of the MC and HS models, the MC and HS models are employed to simulate the triaxial test in PLAXIS. The triaxial test can be simply modeled by means of an axisymmetric geometry of unit dimension (1x1), which

represents a quadrant of soil specimen. A set of model parameters as listed in Table 3.3, representing dense sand and soft clay, is considered.

The results of the triaxial are presented in the Figure 3.15. As can be seen, the MC model has constant stiffness while stiffness of the HS model decreases with increases in strain. The effective stress path of HS model is closer to real soil than that of MC model which is vertical straight line in stress space. Furthermore, as discussed in Chapter 2, the soil element close to the pile has complex stress history, especially for displacement pile. The soil is significantly loaded during the installation and the pile is unloaded prior to construction of the supported building, or load testing of the completed pile. During this time, pore pressure dissipation may occur which will change the strength and stiffness of soil. The MC model with constant stiffness cannot capture these features of soil while the HS model does. The so called loading-unloading-consolidation-reloading stress process is simulated by using the HS model in undrained triaxial space. The soil parameters are the same as parameters used in CU test. The results are presented in the Figure 3.16 in term of effective stress path (ESP), e-logp' and stress-stain curves.

Table 3-3 Soil parameters for the HS and the MC models

| Parameter | CD | | CIU | | |
	HS	MC	HS	MC	Unit
E_{50}^{ref}	30000	30000	4000	4000	kPa
E_{oed}^{ref}	30000	NA	4000	NA	kPa
E_{ur}^{ref}	90000	NA	30000	NA	kPa
p^{ref}	100	NA	100	NA	kPa
c	0.01	0.01	0.01	0.01	kPa
φ'	42	16	25	25	°
ψ	42	16	0	0	°
v_{ur}	0.2	0.2	0.2	0.2	-
m	0.55	NA	1	NA	-

As can be seen from the results, the soil gets higher ultimate deviatoric stress when it is reloaded after consolidation in undrained triaxial space. This can be explained by the fact of the cap yield surface f^c, which is described in section 3.2.2, has expanded after soil is consolidated. It can be observed from the e-logp' curve. The pre-consolidation pressure p'_c increases from p'_c to p'^*_c. Thus soil becomes overconsolidated. This is why the effective stress path is firstly vertical straight line in stress space when soil is reloaded. In addition, the soil becomes stiffer when it is reloaded ($E_{ur} \geq 3E_{50}$). This may explain why the displacement pile normally has stiffer behavior and higher capacity than the bored pile in the same soil condition which is reported by Fioravante *et al*. (1994) and Faray *et al*. (1989). However, the MC model cannot capture these behaviors, thus the HS model can simulate more realistic soil

behavior and it is employed for all the following analyses, unless otherwise stated.

3.4.2 Evaluation of the HYP model

The performance of the enhanced hypoplastic model was evaluated using the concept of normalized incremental stress response envelopes (NIREs). The NIRE was developed based on incremental response envelopes and rate response envelops by Masin and Herle (2005). The results were generated by TRIAX which is a single element program for soil mechanics (Masin 2005). All the model parameters were calibrated from the results of the basic laboratory experiments on the reconstituted and natural Singapore marine clay (SMC) reported by Chong (2002) and Xiao (2009). The parameters N, λ^*, κ^* were calibrated on the isotropic compression test on reconstituted SMCs (Figure 3.17). The φ_c was found from three CIU tests under different confining stress. The parameter r was calibrated on the basis of a parametric study using a CIU test (Figure 3.18). The parameters k and A were calibrated by the simulation of the oedometer test and the triaxial shear test on natural SMCs (Figure 3.19). All the model parameters are summarized in Table 3.4. Figure 3.20 shows the NIREs at different $\| \Delta \varepsilon \|$. As can be seen, the shape of NIREs at small $\| \Delta \varepsilon \|$ (stress state inside the SBS, Figure 3.20a) for basic and enhanced hypoplastic model are similar. The sizes of the NIREs of the enhanced hypoplastic model are larger than those of the basic hypoplastic model. For larger $\| \Delta \varepsilon \|$ (when NIRE touches the SBS of the enhanced hypoplastic model, as shown in Figure 3.20b), the NIREs of the enhanced hypoplastic

model shrink back towards the SBS of the basic hypoplastic model due to the structure

degradation. The same feature of the enhanced hypoplastic model was also presented

by Masin (2007). With this structure degradation, the enhanced hypoplastic model is

capable of predicting the strain softening behavior of sensitive clays. In next section

(3.5), the application of the enhanced hypoplastic model to simulate the strain

softening behavior of a pile-soil interface is presented.

Table 3-4 Parameters of hypoplastic model for Singapore Marine clay

$\varphi_c\,(Deg)$	$\lambda*$	$\kappa*$	N	r	k	A	s_f
23.0	0.122	0.0135	1.383	0.35	0.4	0.2	1

3.5 APPLICATIONS

3.5.1 Strain softening behavior of pile-soil interface

As discussed in Chapter 2, the soil in contact with the pile face normally is completely

disturbed by the different methods of installation. The soil in contact with the pile face

is more like reconstituted soil, especially for driven and Jack-in piles. Thus, the

behavior of pile-soil interface normally does not have strain softening. However, in

some cases, the structure of soil forms after the pile has been installed. Then the

structure degradation of the soil due to shearing gives a typical softening behavior of

pile-soil interface.

A series of interface shear tests of the stiffened Deep Cement Mixing (SDCM) pile

were conducted by Tanchaisawat et al. (2006) in the laboratory. The SDCM pile is a

new type of Deep Cement Mixing (DCM) pile reinforced by concrete core pile. The concreter core pile is inserted after the installation of the DCM pile. During the curing time, the structure of cement-admixed soil in contact with the pile face will form. As a result, obvious strain softening behavior of pile-soil interface has been found in interface shear tests (Figure 3.21). The similar pile-soil interface behavior in the field was reported by Tan and Fellenius (2012). The O-cell test and the conventional head test were performed on a deep barrette (named BR-15) constructed in weathered sedimentary rock of the Jurong formation in Singapore. The O-cell test started about half month after the barrette installation. The result of O-cell showed that the upper shaft could mobilize only between 30 kPa and 60 kPa unit shaft resistance in very stiff residual soils and hard siltstones/sandstones. Tan and Fellenius explained that the de-bonded of BR-15 is probably because of the failure of the maintenance of the de-sanding process for the bentonite slurry. As a result, a soil-bentonite cake layer was formed around the upper barrette shaft leading to premature failure of the upper shaft in the O-cell test. Then a conventional head down test with the O-cell opening vented was performed six months after the O-cell test. The head down test mobilized shaft shear in opposite direction to O-Cell test agrees quite well with the result from the O-cell test and typical strain softening behavior of pile-soil interface was clearly observed (see Figure 3.22).

3.5.2 Numerical simulation of strain softening at pile-soil interface

Tan and Fellenius (2012) attempted to model BR-15 barrette using PLAXIS. Barrette BR-15 cross section was 2.8x1.5m and it was constructed to 44.5m depth, about 25m into the Jurong formation with 33.0m length of the shaft resistance above the O-cell assembly level. The barrette was modeled by an equivalent circular pile in axi-symmetry. The axi-symmetric model maintains the same perimeter as the rectangular barrette (so that unit shaft resistance is correctly estimated) and the same axial stiffness, EA, as the barrette.

The behavior of interface is described with an elastic-plastic model (similar as the MC model) in PLAXIS. To distinguish between elastic and plastic behavior the Coulomb criterion is used:

$$\tau_f = \sigma'_h \cdot \tan \phi_i + c_i \qquad\qquad (3.29)$$

where σ'_h is the normal effective stress on the pile shaft. ϕ_i and c_i are the friction angle and the cohesion of the interface element respectively.

In PLAXIS, they are calculated from the strength of the soil using following Equation.

$$c_i = R_{inter} \cdot c_{soil} \ \text{ and } \ \tan \phi_i = R_{inter} \cdot \tan \phi_{soil} \qquad\qquad (3.30)$$

where R_{inter} is the strength reduction factor.

In order to model the weak soil cake layer formed around the barrette shaft, the parametric study of R_{inter} was conducted by Tan and Fellenius (2012) and the results of modeling of the head down test is shown in Figure 3.23. The FEM modeling of the

results of the test showed that the upper shaft is likely to fail between 2.3 MN ($R_{\mathrm{int}er} = 0.05$) and 4.8MN ($R_{\mathrm{int}er} = 0.1$) applied load as in Figure 3.24. However, it did not manage to simulate the small relative pile/soil displacements needed to mobilize the upper shaft resistance and capture the strain softening behavior of pile-soil interface. The excessively larger elastic displacement of the interface is due to too low value of $R_{\mathrm{int}er}$. Since the shear modulus of interface is defined as:

$$G = R_{\mathrm{int}er}^2 G_{soil} \tag{3.31}$$

The correct stiffness of the interface can be obtained by defining an additional material for the interface element. However, the strain softening behavior cannot be modeled due to the nature of the MC elastic-plastic model used for interface element. Therefore, a very thin layer, instead of interface element, is used to model the pile-soil interaction in PLAXIS. The enhanced hypoplastic model is used to simulate the softening behavior of weak soil cake layer formed around the barrette shaft. The set of parameters for the numerical simulation were estimated using the parameters for natural Singapore marine clay due to the lack of experimental data of this weak soil cake bentonite contaminated layer, given in Table 3.6. The result of FEM modeling with the enhanced hypoplastic model using different s_o is shown in Figure 3.25. As can be seen, a better fit of head-down test data is achieved by using the value of $s_o=3$. Both the small relative pile/soil displacements needed to mobilize the upper shaft resistance and the softening behavior of pile-soil interface are captured by using the enhanced hypoplastic model.

Table 3-5 Parameters of hypoplastic model for simulation of head-down test

φ_c (Deg)	$\lambda *$	$\kappa *$	N	r	k	A	s_f
20.6	0.14	0.01	1.56	0.3	0.32	0.25	1.9

3.6 SUMMARY

Three constitutive soil models (the Mohr-Coulomb model, the Hardening Soil model and the Hypoplastic model) were studied in this thesis. The MC model is a simple elastoplastic model with fixed yield surface. Although the MC model has many limitations for modeling the soil behavior, it can be used as the first model in FEM calculation to get a better understanding of the problem and to verify FEM results with analytical solutions before using the advanced soil model. In contrast to the MC model, a cap type yield surface and a cone type yield surface are introduced in the HS model to the model compression hardening and the shear hardening respectively. The stiffness in the HS model is stress-dependent and distinguishes between 'primary loading' and 'unloading'/'reloading'. The basic Hypoplastic model combines hypoplasticity principles with the traditional critical state soil mechanics. Based on this basic model, the enhanced hypoplastic model modifies the barotropy and the pyknotropy factors to take the structure degradation into account. This feature opens a way to model the strain softening behavior of pile-soil interface. This has been validated through field test results. The numerical simulation gives good agreement with a field test result by using the enhanced hypoplastic model.

Most parameters for the HS model and the HY model can be calibrated on the basis of standard laboratory tests. However, E_{ur}^{ref} and E_{50}^{ref} will be underestimated through the standard CD triaxial test due to the effect of sampling disturbance in reality, especially for modeling the end bearing capacity of a pile . The reasonable value of E_{ur}^{ref} and E_{50}^{ref} could be obtained through the FE-simulation of back-analysis of the pressuremeter test.

Compared to the MC model, more advanced features of HS model (including the cap type yield surface and a cone type yield surface; stiffness is stress-dependent and distinguishes between 'primary loading' and 'unloading'/'reloading) allow the HS model to simulate more realistic soil behavior and it has been validated through the unloading-consolidation-reloading stress process simulation using the HS model in undrained triaxial space. The soil element close to the pile has complex stress history during the pile installation and these stress change significantly affect the pile bearing capacity. Hence, the HS model is superior to the MC model for modeling displacement pile.

.
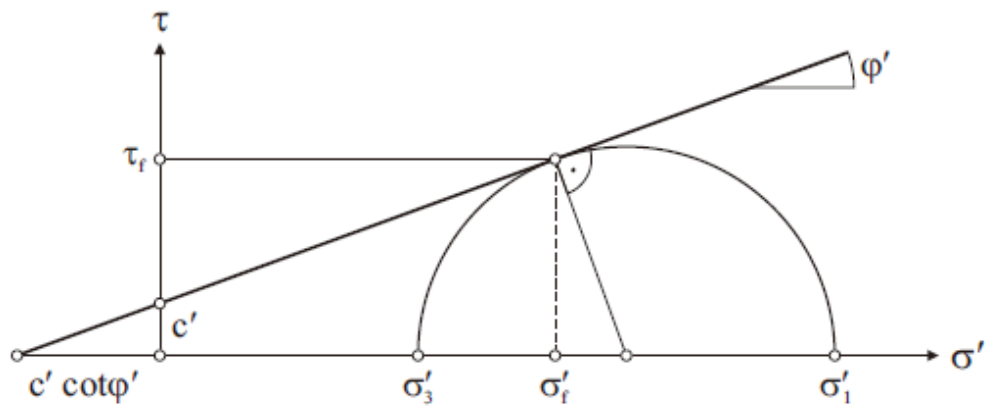
Figure 3-1 The failure criterion of the Mohr-Coulomb model.
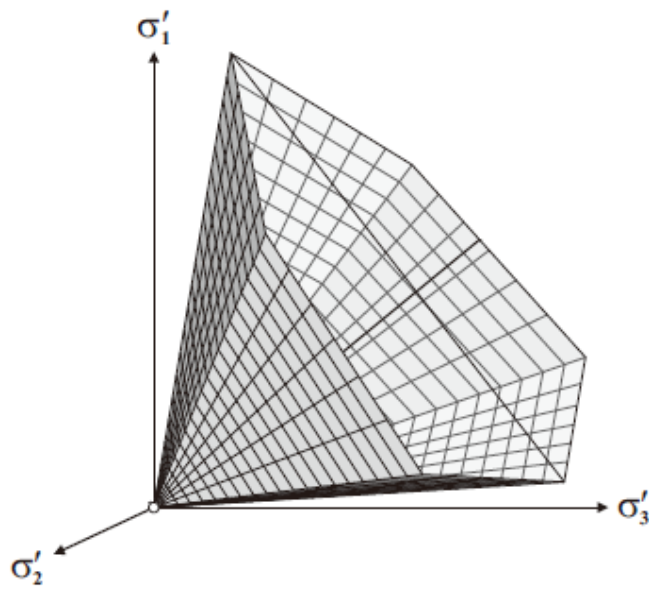
Figure 3-2 The Mohr-Coulomb yield surface in principal stress space.
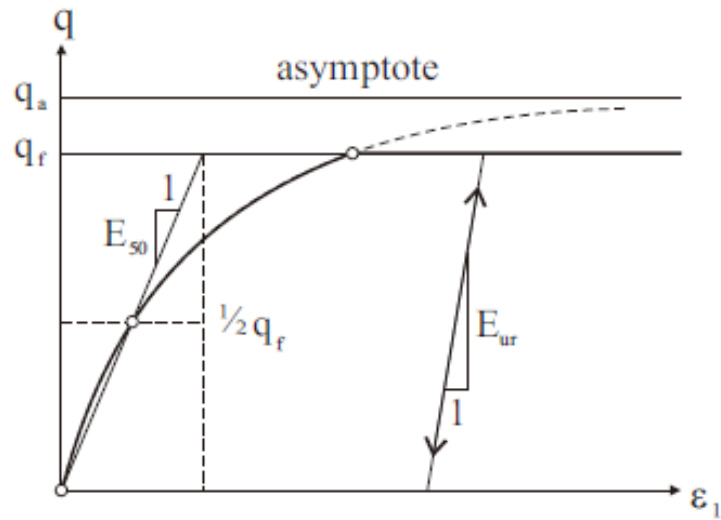
Figure 3-3 Hyperbolic stress-strain relationship in primary loading for the Hardening Soil model.
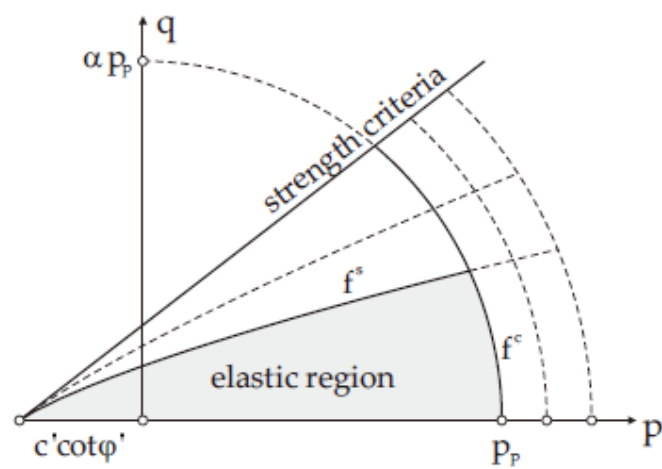
Figure 3-4 The flow surface of the Hardening Soil model.
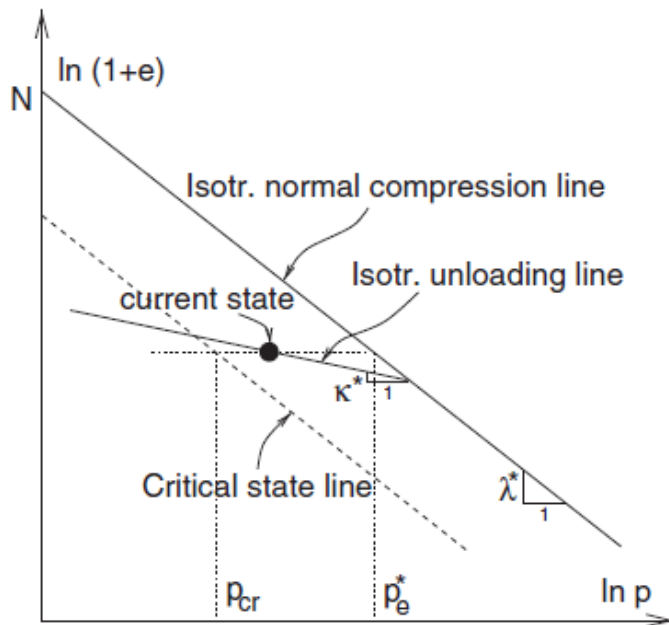
Figure 3-5 Definition of parameters N, λ^* and κ^* (Masin 2005).
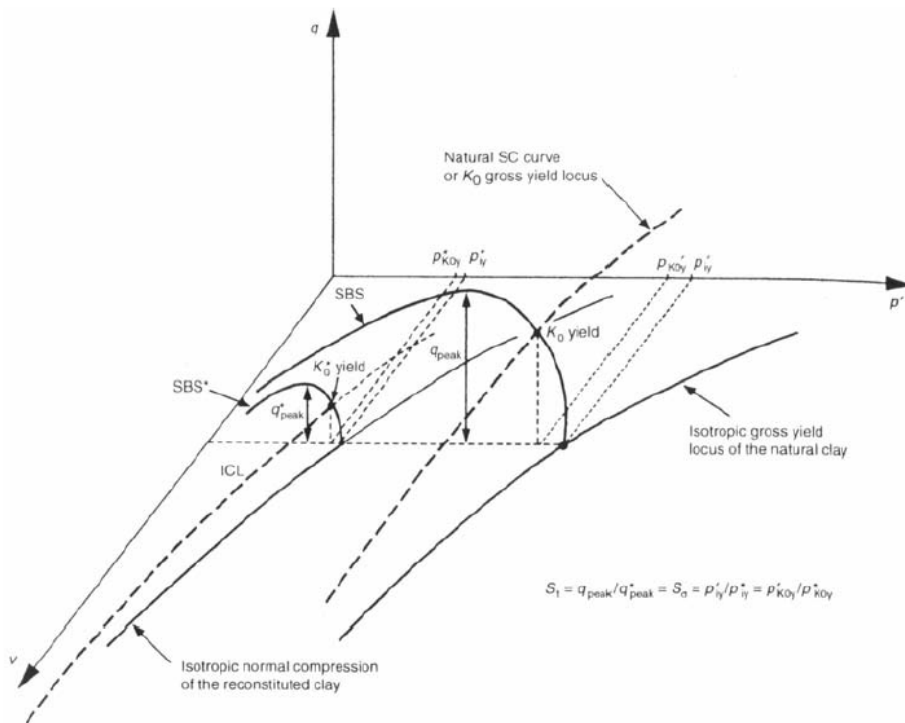
Figure 3-6 Framework for structure fine-grained materials (Cotecchia and Chandler 2000).
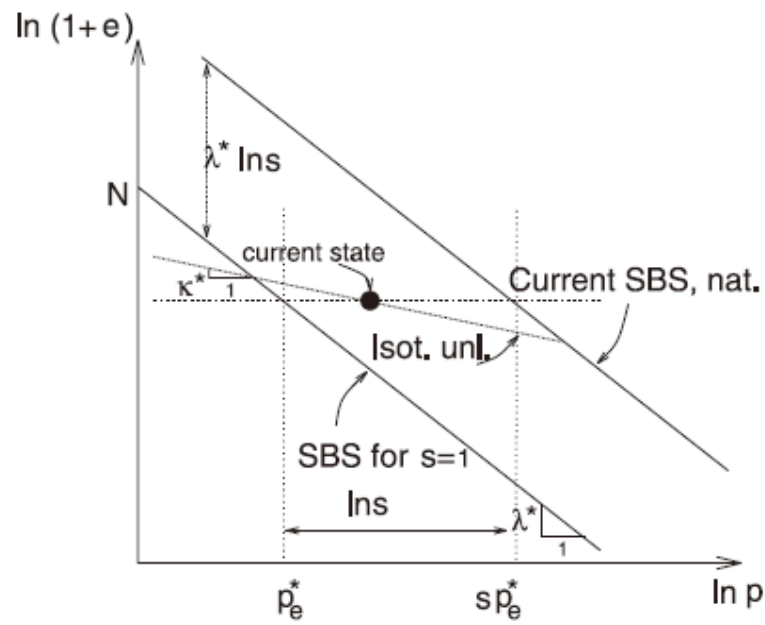
Figure 3-7 Definition of parameter s (Masin 2007).

$$d = \frac{2c'\cos\varphi' + 2\sigma'_3 \sin\varphi'}{1-\sin\varphi'}$$
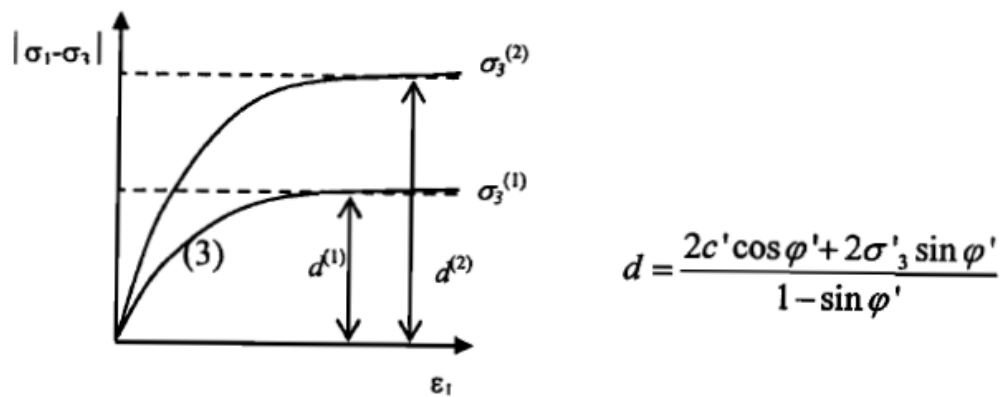
Figure 3-8 Calculation of φ' and c' from triaxial tests at different confining pressure (Brinkgreve 2005).
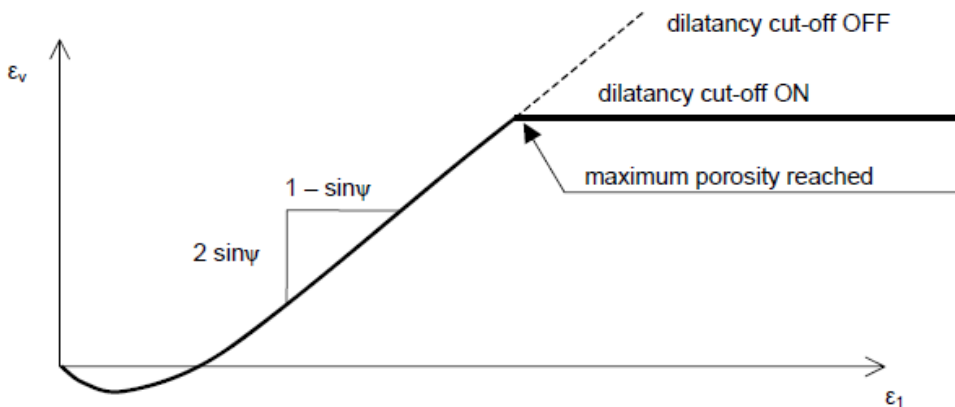
Figure 3-9 Selection of dilatacy angle from the results of drained triaxial test when including dilatacy cut-off for the Hardening Soil model.
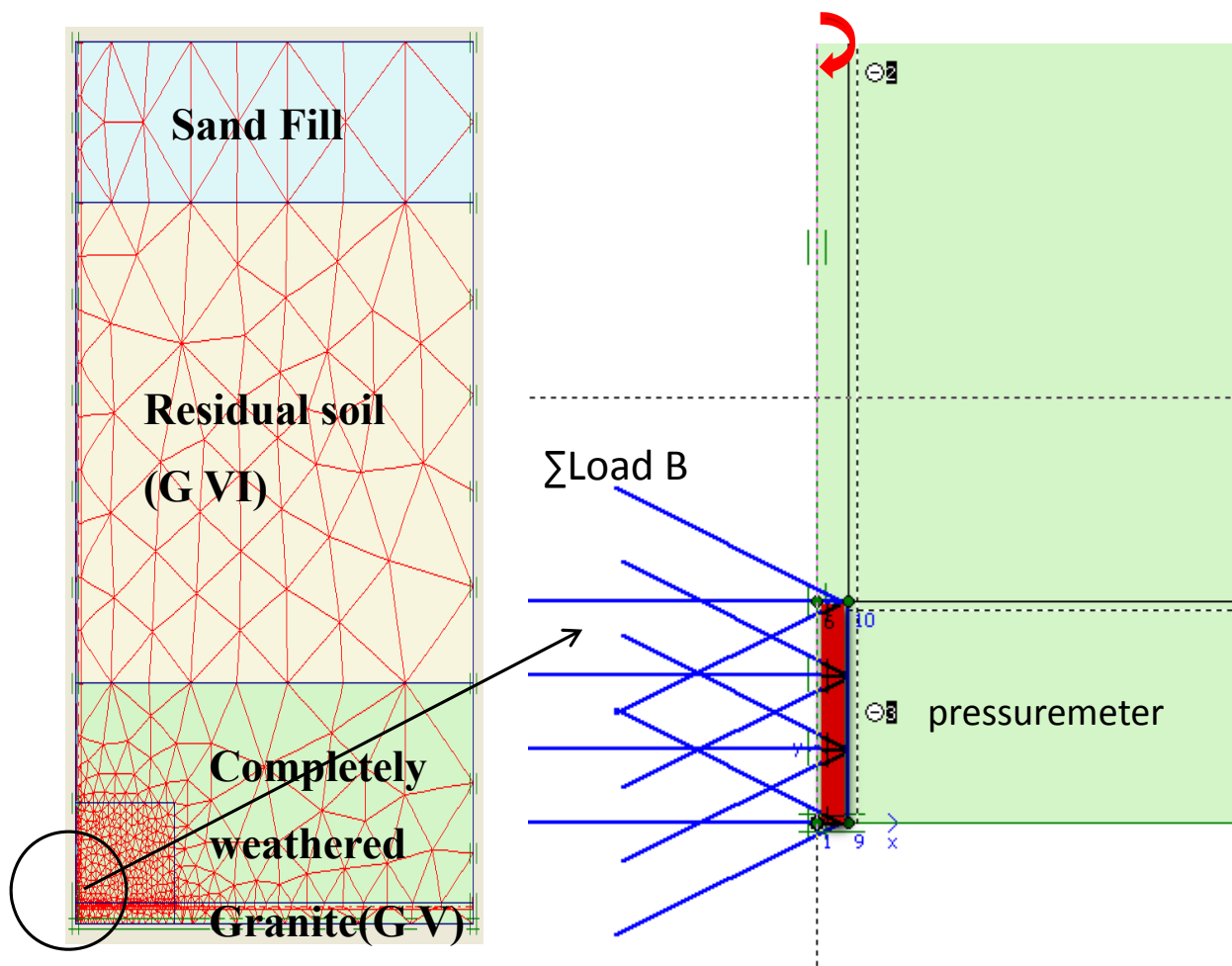
Figure 3-10 Typical mesh for simulation of the pressuremeter test in PLAXIS.
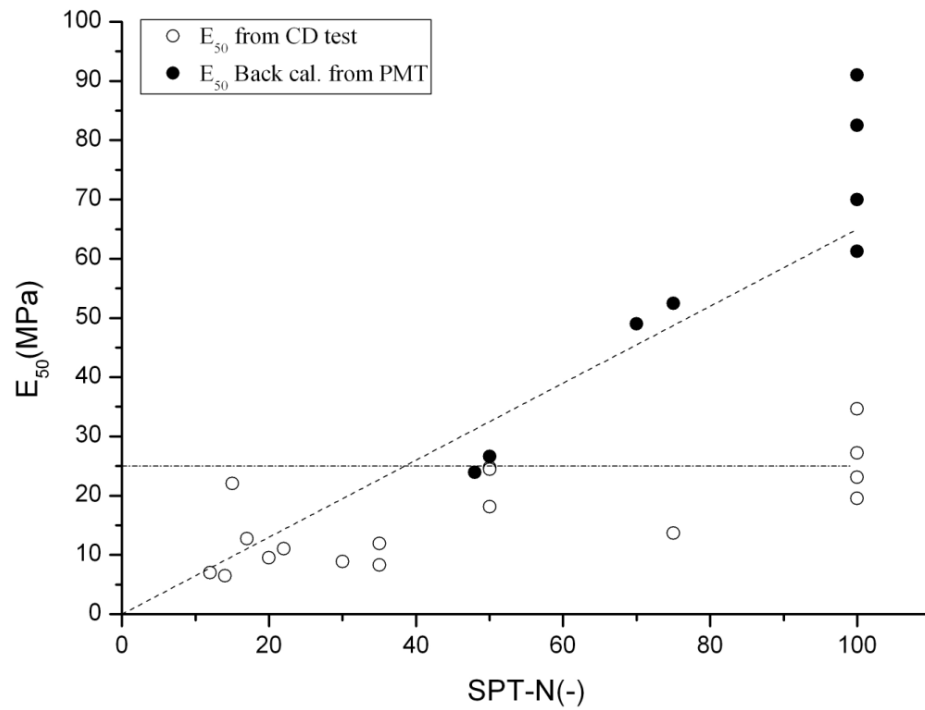
Figure 3-11 E_{50} determined by different method versus SPT-N value.
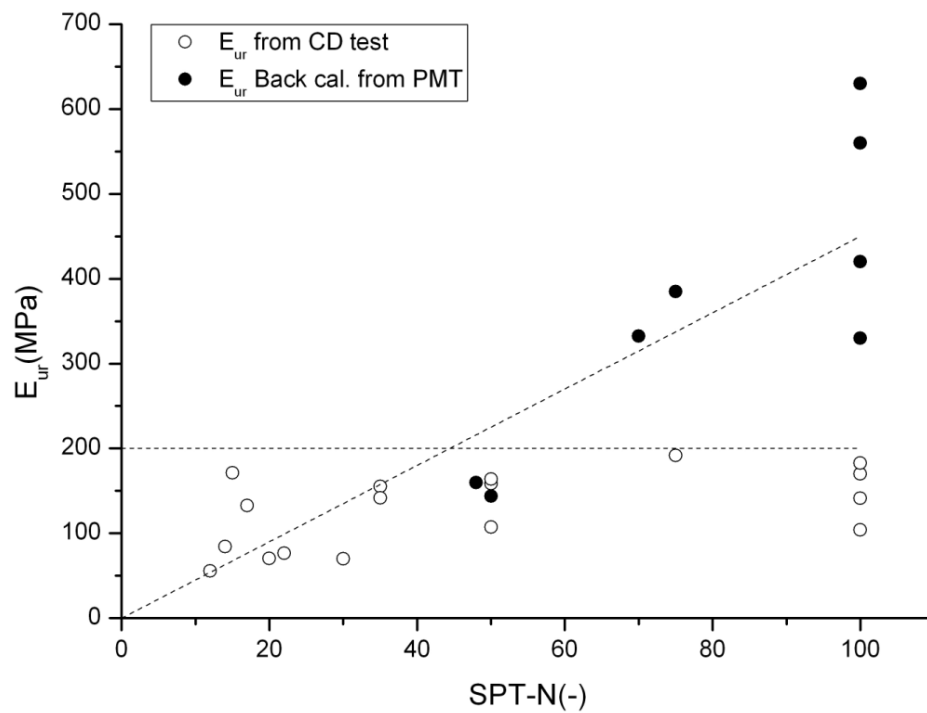
Figure 3-12 E_{ur} determined by different method versus SPT-N value.
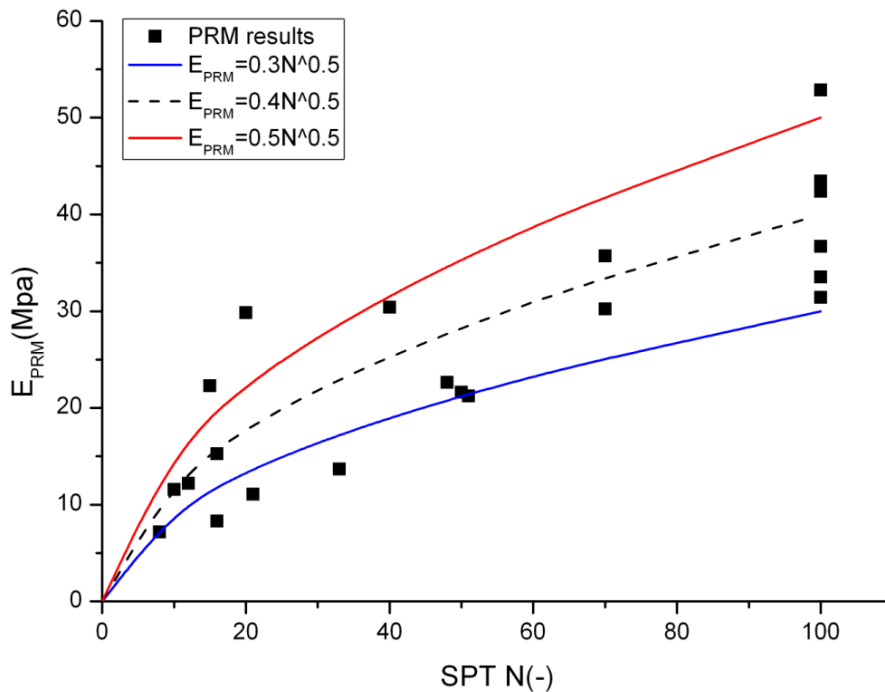
Figure 3-13 Loading stiffness E_{PRM} versus SPT-N value from the pressuremeter test.
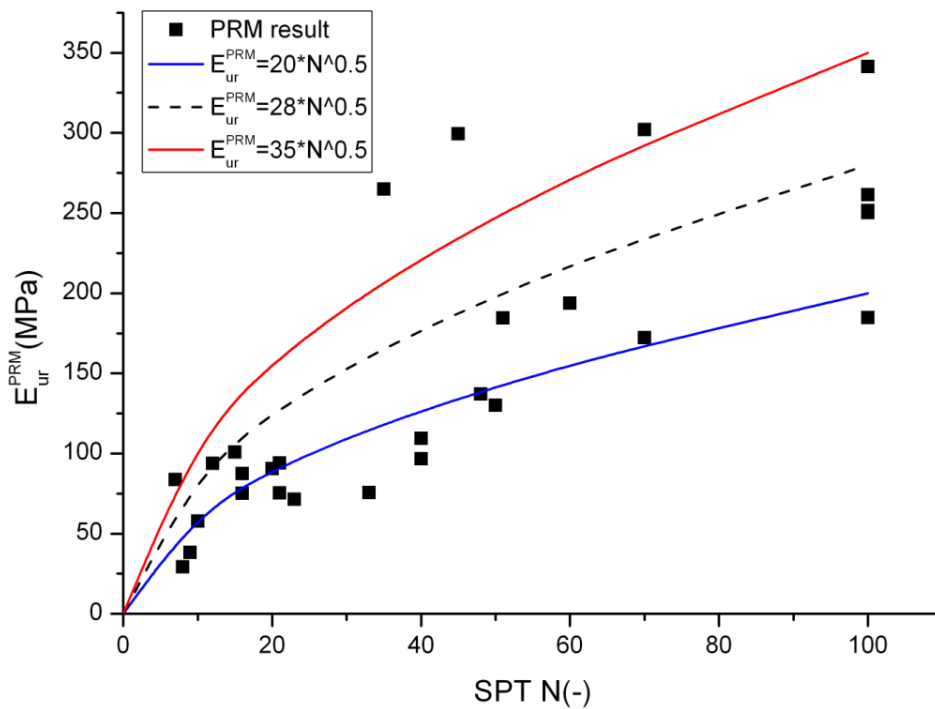
Figure 3-14 Unloading / reloading stiffness E_{ur}^{PRM} versus SPT-N value from the pressuremeter test.
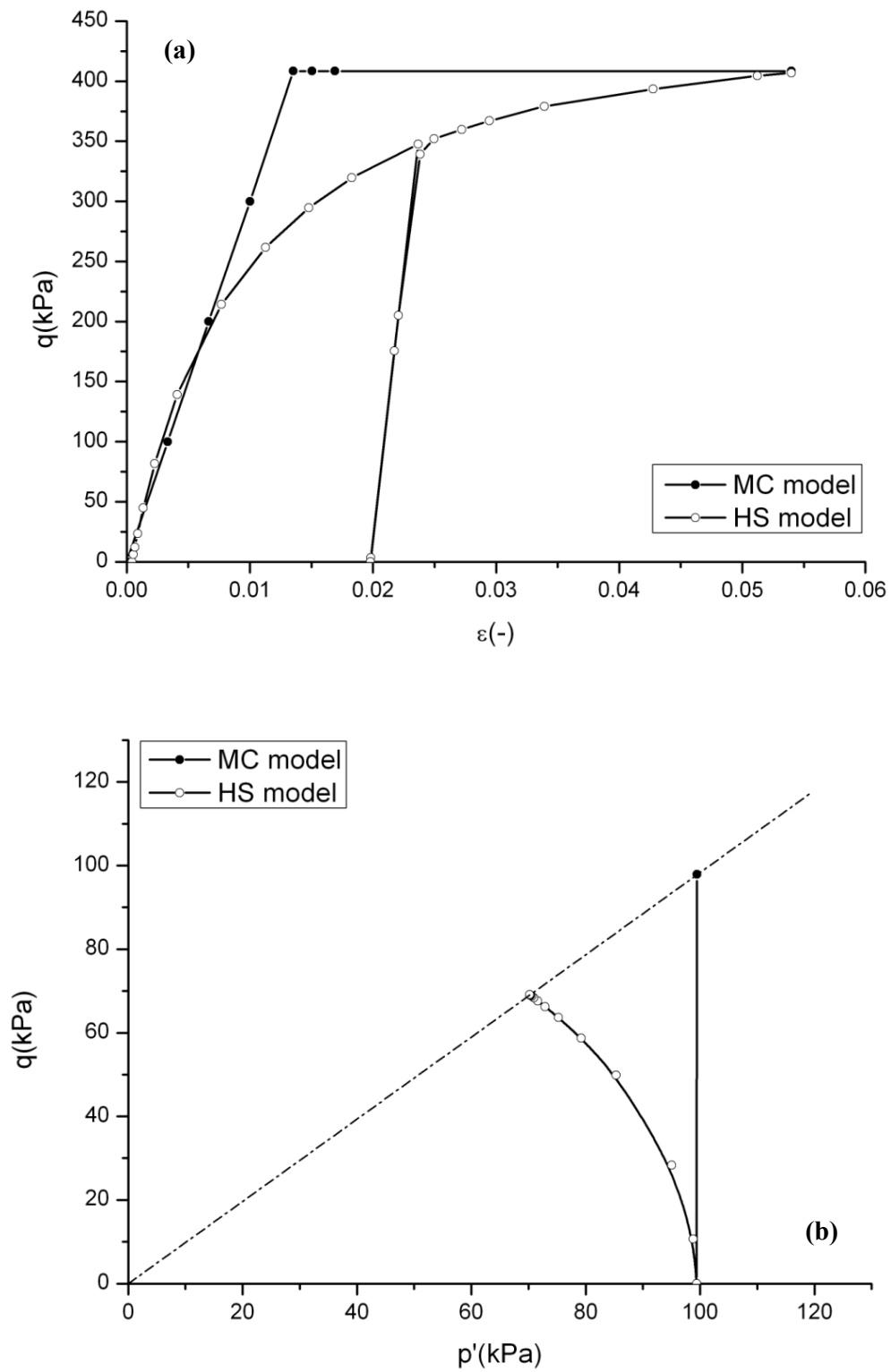
Figure 3-15 Results of triaxial tests using the MC and HS models, (a) principal stress difference versus axial strain in CD test and (b) ESP in CIU test.
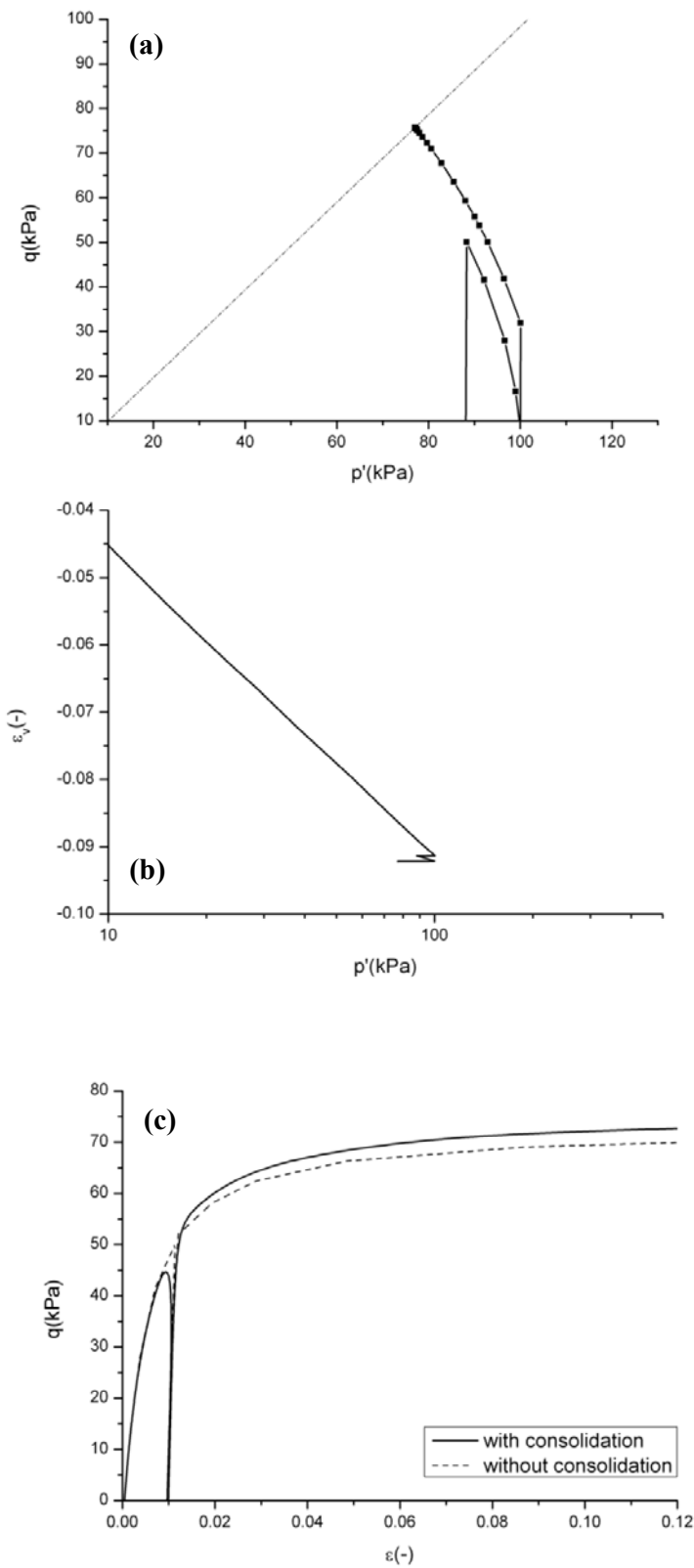
Figure 3-16 Resutls of CIU test using the HS model (a) ESP in p'~q space,(b) e-logp'
and (c) principal stress diffenence (q) versus axial strain.
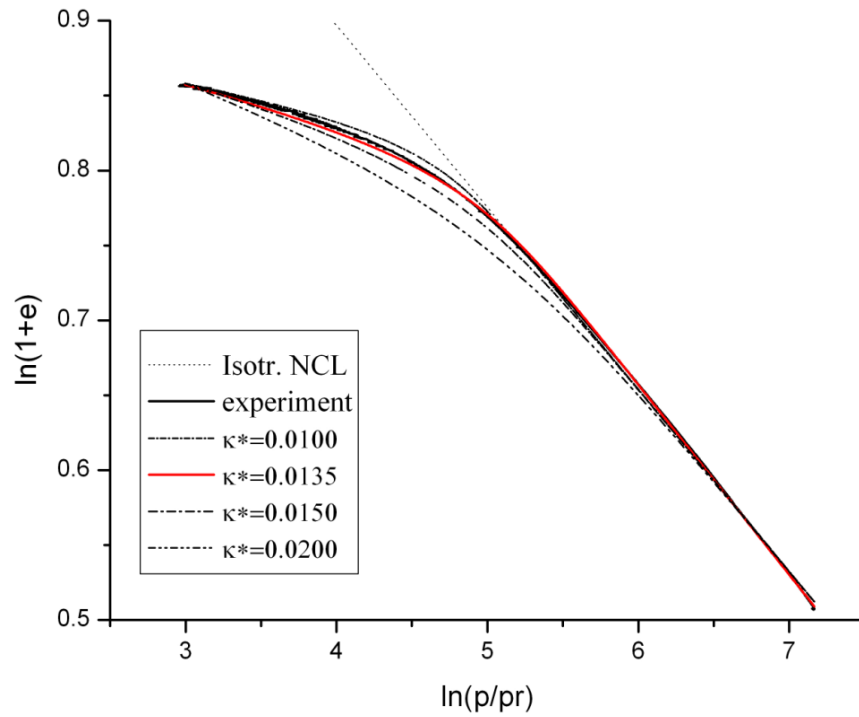
Figure 3-17 Calibration on N, λ^* and κ^* on an isotropic compression test on reconstituted Singapore Marine clay.
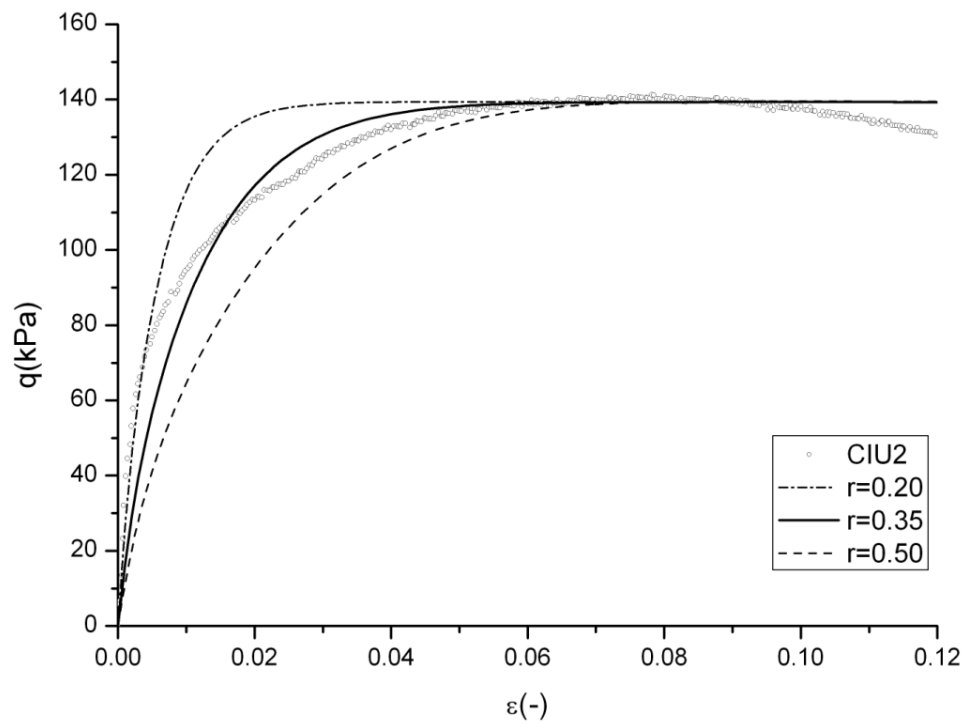
Figure 3-18 A parameter study for the calibration of r.
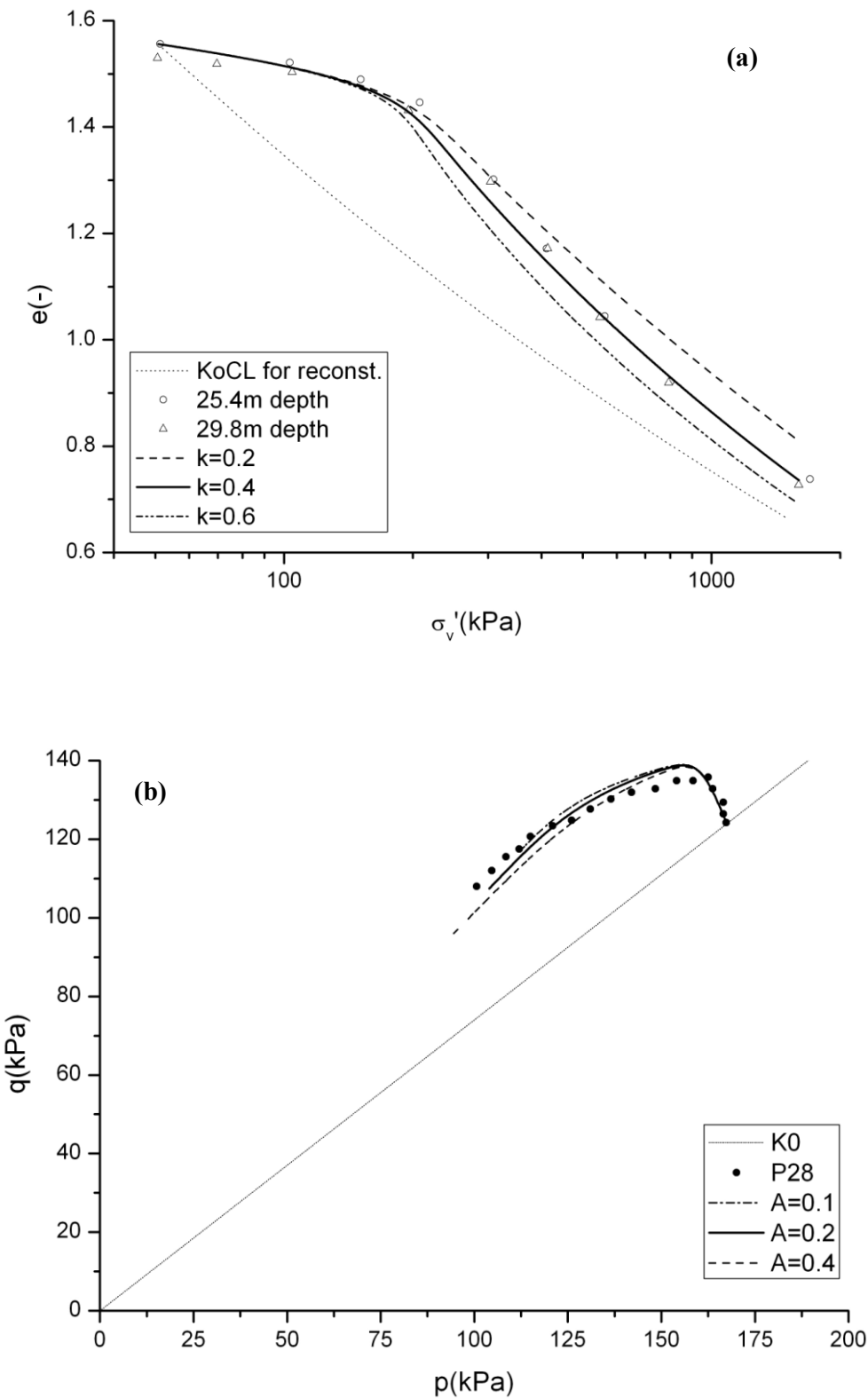
Figure 3-19 Calibration of (a) *k* on the odemeter test and (b) *A* on the triaxial shear test on nature Singapore Marine clay.
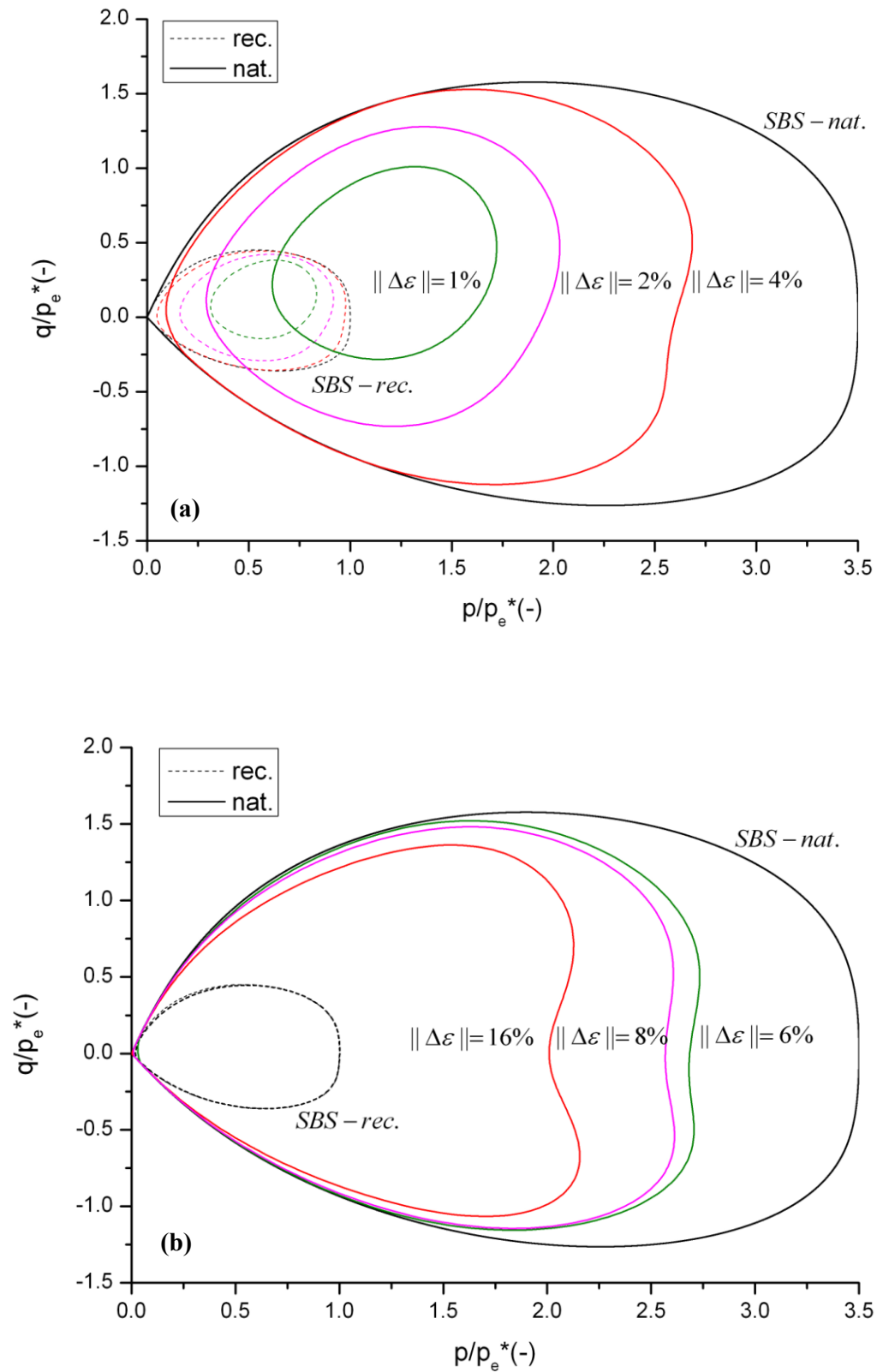
Figure 3-20 Normalized incremental stress response envelopes (NIREs) of the enhanced hypoplastic model for (a) medium and (b) large strain ranges.

(a) D_{DCM}=100 mm

(b) D_{DCM}=50 mm
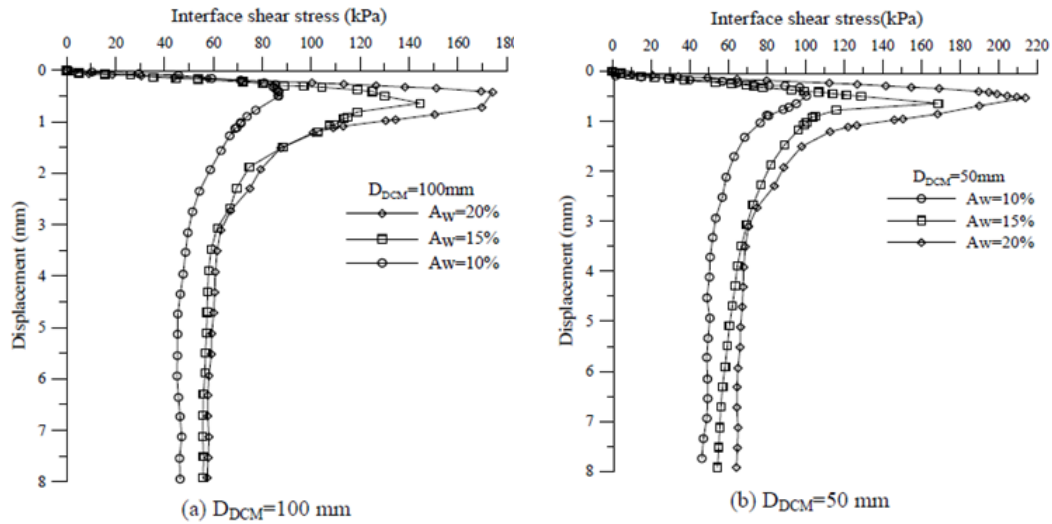
Figure 3-21 Interface shear stress versus displacement (Tanchaisawat et al. 2006).
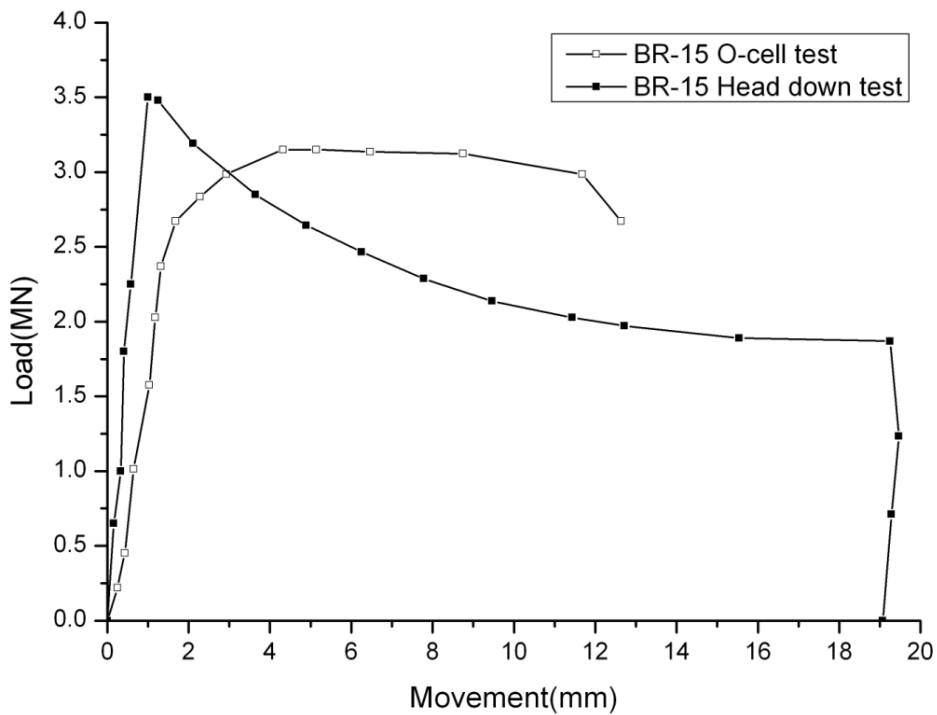
Figure 3-22 Results of first Cycle O-cell test and head-down test on BR15 (after Tan and Fellenius 2012).

The soil-bentonite cake layer is simulated by thin layer

void
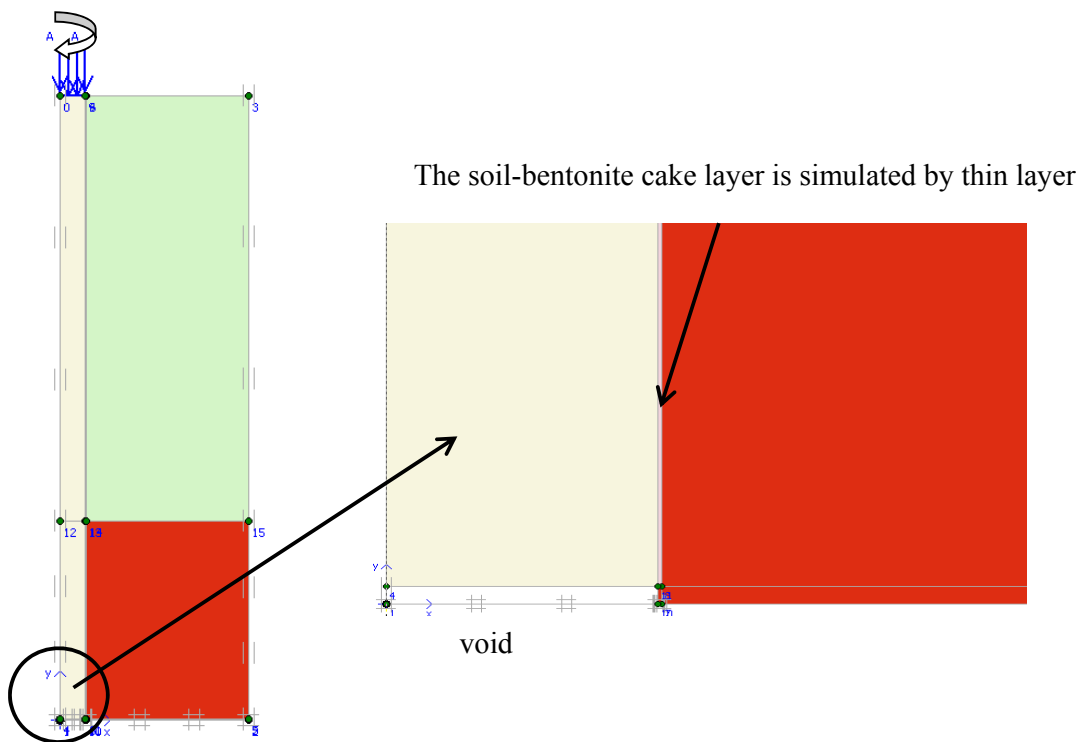
Figure 3-23 Axisymmetric configuration for the FEM simulation.
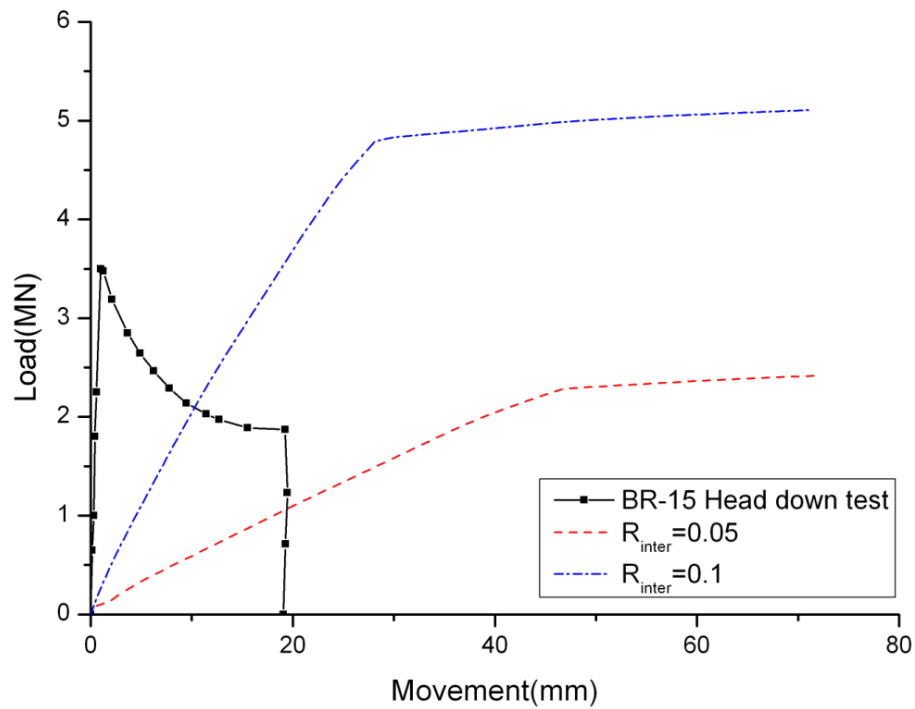
Figure 3-24 Head-down load-movement responses for R_inter values of 0.05 and 0.1 simulations and actual test values (after Tan and Fellenius 2012).
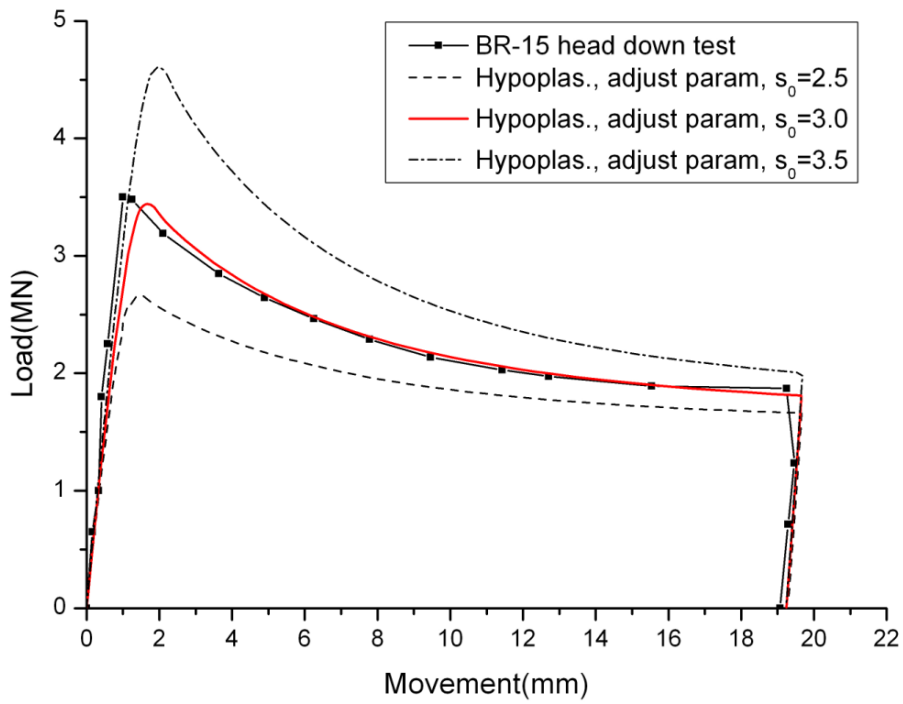
Figure 3-25 Comparison of the head-down load-movement responses for test results with the numerical simulation with the enhanced hypoplastic model using different s_o.

CHAPTER 4 NUMERICAL PROCEDURE FOR MODELING INSTALLATION EFFECTS FOR DISPLACEMENT PILES

4.1 INTRODUCTION

The literature review presented in Chapter 2 demonstrated that there is a lack of modeling installation effects of displacement piles using Finite Element Method (FEM). This chapter describes the development of an improved numerical procedure for modeling the installation effect in the displacement pile and compares its performance to previous methods using the centrifuge test results.

First a review of the modeling of non-displacement pile showed the importance of interface elements and mesh design in computing the load capacity of the pile. Next, Broere & van Tol's (2006) method of modeling installation effect of a displacement pile was revisited. Based on their method, the improved numerical procedure is proposed. This procedure combines use of volumetric strains for end bearing resistance and the prescribed displacements for shaft resistance. Finally, the results obtained from the improved numerical procedure are compared with centrifuge pile load tests.

4.2 MODELLING PILE

4.2.1 Numerical modeling procedure

The Finite element (FE) model used is an axisymmetric model since only circular in cross section is considered and only vertical loading is applied to the pile. Pile and soil are modeled using 15-noded triangular elements with 12 Gauss points for numerical integration. As suggested by Wehnert and Vermeer (2004), the pile is modeled as a cluster of volume elements having the dimensions and location of the pile installed at depth. Soil is modeled around and below the pile, such that the boundaries of the model are sufficiently far away from the pile. Li (2004) concluded that the boundary effects can be ignored if the boundaries are more than two times length of the pile away from the pile. For this reason, more than two times length of the pile away from the pile's boundaries were employed for all the following analyses, unless otherwise stated. In addition, a vertical distributed load is modeled on the top of pile.

The procedure of the numerical analysis of pile is divided into four phases. The steps are:

(1) Generate the axi-symmetric mesh. The size of mesh is larger than two times length of the pile in radius and in height. Thus the boundary effects can be ignored. At zone close to the pile (5D from center of pile and 5D below the pile tip), local mesh refinement is necessary. The mesh dependency will be discussed in section 4.2.2.

(2) Generate initial stresses and water pressures. The initial effective stresses are generated following the Ko procedure: $\sigma'_{vo} = \gamma' z; \sigma'_{ho} = K_o \times \gamma' z$ The value of Ko is defined as follow in PLAXIS:

$$K_o^{nc} = 1 - \sin \phi' \text{ for normally consolidated (NC) soil} \qquad (4.1)$$

$$K_o = K_o^{nc} OCR - \frac{v_{ur}}{1 - v_{ur}}(OCR - 1) \text{ for overconsolidated (OC) soil} \qquad (4.2)$$

(3) The material of the pile cluster is replaced by the linear elastic concrete material and, if present, the interface elements between soil and pile are activated. The pile weight is larger than the soil weight so that the state of stress is slightly changed. This approach is used to model the installation process of non-displacement pile. Katzenbach & Arslan (1995) showed that the change of in-situ stress state next to the pile shaft is only marginal while installing a bored piles with casing. However, this simple approach cannot be used to model displacement pile, like Jack-in pile or driven pile, since the stresses of soil around the pile are significantly changed during the installation. Therefore, the pile installation effects will be simulated using other methods, as described in Section 4.3.

(4) At this stage, the displacement is set to zero and the loading begins. First, a unit distributed load is activated on the top of the pile. Subsequently this load is increased until the automatic load-increment routine in the PLAXIS is unable to increase the load further.

4.2.2 Mesh dependency

Based on the numerical modeling procedure described above, a series of analyses was performed to investigate the mesh dependency. Assuming pile is 1m diameter and 10m length and the pile is installed in uniform soil. The soil parameters for analyses are shown in Table 4.1. Three different mesh densities with interface elements and without interface elements were compared denoted as "global coarse", "global very fine" and "global extra fine". The different meshes are shown in Figure 4.1. All the meshes are axi-symmetric and are composed of 15-noded elements.

Table 4-1 Soil parameters for mesh dependency analyses

Parameter	Soil	Pile	
Model	MC	Linear elastic	Unit
E_{50}^{ref}	30000	3×10^7	kPa
c'	0.01	NA	kPa
φ'	30	NA	°
ψ	0	NA	°
v	0.3	0.2	-

The results are illustrated for the MC model in Figure 4.2. From these results, the advantage of interface elements can be clearly seen. Without interface elements, there is a clear difference between the results from the "global coarse", "global very fine" and "global extra fine mesh". When interface elements are used, the differences between results with "global coarse" and "global fine mesh" are much smaller than those without using interface elements. This is in accordance with the findings by

Wehnert and Vermeer (2004) and Broere and van Tol (2006). However, the difference between "very fine mesh" and "extra fine mesh" is still present. It seems that the global refine mesh procedure does not work effectively on mesh convergence.

The judicious mesh refinement mesh is used instead of global refinement mesh. Base mesh is "global coarse" and the mesh is locally refined around the pile and near the pile tip: line refinement for the pile skin interface and cluster refinement for pile base of 5D socket in the soil. Four different meshes are analysed, one time refinement, two times refinement, three times refinement and four times refinement, each increment of refinement meant a doubling of the mesh size in the selected cluster. The different meshes are shown in Figure 4.3. The load-settlement curves that results from these calculations are shown in Figure 4.4. As can be seen, the difference between two times refinement and three times refinement is still present, but the difference between calculation with three times refinement and four times refinement is negligible. The judicious mesh refinement mesh does effectively work for mesh convergence. To be optimum in calculation accuracy and time, the refine three times mesh (cluster refinement of 5D for shaft and base) was employed for all analyses.

4.3 MODELLING OF DISPLACMENT PILE BY PRESCRIBING BOUNDARY CONDITION

Displacement pile is different from non-displacement pile. The installation process of

displacement pile results in a compaction of the soil and a significant increase in the

stresses surrounding the pile. All of these complicate the stresses around the pile.

4.3.1 Overview

As discussed in Chapter 2, although the Arbitrary Lagrangian Eulerian (ALE)

approach is suitable for modeling the installation process of displacement piles and

could give reasonable stress changes and density response during the installation, but

the computed bearing capacity by the ALE approach is much overestimated.

Moreover, the time-consuming nature and difficulty of the ALE approach makes it

difficult to employ for engineering design. The simpler technique of prescribed

boundary conditions at the pile-soil interface, developed by Broere & van Tol (2006),

shows the capability of modeling the installation effect of the displacement pile in

regular Finite Element environment and was employed here.

4.3.2 Numerical modeling procedure

PLAXIS does not allow direct simulation of the actual installation process of

displacement pile. The installation effect, as suggested by Broere & van Tol (2006), is

simulated after the initial stress generation by increasing the volume of the pile cluster

around the pile shaft by the prescribed displacements at the pile-soil boundary. After

that the material of the pile cluster is replaced by the linear elastic concrete material

and then the interface elements between soil and pile are re-activated. The stress state

obtained in this step is maintained and all displacements are set to zero. Thereafter, a unit distributed load is activated on the top of the pile. Subsequently this load is increased to simulate the pile load test. Since the soil stress around pile is significantly changed during the installation process, the mesh should be locally refined in the cluster 5D around the pile shaft and 5D below the pile tip. The typical mesh is shown in Figure 4.5.

4.3.3 Results and discussion

The numerical results are compared to a centrifuge pile test performed at GeoDelft (Allard, 1996). In this test, a 0.5 diameter pile continuously jacked into a uniform saturated sand layer to a depth of 15m was modeled by a 14.14 mm model pile scale pile at 35.4g acceleration. The velocity during this test was chosen sufficiently small that no excess pore pressure was generated. During the test both total jack-in force and base load were recorded.

The Hardening Soil (HS) model is employed to model the behavior of sand and the soil parameters are taken from Broere & van Tol (2006) and shown in Table 4.2. The same numerical procedures, suggested by Broere & van Tol (2006) in their numerical study of GeoDelft test, are used and different calculation cases are summarized here:

Case 1. Ignore the installation effect of the displacement pile, using the same numerical modeling procedure for modeling the non-displacement pile described in

section 4.2.1.

Case 2. Using the volumetric strain to model the installation effect, ε_v=100%.

Case 3. Using the prescribed displacements to model the installation effect. $u_x = 15mm$ and $u_y = 1500mm$ are applied.

The results from the calculations are given in Figure 4.6 and Table 4.3. As can be seen from the graph, if the installation effect is ignored, the calculated pile capacity is too low compared to the test result. When the prescribed displacements are used to model the installation effect, the total pile capacity is predicted correctly. The calculated load capacity is 2.31 MN and 2.36 MN for case 2 and case 3 respectively, and errors are within 5%. Furthermore, the separate shaft friction and the base resistance are predicted accurately in case 3. The prescribed displacement method offers more flexibility since the horizontal and the vertical displacement component can be set independently. However, as mentioned in Chapter 2, the current prescribed boundary conditions at the pile-soil interface to model the installation effect still has limitation in prediction of distribution of shaft friction and more detail are shown in the section 4.3.4.

Table 4-2 GeoDelft centrifuge test soil parameters (after Broere & van Tol (2006))

Name	Symbol	HS model	Unit
Dry weight	γ_{unsat}	20	kN/m^3
Wet weight	γ_{sat}	20	kN/m^3
Young's modulus	E_{50}^{ref}	1.1×10^4	kN/m^2
Oedometer modulus	E_{oed}^{ref}	9.6×10^3	kN/m^2
Power	M	0.5	-
Unloading modulus	E_{ur}^{ref}	3.3×10^4	kN/m^2
Poisson's ratio	N	0.2	-
Reference stress	P	100	kN/m^2
Cohesion	C	0.1	kN/m^2
Friction angle	Φ	37	°
Dilatancy angle	Ψ	0	°
Interface strength reduction	R_{inter}	0.75	-

Table 4-3 Calculation results of the GeoDelft centrifuge test (Allard 1996)

	F_{total} : MN	F_{shaft} : MN	F_{base} : MN	Error*: %
Case 1	0.65	0.22	0.43	-72.2
Case 2	2.31	1.50	0.81	-1.3
Case 3	2.36	1.07	1.27	0.9
Centrifuge test	2.34	1.12	1.22	-

Error*: $\dfrac{F_{total}(calculated) - F_{total}(test)}{F_{total}(test)} \times 100\%$

4.3.4 The limitation of the current prescribed boundary method

As pointed out in section 2.4.2, although the current prescribed boundary method improved predictions of the displacement pile behavior significantly, several limitations can be identified. The normal effective stress and the shear stress on the

pile-soil interface along the pile shaft after installation and at failure are shown in

Figure 4.7. As can be seen, the normal effective stress along pile increases with depth

but decreases again some two meters above the pile tip. This stress distribution differs

from Mahutka *et al* (2006) calculation which is increasing along depth without any

reduction described in Chapter 2. The distribution is also different from the findings by

White and Lehane (2004), which is a monotonic increase of normal stress with depth.

Further, the full shaft friction of the pile at failure also shows the same drop near the

pile tip as the normal effective stress. Again, this result differs from the findings by

many authors (i.e. Lehane *et al* (1993), Nicola (1996), Tomlinson (2001)), who find an

increase of shaft friction towards the pile tip. The only similar case is found by Klotz

(2001). However, he did not give any explanations on the contrasting observations.

Clearly, the stress state around pile using the current prescribed boundary method

(Broere & van Tol, 2006) is different from several reported experimental findings, and

their numerical model does not capture all installation effects although it can predict

the bearing capacity of the displacement pile.

As discussed in Chapter 3, the behavior of shaft friction is described with an elastic-

plastic model in PLAXIS by using the interface element. The Coulomb criterion is

used to distinguish between elastic and plastic behavior, followed in Eq. 3.29 and 3.30.

It is clear that the shaft friction is fully dependent on the normal effective stress for the

given soil. Thus, the shaft friction drops near the pile tip is due to the decrease of

normal effective stress some distance above the pile tip.

Applying the horizontal displacement to the pile-soil interface to simulate the installation effect on the pile shaft is similar to the cylindrical cavity expansion theory (Castro and Karstunen 2010). Randolph et al. (1979) and Yu (2004) used the cylindrical cavity expansion theory for the analysis of shaft resistance of displacement pile. The cylindrical cavity is expanded from a very small initial radius to the actual pile radius in their analysis. While, the cylindrical cavity expansion starts from the actual pile radius and ends at small amount increment (normally 10mm to 20mm) in the current prescribed boundary method. The installation effect of the displacement pile shaft modeled as the cylindrical cavity expanded from a very small initial radius to the actual pile radius seems to be logical. Since, in reality, the creation of a cylindrical space starts from zero radius to the actual pile radius as the pile tip pushes the soil away from the path of the pile. However, Azzouz et al. (1990) showed that modeling pile installation solely through cylindrical cavity expansion (from a very small initial radius to the actual pile radius) leads to overestimate of the effective radial stress on the pile shaft by a factor of 2, compared to those from the strain path method. Basu et al. (2011) deemed that the installation of a displacement pile need to be considered as three stages (demonstrated in Figure 4.8 a) and the vertical shearing along the pile shaft after the cylindrical cavity expansion cause the effective radial stress at given depth to decrease (So-call friction fatigue or "h/R" effect mentioned in Chapter 2). Basu et al. (2011) further showed that the vertical shearing happening

during the pile passing down is essential for the estimation of shaft capacity through

their 1-D FEM analysis and this vertical shearing eliminates the overestimation of the

effective radial stress from cylindrical cavity expansion only (Figure 4.9) . In order to

investigate the prescribed boundary conditions at pile-soil interface that will give a

reasonable distribution of the effective radial stress at pile shaft, the following

different numerical procedures were conducted to model the installation effect of the

displacement. A 0.5m diameter and 9m long pile is jacked in uniform sand layer. The

HS model is applied to model the sand behavior and the model parameters are the

same shown in Table 4.2.

Method 1. The effective radial stress was captured using the combining cylindrical

cavity expansion with vertical shearing, suggested by Basu et al. (2011). The cavity

expansion phase starts from a very small initial radius $r_o = 0.02m$ and ends when the

cavity radius becomes equal to the actual pile radius $r = 0.25m$ ($u_x = 0.23m$). Since it

is a large strain problem, the updated mesh option is used in the calculation. Then, the

vertical prescribed displacement is applied on the pile shaft ($u_y = 0.03m$) to simulate

the vertical shearing as the pile passes downward.

Method 2. The effective radial stress was captured using the simple approach of

prescribed boundary conditions at the pile-soil interface. The horizontal prescribed

displacement is applied on the pile shaft ($u_x = 0.02m$).

The effective radial stresses along the pile shaft obtained in Method 1 and Method 2

then are compared and shown in Figure 4.10. As can be seen, the effective radial stress

at end of the cavity expansion is very large and significantly greater than the initial

value ($\sigma'_{ho} = K_o \times \gamma'z$). When the primary vertical shearing phase is considered, the

effective radial stress trends to relax. Basu et al. (2011) explained that this relaxation

of the effective radial stress is due to the direction of loading changes from horizontal

to vertical. At end of the vertical shearing, approximate 40% of the effective radial

stress is lost due to such changes in the shearing direction and the effective radial

stress is similar to those from Method 2. The small difference is observed in Figure

4.10. The FEM results were also compared with the prediction from Eq. 4.3,

expressed:

$$\sigma'_h = K \times \gamma'z \; ; \; \frac{K}{K_o} = 0.93 \exp\left[\frac{D_R}{100}\left(2.8 - 0.45\ln\left(\frac{\sigma'_{vo}}{p_a}\right)\right)\right] \quad (4.3)$$

where D_R is the relative density, expressed as percentage (%); σ'_{vo} is the in situ vertical

effective stress; K_o is the coefficient of lateral earth pressure at-rest, expressed as Eq.

4.1, for NC soil.

Eq. 4.3 was developed by Basu et al. (2011) based on their 1-D FEM analysis using

the similar combining cylindrical cavity expansion with vertical shearing (as method

1). As shown in Figure 4.10, the distribution of the effective radial stress from method

1 and method 2 are comparable with that from Eq. 4.3, except some results which are

near the ground surface and the pile tip. This is because that the prediction from Eq.

4.3 is based on 1-D FEM analysis and it is suitable for depth which the displacement is

mainly in the radial direction. While, for 2-D FEM analysis (method 1 and method 2)

the displacement near the ground surface and the pile tip are affected by the ground

surface (free surface) and the pile tip respectively. In summary, although the simplified

numerical procedure, prescribing boundary conditions at the pile-soil interface, cannot

give the reasonable development of effective radial stress along the pile shaft, the

reasonable stress states around the pile shaft at end of the installation of the

displacement pile can be obtained by using the proposed simplified numerical

procedure.

Clearly, modeling installation effect to the pile shaft using prescribed boundary

conditions with vertical shearing at the pile-soil interface gives reasonable stress states

around the pile shaft. The following calculations make an attempt to explain why the

normal effective stress reduces when the current prescribing boundary method (Broere

& Tol 2006) is used. Three cases are considered:

Case 1: the prescribed displacements $u_x = 15mm$ and $u_y = 0mm$ are applied

Case 2: the prescribed displacements $u_x = 0mm$ and $u_y = 1500mm$ are applied

Case 3: the prescribed displacements $u_x = 15mm$ and $u_y = 1500mm$ are applied

The normal stress states along the pile shaft obtained in Case1~3 then are checked and

the results are shown in Figure 4.11. As can be seen from the graphs, Case 1 which is

no more vertical displacement applied shows the reasonable distribution of the normal

effective stress along the pile shaft. This is similar trend as Mahutka *et al* (2006)

calculation. Very high horizontal stresses can be observed at the pile toe. Case 2 which

is only applied the vertical displacement at the pile tip shows significant reduction on the normal effective stress some distance above the pile tip, from initial value 60kPa, decreasing to 6kPa. It is due to the relaxation of the stress occurs as the prescribed displacement deactivate when the pile cluster material is activated owing to the numerical implementation in PLAXIS. As a result, when these two prescribed displacements combined together (Case 3), it is not surprised that the decreasing normal effective stress near the pile tip can be observed (Figure 4.11). Clearly, applying the horizontal displacement to the pile shaft gives the reasonable distribution of the normal effective stress, while applying the simple vertical prescribed displacement to the pile tip to simulate the installation effect will give unreasonable behavior of shaft friction. Prediction from the Strain Path Method (SPM) (Teh & Houlsby, 1991) and model tests reported by White (2002) showed that soil below the pile tip flows around the pile tip, which is not simply a vertical movement (Figure 4.12~4.14). Therefore other method is sought to improve the numerical procedure.

4.3.5 Spherical cavity expansion

As discussed in Chapter 2, the pile/cone penetration can be simulated by expanding a cavity of an initial zero radius or finite radius. Many authors (i.e. Vesic (1977), Ladanyi (1961), Randolph *et al.* (1994) and Yasufuku *et al.* (2001)) believe that the soil displacements in front of the pile/cone tip may be considered closer to those undergoing spherical expansion, as schematically illustrated in Figure 4.14. Thus

spherical cavity expansion is applied to the soil cluster below the pile tip to simulate

the installation effect to the soil below. Prior to that, the numerical model for spherical

expansion in PLAXIS was tested by comparing the computed pressure-expansion

curves with those given by the closed-form solutions in the section 4.4.

4.4 ANALYSIS OF SPHERICAL CAVITY EXPANSION

4.4.1 Spherical cavity expansion in PLAXIS

Volumetric strain is applied to the spherical cavity to simulate the spherical cavity

expansion in PLAXIS. Volumetric strain was firstly utilized as the input parameter to

simulate the overall effects of displacement grouting by Schweiger et al. (2004). Xu

(2007) applied these volumetric strains to simulate the spherical cavity expansion. The

numerical procedures are summarized here.

4.4.1.1 Mesh set-up and initial stress generation

The analysis was performed with an axi-symmetric mesh and triangular elements with

15 nodes and 12 gauss stress points were used. The initial radius of the spherical

cavity 'a_o' was set at a nominal value of 0.1m. Xu (2007) suggested that this value

was selected so that the variation in initial stresses adjacent to the cavity had minimal

effect for the analyses performed. The radius of the mesh domain is 12m and the

height is 24m. This mesh boundary is sufficient to represent an infinite large soil mass

for the spherical cavity with initial radius is 0.1m. The standard fixity is applied to the mesh (total fixity at the bottom, free at the top and free fixity in vertical direction only in left and right hand boundaries) and the typical mesh used for predictions in the uniform soil is shown in Figure 4.15.

The water level is at the surface and the initial effective stresses are generated following the Ko procedure: $\sigma_v' = \gamma' \cdot z$ and $\sigma_h' = K_o \cdot \sigma_v'$. Value of Ko is set to be unity all the cases.

4.4.1.2 Calculation

The cavity pressure-expansion relationship can be obtained by selecting appropriate nodes and gauss for output. In all analyses, nine nodes (denoted as A to I) and ten stress points (denoted as J to S) were selected inside the cavity elements (Figure4.16). The average of results from those nodes and stress points enable the determination of the pressure expansion curve.

Then cavity expansion was imposed by applying the positive volumetric strain to the spherical soil cluster incrementally (i.e. +10%) in the calculation phases. This results in incremental expansion of cavity. For large strain problem, the Updated Mesh option in PLAXIS was used.

4.4.1.3 Output

The radial displacement from the nine nodes and the maximum effective principal stress from the ten stress points were obtained. The results are averaged to give the pressure-expansion curve. The maximum pressure from the pressure-expansion curve is determined as the limit pressure.

4.4.2 Numerical model verification in sand

4.4.2.1 Closed-form solutions to the limit pressure

Closed-form solutions for the stress and the displacement fields in the dilatant soil during spherical cavity expansion are given by Yu & Houlsby (1991). The pressure-expansion relationship can be evaluated by using those closed-form solutions. The solutions using the direct integration of strain rate and the logarithmic strain definition has been used so that large-strain effects can be taken into account. The soil adopted is the Mohr-Coulomb yield criterion with a constant rate of dilation. The steps for constructing pressure expansion curve and calculating limit pressure are given in the following:

(1) Choose input soil parameters E (the Young's modulus), ν (the Poisson's ratio), c (the cohesion), φ (the friction angle), ψ (the dilation angle), and p_o (the initial mean effective stress).

(2) Calculate the derived parameters from input parameters: (Parameter 'm' is used to

indicate cylindrical analysis (m=1) or spherical analysis (m=2))

$$G = \frac{E}{2(1+v)} \tag{4.3}$$

$$M = \frac{E}{1-v^2(2-m)} \tag{4.4}$$

$$Y = \frac{2c\cos\varphi}{1-v^2(2-m)} \tag{4.5}$$

$$\alpha = \frac{1+\sin\varphi}{1-\sin\varphi} \tag{4.6}$$

$$\beta = \frac{1+\sin\psi}{1-\sin\psi} \tag{4.7}$$

$$\gamma = \frac{\alpha\cdot(\beta+m)}{m\cdot(\alpha-1)\cdot\beta} \tag{4.8}$$

$$\delta = \frac{Y+(\alpha-1)\cdot p_o}{2\cdot(m+\alpha)\cdot G} \tag{4.9}$$

$$\eta = \exp\{\frac{(\beta+m)\cdot(1-2v)\cdot[Y+(\alpha-1)\cdot p_o]\cdot[1+(2-m)\cdot v]}{E\cdot(\alpha-1)\cdot\beta}\} \tag{4.10}$$

$$\xi = \frac{[1-v^2(2-m)](1+m)\delta}{(1+v)(\alpha-1)\beta}$$

$$\times[\alpha\cdot\beta+m\cdot(1-2v)+2v-\frac{m\cdot v\cdot(\alpha+\beta)}{1-v\cdot(2-m)}] \tag{4.11}$$

(3) If the cavity pressure is less than the pressure p_1 required to initiate plasticity,

$p_1 = 2m\cdot G\cdot\delta + p_o$, calculate the cavity radius from the small strain elastic

expression $(a-a_o)/a_o = (p-p_o)/2mG$. The initial radius of the cavity is referred

as 'a_o', while the current radius during expansion is referred as 'a'.

(4) For the given value of p (cavity pressure which is greater than p_1 and than the limit

pressure p_∞), calculate the cavity pressure ratio 'R' by using following Equation:

$$R = \frac{(m+\alpha)\cdot[Y+(\alpha-1)\cdot p]}{\alpha\cdot(m+1)\cdot[Y+(\alpha-1)\cdot p_o]} \qquad (4.12)$$

(5) Evaluate a/a_o from the following Equations:

$$\frac{a}{a_o} = \{\frac{R^{-\gamma}}{(1-\delta)^{(\beta+m)/\beta} - (\gamma/\eta)\Lambda_1(R,\xi)}\}^{\beta/(\beta+m)} \qquad (4.13)$$

where $\Lambda_1(R,\xi) = \sum_{n=0}^{\infty} A_n^1$ $\qquad (4.14)$

in which

$$A_n^1 = \frac{\xi^n}{n!}\ln R \qquad \text{if } n = \gamma$$

$$\qquad (4.15)$$

$$A_n^1 = \frac{\xi^n}{n!(n-\gamma)}(R^{n-\gamma}-1) \qquad \text{otherwise}$$

Only a few terms will be sufficient.

The procedures from (4) to (5) can be repeated to construct the complete cavity

pressure expansion relationship. Note that displacement $u = a - a_o$.

By putting $(a/a_o) \rightarrow +\infty$ in Equation 4.13, R_∞ can be found from

$$\Lambda_1(R_\infty, \xi) = (\eta / \gamma)(1-\delta)^{(\beta+m)/\beta} \tag{4.16}$$

Then from

$$R_\infty = \frac{(m+\alpha)\cdot[Y+(\alpha-1)\cdot p_\infty]}{\alpha\cdot(m+1)\cdot[Y+(\alpha-1)\cdot p_o]} \tag{4.17}$$

The limit cavity pressure p_∞ can be obtained.

4.4.2.2 Comparisons with numerical results

To validate the accuracy of the numerical model, the pressure-expansion curves derived using PLAXIS are compared with the closed-form solutions of Yu and Houlsby (1991) for a linear elastic-perfectly plastic Mohr-Coulomb soil model which are described in the section 3.2.1. In total, three cases were considered, labeled MC1, MC2 and MC3. The soil parameters are shown in the Table 4.4. Cases MC1 to MC3 cover a wide range of E, φ, ψ values.

The PLAXIS calculations and the closed-form calculations are shown in Figure 4.17. As can be seen, the PLAXIS predictions generally show very good agreement with the closed-form solutions. The difference between these two calculations on limit pressure calculation is shown in the Table 4.4 and they are all within 5% for the cases studied. These are in accordance with the findings from Xu (2007).

Table 4-4 Material parameters and the limit pressure in the verification calculations

	p_o: kPa	a_o: m	E: MPa	v	φ	ψ	p_{lc} (closed-form): kPa	p_{lp} (Plaxis): kPa	e*: %
MC1	120	0.1	5	0.2	20	0	550	558	1.5
MC2	120	0.1	50	0.2	40	0	3008	2974	-1.1
MC3	120	0.1	100	0.2	40	10	7350	7531	2.5

$$* \quad e = \frac{p_{lp} - p_{lc}}{p_{lc}}$$

4.4.3 Numerical model verification in clay

4.4.3.1 Closed-form solutions to limit total stress and excess pore pressure

Collins and Yu (1996) developed analytical solutions of undrained cavity expansion in clays. In undrained deformations it is common to work with total stresses (i.e. Gibson and Anderson (1961)). However, this is no longer appropriate in models where the strength of the soil is a variable since the strength is function of the effective stresses rather than the total stresses. Collins and Yu's approach is based on the effective stress analysis.

The closed-form for critical state soil model, like the modified Cam Clay model, sometimes cannot be obtained and instead a numerical integration must be used. Here the perfectly plastic model with the Tresca yield criterion: $\sigma_1 - \sigma_3 = Y$ (here $Y = 2c_u$ and c_u is undrained shear strength) is considered to simplify the problem. Thus the in situ soil behave purely elastically before reaching the critical state under undrained loading and mean effective stress are constant. The effective stress path for Tresca

model of cavity expansion is shown in the Figure 4.18.

The excess pore pressure at the cavity wall for given value of 'a' is given by the following Equations:

$$\Delta U_c = \frac{k}{k+1} q_o [\ln(1 - (\frac{a_o}{a})^{k+1} + \ln I_r]$$
(4.18)

where:

$$q_o = 2c_u$$
(4.19)

$$I_r = \frac{1}{\gamma_o}$$
(4.20)

$$\gamma_o = \frac{q_o}{2G}$$
(4.21)

Using the above Equation, the total radial stress solution at cavity wall is obtained by

$$\sigma_r = p_o + \frac{k}{k+1} q_o [1 + \ln(1 - (\frac{a_o}{a})^{k+1} + \ln I_r]$$
(4.22)

where: p_o is the in-suit soil total stress

The Equations 4.18 and 4.22 can be repeated by using different value of 'a' to construct the complete cavity expansion curve. By setting $(a/a_o) \rightarrow +\infty$ in Equation 4.22, the limit total stress can be obtained.

4.4.3.2 Comparisons with numerical results

To validate the accuracy of the numerical model, the computed cavity expansion curve and the limit total stress by PLAXIS are compared with those of the closed-form solutions above. In PLAXIS, the MC soil model is used. Furthermore, φ is put to zero and c is equal to the undrained shear stress of soil. Then the yield surface of MC model is same as Tresca model's. The parameters used in the calculations are list in Table 4.5. There is some difference between numerical model in sand (drained calculation) and in clay (undrained calculation) on selection of stress points for output. As cavity expansion progresses, the stress points for correct excess pore pressure output should be selected at cavity wall outside cavity.

The FE calculations are shown in Figure 4.19 and Table 4.6. As shown in Figure 4.19, the numerical results, obtained using PLAXIS, show good agreement with closed-form solutions in both total stresses and excess pore pressure-expansion curves. The difference between the FEM results and the closed-form solutions is within 5%, similar to the drained cavity expansion cases.

Table 4-5 Material parameters adopted in the verification calculations

p_o : (kPa)	a_o : (m)	E' : (MPa)	v	φ	c : (kPa)	q_o : (kPa)
240	0.1	6.5	0.3	0	30	60

Table 4-6 Limit excess pore pressure and pressure in the verification calculations

	Closed-form: (kPa)	Plaxis: (kPa)	e: (%)
Limit excess pore pressure	176.7	168	-5%
Limit total stress	456.8	457.5	0.2

4.5 DEVELOPMENT OF NEW NUMERICAL PROCEDURE

4.5.1 Methodology

The pile is first modeled as a cluster of volume elements having the dimensions and location of the pile installed at depth. Soil is modeled around and below the pile, such that the boundaries of the model are sufficiently far away from the pile. On the top of the pile a distributed load is modeled of 1 kPa. Interface elements are modeled on the outside of the cluster representing the pile.

As discussed in the section 4.3.5, the spherical cavity volume expansion will be applied to the soil cluster below the pile tip and the prescribed horizontal displacement is applied at the interface between pile and soil along the shaft (Figure 4.20). The combination of the spherical cavity volume expansion at the pile tip and the prescribed horizontal displacement at the pile shaft is to simulate the installation effects of the displacement pile.

The relationship between the geometry of the cavity and the pile is schematically shown in Figure 4.21. 'd' is diameter of the pile and 'a' is radius of the spherical cavity. Based on the assumption that the angle of the soil wedge, $\angle ABC = 45° + \varphi'/2$. The radius of the spherical cavity 'a' equals $d/2 \times \tan(45° + \varphi'/2)$.

The procedure of the numerical analysis of displacement pile is divided into four phases. The steps are:

(i) Set-up and generate the axi-symmetric mesh. Refine cluster 5D around the pile shaft and 5D below the pile tip. Standard fixity is applied to the mesh. HS model is assigned to the soil. The interface elements are modeled on the outside of the cluster to model the interface behavior between pile and soil. The pile is wish-in-place at the installed depth. The prescribed horizontal displacement is applied at the interface between pile and the soil along shaft.

(ii) Generate the initial stress and the water pressure. The initial effective stresses are generated following the Ko procedure: $\sigma'_{vo} = \gamma' z$; $\sigma'_{ho} = K_o \times \gamma' z$. The value of Ko is calculated by Equation 4.1 and 4.2.

(iii) Define the calculation phases. The first calculation phase is to simulate the installation effect. The prescribed horizontal displacement at the interface between pile and soil along the shaft is activated and the positive volumetric strain is applied to the spherical soil cluster above the pile tip (Figure 4.21). In the second phase, the material

of the pile cluster is replaced by the linear elastic concrete material and the interface

elements between soil and pile are activated, the prescribed horizontal displacement

deactivated.

(iv) Compute the bearing capacity of the pile. At this stage, the displacement is set to

zero and the loading begins. First, a unit distributed load is activated on the top of the

pile. Subsequently this load is increased until the automatic load-increment routine in

the PLAXIS is unable to increase the load further.

4.5.2 Evaluation of the improved numerical procedure's predictions

The proposed numerical procedure was evaluated on the following centrifuge

experiments on sand.

4.5.2.1 GeoDelft centrifuge test

The predicted performance of a displacement pile is evaluated through the

comparisons with the centrifuge test discussed in section 4.3.3. First, the prescribed

horizontal displacement Δu_x is equal to 15mm suggested by Broere & van Tol (2006)

and the positive volumetric strain of 100% is used. The results are given in Figure

4.22. The shaft friction found with $\Delta u_x = 15mm$ is too high. As might be expected, the

shaft friction is influenced mainly by the amount of horizontal prestressing. Therefore

it was decide to perform several calculations with Δu_x less than 15mm. Figure 4.19

shows the load-settlement curves for these cases. The case with a Δu_x of 10mm, shaft

friction is 1.1MN, close to the centrifuge test's result, while base resistance is too low,

therefore further calculations were made varying the amount of positive volumetric

strain and keeping the Δu_x at 10mm. As can be seen in Figure 4.23, the case with Δu_x

of 10mm and $\Delta \varepsilon_v$ of 150% fits the centrifuge test results best. Both the shaft friction

and base resistance are predicted to within 5%. It should be noted that all the

predictions show soften behavior compared to test result. However, the main objective

here is to vary the modeling procedure to obtain a reliable prediction of pile capacity

instead of best fit test results.

Table 4-7 Parameter variation and calculation results of the GeoDelft centrifuge test

Δu_x :mm	$\Delta \varepsilon_v$:%	F_{total} : MN	F_{shaft} : MN	F_{base} : MN
15	100	2.18	1.23	0.95
12	100	2.09	1.15	0.94
10	100	2.04	1.10	0.94
10	125	2.17	1.13	1.04
10	150	2.32	1.15	1.17
-	-	2.34*	1.12*	1.22*

* The centrifuge test results

In order to further judge the correctness of the FEM results, the following issues are

considered:

(1) The lateral earth pressure in the vertical cross section

(2) The shear stress on the pile-soil interface along the pile shaft at failure.

(3) The total load capacity of the pile at failure and distribution between the shaft friction and base resistance.

The results of the radial stress in the vertical cross section in a distance at 0.3m from the pile shaft after installation are shown in Figure 4.23. As can be seen, very high horizontal effective stresses can be found at the pile tip. Below the peak stress the radial stresses drop down to a value below Ko. This distribution of radial stress is in accordance with findings by Mahutka et al. (2006).

The distribution of shear stress on the pile-soil interface along the pile shaft at failure are shown in Figure 4.24 compared to the results form Broere & van Tol (2006)'s method and the design approach proposed by Randolph et al. (1994) which is discussed in Chapter 2. As can be seen, shear stress calculated from model with spherical expansion around the pile tip generally increases with depth and has a very high value near the pile tip. This pattern is similar to those from design approach proposed by Randolph et al. (1994). While Broere & van Tol (2006)'s method gives different trend near the pile tip where the shear stress decreases to zero at pile tip.

Figure 4.22 shows the load-settlement curve for new model and Broere & van Tol (2006) method, compared to the centrifuge test. As can be seen, the load-settlement curve from the proposed numerical procedure is a much better fit to the test results. Both the shaft friction and base resistance are predicted better than those from Broere

& van Tol (2006) method (Table 4.8). The ratio between shaft friction and base

resistance from GeoDeflt Centrifuge test is reported as 0.92. The ratio given by new

model is 0.98, compared to value of 0.85 from Broere & van Tol's method.

Table 4-8 FEM results from different models compared with GeoDeflt test results

	F_{total} : MN	F_{shaft} : MN	F_{base} : MN
Broere & van Tol's method	2.33	1.07	1.26
Improved model	2.32	1.15	1.17
GeoDeflt Centrifuge test	2.34	1.12	1.22

4.5.2.2 City University centrifuge test

The same numerical procedure has been applied to a pile from a series of centrifuge

test which were reported by Klotz and Coop (2001). A horizontal prescribed

displacement of 4% of the pile radius same used in previous section and 160% positive

volumetric strain is applied to the spherical soil cluster above the pile tip.

The prototype pile in this test has a 1.6 m diameter and been installed 36m in a dry

sand with a relative density of 57%. The aluminum model pile has 16mm diameter and

test was performance at 100g. Pile load tests were conducted by Klotz and Coop

(2001) after the pile installation. A base resistance of 31.2MN and a shaft friction of

12.5MN are reported. The Hardening Soil (HS) model is applied and the soil

parameters for modeling are taken based on Klotz and Coop (2001) shown in Table

4.9.

Results of calculations are given in Figure 4.25, compared to the results from centrifuge test and Broere & van Tol (2006)'s method. Although both FEM results overestimate the bearing capacity of the pile, the improved model proposed in this chapter gave a total load capacity of 44.2MN which is much closer to 43.7MN from centrifuge test than 47.4MN from Broere & van Tol (2006)'s method. Furthermore, 31.1 MN base resistance and 13.1 MN shaft friction are found from the calculation using proposed numerical procedure. Both of these are predicted within 5% of test results.

Table 4-9 Soil parameter for calculation results of the City university centrifuge test

Name	Symbol	HS model	Unit
Dry weight	γ_{unsat}	14.5	kN/m^3
Young's modulus	E_{50}^{ref}	1.2×10^4	kN/m^2
Oedometer modulus	E_{oed}	1.1×10^4	kN/m^2
Power	M	0.5	-
Unloading modulus	E_{ur}^{ref}	3.6×10^4	kN/m^2
Poisson's ratio	N	0.2	-
Friction angle	Φ	32	°
Dilatancy angle	Ψ	0	°
Interface strength reduction	R_{inter}	0.43	-

Table 4-10 FEM results from different models compared with City University test results

	F_{total} : MN	F_{shaft} : MN	F_{base} : MN
Broere & Tol's method	47.4	20.4	27
Improved model	44.2	13.1	31.1
City University Centrifuge test	43.7	12.5	31.2

4.6 CONCLUSIONS

Firstly, the importance of interface elements was found. Without the interface elements, the results of using FEM calculations are heavily mesh dependent when the HS model is used. The judicious refinement mesh the line refinement for the pile skin interface and the cluster refinement for 5D around pile shaft and 5D around pile base results in effective mesh convergence.

The stress increase due to pile installation was successfully modeled with a few relatively simple steps. Applying horizontal prescribed displacement to the pile shaft gives a reasonable distribution of the normal effective stress around the pile shaft at end of installation, while applying the simple vertical prescribed displacement to the pile tip to simulate the installation effect gives unreasonable behavior of shaft friction near the pile tip compared to experimental results. The combination of applying horizontal prescribed displacement to the pile shaft and applying vertical displacement to pile tip, like Broere and van Tol's method, overestimates the total shaft friction and underestimates the total end bearing capacity. In order to improve these limitations,

the improved numerical procedure is proposed. Contrasting to Broere & van Tol's (2006) method, the spherical cavity expansion is applied to the soil cluster below the pile tip instead of the vertical prescribed displacement; while the horizontal prescribed displacement is applied at the interface between pile and soil along the shaft similar to Broere & van Tol's procedure.

The predictions of the new improved numerical procedure showed reasonable stress state around the pile shaft and pile tip after installation, and are in closer agreement with reported experimental findings and studies. Prediction of the bearing capacity of the displacement pile can be obtained using this improved numerical procedure and the distribution between the base resistance and the shaft friction is correctly determined in good agreement with pile installation centrifuge tests data.
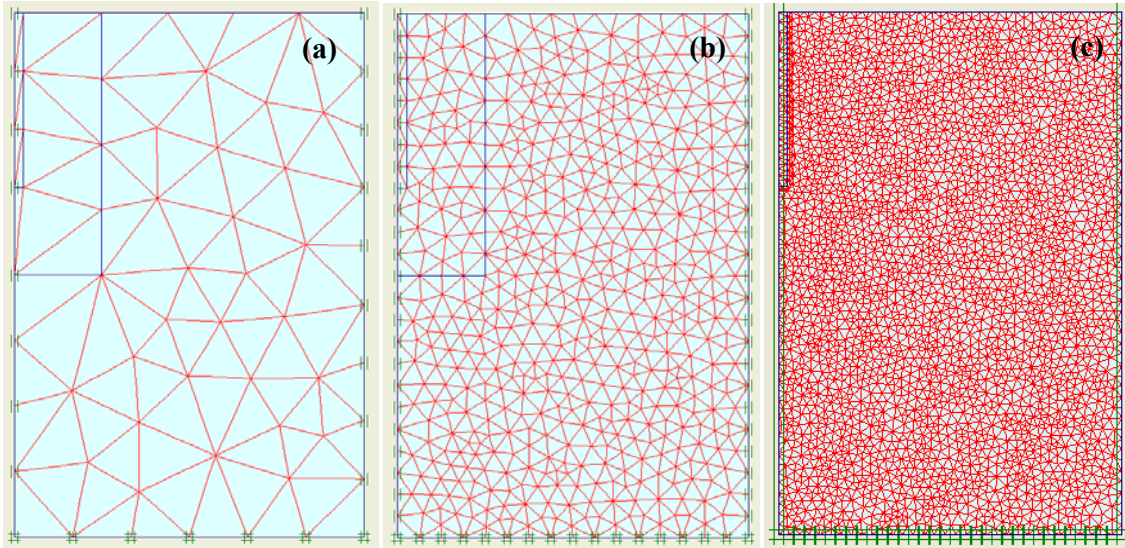
Figure 4-1 Different mesh for calculations (a) Global coarse mesh, (b) Global fine mesh, and (c) Global extra fine mesh.
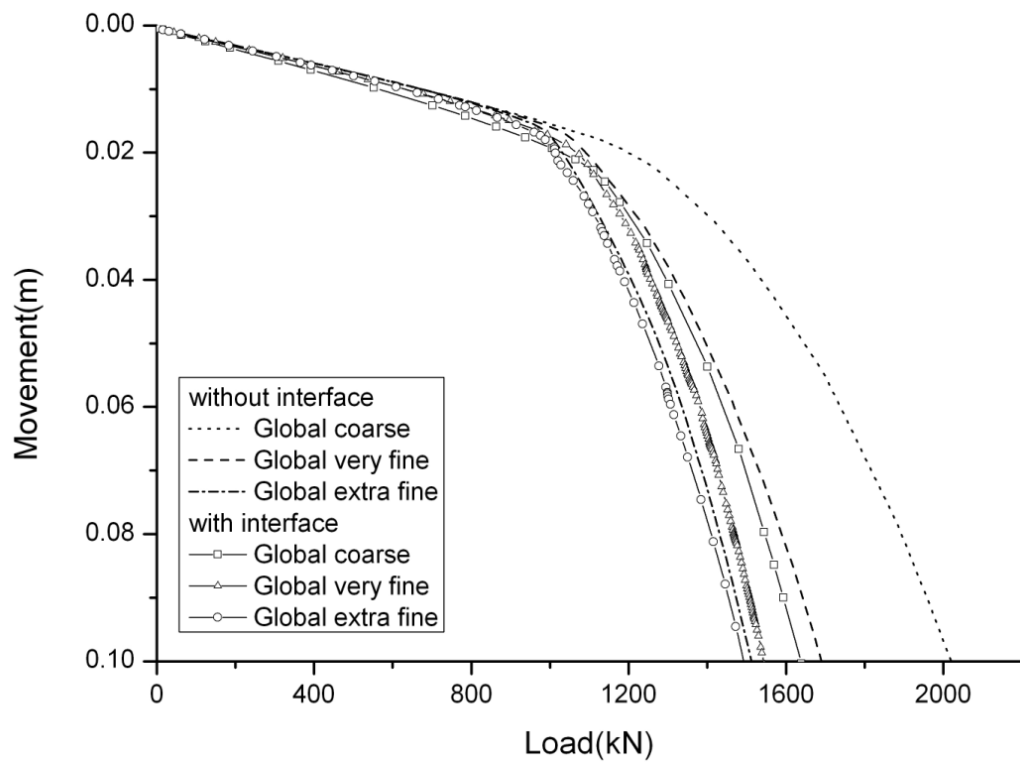
Figure 4-2 Mesh dependency for the MC model without interface element and with interface element.
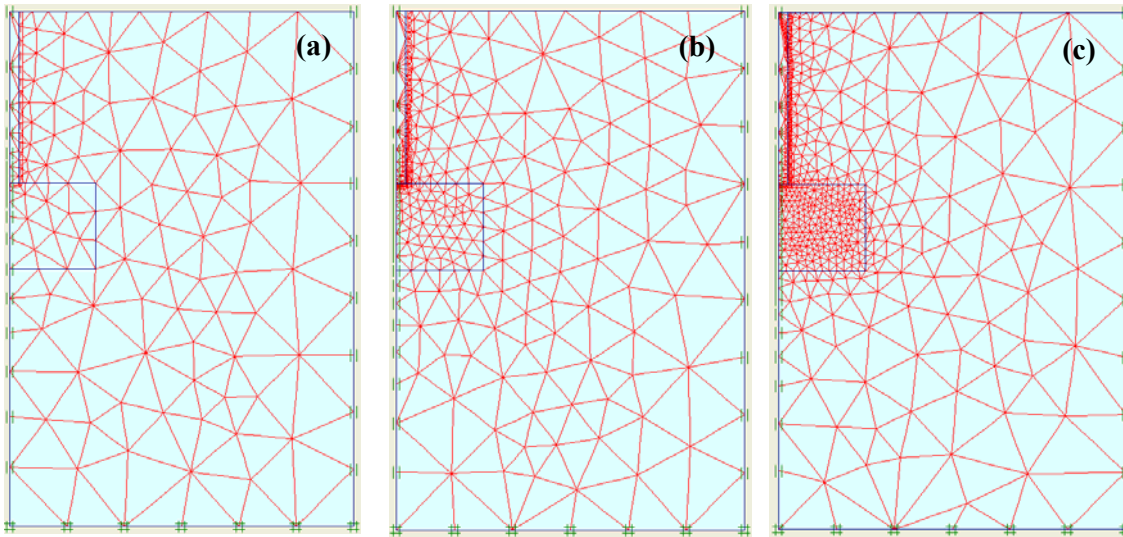
Figure 4-3 Different mesh for calculations (a) Refine 1 time, (b) Refine 2 times, and (c) Refine 4 times.
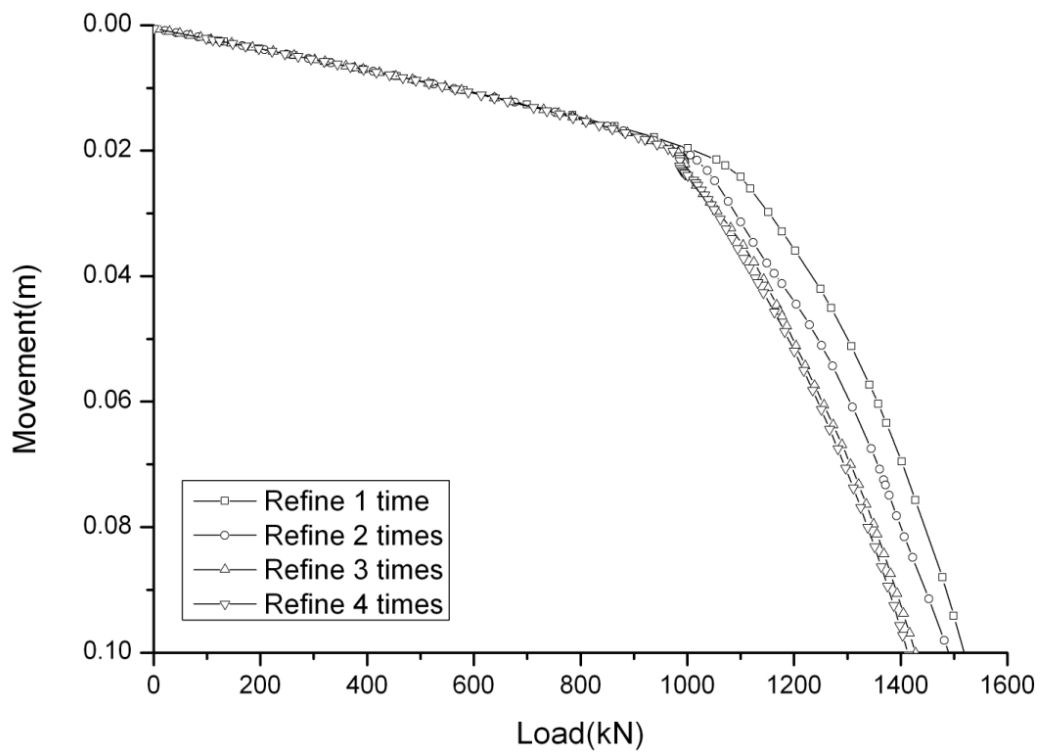
Figure 4-4 Mesh dependency for the MC model for judicious refinement with interface elements.
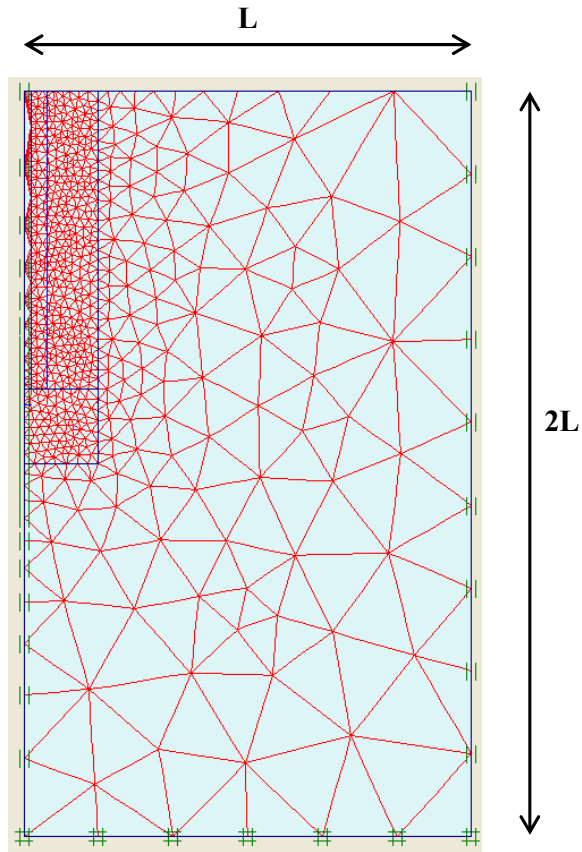
Figure 4-5 Typical FEM mesh for GeoDeflt centrifuge.
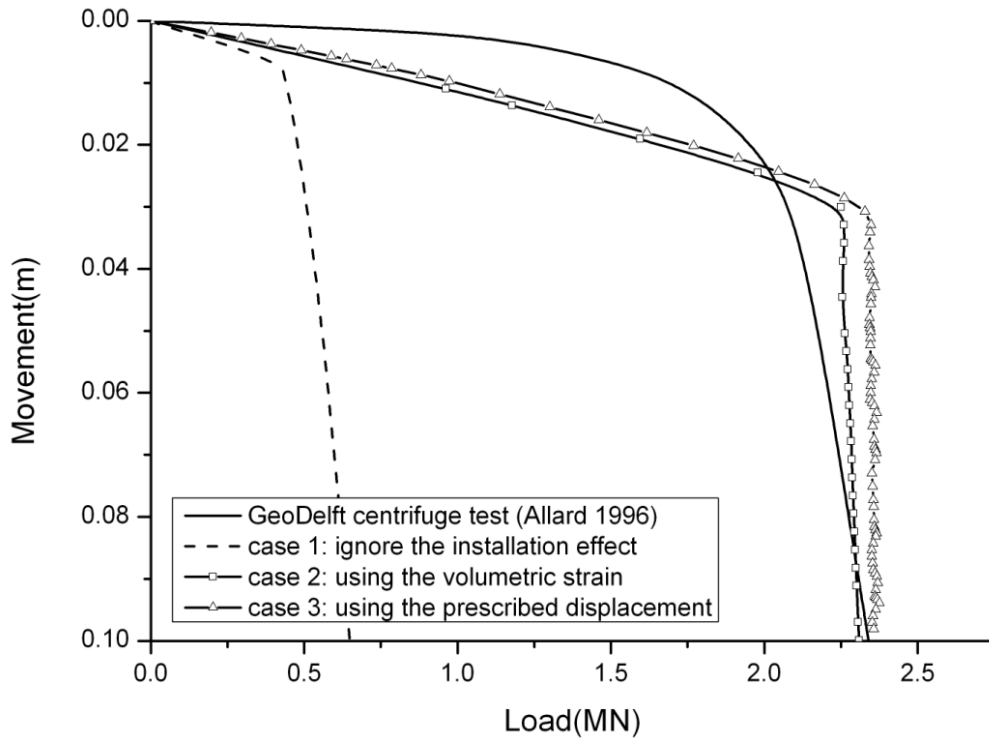
Figure 4-6 Load-movement curves for different cases, compared with test result.
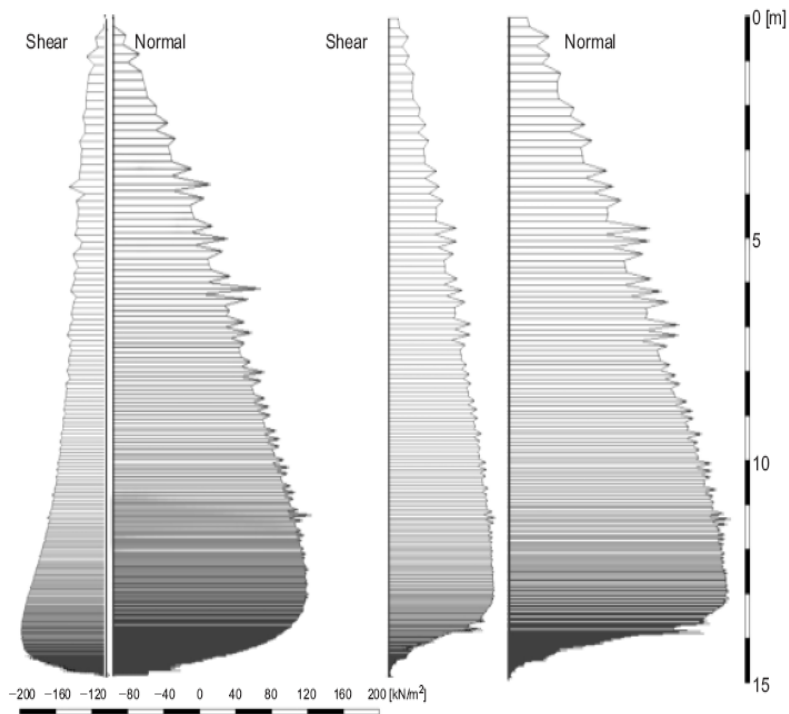
Figure 4-7 Normal and shear stresses after the installation (left) and at failure (right) (Broere and van Tol 2006).
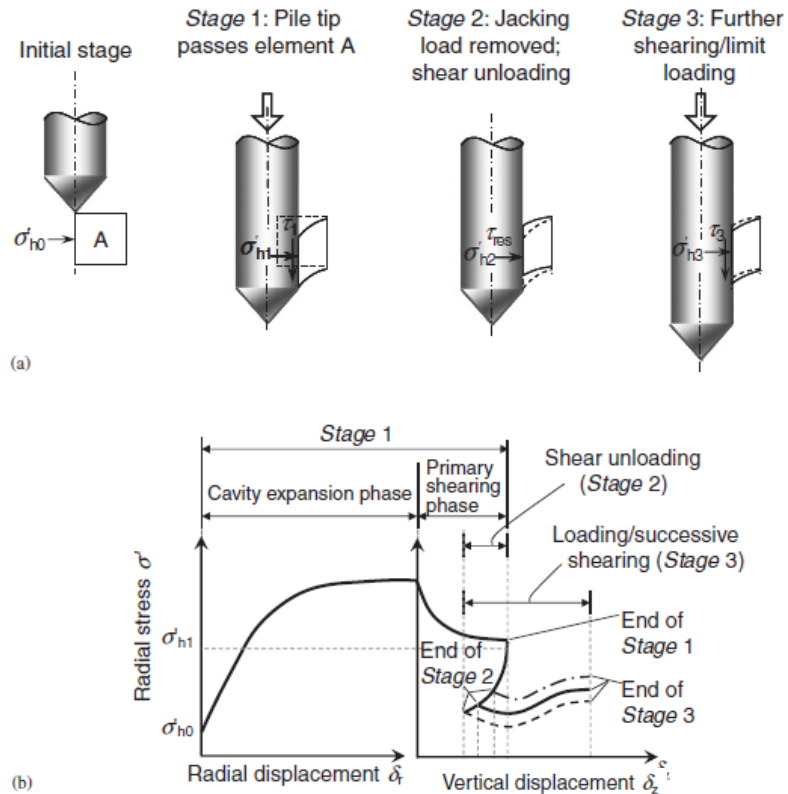
Figure 4-8 Installation of jacked piles: (a) analysis stages and (b) evolution of normal stress at pile shaft. (Basu et al., 2011).
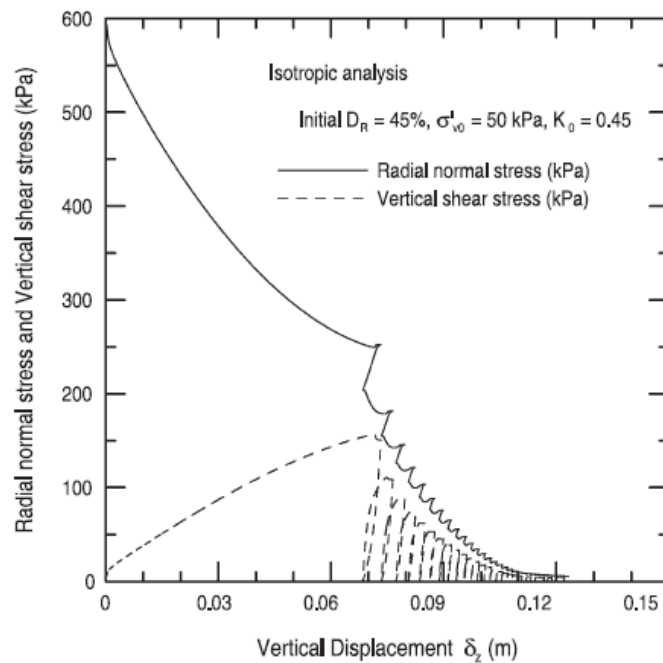
Figure 4-9 Evolution of the normal and shear stress on the pile shaft during vertical shearing. (Basu et al., 2011).
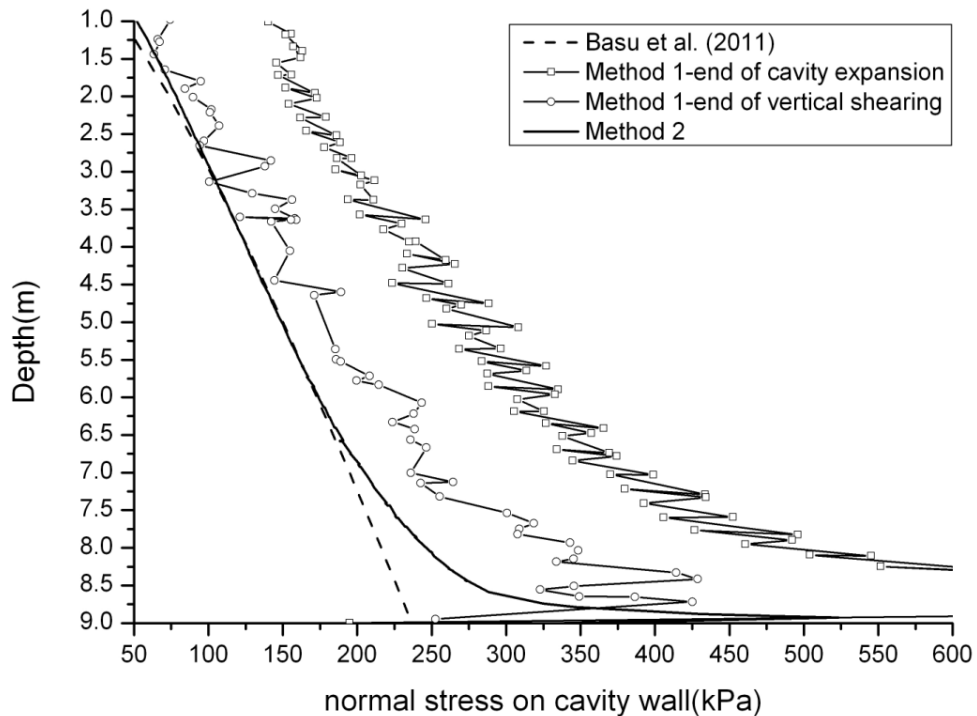
Figure 4-10 The distribution of normal stress for different methods.
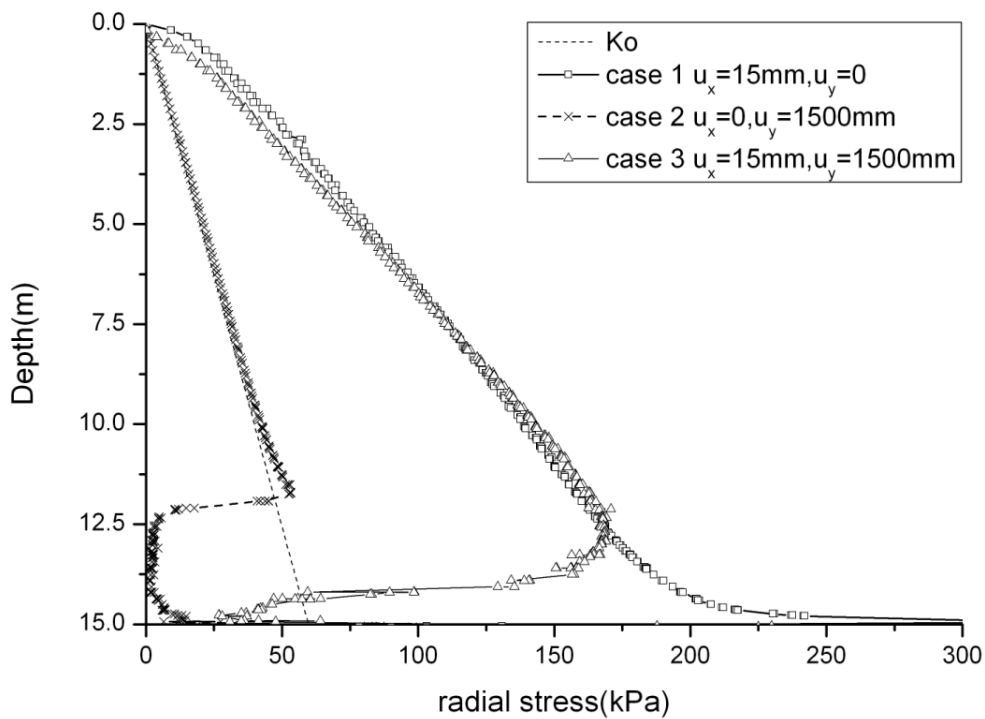
Figure 4-11 The distribution of radial stress for different cases.
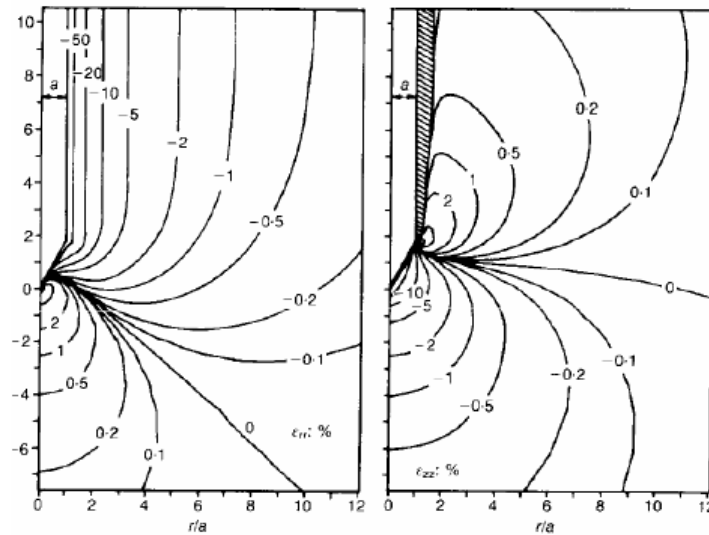
Figure 4-12 Radial and vertical strain contours around a cone. (Teh and Houlsby 1991).
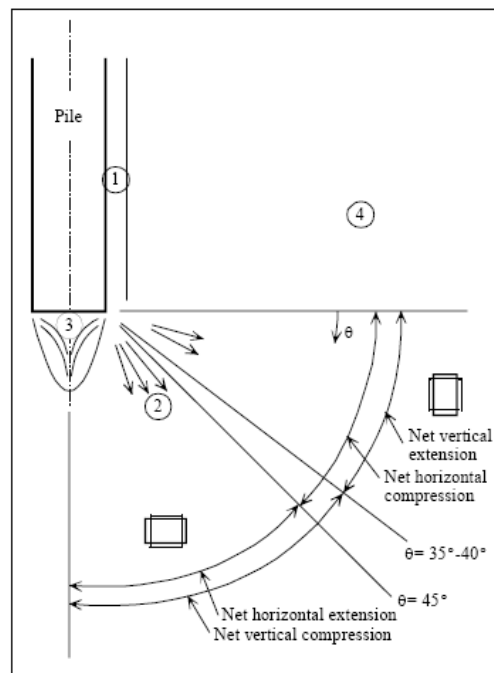
① Very dense zone. Significant particle breakage.
Slight contraction with increasing pile penetration

② Very high shear strain reducing with distance
from pile shoulder, constant with θ

③ 'Nose cone' of very dense soil. Significant breakage. Not rigid.
Soil flows through nose cone and around shoulder

④ Slight densification, decreasing with offset from shaft.
Horizontal extension with increasing pile penetration

Figure 4-13 Generalized patterns of strain after the pile installation. (White 2002).

(a) Ladanyi (1961)   (b) Yasufuku et al. (2001)
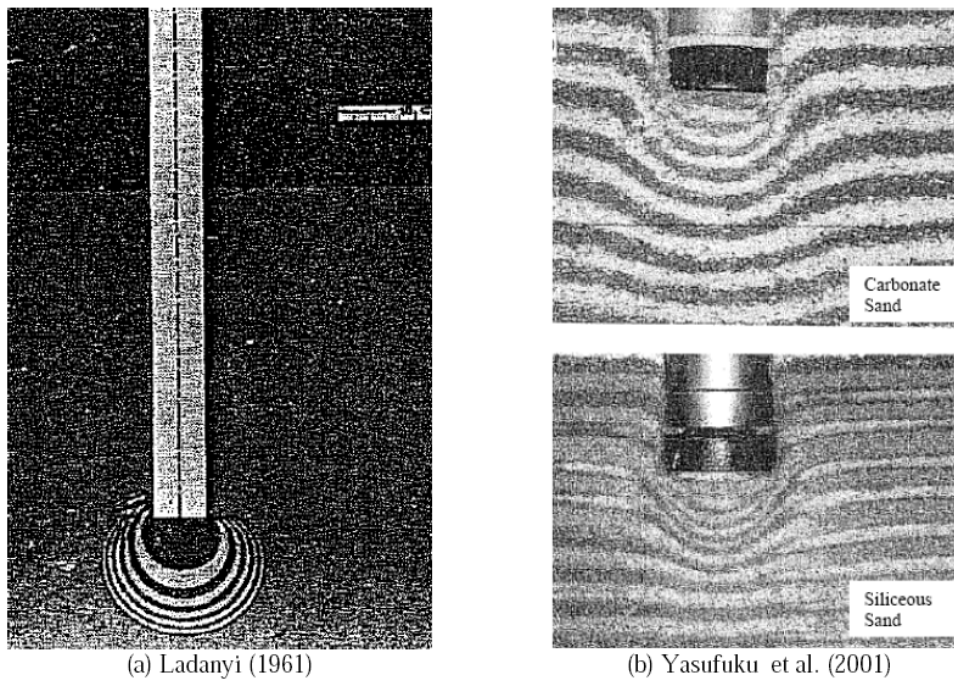
Figure 4-14 Failure mode under the pile tip.
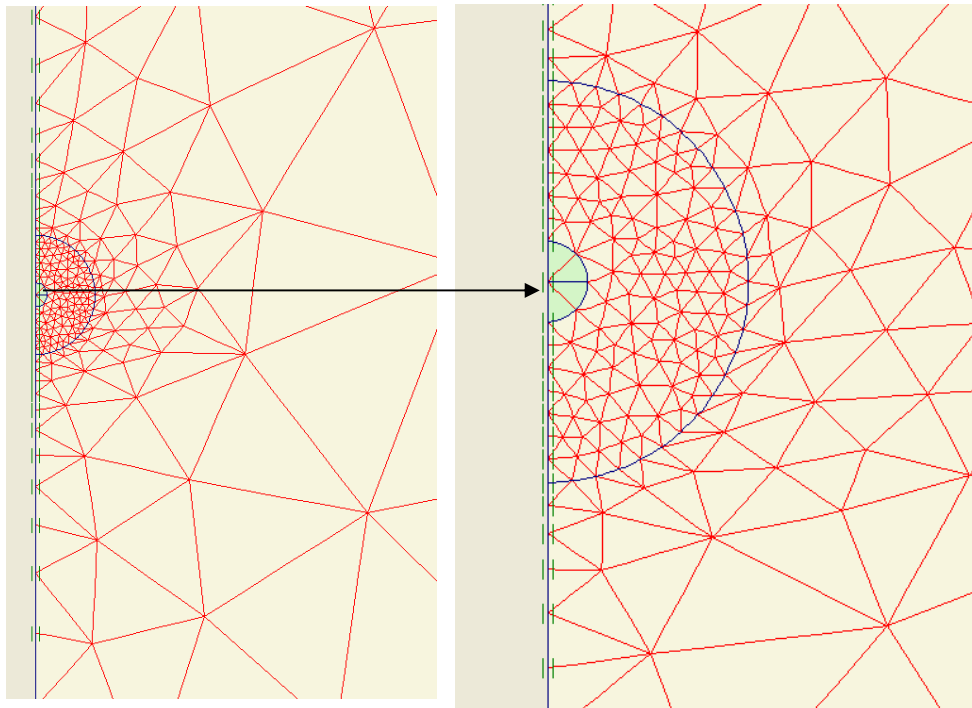
Figure 4-15 Typical mesh for the spherical cavity expansion in FEM simulation.
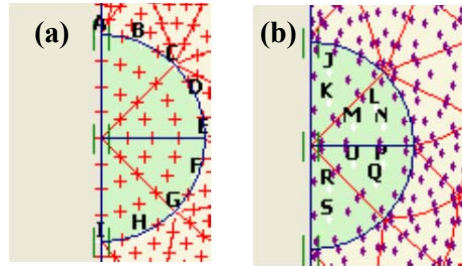
Figure 4-16 Selected nodes and stress points from the spherical soil cluster, (a) node and (b) stress point.
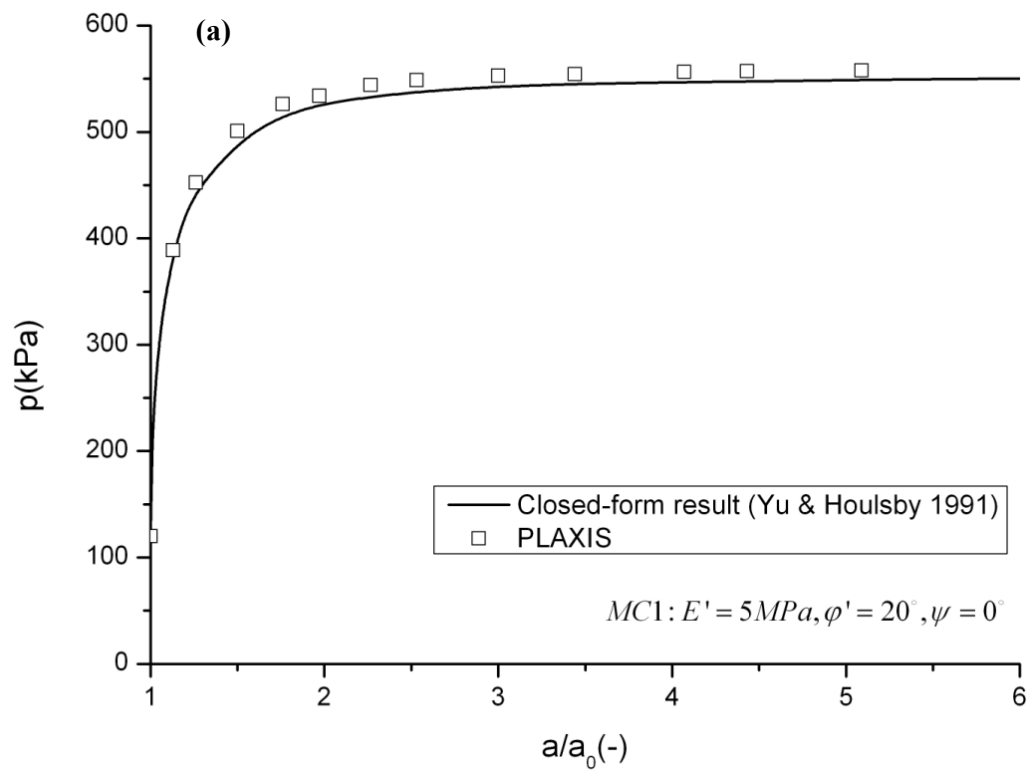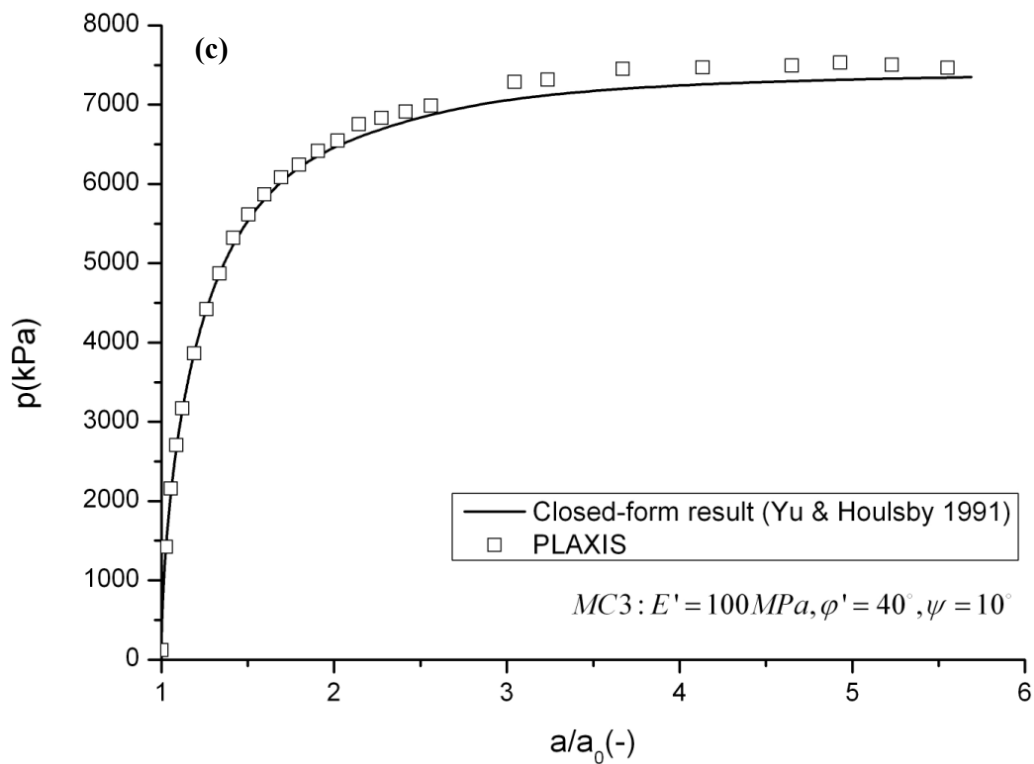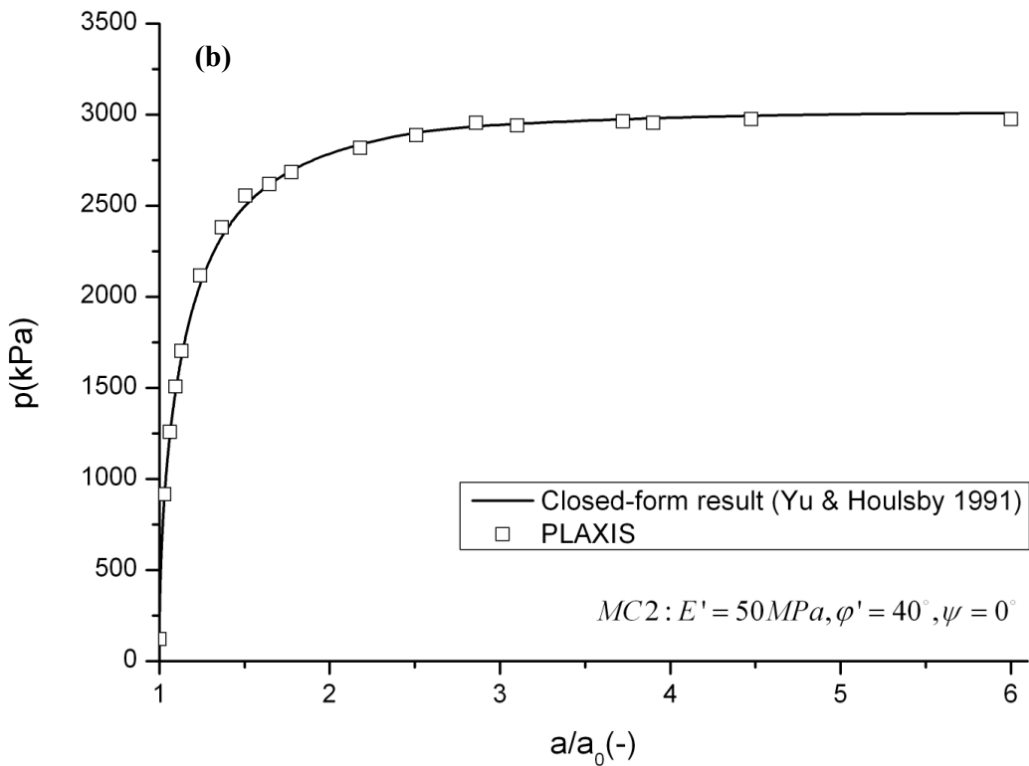
Figure 4-17 Relationships between the radial displacement and the cavity pressure in sand (drained condition).
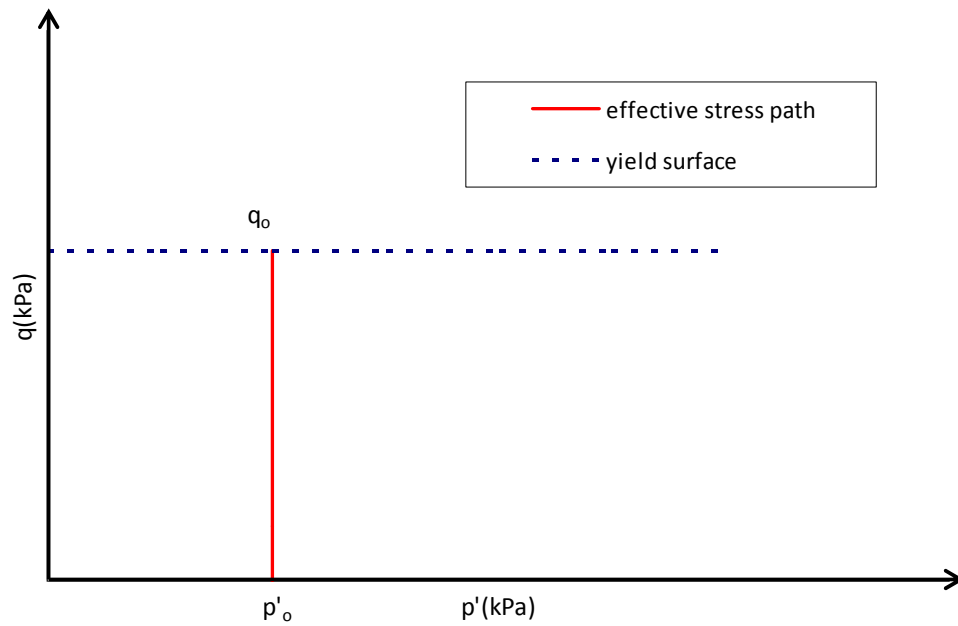
Figure 4-18 Effective stress path for the cavity expansion in Tresca model.
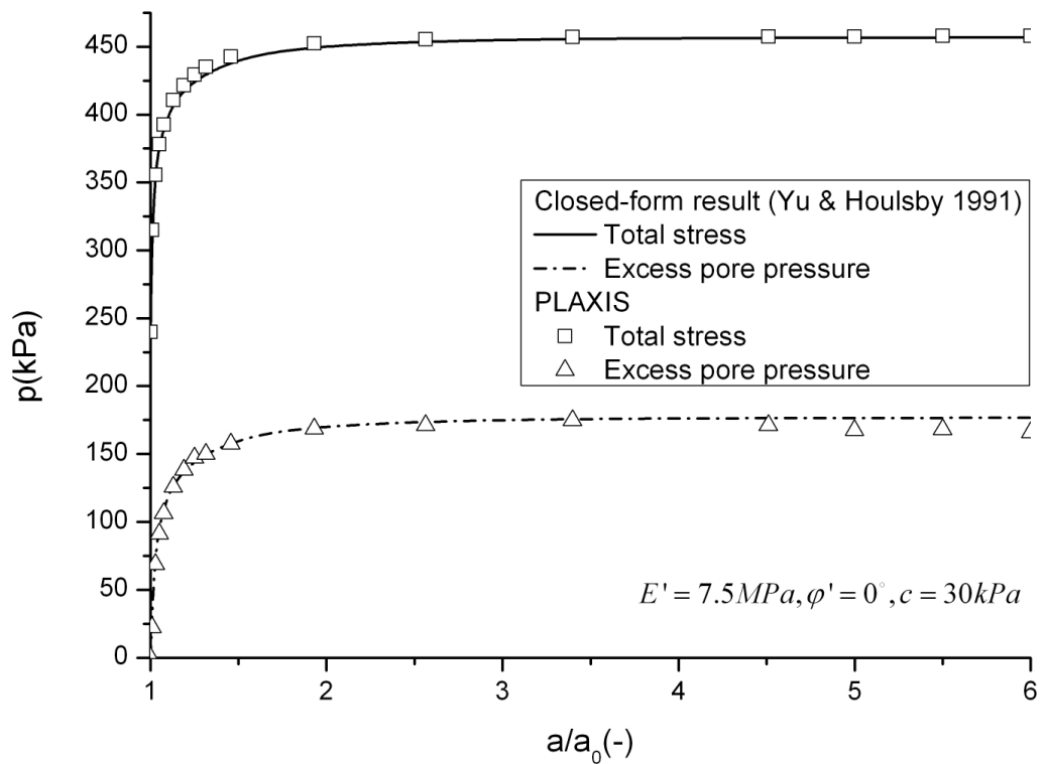
Figure 4-19 Relationships between radial displacement and cavity pressure as well as excess pore pressure in clay (undrained condition).
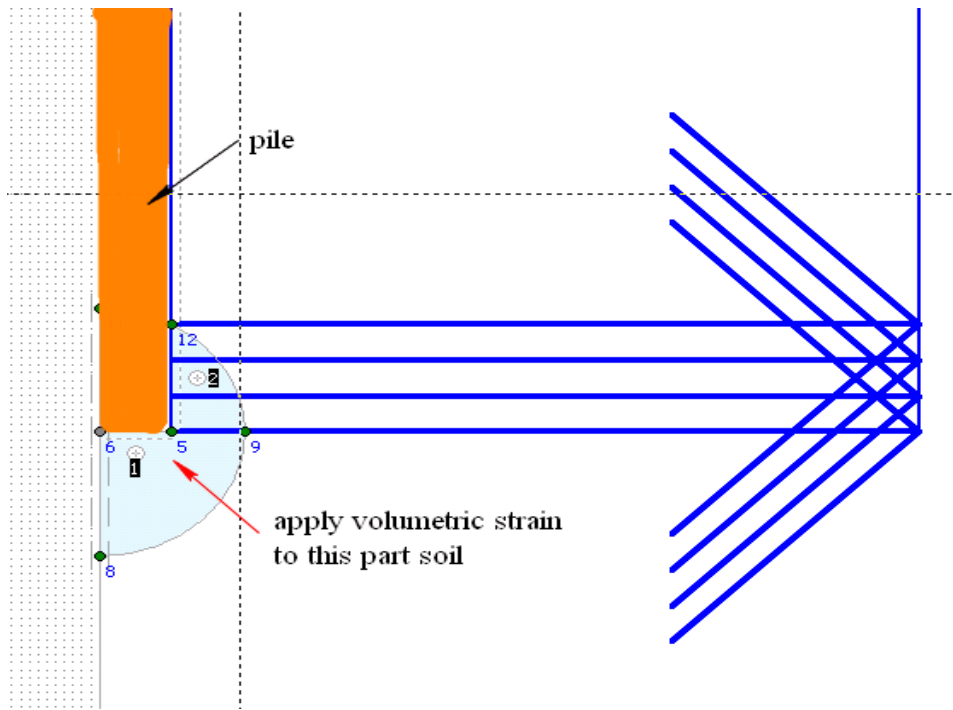
Figure 4-20 Schematic diagram of proposed numerical method.
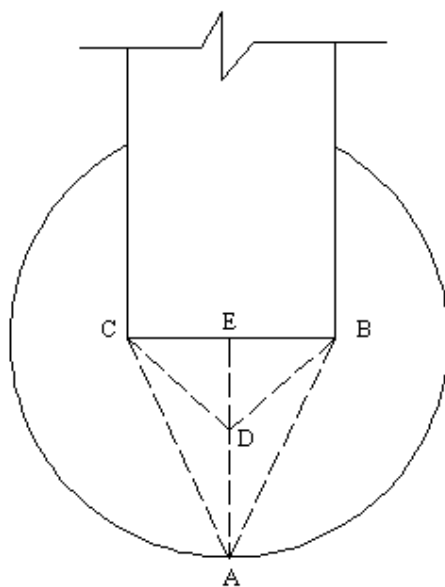
$$\angle ABC = \angle ACB = 45° + \varphi / 2$$
$$\angle CBD = \varphi$$
$$AE = a$$
$$BC = d$$
$$a = d / 2 \times \tan(45° + \varphi / 2)$$

Figure 4-21 Schematic diagram of relationship between geometry of the cavity and the pile.
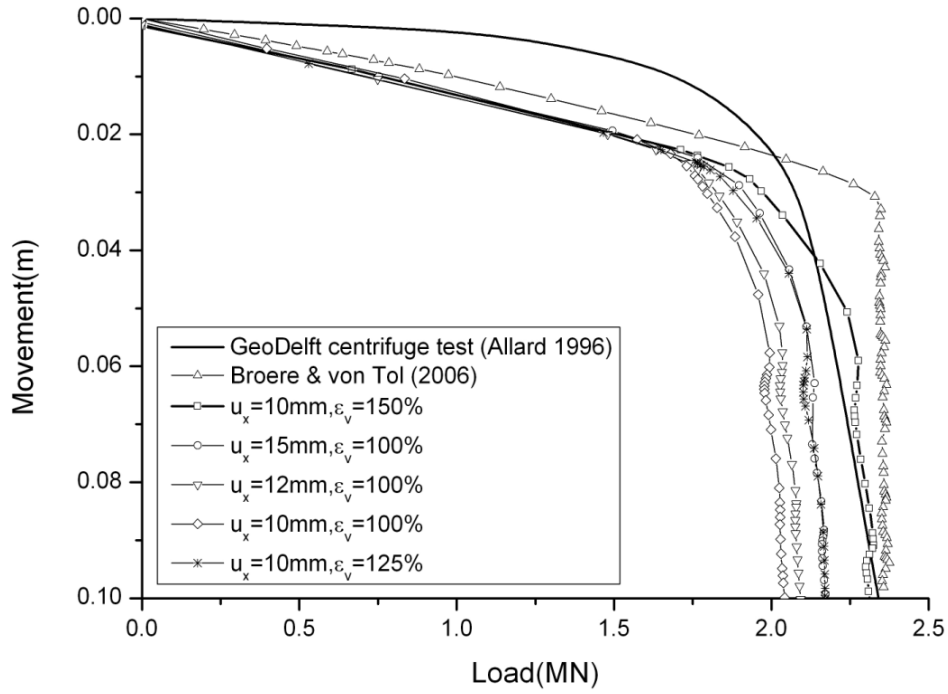
Figure 4-22 Load-settlement curves for the GeoDeflt test with an initial prescribed displacement and volumetric strain, compared to Broere & van Tol model (2006).
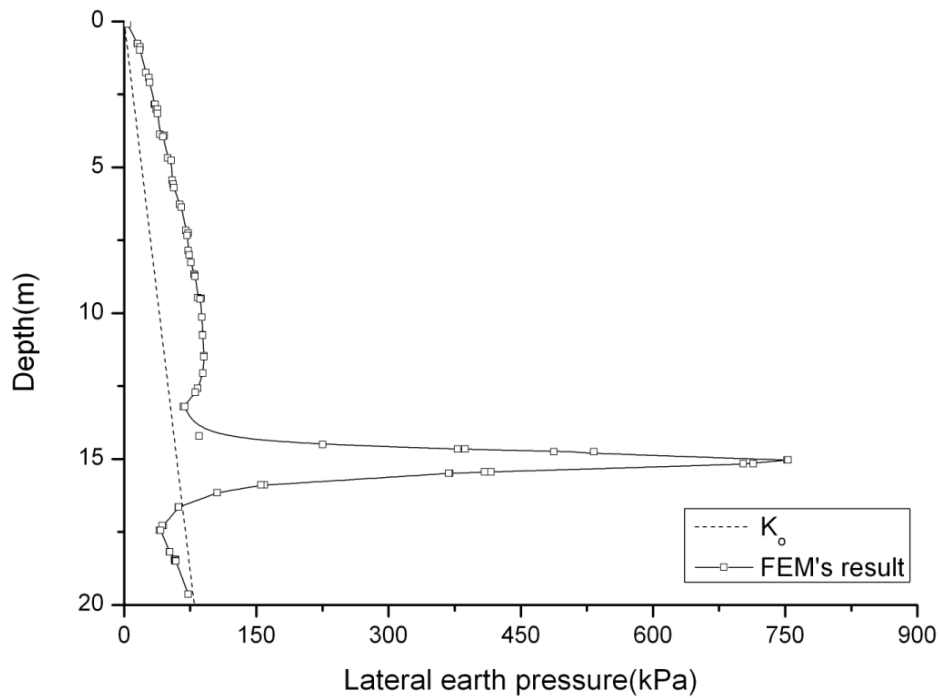
Figure 4-23 Lateral earth pressure after pile jacking along the vertical section.
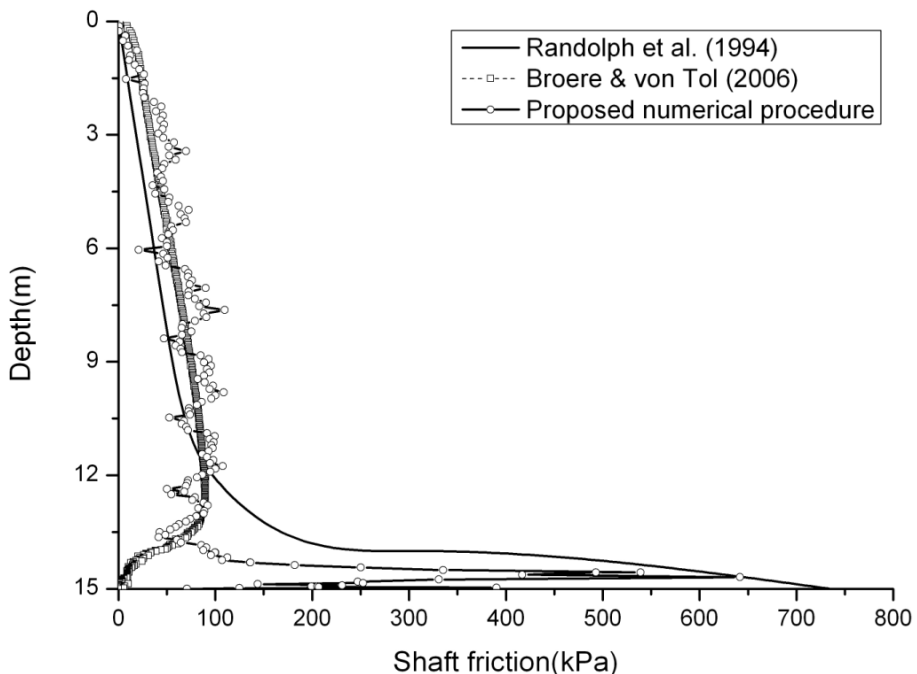
Figure 4-24 Shaft friction along the pile shaft at failure, compared with the results from Broere and van Tol (2006) and Randolph et al. (1994).
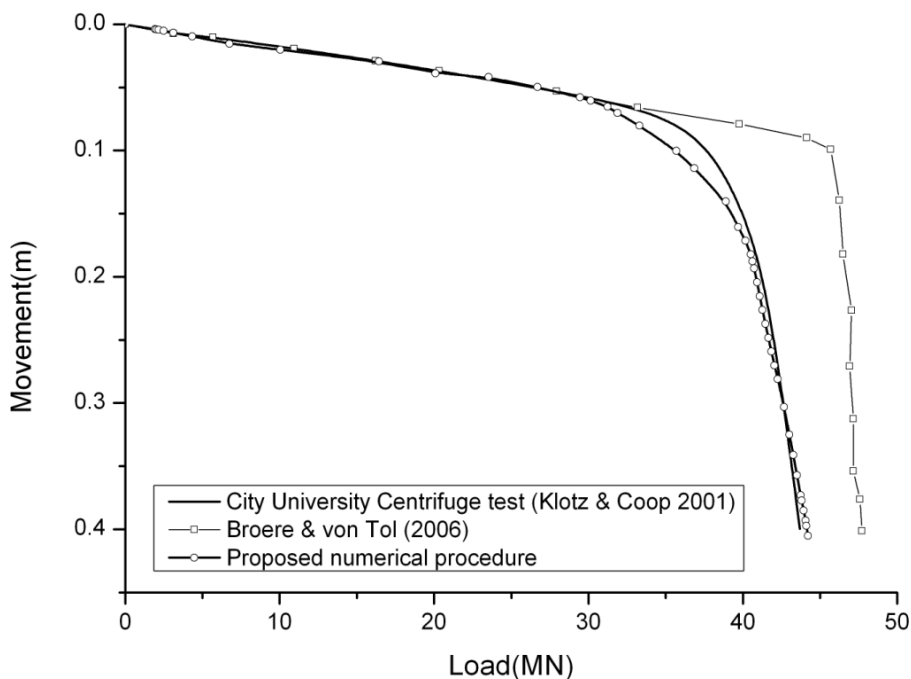
Figure 4-25 Load-settlement curves for the City University test with new model, compared to Broere & van Tol method (2006).

CHAPTER 5 FIELD TESTS AT TUAS VIEW

5.1 INTRODUCTION

This Chapter presents the pile field testing programme at Tuas South Ave 2 site. One of the primary objectives was to provide independent data that could be used in the validation of the general applicability of the proposed numerical procedure for simulation of installation effects of Jack-in piles as presented in Chapter 4. Other aspects regarding the effects of Jack-in force magnitude on the ultimate bearing capacity of Jack-in pile. Static loading tests were performed on three 600mm diameter Jacked-in spun piles, constructed to depths of 28.7m (TP1), 29.9m (TP2) and 31.7m (TP3) at same site due to different Jack-in forces. Both pile toes were located in the completely weathered Jurong soils (see description in section 5.2). TP1 was jacked-into completely weathered Jurong sandstone (SPT-N=70) at 4475 kN jack load (1.5×W.L.). TP2 and TP3 were jacked-into completely weathered Jurong mudstone (SPT-N=100) by 5903 kN jack load (2×W.L.) and 6620 kN jack load (2.25×W.L.) respectively.

The soil conditions at the testing site are first discussed based on in situ CPUT tests. Next the experimental set-up and testing procedures are described. Then, the results and analysis of the pile installation and static load test results are presented. Finally, the comparisons between numerical results and test results are discussed.

5.2 SOIL CONDITION

5.2.1 Tuas South Ave 2 site

The experimental site is located in Tuas South Ave 2, western end of Singapore. The stratigraphy, summarized in Figure 5.1, comprises a 10m-12m of loose to medium dense reclaimed sand fill overlying approximately 4m soft marine clay; this deposit is underlain by stiff to very stiff sandy clay and completely weathered sandstone/mudstone (Jurong Formation). The water level is at an average depth of about 3m below the ground surface.

5.2.2 In-Situ Tests

The extensive in-situ investigations, including standard penetration test (SPT), pressuremeter test (PMT) and piezocone penetration test (CPTU), were conducted in the experimental site. This gave valuable data for better understanding of the soil condition around the test piles. The site layout map Figure 5.2, shows the location of borings, SPT, PMT and CPTU soundings relative to the test pile.

Total three (3) borings BH-1, BH-2 and BH-3, about 8.4m to 15m apart, were drilled for the purpose of collecting soil samples and conducting SPTs and PMTs at specific depths. Figure 5.3 presents the SPT results of three boreholes. The subject test piles, Piles TP1, TP2 and TP3, were constructed at the positions of BH-1, BH-2 and BH-3,

respectively. As can be seen, the soil conditions for all test piles are very similar and do not vary significantly. As mentioned in Chapter 3, stiffness properties of the soil below the pile tip are more important in modeling pile behavior, especially for modeling of the end bearing resistance of the pile. The reasonable value of E_{ur}^{ref} and E_{50}^{ref} for the HS model can be obtained through the FE-simulation of the PMT (Appendix C). As a result, three (3) PMTs were performed at similar depths below the test piles. Another three (3) PMTs were performed at the depth where the soft Marine clay is. The results of total six (6) PMTs are summarized in Table 5.1.

Table 5-1 Summary of the Pressuremeter Test Results

Borehole	Depth(m)	Soil Type	SPT-N	E_{PMT} (kPa)	E_{ur}^{PMT} (kPa)
BH1(TP1)	16.5	M	10	13034	68911
BH1(TP1)	33.0	S V	100	78778	303570
BH2(TP2)	15.0	M	4	3518	24563
BH2(TP2)	32.5	S V	100	44357	768739
BH3(TP3)	17.0	M	10	20770	103936
BH3(TP3)	34.7	S V	100	81119	525934

M (Kallang Marine clay)
S V (Completely Weathered sandstone/mudstone in Jurong Formation, consists of sandy SILY/CLAY)

The in-situ cone penetration tests with piezocone (CPTU) were performed using a 10 tonne truck mounted CPT rig. In total, twenty (20) CPTUs were conducted close to the pile testing locations, from 0.6m to 3m relative to the center of each test pile. CPTUs were conducted in two stages: before and after the pile installation period. They are designated as CPT1 to CPT10 for "before installation" period and CPT11 to CPT20 for "after installation" period. Figure 5.4 and Figure 5.5 show the penetration results of

CPT1 to CPT10. It can be observed that despite the variation in q_t value between each CPTU, there is a good agreement in the trend of the penetration results which indicate the soils have a similar geological profile. The results of the pore pressure, measured by pressure transducer with the filter located immediately behind the cone tip, indicate that sand type soil extends from ground to approximate 12m depth. Then excess pore pressure was observed from 12m depth to 30m which means clay type soil underlying the sandy fill layer. The negative pore pressure, found from 17m depth to 22m depth, indicates that the clay type soil in this layer may be over-consolidated. The more detail soil profile was determined based on Eslami-Fellenius's soil profiling chart (Eslami and Fellenius, 1997) from CTP1-CPT10 and the results are summarized in Figure 5.6. As can be seen, there are four distinct layers apparent in the profiles and the spatial variability between each location is limited. Fill layer is found starting from ground surface to approximate 12m. Soft clay is found underlying the fill layer. The thickness of this formation approximate ranges from 3m to 4.5m. Silty clay and sandy silt are found underlying the soft clay layer. These soil profiles are in agreement with the borehole results. In summary, all the borings as well as the CPTU tests showed very similar soil conditions around the three test piles.

The comparison of the penetration results of the CPTU tests before and after the pile installation are shown in Figure 5.7. A noticeable increase in cone resistance was observed in the sand fill layer after pile installations. The magnitude of the increase of the cone resistance reduces as the normalize radii (r/r_o) increases, shown in Figure

5.8. However, the cone resistance does not change significantly in the soft marine clay layer and the sandy silt layer.

5.2.3 Laboratory Tests

Undisturbed samples were taken from the experimental site, in the three boreholes at specific depths. The laboratory tests comprised of index tests, six (6) sets of CIU triaxial tests and three (3) oedometer tests. The results of the laboratory tests are summarized in Table 5.2. The plasticity index (PI) for Kallang Marine clay (M) is 39%, and for Residual soil (S VI) and Completely Weathered sandstone/mudstone (S V) in Jurong Formation are 21%, 14% respective. The CIU triaxial tests are more focused on obtaining the strength parameters for the design and the numerical study. The average c' and φ' for S VI and S V are 2.5 kPa, $28.5°$ and 25kPa, $32.5°$. High cohesion is found in Completely Weathered sandstone/mudstone (S V). The over-consolidation ratio (OCR) can be obtained from the oedometer tests. The average values of OCR for Kallang Marine clay and Residual soil are 1 and 1.15 respective. Due to highly disturbed sample, no results are obtained from the oedometer tests for Completely Weathered sandstone/mudstone (S V).

Table 5-2 Summary of the Laboratory Test Results

Borehole	Depth (m)	Soil* type	Bulk Density (Mg/m₃)	Water Content (%)	c' (kPa)	φ'(Deg)	Liquid Limit (%)	Plastic Limit (%)	Plasticity Index (%)	Preconslidation Pressure (kPa)	Compression Index
BH1(TP1)	14.5-15.4	S VI	2.02	27	5	27	40	21	19	211	0.147
BH1(TP1)	30.5-31.5	S V	2.14	21	27	33	35	23	12	-	-
BH2(TP2)	12.0-12.9	M	1.76	53	0	22	69	30	39	124	0.585
BH2(TP2)	30.5-31.5	S V	-	22	-	-	43	28	15	-	-
BH3(TP3)	15.0-15.5	S VI	2.02	28	0	30	43	20	23	184	0.153
BH3(TP3)	30.5-31.5	S V	2.10	22	23	32	43	27	16	-	-

* M (Kallang Marine clay)

 S VI (Residual soil in Jurong Formation, consists of sandy SILY/CLAY)

  S V (Completely Weathered sandstone/mudstone in Jurong Formation, consists of sandy SILY/CLAY)

5.3 SOIL PARAMETER EVALUATIONS

In order to get better understanding of the soil stress state, the evaluations of the selected soil parameters (effective friction angle φ', over-consolidation ratio (OCR) and lateral effective stress coefficient at rest, K_o) are estimated, based on empirical methods from CPTU results.

5.3.1 Friction angle

The strength of soils is controlled by the effective stress frictional envelope, often represented in terms of the Mohr-Coulomb parameters: φ'= effective friction angle and c' = effective cohesion intercept. For clean sands, a commonly-used CPT interpretation is based on considerations of an inverted bearing capacity theory supplemented with CPT calibration chamber data from 5 sands (Robertson & Campanella, 1983). However, the flexible-walled chamber test results were not corrected for boundary size effects. The improved interpretation derived from a much larger compilation of calibration chamber database from 24 sands where the cone tip stresses were adjusted accordingly for relative size of chamber and cone diameter (D/d ratio) was proposed by Kulhawy & Mayne (1990) (Figure 5.9), expressed as:

$$\varphi'=17.6° +11.0° \log\left(\frac{q_t}{\sqrt{\sigma_{vo}'\sigma_{atm}}}\right) \tag{5.1}$$

where σ_{vo}' is the effective overburden stress; σ_{atm} is the reference stress equals to one atmosphere.

It should be noted that Eq.5.1 is suitable for the granular soils only. In order to evaluate the effective friction angle of the cohesive soil, an approach by the Norwegian University of Science & Technology (NTNU) is introduced (Figure 5.10). This approach is an effective stress limit plasticity solution to obtain the effective stress friction angle for all soil types (Senneset, et al.1988, 1989). For the simple case of Terzaghi-type deep bearing capacity (angle of plastification β= 0) and adopting an effective cohesion intercept c' = 0, Mayne & Campanella (2005) proposed an approximate form for deterministic line-by-line evaluation, expressed as:

$$\varphi' = 29.5 \times B_q^{0.121} \times \left[0.256 + 0.336 \times B_q + \log Q \right] \qquad (5.2)$$

where $B_q = \dfrac{u_2 - u_o}{(q_t - \sigma_{vo})}$; $Q = \dfrac{(q_t - \sigma_{vo})}{\sigma_{vo}'}$; u_2 is pore pressure measured behind the cone tip; u_2 is hydrostatic pore pressure; σ_{vo} is the total overburden stress;

Eq. 5.2 is applicable for 0.1 < Bq < 1.0 and range: $20° < \varphi' < 45°$. For Bq < 0.1 corresponding to granular soils, Eq. 5.1 for clean sands would apply.

The evaluations of all the tests are summarized on Figure 5.11. The averages and coefficient of variations (COVs) for the effective friction angel values are summarized in Figure 5.12 and Figure 5.13. It can be observed that:

1) The average effective friction angle for sand fill layer is $35°$ and does not change significantly along the depth. The coefficient of variations (COVs) is approximate 5% which indicates the sand layer in experimental site is relatively uniform.

2) The average effective friction angle for Kallang Marine Clay (M) and residual soil (S VI) is $25°$, $29°$ respectively. Due to the high sleeve friction (exceed 300 kPa) in completely weathered sandstone/mudstone (S V), most CPTUs were terminated at depth of 15m~21m. The coefficient of variations (COVs) is approximately 7% which indicates that the effective friction angle of Kallang Marine Clay (M) and residual soil (S VI) around all test piles are very similar and do not vary significantly. The effective friction angle of completely weathered sandstone/mudstone (S V) was evaluated only from CPT8. As can be seen in Figure 5.12, the effective friction angle is approximately $31°$.

3) The evaluations of the effective friction angle were also compared with the results from CIU tests. Both of the tests gave very similar effective friction angles.

5.3.2 Over-consolidation ratio (OCR)

The stress history of clay soils (over-consolidation ratio) is classically determined from one-dimensional oedometer tests on high-quality undisturbed samples. For intact clays, a first-order estimate of the over-consolidation ratio also can be obtained from the net cone tip resistance (Mayne, 1995; Demers & Leroueil, 2002), shown in Figure 5.14.

$$OCR = \frac{0.33\left(q_t - \sigma_{vo}\right)}{\sigma_{vo}'} \qquad (5.3)$$

Unlike clay soils, the evaluation of stress history for clean, uncemented, unaged quartz sands is a more challenging assignment. Based on the multiple regression analyses of

the chamber test data (n=636) from anisotropically-consolidated sands, Mayne (2005) found that the OCR is a function of the applied effective vertical stress (σ_{vo}'), effective horizontal stress (σ_{ho}'), and measured cone tip resistance (qt), as indicated by Figure 5.15. Then Mayne (2005) proposed the following closed-form expression (Mayne, 2005):

$$OCR = \left[\frac{0.192\left(q_t / \sigma_{atm}\right)^{0.2}}{\left(1 - \sin\varphi'\right)\left(\sigma_{vo}'/\sigma_{atm}\right)^{0.31}} \right]^{\frac{1}{\sin\varphi'-0.27}} \tag{5.4}$$

The evaluations of OCR based on Eq.5.3 and 5.4 are summarized on Figure 5.16. The averages and coefficient of variations (COVs) for OCR values are summarized in Figure 5.17 and Figure 5.18. As can be seen:

1) The values of OCR do not vary significantly along the depth in sand layer. The average value is approximately one (1), expected of a young reclaimed sand. Although, the sand fill is relatively uniform, the coefficient of variation in OCR of about 20% is expected in natural deposits of geomaterials.

2) The values of OCR increase with depth varied from approximately 1 to 3 in clay soils. The average OCR for Kallang Marine Clay (M) is 1 (normally consolidated reclaimed land). The average OCR for residual soil (S VI) is 1.5 for the depth of 15m to 18m and 3 from the depth of 18m to 22m.This high OCR value in the lower part of residual soil (S VI) may explain why the negative pore pressures were observed from 17m depth to 22m depth in CPTU data. Like the sand fill layer, the coefficient of variation in OCR of about 20% was found in the clayey

soils.

3) Since the evaluations of OCR were first-order, the values were also compared with the results from oedometer tests. A good agreement between the laboratory results and CPTU method for soft Kallang marine clay is observed in Figure 5.16.

5.3.3 Lateral stress coefficient (Ko)

In general, laboratory data on small triaxial specimens and instrumented oedometer tests indicate the following relationship can be adapted in uncemented sands and well-behaved clays of low to medium sensitivity:

$$K_o = (1 - \sin \varphi')OCR^{\sin \varphi'} \tag{5.5}$$

Alternatively, K_o can be estimated from the correlations with in-situ measurements, like CPTU sounding. Eq. 5.6 presents one method given by Kullawy and Mayne (1990).

$$K_o = 0.1(q_t - \sigma_{vo})/\sigma_{vo}' \tag{5.6}$$

This correlation is suitable for clay soils. For clean sands, K_o can be estimated from Eq.5.7, which combined Eq. 5.4 and Eq. 5.5.

$$K_o = 0.192(q_t/\sigma_{atm})^{0.22}(\sigma_{atm}/\sigma_{vo}')^{0.31}OCR^{0.27} \tag{5.7}$$

It should be noted that K_o estimated from Eq.5.6 and Eq.5.7 can be unrealistic when q_t is very large. The maximum value for K_o can be set equal to the passive stress coefficient (K_p) which for a simple Rankine case is given by:

$$K_p = \frac{1 + \sin \varphi'}{1 - \sin \varphi'}$$ (5.8)

The K_p limit is set for estimations for K_o obtained from Eq.5.6 and Eq.5.7.

The evaluations of K_o based on Eq.5.6 and 5.7 are summarized on Figure 5.19. The averages and coefficient of variations (COVs) for OCR values are summarized in Figure 5.20 and Figure 5.21. It can be observed that:

1) The values of K_o are almost constant along the depth in sand layer. The average value is approximate 0.43. The coefficient of variation in K_o is about 10% which indicated that K_o for the sand layer around all test piles are very similar and do not vary significantly.

2) The same trend is observed as the values of OCR. The K_o increases with depth from approximately 0.45 to 1 in clay soils. The average K_o for Kallang Marine Clay (M) is 0.45. The average K_o for residual soil (S VI) is 0.73 from the depth of 15m to 18m and 1.25 from the depth of 18m to 22m. The values of K_o is larger than those from Eq.5.5 in residual soil (S VI) layer. However, the differences are not significant. The same as for OCR, the coefficient of variation in K_o of about 20% was found.

5.4 TEST ARRANGEMENT AND TESTING PROGRAMME

5.4.1 Test programme

The experiment was conducted between October 22, 2009 and November 27, 2009 at Tuas View Ave 2. Three closed-ended spun piles (TP1, TP2 and TP3) were jacked into the ground under different Jack-in forces. A month later, three static load tests were conducted on the test piles. The relative positions of the test piles and CPTUs are shown in Figure 5.3. The three piles installed at the experimental site are 600 mm diameter prestressed high-strength concrete (PHC) spun piles. The details of the spun pile are summarized in Table 5.3. A steel plate was welded to the toe of all test piles to form the close-end (Figure 5.22).

Table 5-3 PHC Spun pile Properties

Diameter(mm)	Wall Thickness(mm)	Single Section pile length (m)	Concrete Intensity	Theoretical Weight (kg/m)
600	110	8	C80	423

5.4.2 Pile installation and instrumentations

The three test piles, Piles TP1, TP2 and TP3, were jacked-in to depths of 28.7 m, 29.9 m and 31.7 m respectively by jacked-in rig (Figure 5.23), on October 23, October 22 and October 24, 2009, respectively. TP1 was jacked-into the completely weathered Jurong sandstone (SPT-N=70) at 4475 kN jack load (1.5×W.L.). TP2 and TP3 were

jacked-into the completely weathered Jurong mudstone (SPT-N=100) by 5903 kN jack

load ($2 \times$ W.L.) and 6620 kN jack load ($2.25 \times$ W.L.) respectively.

The conventional instrumentation method for driven and jack-in pile is by installing

either an instrumented reinforcement cage or an instrumented pipe, into the hollow

core of spun piles followed by cement grout in filling. However, the infilling of

cement grout substantially alters the structural properties of the spun piles, thus

rendering them significantly different from the actual working spun piles, which are

usually not grouted internally. The change in strain in the post-grouted core under the

applied loading may also not be the same as the change in strain in the prestressed

concrete wall of the pile because of the different stiffness of the two materials of

different mix, strength and age. In order to overcome these obvious shortcomings, a

new strain deformation monitoring system named Global Strain Extensometers

(GLOSTREXT) (Figure 5.24) was developed by Ali and Lee (2008) and was used in

this study. The instrumentation is installed after the installation of the pile. With the

instrumentation set-up as described in Figure 5.25, the state-of-the-art GLOSTREXT

system is able to measure shortening and strains over an entire section of the test pile

during each loading steps of a typical static pile load test. The deformation of the pile

under loading produces relative movement between each and every two anchored

intervals causing a change in the strain gauge wire tension in the vibrating wire

transducers and a corresponding change in its resonant frequency of vibration. The

resonant frequency is measured by the Glostrext sensors to a readout box/data logger,

which also measures the frequency and displays the shortening and strain reading. Since the advantages of using the state-of-the-art Glostrex strain deformation monitoring system, all test piles were prepared with this strain deformation monitoring system for determining the axial load and movements at various levels down the pile shaft including the pile base level. The positions of Global Strain Gauges for all test piles are shown in Appendix A.

5.4.3 Static load test

Three static load tests were conducted from 14th November to 27th November, 2009. A kentledge reaction system of approximately 10.3MN weight was set up to serve as reaction for TP1 and TP3 load tests. A jack-in rig counter-weights reaction system was used for TP2 load test. In the set-up used, the test load was applied using 1 no. hydraulic jack acting against the main beam. The jack was operated by an electric pump. The applied load was indicated by calibrated Vibrating Wire Load Cell as primary load measurement, while the pressure gauge reading was used as the secondary cross-checking purpose.

In each test pile, 4 numbers of Linear Vertical Displacement Transducers (LVDTs) mounted to the reference beams, with plunger pressing vertically against glass plates fixed to pile top (Figure 5.26). Vertical scales were also provided on the reference beams to monitor frame movement during load testing for correction purposes; and

vertical scale rules fixed to pile top sighted by a survey precise level instrument (with

the use of temporary bench mark (TBM) reference for correction purposes). All

instrumentation was connected to a data logger (Micro-10x Data logger) and the test

data were recorded and stored automatically at 60 second intervals throughout both

tests by using Multilogger software.

The testing programme consisted of testing TP1 and TP3 piles in four cycles applied

using the Quick Load Test Method for Individual pile (ASTM 1143-81). The applied

load of 4 cycles were 2930 kN (1×W.L.), 5860 kN (2×W.L.), 7325 kN (2.5×W.L.)

and 10255 kN (3.5×W.L.) or failure load. In the first cycle, the loading was increased

by equal loading increments of 740 kN to 2930 kN and remained 24 hours at the

maximum load before decreased to zero by equal unloading step of 740 kN. Similarly,

the second cycle was followed by equal loading/ unloading step of 740 kN and third

cycle was 1480 kN. In the fourth cycle, the pile was to be loaded to maximum load,

10255 kN, or failure load, whichever comes first. The testing programme consists of

testing TP2 in three cycles due to maximum capacity of the jack-in rig counter-weights

reaction system is 8000 kN. As a result, TP2 was not tested to failure. The load/unload

cycles are same as 1st cycle to 3rd cycle in TP1 and TP3.

5.5 ANALYSIS OF TEST RESULTS

5.5.1 Load-movement behavior of the test piles

The results of load-movement plots for the three static load tests are summarized in Figure 5.27 and Table 5.3. The ultimate bearing capacity of TP1 and TP3 is 7690 kN and 8762 kN respectively when jack-in force increases from 4475 kN (1.5×W.L.) to 6617 kN (2.25×W.L.). The ultimate bearing capacity of TP2 cannot be obtained from load-movement curve since TP2 was not been loaded to failure due to insufficient capacity of jack-in rig counter-weights reaction system. The relationship between ultimate bearing capacity of the test pile and Jack-in force is shown in Figure 5.28. It can be observed that the increment of ultimate bearing capacity is not in linear proportion to the increment of jack-in force. The ultimate bearing capacity of TP2 would be expected between 7690 kN and 8762 kN and closer to 8762 kN.

Table 5-4 Summary of Static load tests

	1st Cycle		2nd Cycle		3rd Cycle		4th Cycle	
	L(kN)	M(mm)	L(kN)	M(mm)	L(kN)	M(mm)	L(kN)	M(mm)
TP1	2970	7.83	5927	19.59	7325	29.92	7690	84.20
TP2	3011	6.67	5919	18.73	7332	26.43	-	-
TP3	2930	7.40	5917	18.22	7405	28.28	8762	94.24

L: Maximum load at each loading cycle

M: Maximum movement at Maximum load at each loading cycle

The comparison of Jack-in pile behavior due to different Jack-in force is shown in Figure 5.29. It is observed TP1, TP2 and TP3, showed almost the same load-movement curves up to 2 time working load (5860 kN) as in Figure 5.29 (a).

Movement of TP1, TP2 and TP3 is 19.59mm, 18.73 mm and 18.22 mm at that load

level respectively. Figure 5.28 (b) shows that TP1 which was jacked-in by 1.5×W.L. is

softer compared to TP2 and TP3 which was jacked-in by 2×W.L. and 2.25×W.L.

respectively.

5.5.2 Pile load-strain relations

In order to assess the load distribution, the analysis of the strain-gauge data is

conducted here.

The strains induced by the loading of the pile head for TP1 are shown in Figures 5.30.

It would be expected in normal cases that the curves are in sequence from left to right.

That is, Gauge Level A, which is unaffected by shaft resistance should show the

largest strains and less and less strain should be shown by the gauge levels deeper in

the pile. As there is little shaft resistance present between Gauge Levels A and B, those

curves should be close to each other. For the other curves, when the shaft resistance is

not fully mobilized, the curves will plot closer together while when the shaft resistance

is mobilized further, the curves will deviate further from one another. These trends are

suggested by Fellenius and Tan (2010).

As can be seen in Figure 5.30, the load-strain curves of TP1 from Gauge Level A to E

respond as expected for all four cycles, the curves from Levels A to E are almost on

top of each other. These strain responses indicate that TP1' has a uniform cross section

(Fellenius and Tan 2010). Moreover, when the load increased in the pile, the curves

deviate further from one another since the shaft resistance is mobilized further as

applied load becomes larger and larger. Similar analysis of the strain data recorded

from the test on Pile TP2 and TP3 showed that all Gage Levels seemed reasonable

(shown in Appendix B), and data from these levels were used in the analysis. Overall,

none of strain data has functioned erratically and all of them seem reasonably correct.

5.5.3 Residual load and true load distribution in the pile

The load distribution along the pile shaft and the base can be derived from

computations based on the measured changes of the global strain gauge readings and

the estimated pile properties. Load transferred at each global strain gauge can be

calculated as:

$$P = (\varepsilon \times E_s)A_c \tag{5.9}$$

where ε is average change in global strain gauge readings; E_s is secant modulus of

concrete; A_c is cross-section area of the pile

For the manufactured spun pile, A_c does not vary much along the pile shaft. The strain

responses also give that evidence in section 5.5.2. E_s becomes very important in

computing the transferred load. Generally, the concrete modulus is not constant over

the large strain range imposed in the static load test. It reduces with the increasing

strain value. It is indicated that secant modulus can be best determined from a so-called "tangent stiffness" plot, which presents the applied increment of load over the induced increment of strain (Fellenius 1989). When the shaft friction fully mobilizes, the "tangent stiffness" will plot along a slightly sloping line and then the "tangent stiffness" is directly converted to secant modulus, E_s.

The "tangent stiffness" plots for the last cycle of each test pile are shown in Figure 5.31. For TP1 and TP2, the "tangent stiffness" lines in Figure 5.31 indicated that secant modulus, E_s, equals to 50-0.005 $\mu\varepsilon$ (GPa). The similar analysis for TP3 shows E_s equals to 55-0.006 $\mu\varepsilon$ (GPa). The high values of E_s were obtained is due to the high-strength concrete used for the manufactured spun pile, shown in Table 5.4.

Figure 5.32 shows the load distribution curves for the last cycle of each test pile. However, these load distributions are not true resistances. This is because of the existence of the residual load and it is well demonstrated to exist in numbers of driven and jack-in pile tests. In the driven piles or Jack-in piles, residual load results from shear stress developed between the pile and the soil during the installation. The measured load distributions shown in Figure 5.32 were evaluated based on "zeroing" all gages immediately before the start of the load test. As a result, strain gauge readings did not provide any information about the residual loads, and the shaft resistance was overestimated and the base resistance was underestimated based on the measured data.

Fellenius proposed a method to determine the residual load from the static load test , based on the effective stress method (commonly termed as β method) and the fact that the shear resistance is independent of the direction of shear (Fellenius 2002). It can be assumed that the residual load is developed fully in the upper part of the pile. The residual load must be unloaded before the positive skin friction is mobilized during the static load test. Therefore, if the negative skin friction is fully mobilized, the reduction of load along the upper part of the pile is twice the true shaft resistance. It is also recognized that the soil becomes stiffer with depth (as indicated by the SPT-N value). As a result, the full shaft friction may not be mobilized in the lower proportion of the pile. Because of the loading/unloading actions, the evaluation of the residual load needed some judgments. The distributions of the residual load for the test piles shown in Figure 5.32 are considered the most probable distribution. The unit negative skin friction along the upper about 15 m length of the piles corresponds to a beta-coefficient of 0.55 in sand fill layer and 0.35 in soft clay layer in the effective stress analysis. As can be seen, the residual load develops fully in the upper part of the pile. Then the residual load tends to reduce with depth. The evaluated residual loads at pile toe are 618kN, 500kN and 335kN for TP1, TP2 and TP3 respectively. The residual loads at pile toe reduce as the pile is deeper in the completely weathered Jurong mudstone. This might be caused by more and more positive shaft resistance mobilized in the lower part of the pile.

It would be expected that the total ultimate shaft friction should be approximately proportional to the pile depth since the soil condition does not vary very much between the three piles. But the total ultimate shaft friction for TP1 (28.7m), TP2 (29.9m) and TP3 (31.7m) are 6200 kN, 6020 kN and 6190 kN respectively from the measured data. These are not consistent with the expected behavior. When the residual load is considered, the total ultimate shaft friction for TP1 (28.7m), TP2 (29.9m) and TP3 (31.7m) are 5400 kN, 5662 kN and 5900 kN respectively. These results showed agreement with the expected pile behavior and it is indicated that the shaft friction for the same pile in the similar soil does not vary with the magnitude of jack-in force to install pile.

Since the shaft friction does not vary with the magnitude of jack-in force among test piles, the different behaviors between test piles must be caused by different the toe stiffness response of TP1, TP2 and TP3. The differences in toe stiffness between the piles, TP1, TP2, and TP3 are due to the different jack-in forces. The difference in toe stiffness, considering the residual load, between TP1 and TP3 is shown in Figure 5.33. From Figure 5.33 we can see, when jack-in force increases, the behaviors of the pile toe becomes stiffer and if the ultimate end bearing resistance q_b is defined by settlement criterion of D/10, q_b is increased from 4900 kPa to 8900 kPa when jack-in force increases from 4475 kN (1.5×W.L.) to 6617 kN (2.25×W.L.). This toe resistance behavior is consistent with the Jack-in construction method, which prestresses the soil below the pile toe and ensures a larger stiffness of the toe response. At start of the

static load test, the toe was already subjected to the Jack-in load and the load-movement curve displays an initial stiffer reloading portion. When the toe load-movement curve for TP1 was shifted a bit to the left, the two responses for TP1 and TP3 seem to have the same virgin compression line, as in Figure 5.34. The larger the Jack-in force, the larger volumetric compression of the bulb of soil below the toe of the piles. As a result, the larger reloading portion causes the larger stiffening effect when the pile is loaded after the installation.

5.6 NUMERICAL ANALYSIS OF TEST PILES

5.6.1 FEM mesh and soil parameters

The axi-symmetric configuration for simulation of behavior of test piles using PLAXIS 2D is shown in Figure 5.35. The FEM mesh features 15-noded triangular elements with 12 Gauss points for numerical integration. Since the soil stress around the pile is significantly changed during the installation process, the mesh is not only locally refined around the pile shaft using line refinement, but also refine the clusters 5D around the pile shaft and 5D below the pile tip. The soil profile is a simulation of the soil condition around the test pile based on the initial soil investigations. The FEM profile is a 12m-thick sand fill layer overlies the soft marine clay layer of 3m thickness on the top of residual soil and weathered sandstone/mudstone (Jurong formation) as in Figure 5.35. The ground water level is set at 3m below the ground level, according to the soil investigation.

Hardening soil model was used to model the soil behavior. The soil parameters for the calculations were taken from field tests and laboratory tests described in section 5.2. As discussed in section 5.3, the soil conditions and stress state around all test piles are very similar and do not vary significantly. As a result, the same soil parameters were used for all test piles, shown in Table 5.5. Construction rate was assumed to be faster, compared to consolidation rate of soils. Thus undrained response of the soil can be assumed for soil layers such as soft marine clay, residual soil and weathered sandstone/mudstone. The interface element is applied to simulate the interaction between the pile and the soil.

The spun pile was modeled by an equivalent circular solid pile in axi-symmetry. The axi-symmetric model maintains the same perimeter as the spun pile (so that unit shaft resistance is correctly estimated) and the same axial stiffness, EA, as the spun pile. The linear elastic model was used to model the concrete material. The equivalent $E = 2.5 \times 10^7 \, kPa$ for TP1 and TP2 and $E = 2.9 \times 10^7 \, kPa$ for TP3, volumetric weight $\gamma = 24 kN/m^3$ and a Poisson's ratio $v = 0.2$.

The installation effects of the Jack-in pile were modeled using the numerical procedure described in Chapter 4. A horizontal prescribed displacement of 2% of the pile radius is applied to the pile shaft. This value was chosen by varying the horizontal prescribed displacement to best fit test results. As discussed in section 5.5.3, the larger the Jack-in forces, the larger volumetric compression of the bulb of soil below the toe

of the piles. As a result, the volumetric strain applied to the spherical soil cluster above

the pile tip increases with the Jack-in force in the numerical analysis, using 70%,

100%, 150% for TP1, TP2 and TP3 respectively. The value for volumetric strain

comes from two components. One is the volumetric compression of the bulb of soil

below the toe of the pile due to preload during pile installation. This preload effect

increases as the Jack-in force increases. Another is a highly compressed zone of soil

below the pile tip- hereafter referred to as a 'nose cone' which comes from the sand fill

layer dragged down with the pile tip by the process of jack-in pile installation. This

behavior was observed in the centrifuge test (White, 2002).

Table 5-5 Soil parameters for TP1, TP2 and TP3

Parameter	Unit	Symbol	1-Backfill	2-Soft Marine clay	3-Residual Soil (sandy Silt)	4-Weathered Sandstone/ Mudstone
Type of behavior			Drained	Undrained	Undrained	Undrained
Dry weight	kN/m^3	γ_{unsat}	20	16	19	22
Wet weight	kN/m^3	γ_{sat}	20	16	19	22
Young's modulus	kN/m^2	E_{50}^{ref}	3.34E+04	7000	1.25E+05	4.50E+05
Oedometer modulus	kN/m^2	E_{oed}	3.34E+04	6962.5	1.25E+05	4.50E+05
Power		M	0.8	1	0.7	0.8
Unloading modulus	kN/m^2	E_{ur}^{ref}	1.00E+05	2.10E+04	3.76E+05	1.35E+06
Poisson's ratio		N	0.20	0.20	0.20	0.20
Reference stress	kN/m^2	P	100	100	100	100
Cohesion	kN/m^2	C	0	0	0	33
Friction angle	°	Φ	35	22	30	33
Dilatancy angle	°	Ψ	0	0	0	0
Interface strength reduction		R_{inter}	0.80	1	1	1
OCR		OCR	1.0	1.0	1.5	1.0

5.6.2 Results and discussion

There are total three scenarios were simulated using PLAXIS: 1) without installation

effect;2)immediately after installation; 3)30days after installation. The ratio K/K_o

after the installation along the pile shaft is shown in Figure 5.36. The ratio from the

numerical analysis decreases rapidly in the first meters from 5 to 2.3 and remain

constant in the sand fill layer. This is a bit smaller than that from the field test

measurements for TP1, TP2 and TP3, which equals to 2.38. The ratio K/K_o in the

sand fill is also compared with the results from Eq.4.3 based on 1D analysis and two

design approaches proposed by Randolph et al. (1994) and Jardine & Chow (1996),

described in Chapter 2, also shown in Figure 5.36. As can be seen, the similar trend is

obtained by different methods. The results from the 1D analysis and the numerical

procedure proposed in Chapter 4 match better with the field test results. The ratio

K/K_o estimated using two design methods is lower than the field test results, ranging

from 1.25 to 1.7. This is because that lateral effective stress acting on the pile shaft

decreases significantly when the number of loading cycles increases, due to so called

"friction fatigue" effects. Both the design approaches are developed for driven piles,

partly based on field or experimental data on driven piles. Clearly, the number of

loading cycle in Jack-in pile is much smaller than that in driven piles. As a result, the

design approaches will underestimate the ratio K/K_o for the Jack-in piles. The

situation of the ratio K/K_o is complex in the clay layer. The installation process is

undrained and the surrounding soils immediately around the pile shaft and base are

subjected to very high stresses that would produce excess pore pressures in the clay

type soil. As a result, the ratio K/K_o will be minimum shortly after installation and

increase with time as the consolidation occurs in the soil around the pile. The ratio

K / K_o shown in Figure 5.36 was obtained from two stages, stage I: immediately after installation and stage II: 30 days after installation, which is the load test period. As can be seen, the ratio K / K_o increases with time which is agreement with the expected response. The increments of K / K_o are not uniform along the pile shaft. Very little change of the ratio K / K_o was observed in top of the clay layer from depth 12m to 15m. While, significant increase of K / K_o was found near the pile toe. This is because very high excess pore pressure was created during the installation near and above the pile toe as observed in FEM results (Figure 5.37). As a result, the lateral effective stress significantly increases after some consolidation. The results from the numerical analysis were compared with the field test results and design approach proposed by Jardine & Chow (1996). The ratio K / K_o profiles from the numerical analysis (stage II) and the design approach showed trends similar to those measured at the experimental site from depth 12m to 22m. After that, the numerical analysis underestimates the ratio K / K_o, while the design approach overestimate those compared with measurements. Moreover, both the numerical analysis and design approach give large ratio K / K_o, which means very high lateral effective stress is near the pile toe. However, the last strain gauge was installed 0.5m above the pile tip. Thus, there is no measurement near the pile tip. The ratio K / K_o profiles in a vertical cross section at different distance from the center of the pile after the installation are shown in Figure 5.38. The value of K / K_o reduces as the normalized radii (R / r_o) increases, which indicates the magnitude of the increase of the lateral effective stress reduces when the soil is further from the pile. There is a slight increase in the K / K_o, $5r_o$ away

from the pile in the sand fill layer. This trend is consistent with the CPTU result (CPT11-CPT20), shown in Figure 5.7. The similar trend was also observed in the clay layers, except soil layer 5m or 6m above the pile toe. There is still about 10% increase of K/K_o found near the pile toe depth $20r_o$ away from the pile. Generally, the stress changes around the pile shaft due to pile installation can be reasonably captured by prescribing outward radial displacement at pile shaft.

The load-movement behavior from FEM simulation for TP1 during the pile load tests is shown in Figure 5.39(a), compared with field test results. Clearly, the evaluation of the bearing capacity of the displacement (Jack-in) pile was underestimated by 30%, if the installation effect was not considered. Since half of the pile was jacked into clay type soils, the bearing capacity of the displacement pile should increase with time, commonly known as the pile set-up. The calculated bearing capacity increases from 6360 kN to 7685 kN 30 days after the installation, is as expected. The load-movement behavior at 30 days after the installation (static load test periods), which was evaluated using the proposed numerical procedure, matches quite well with the test result. Similar results were also observed in TP2 and TP3, shown in Figure 5.39 (b-c). The hysteresis in the unloading/reloading cycle was observed in the test results. However, the numerical results cannot capture this entirely due to the limitation of the HS model. In the HS model, unloading/reloading is treated as linear elastic behavior.

Figure 5.40 shows the load distribution for TP1 at different load levels in the 4th

loading cycle. As can be seen, the FEM prediction of axial forces inside the test pile are in very good agreement with the test results at 2950kN (1×W.L.), 5900kN (2×W.L.) and at failure load 7690 kN in the last loading cycle.

5.7 CONCLUSIONS

In order to verify the general applicability of the proposed numerical procedure for modeling the installation effects of Jack-in pile, a comprehensive in-situ investigation and laboratory testing of soils surrounding of three static pile load test on Jacked-in spun piles were conducted.

In general, the very similar soil conditions were observed around three test piles from both borehole and CPTU results. Similar soil parameters were evaluated from well documented empirical methods on CPTU data. A significant increase in the cone resistance was observed in the sand fill layer after pile installation. The magnitude of the increase of the cone resistance reduces with distance away from the center of the pile. However, the cone resistance did not change significantly in the soft marine clay layer and the sandy silt layer after installation due to its undrained response.

The three test pile load tests indicated that the ultimate bearing capacity of Jack-in pile increases as the Jack-in force increases. Generally, the pile developed greater stiffness response in the load-movement curve when it is installed with larger jack-in force.

However, the three test piles showed approximately the same load-movement curves under 2 times working load. The difference in behaviors between test piles is caused by the difference in the toe stiffness response of TP1, TP2 and TP3, as their shaft response are nearly the same for similar soil conditions around the test piles. Due to the Jack-in construction method, at the start of the static load test, the toe was already subjected to the lock-in residual loads and the load-movement curve displays an initial steep (stiff) reloading portion when the pile is loaded after installation. The larger the Jack-in force, the larger the volumetric compression of the bulb of soil below the toe of the piles. As a result, the larger reloading portion causes the larger stiffening effect in the pile load tests.

Numerical analysis have been conducted using geotechnical FEM software package PLAXIS 2D. The FEM analyses of the soil stress state before and after pile installation was carefully simulated. The load-movement behavior of Jack-in spun pile and the load distribution profile along the pile, using the proposed numerical procedure, showed good agreement with the test results in predicting pile load capacity, and accounting for installation effects.

Lessons could be drawn from the numerical study of field test and are summarized as:

1) Shaft friction does not change much for different jack-in force from 1.5 W.L., 2.0 W.L. and 2.25 W.L. Shaft friction for the same pile in the same soil does not vary with the magnitude of jack-in force to install pile.

2) It appears that amount of cylindrical cavity expansion by prescribed outward radial displacement at pile shaft to induce approximate soil setup is about 2% to 4% of pile radius in sand layer. The soil setup of shaft friction is dependent on the elapsed time after installation in clayey soil due to the amount of radial soil reconsolidation around pile shaft.

3) The setup of end bearing is correctly modeled by spherical cavity volume expansion compared to a simple applied vertical prescribed displacement at pile base (which results in incorrect shear stress distribution on the pile shaft near toe).

4) The spherical cavity volume may be reasonably defined by the limit pressure spherical zone proposed by Randolph et al (1994). The approximate amount volumetric strain to apply is dependent on the jack-in force used in pile installation. From the field trial, it appears to be about 70% to 150% for 1.5 W.L. to 2.25 W.L. and it is not a simple linear relation. More studies are needed to define this relation for many other pile types, installation methods and soil conditions. Currently, the amount volumetric strain to apply can be calibrated through pile load test. Once calibrated for particular condition, the numerical model can be used to predict the capacity of Jack-in pile in the similar soil condition.
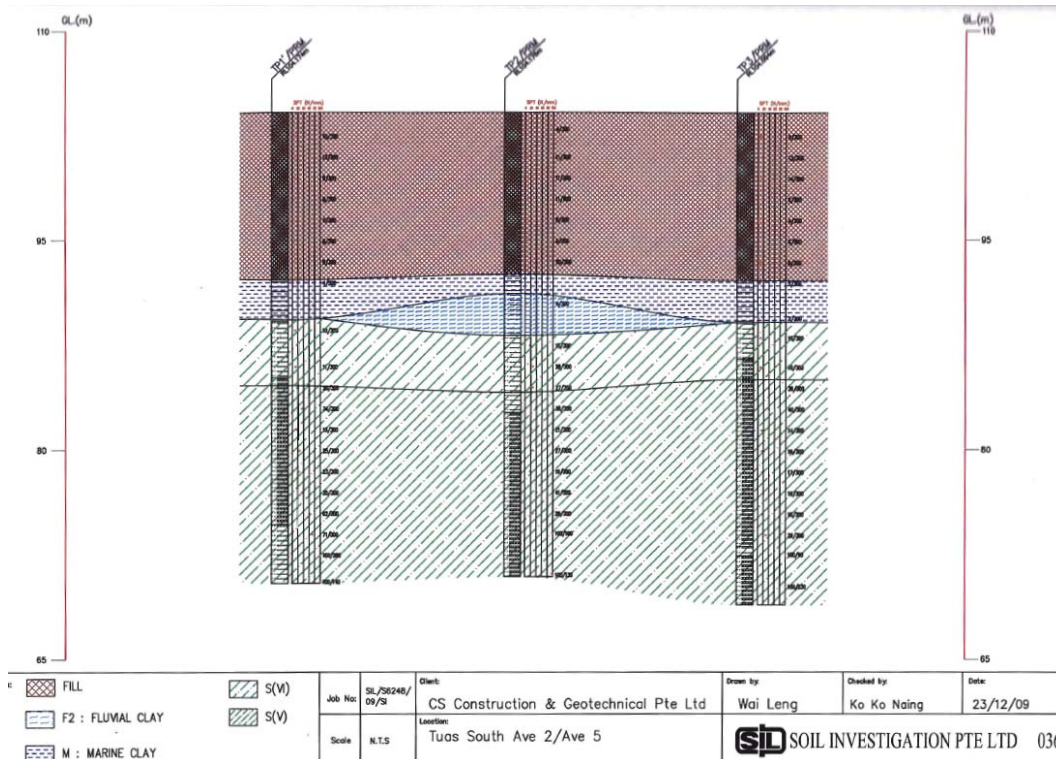
Figure 5-1 The stratigraphy of the experimental site.

Test piles are co-located with BH.

SPT in BH1 to BH3 at each 0.5m depth

PMT in BH1 to BH3 at depth (15m ~17m) and (32.5m~34.7m)

● Before installation
● Immediately after installation
● One day before load test

NOTE: CPT1 (CPT5, CPT8, CPT11, CPT15, CPT18):0.6m from the center of pile.

        CPT2 (CPT6, CPT9, CPT12, CPT16, CPT19):0.9m from the center of pile.

        CPT3 (CPT5, CPT8, CPT11, CPT15, CPT18):1.5m from the center of pile.

        CPT 4 (CPT14):3m from the center of pile.

Figure 5-2 The experimental site layout map.
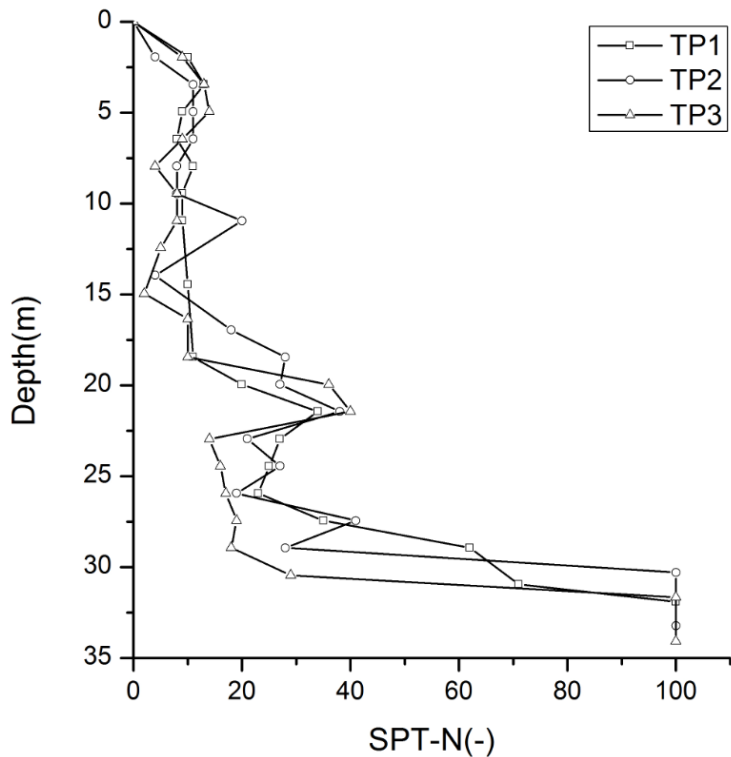
Figure 5-3 The profile of SPT-N value for BH1 to BH3.
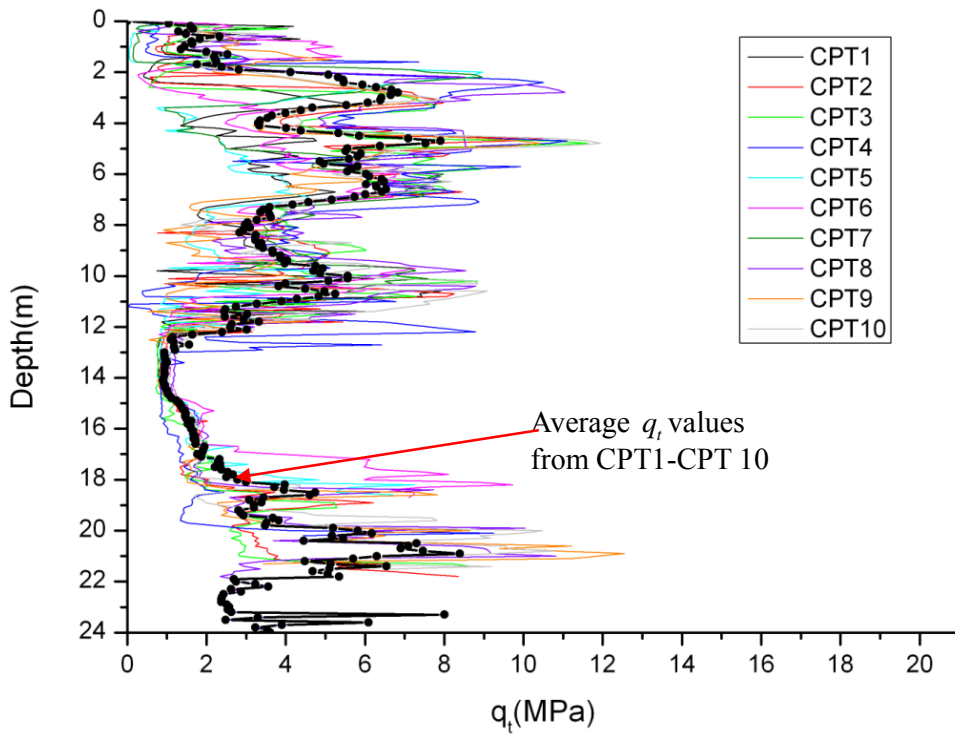
Figure 5-4 CPTU q_t profiles before the pile installation.
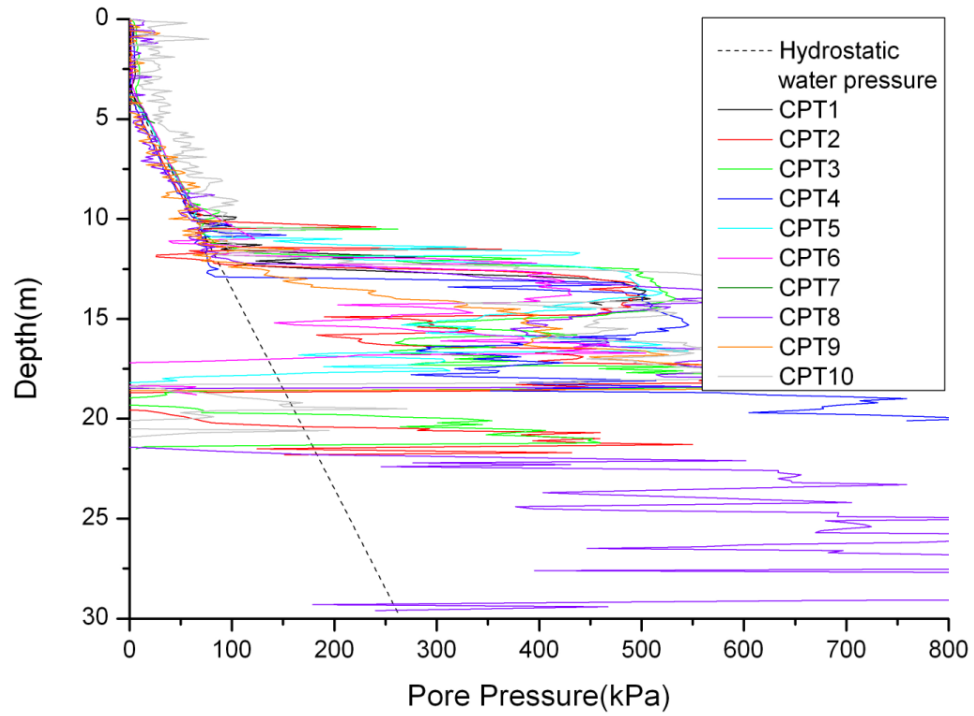
Figure 5-5 CPTU pore pressure profiles before the pile installation.
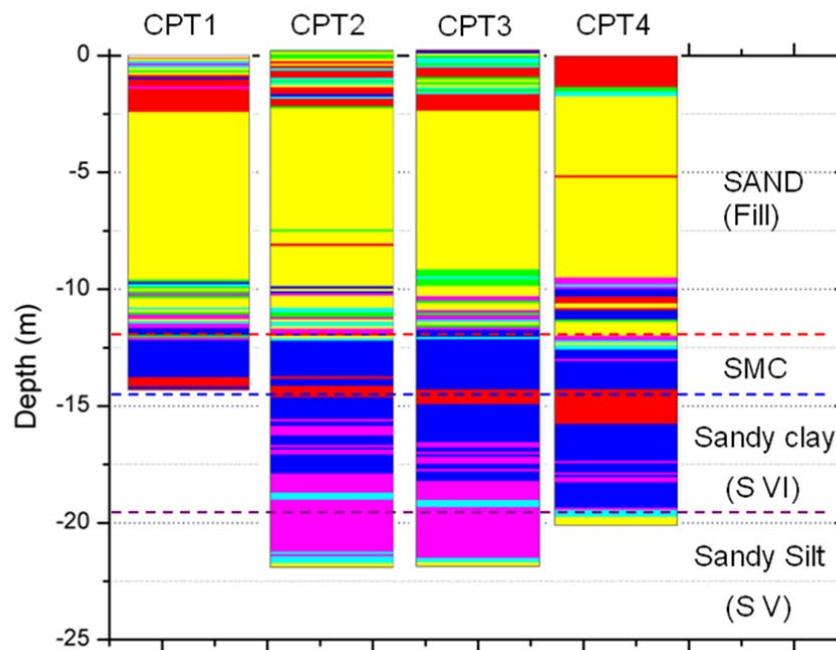
Figure 5-6 The soil profile based on Eslami-Felleninus's soil profiling chart (Eslami and Felleninus, 1997).
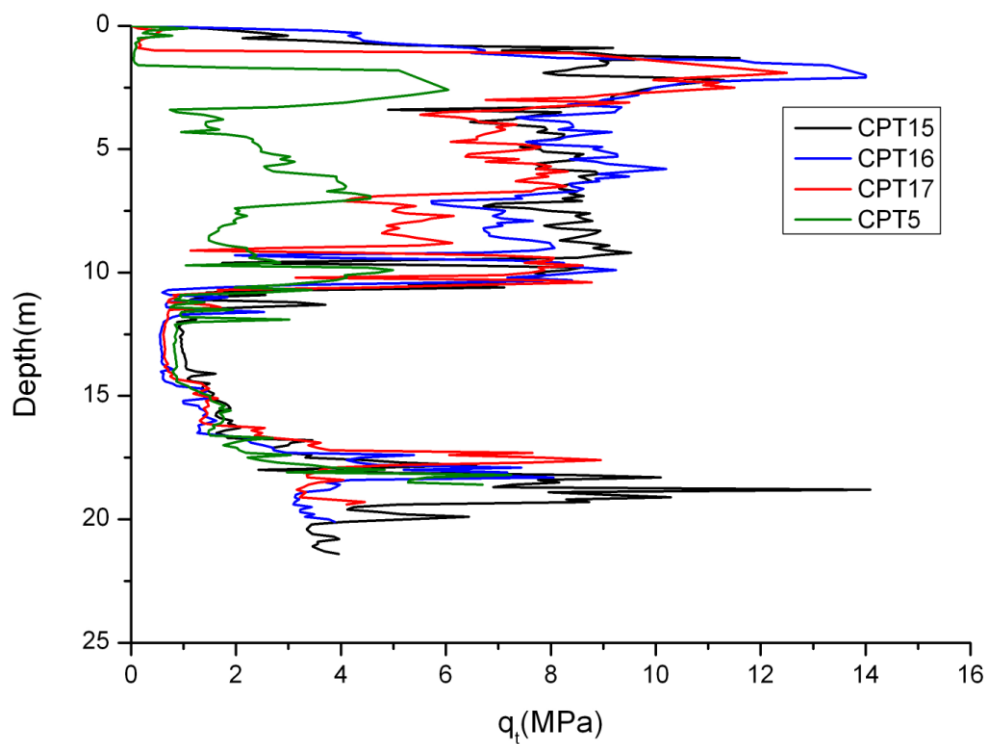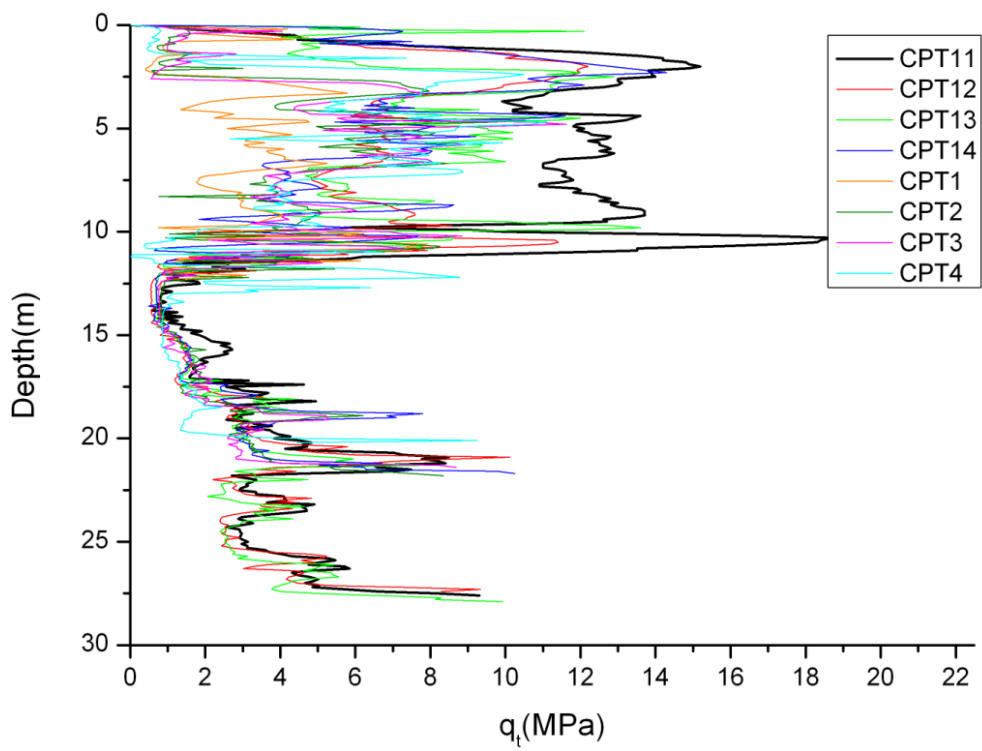
Figure 5-7 Compare CPTU q_t profiles before and after pile installation.
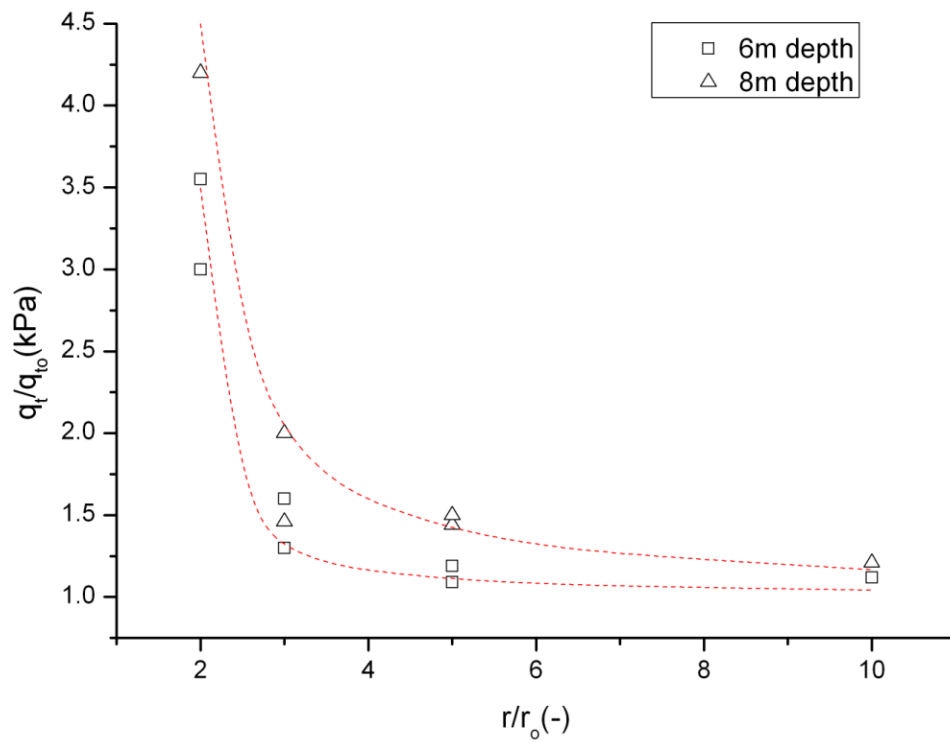
Figure 5-8 Ratio of q_t/q_{to} plotted against the normalized radii.
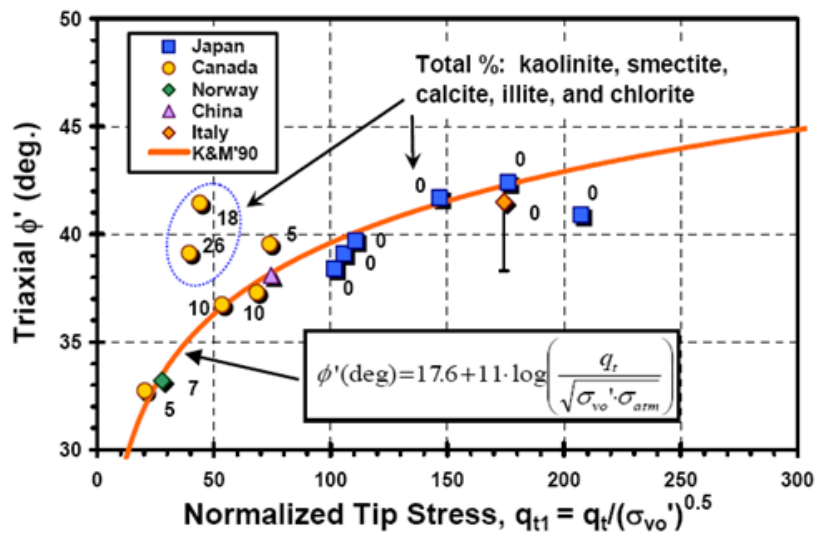
Figure 5-9 Peak triaxial friction angle from undisturbed sands with normalized cone tip resistance. (Kulhawy and Mayne, 1990).
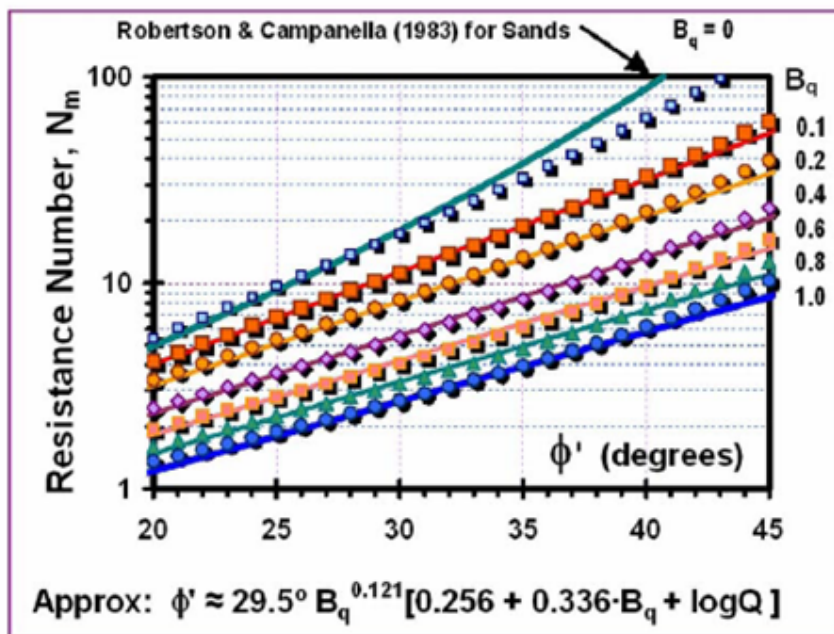
Figure 5-10 The effective friction angle for silts and clays from NTNU Method. (Senneset, et al.1988).
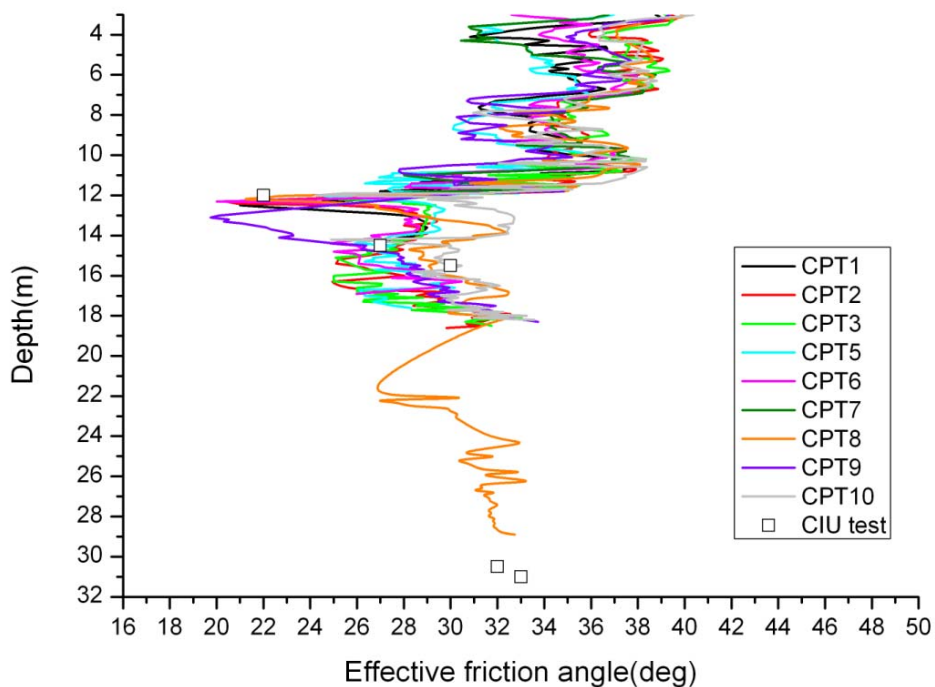
Figure 5-11 The evaluation of effective friction angle profiles from CPT1 to CPT10.
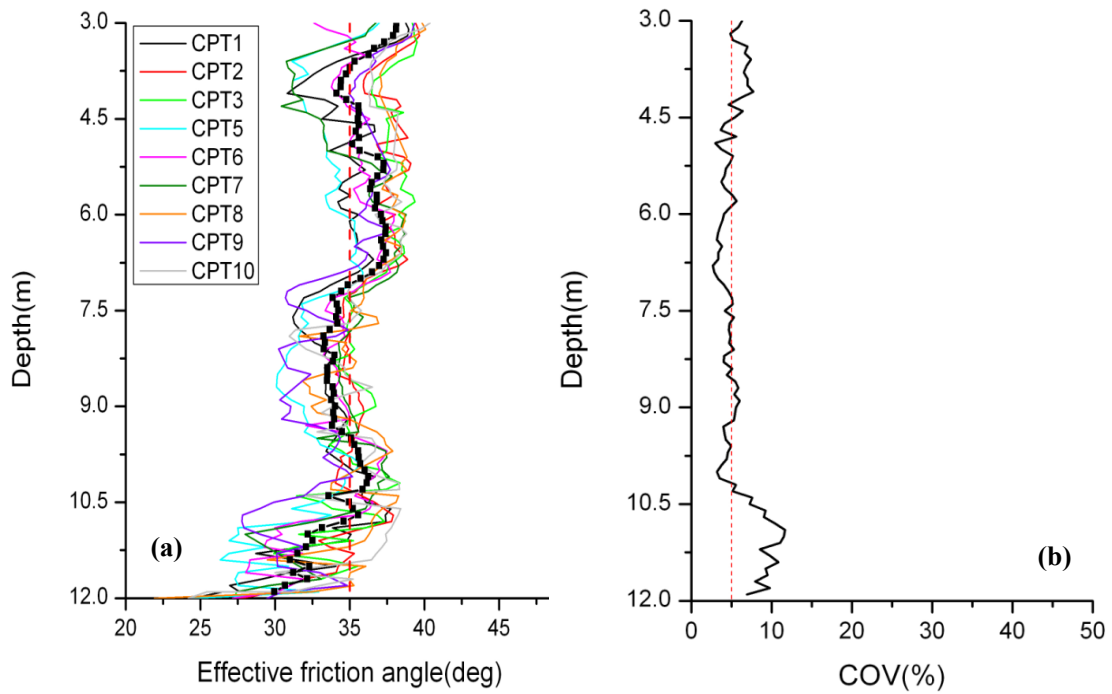
Figure 5-12 (a) The evaluated effective friction angle profile for the granular layer and (b) COV of evaluated effective friction angle.
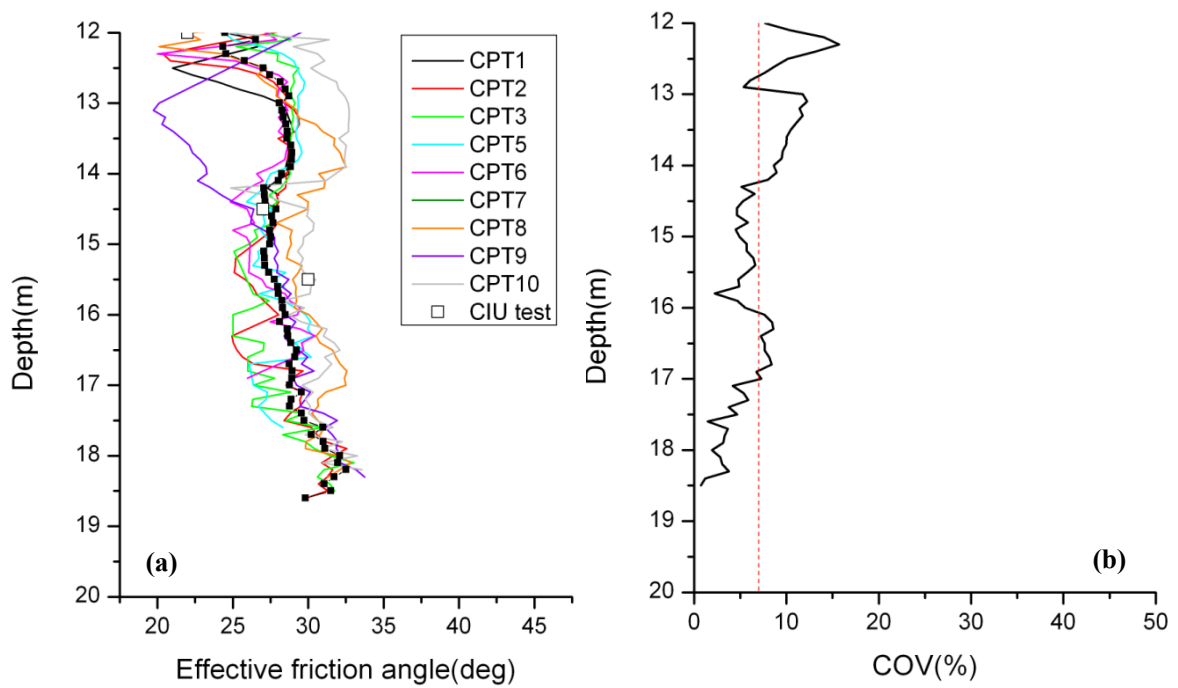
Figure 5-13 (a) The evaluated effective friction angle profile for the clay layer and (b) COV of evaluated effective friction angle.
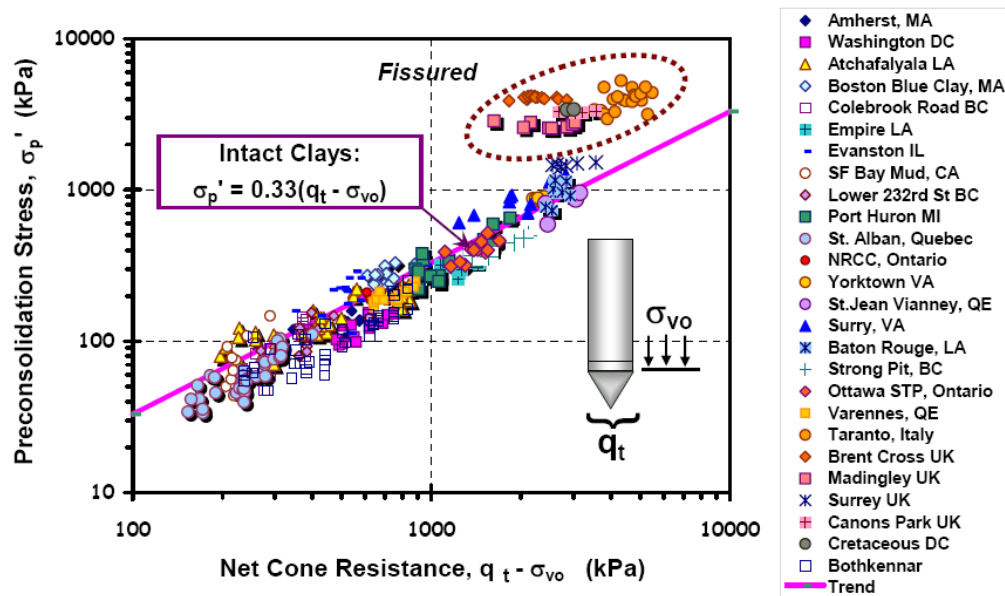
Figure 5-14 First-order relationship for preconsolidation stress from net cone resistance for clays. (Mayne, 1995; Demers & Leroueil, 2002)
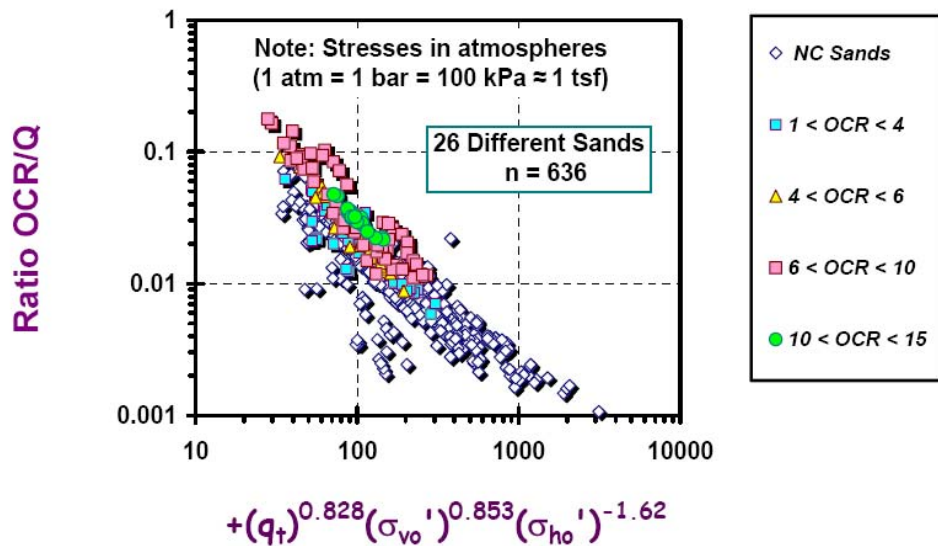
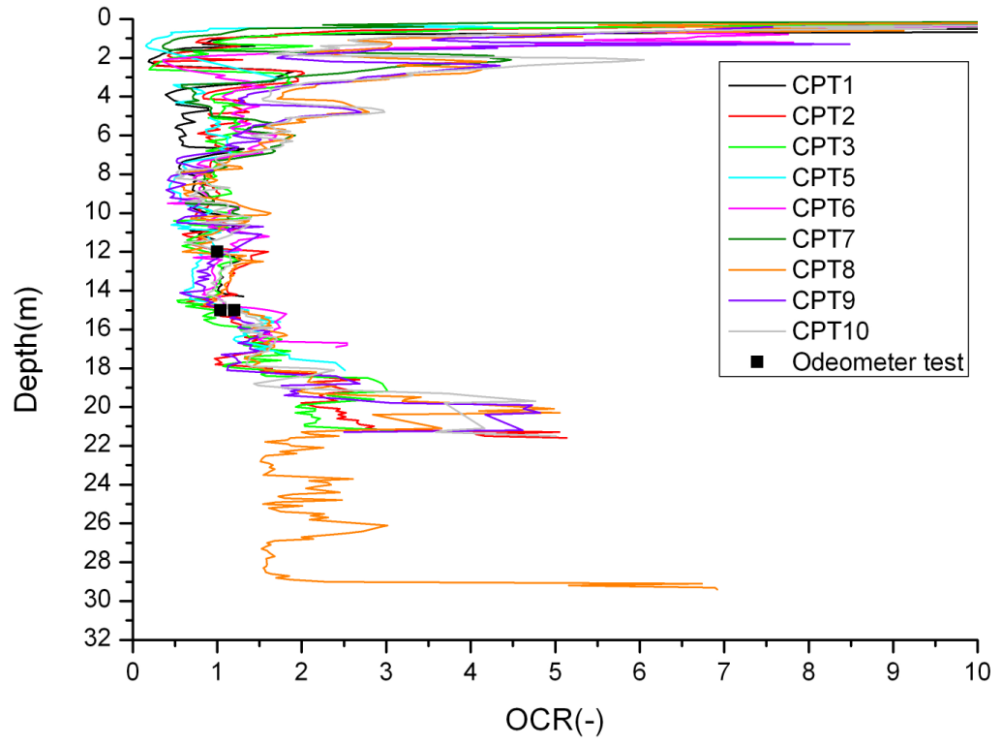Figure 5-15 Chamber test data showing trend for OCR/Q for clean quartz and siliceous sands. (Mayne, 2005).

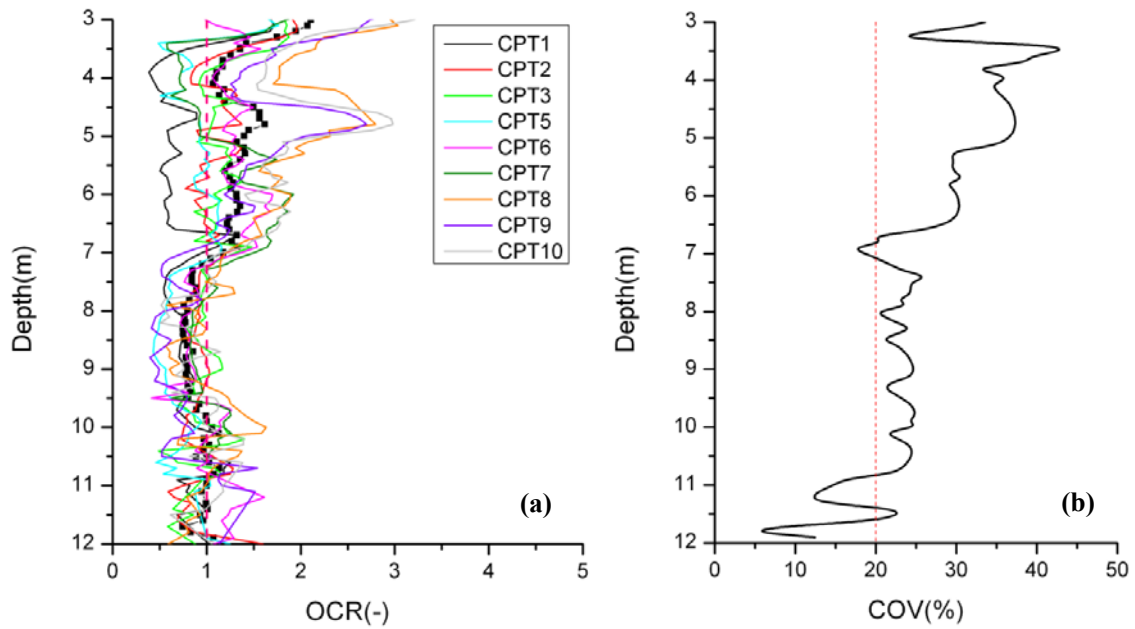Figure 5-16 The evaluation of OCR profiles from CPT1 to CPT10.

Figure 5-17 (a) The evaluated OCR profile for the granular layer and (b) COV of evaluated OCR.
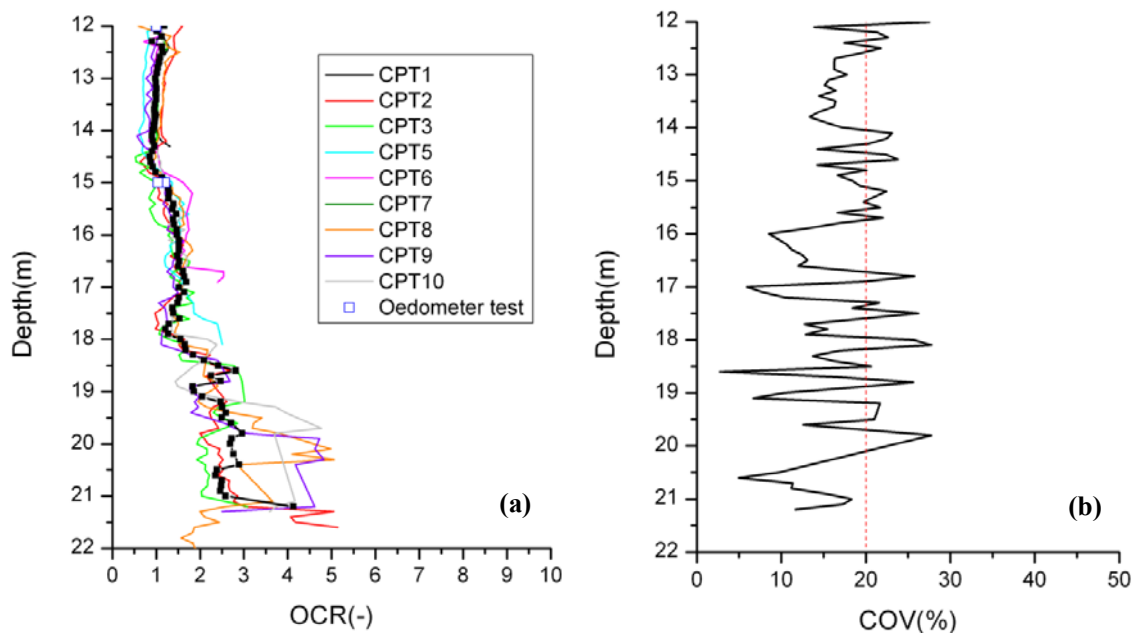
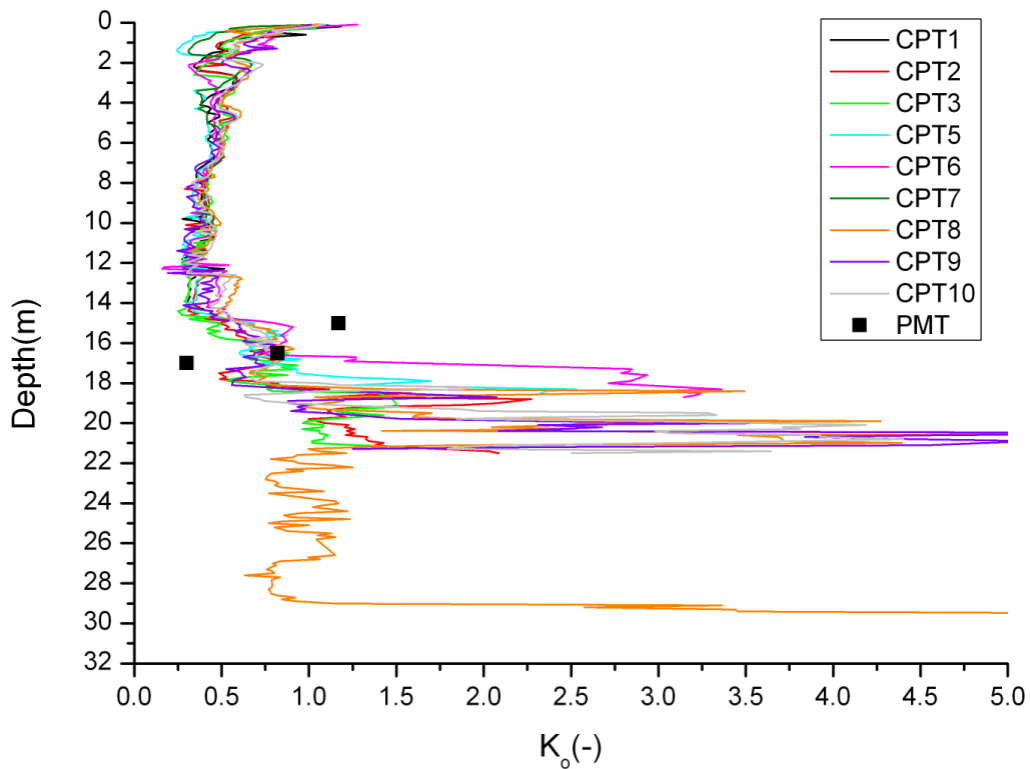Figure 5-18 (a) The evaluated OCR profile for the clay layer and (b) COV of evaluated OCR.

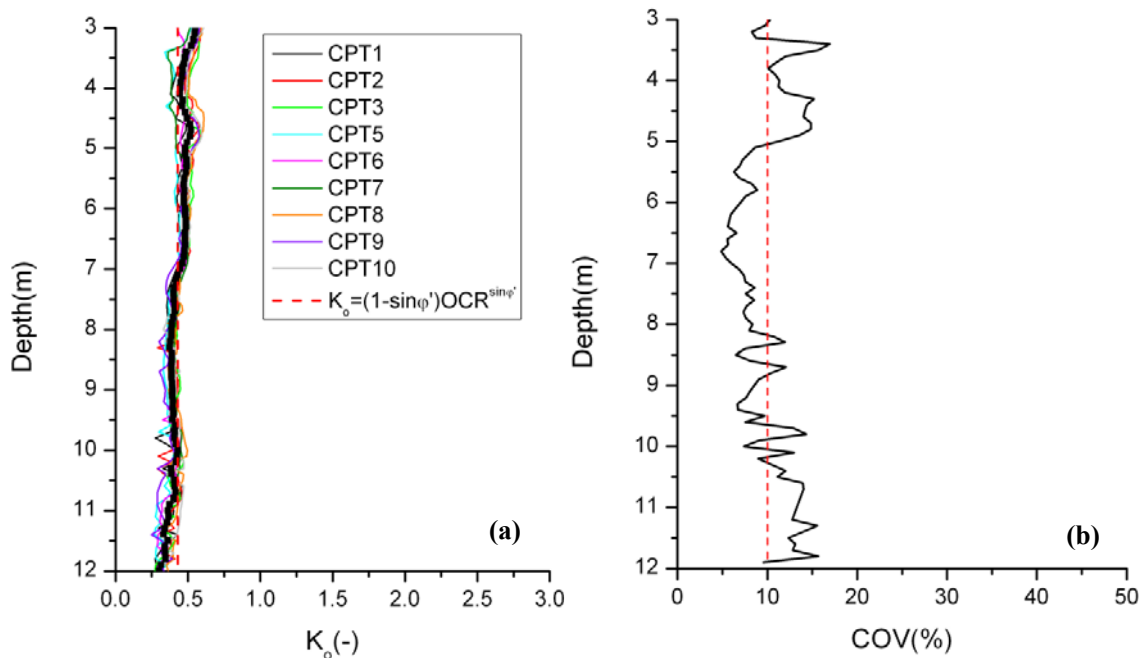Figure 5-19 The evaluation of K_o profiles from CPT1 to CPT10.

Figure 5-20 (a) The evaluated K_o profile for the granular layer and (b) COV of evaluated K_o.
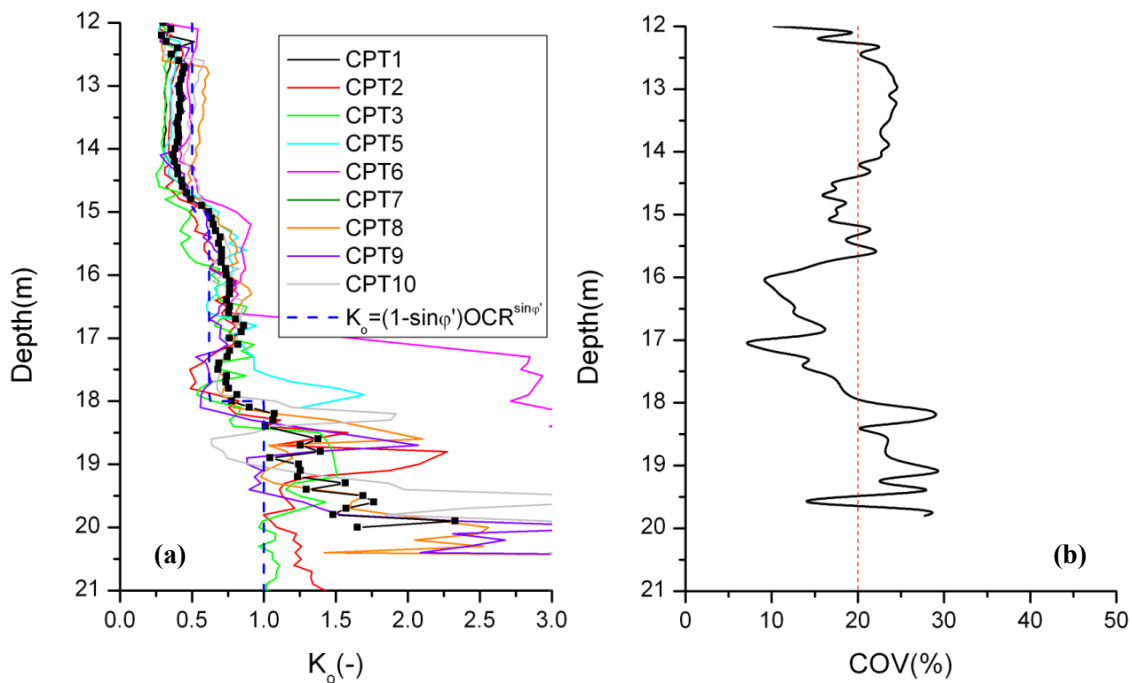

Figure 5-21 (a) The evaluated K_o profile for the clay layer and (b) COV of evaluated K_o.

Figure 5-22 The steel cap welded to the pile toe to form the closed-ended pile.

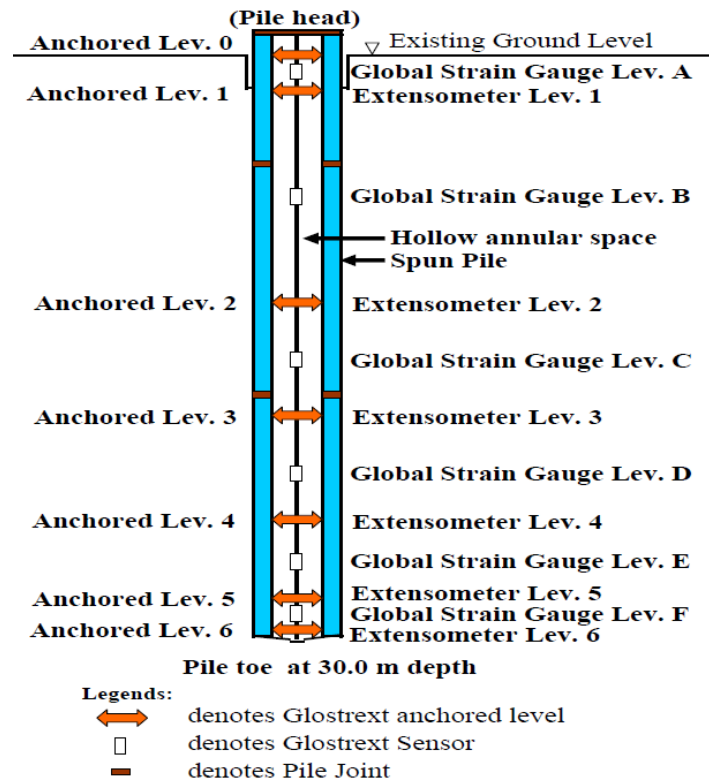Figure 5-23 The photo of jacked-in rig used to install the test piles.

Figure 5-24 Schematic diagram of typical instrumented spun pile Global Strain Extensometer technology. (Ali and Lee,2008).
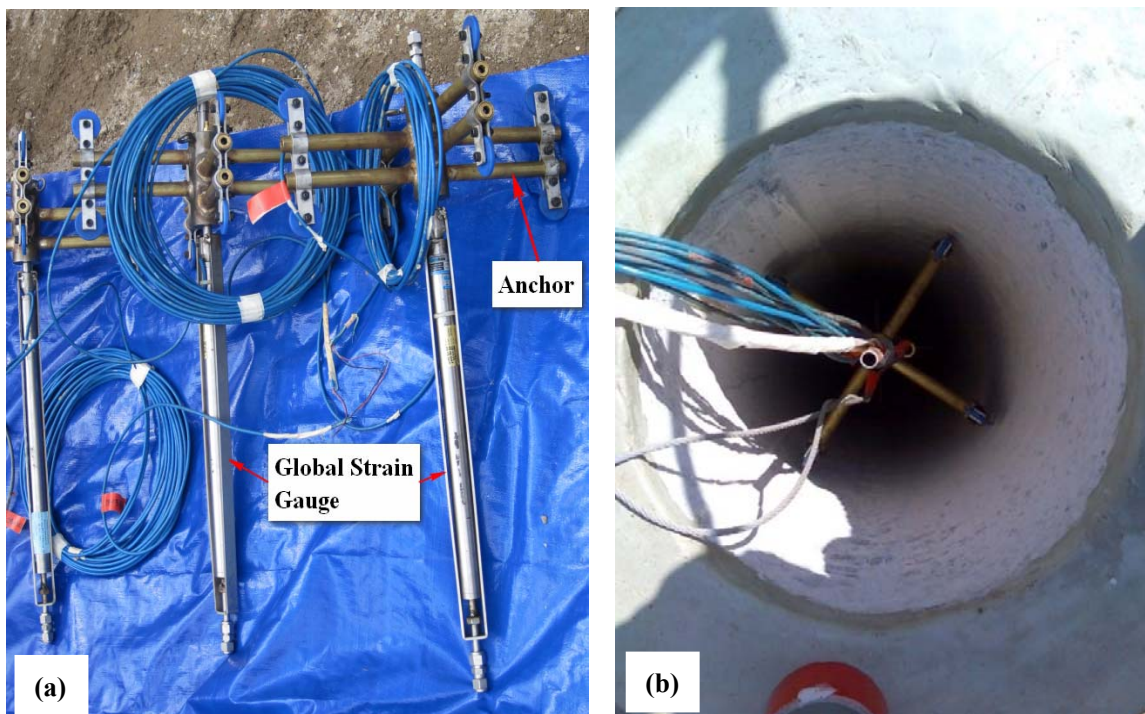

Figure 5-25 (a) photo of the Global strain gauge and anchor and (b) photo of the Global Strain Extensometer inside the test pile.

Figure 5-26 Photo of the experimental set-up for static pile load test.
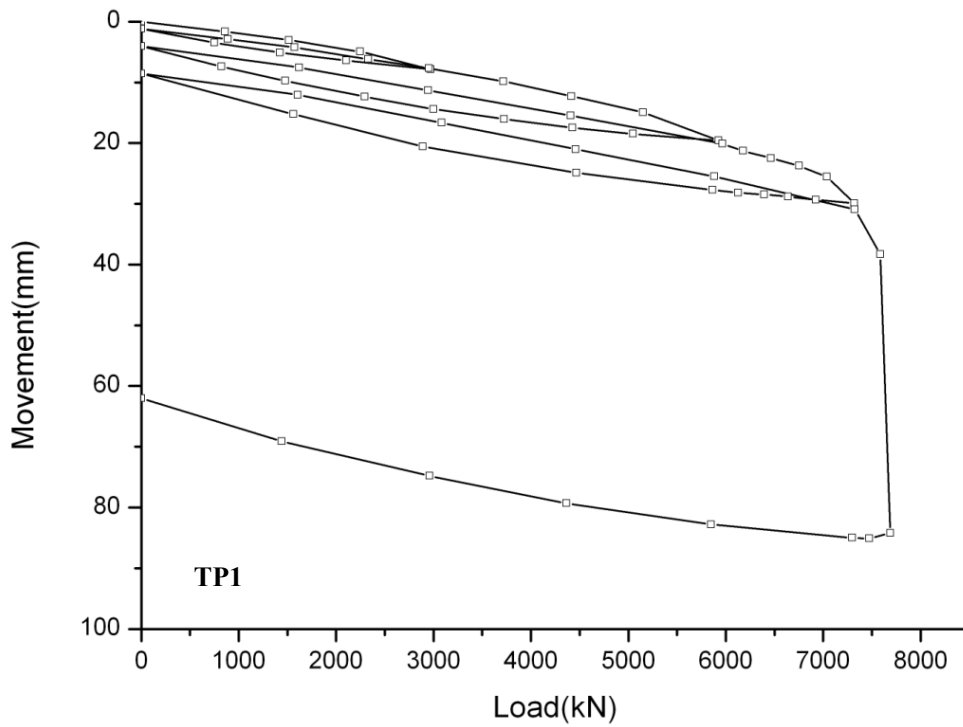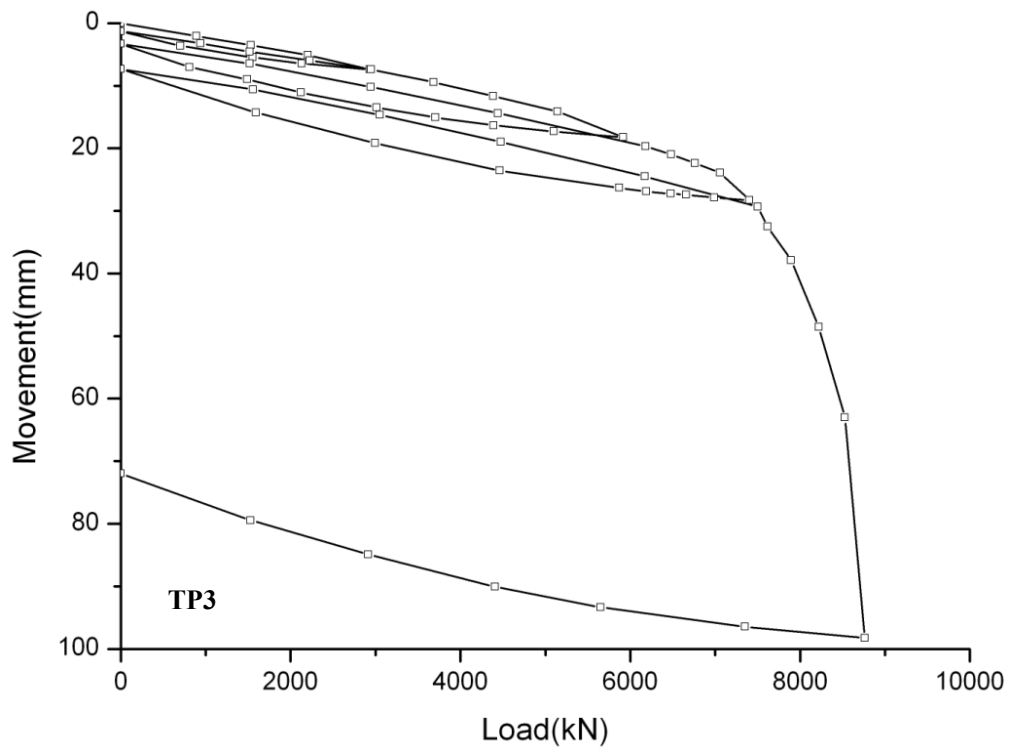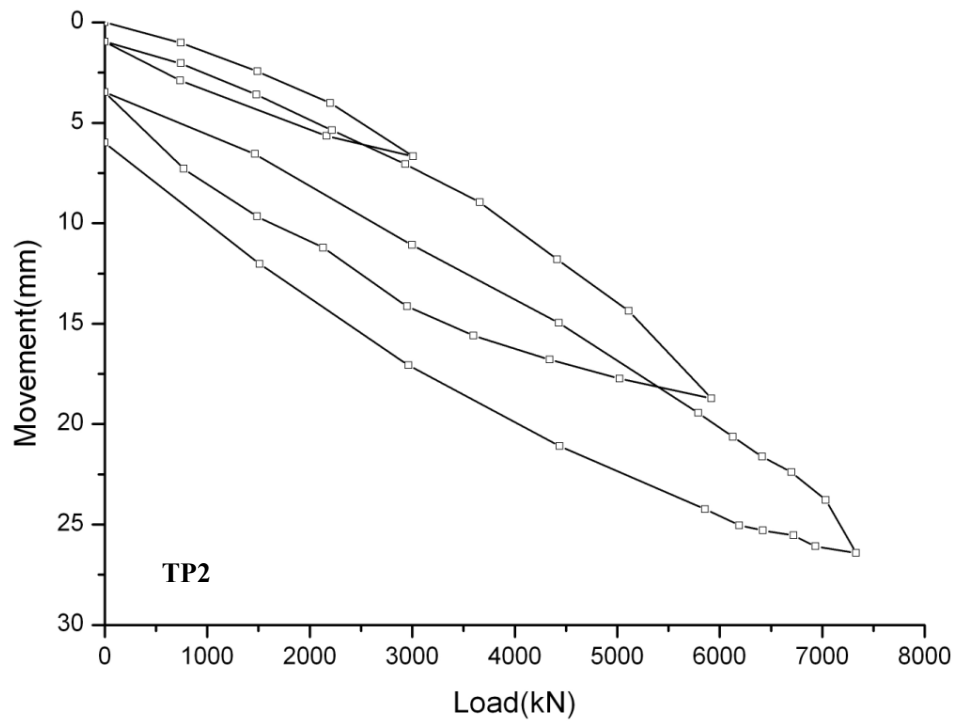
Figure 5-27 Static pile load test results for TP1 to TP3.
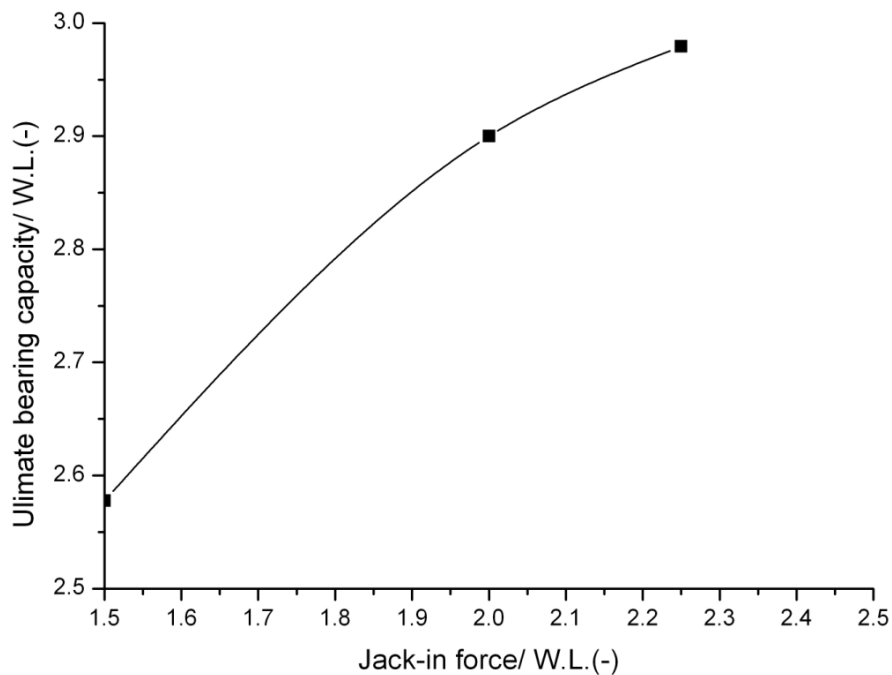
Figure 5-28 The relationship between normalized ultimate bearing capacity of the test pile and the normalized Jack-in force.
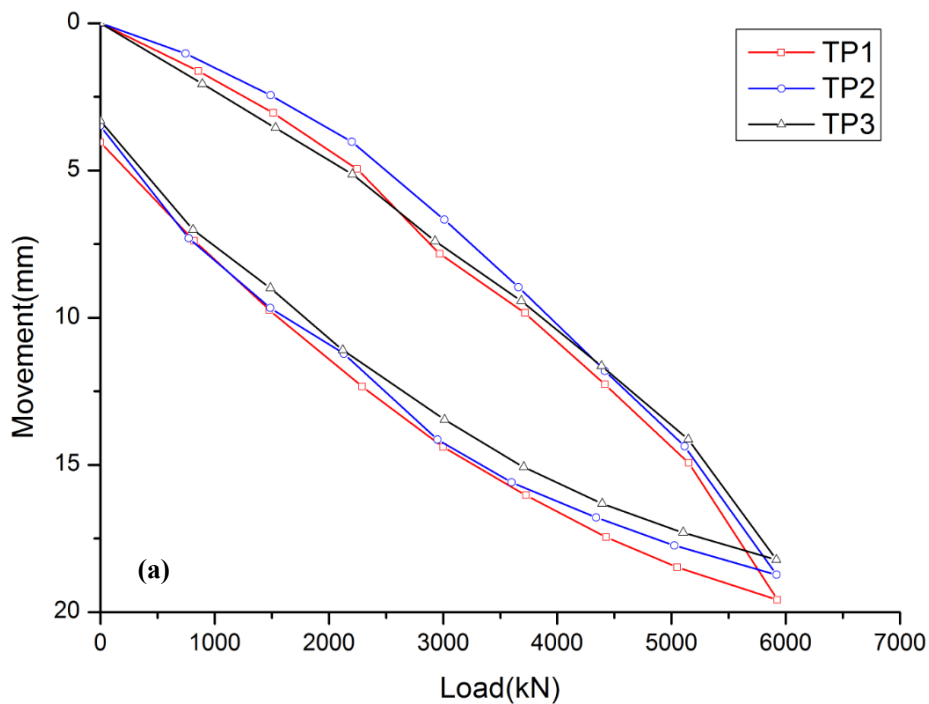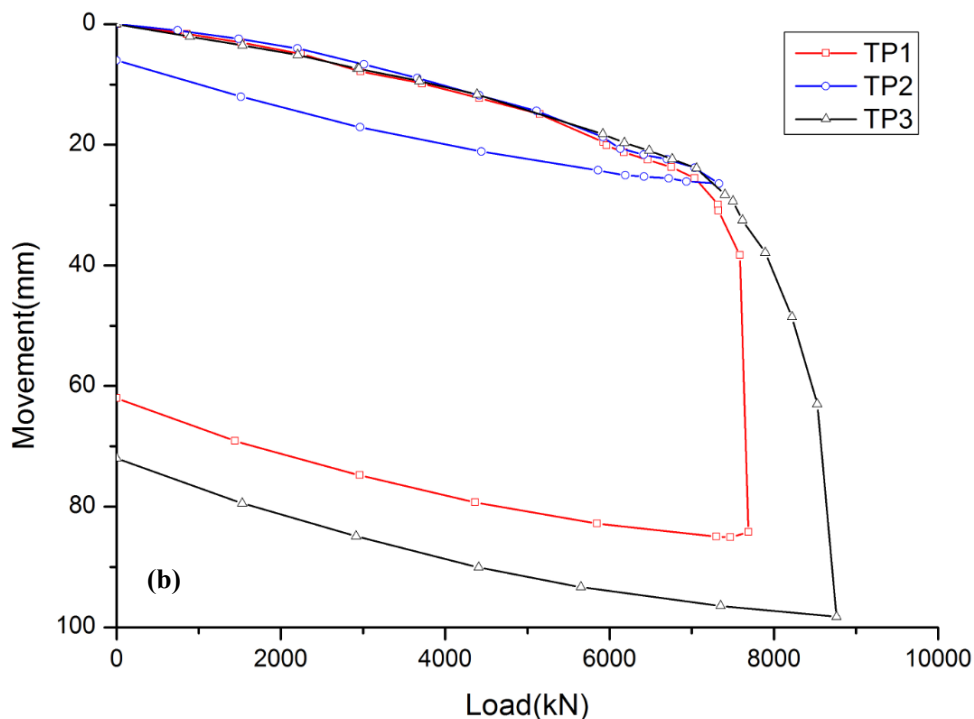
Figure 5-29 The comparison between three test piles (a) under 2 time working load and (b) at the ultimate bearing capacity.

2nd cycle

3rd cycle
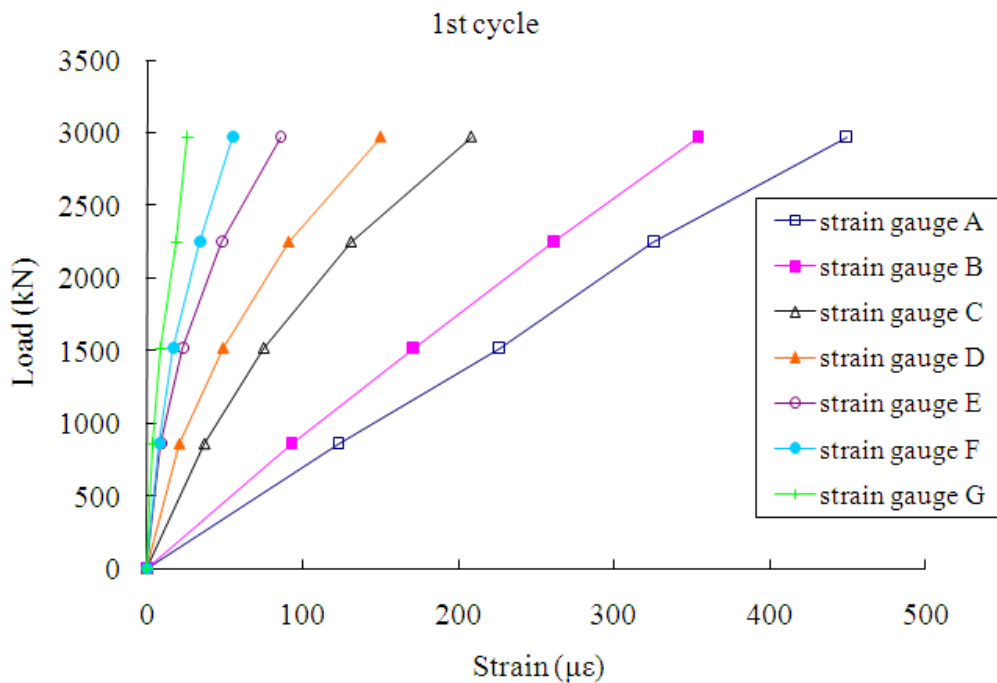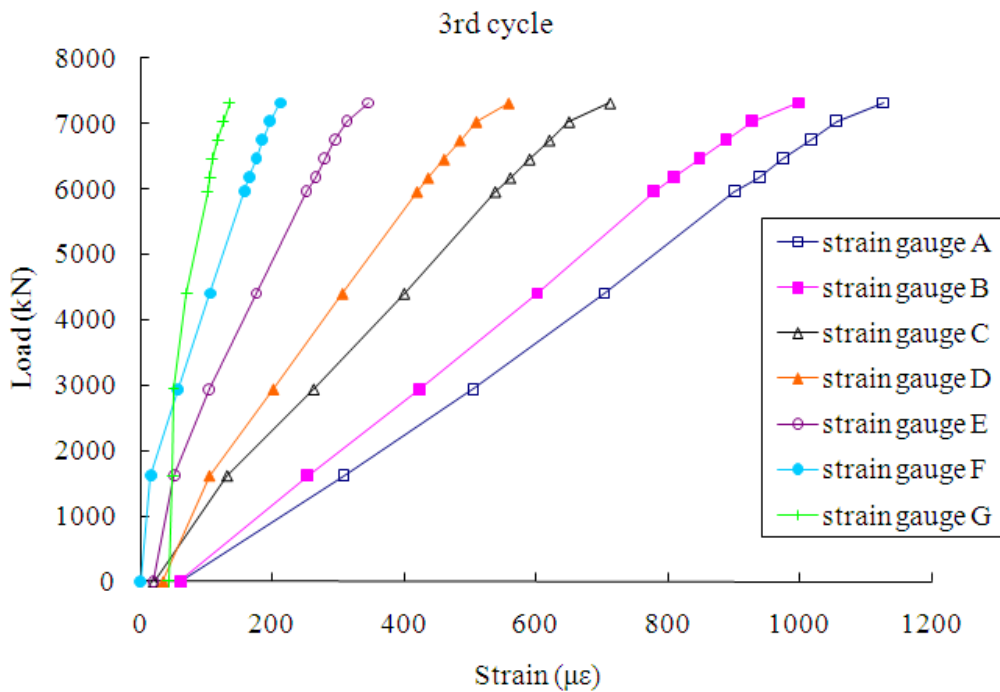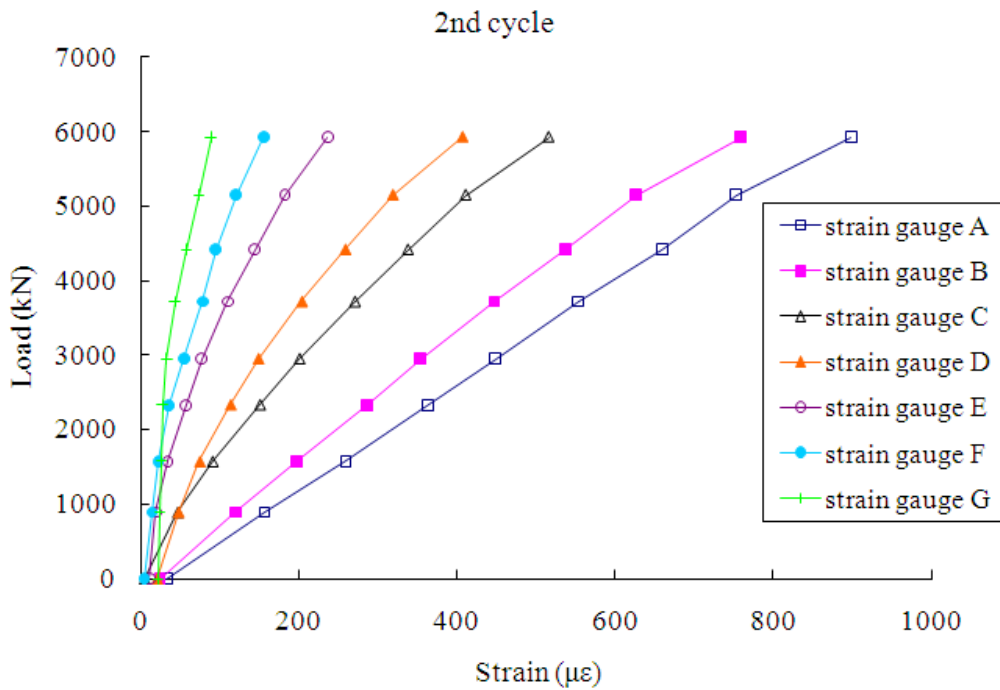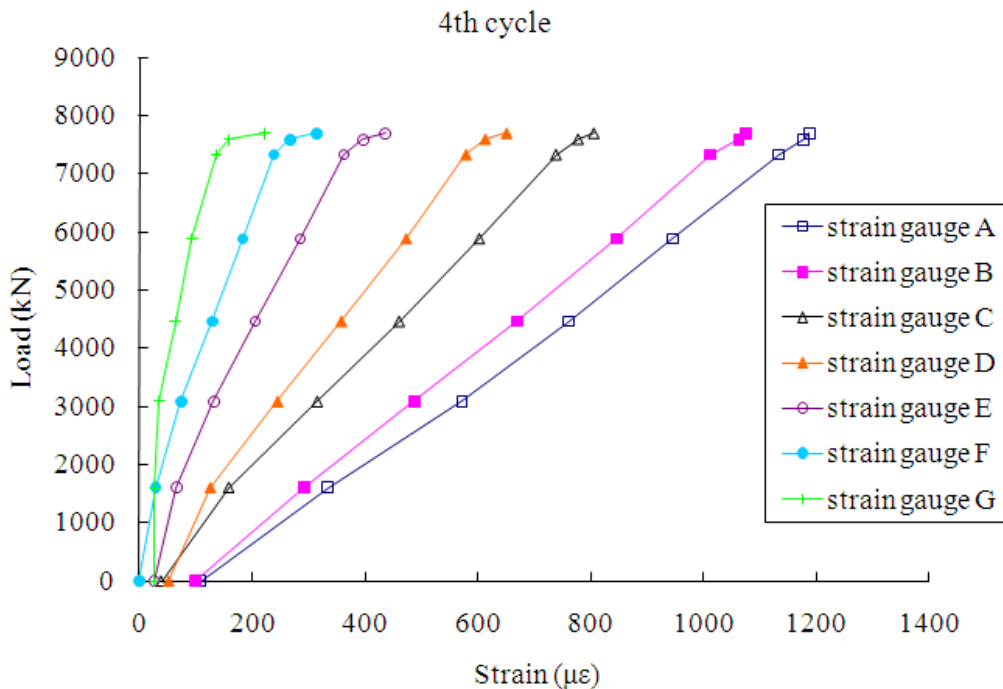
Figure 5-30 Load-strain curves for each gage level as measured for TP1.
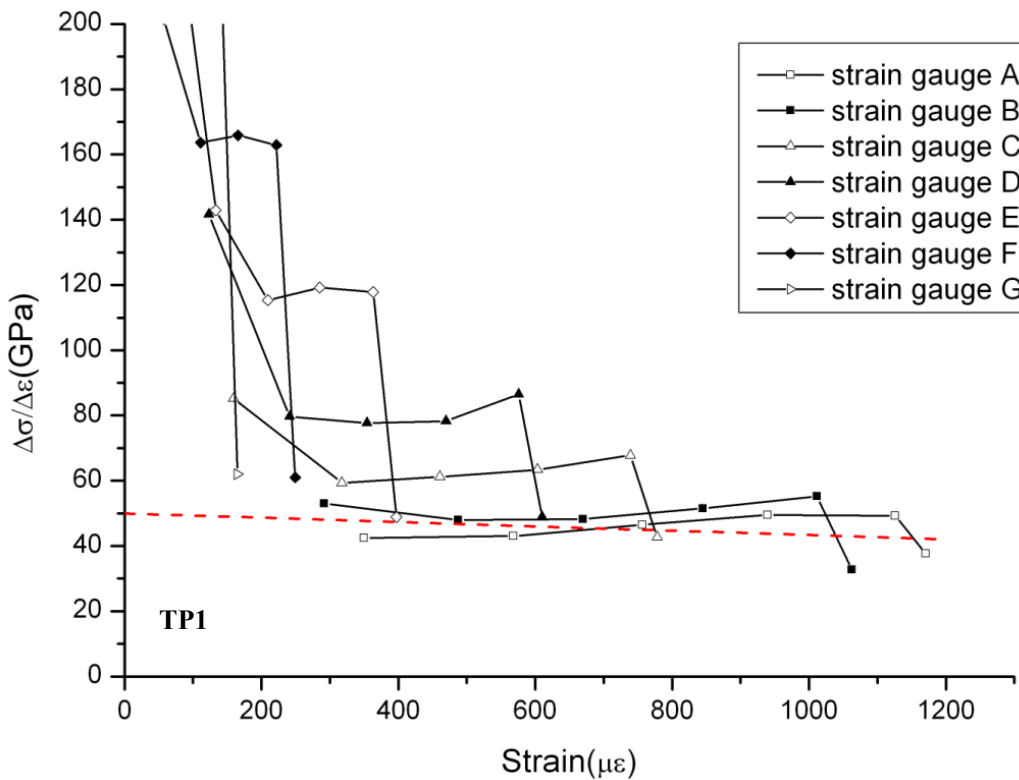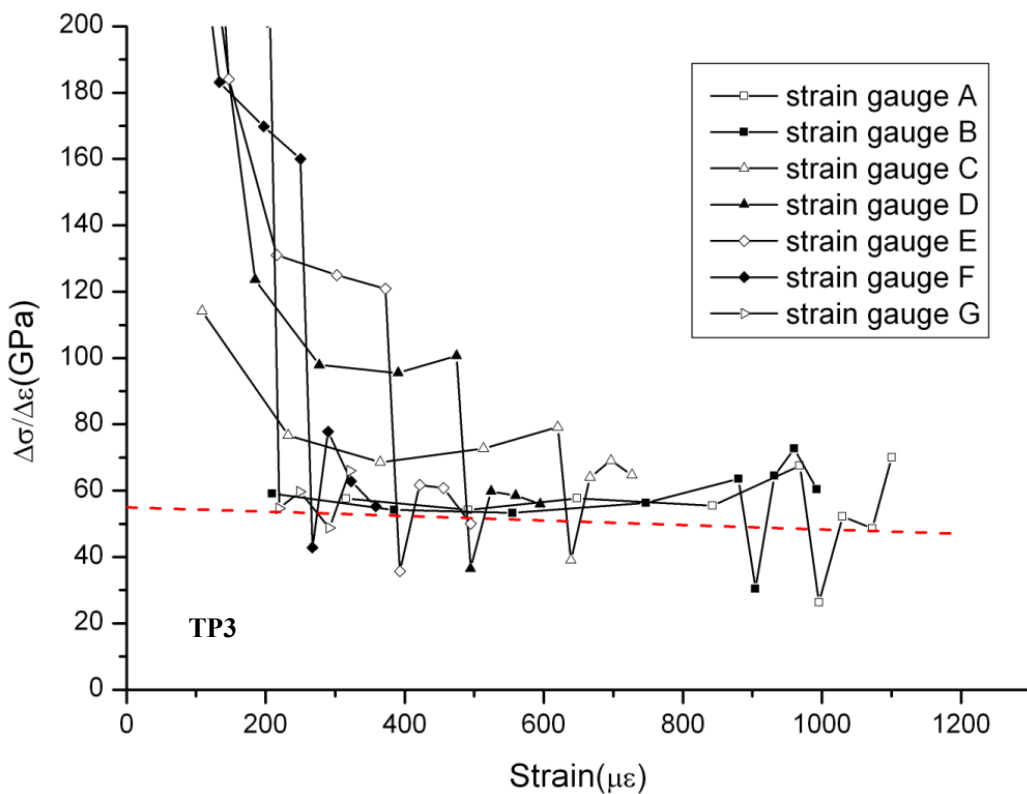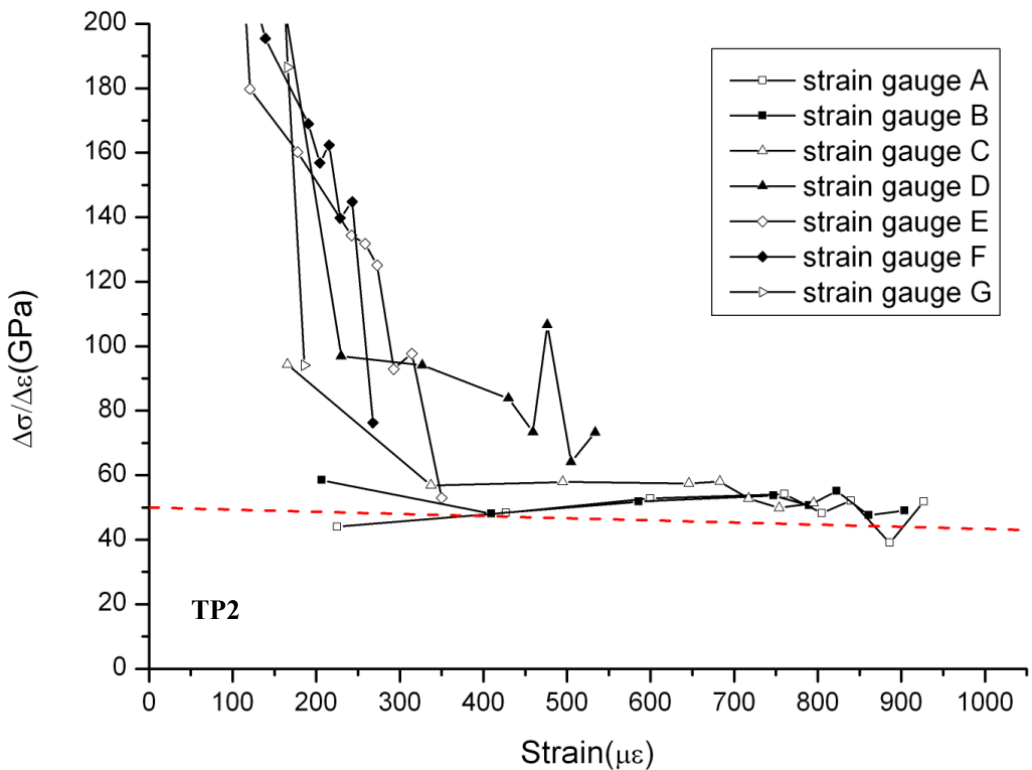
Figure 5-31 Secant modulus plotted against strain at each gage level for the last loading cycle of three test piles.
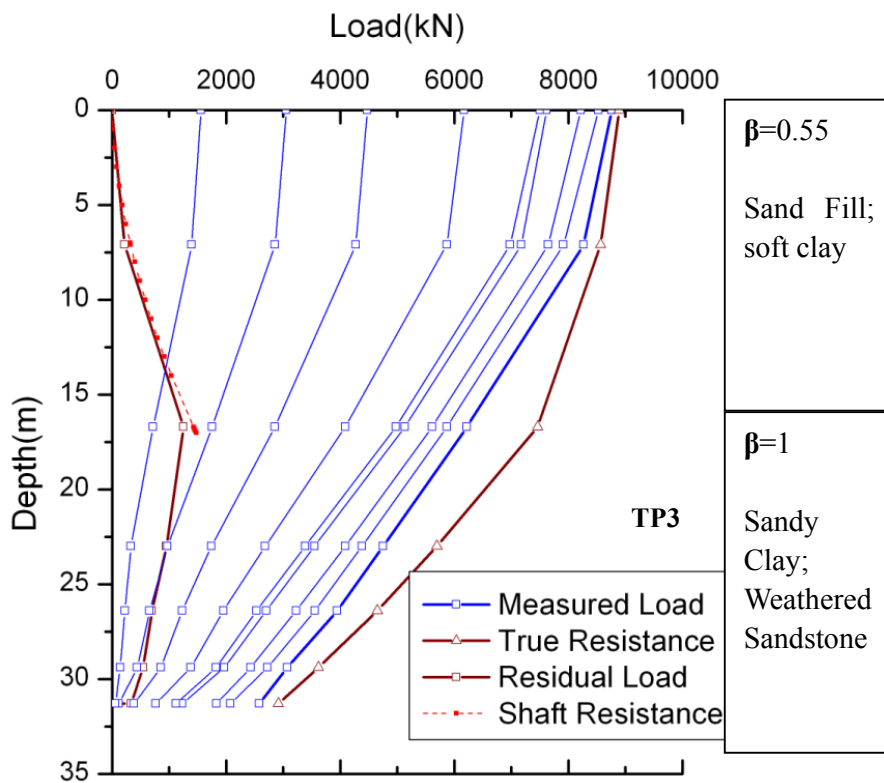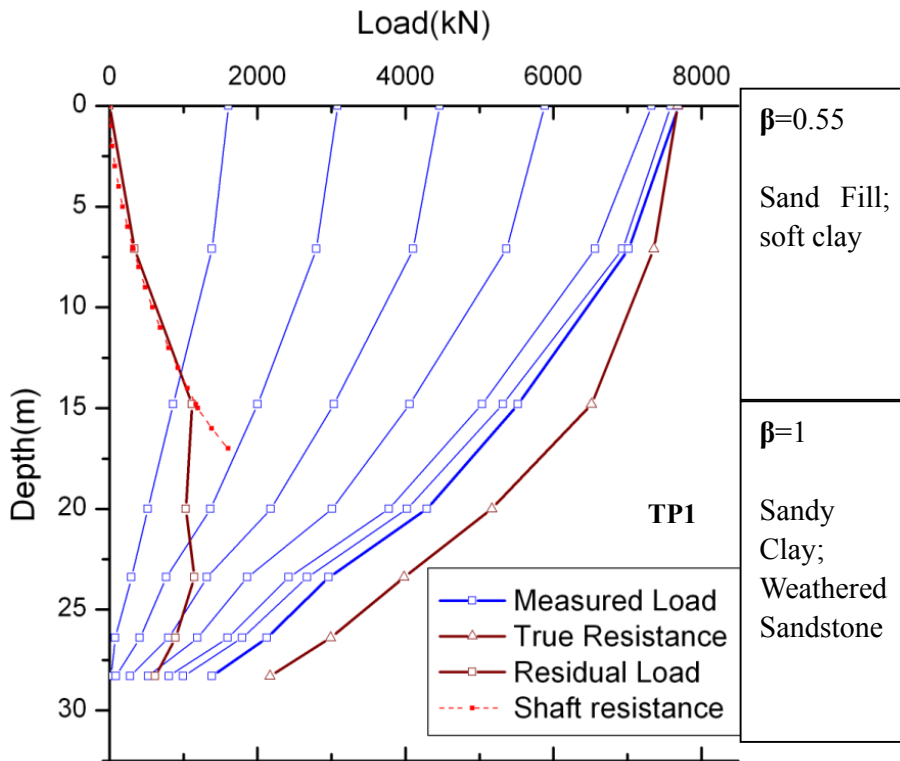
Figure 5-32 Evaluated distributions of measured load, residual load, load corrected for residual load, and shaft resistance based on effective stress method for TP1 and TP3.
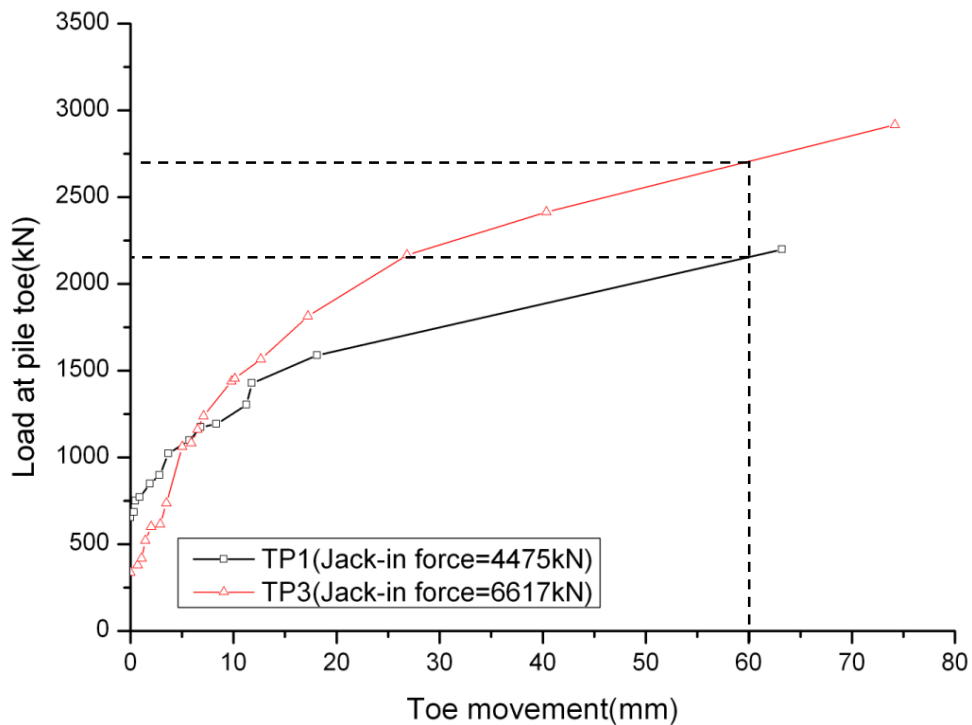
Figure 5-33 Toe load plotted against toe movement.
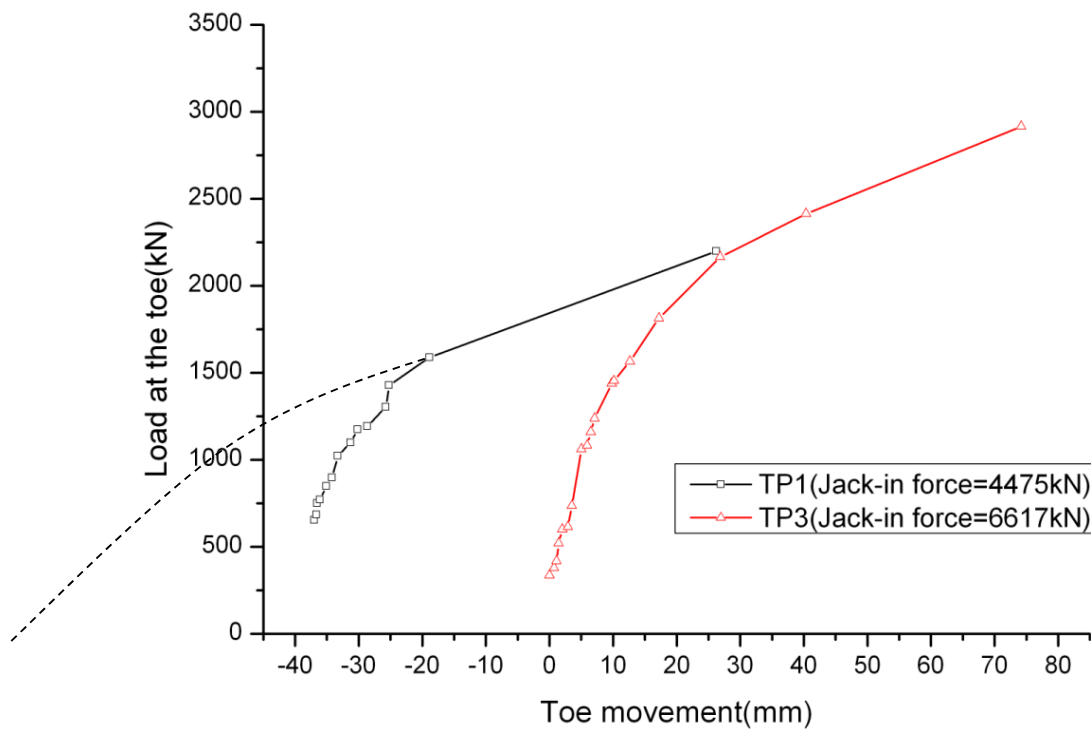
Figure 5-34 Virgin compress curve for pile toe.
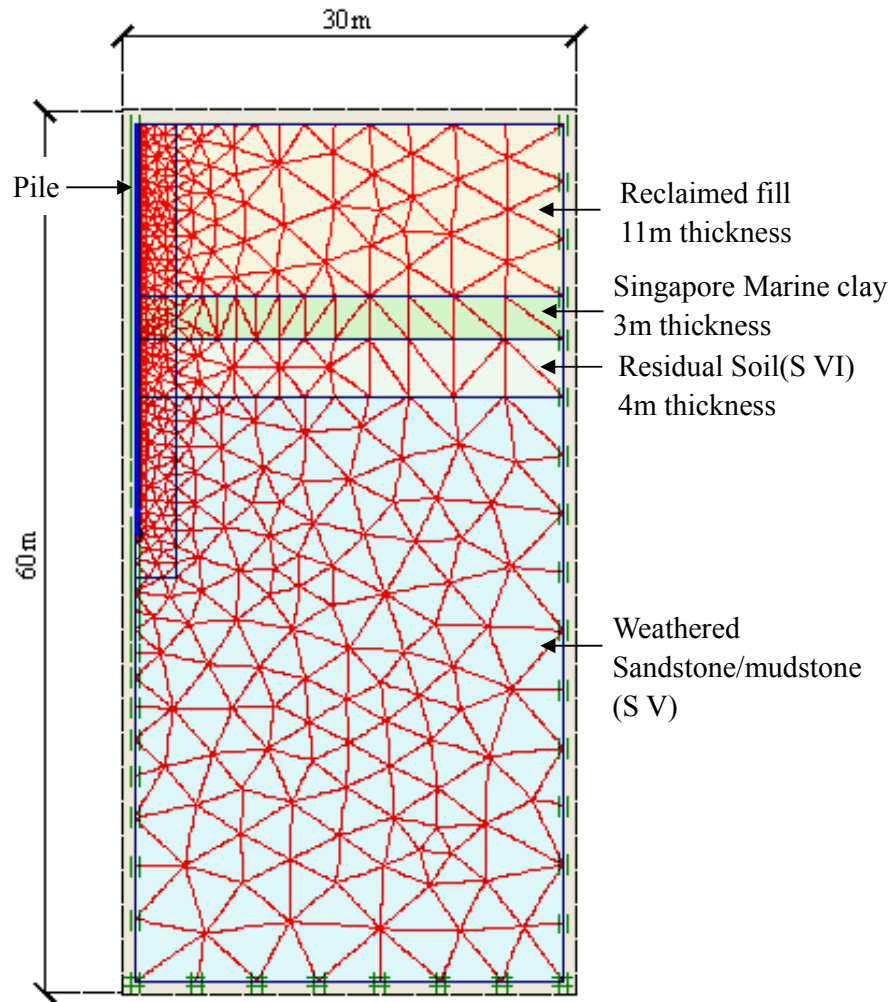
Figure 5-35 FEM mesh for simulation of the behavior of test pile.
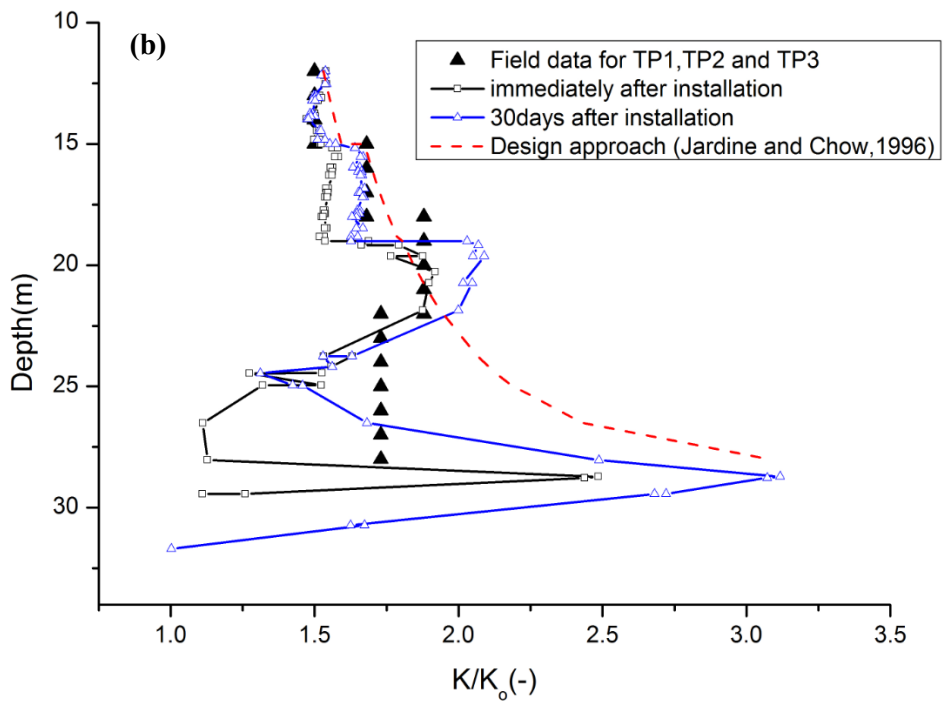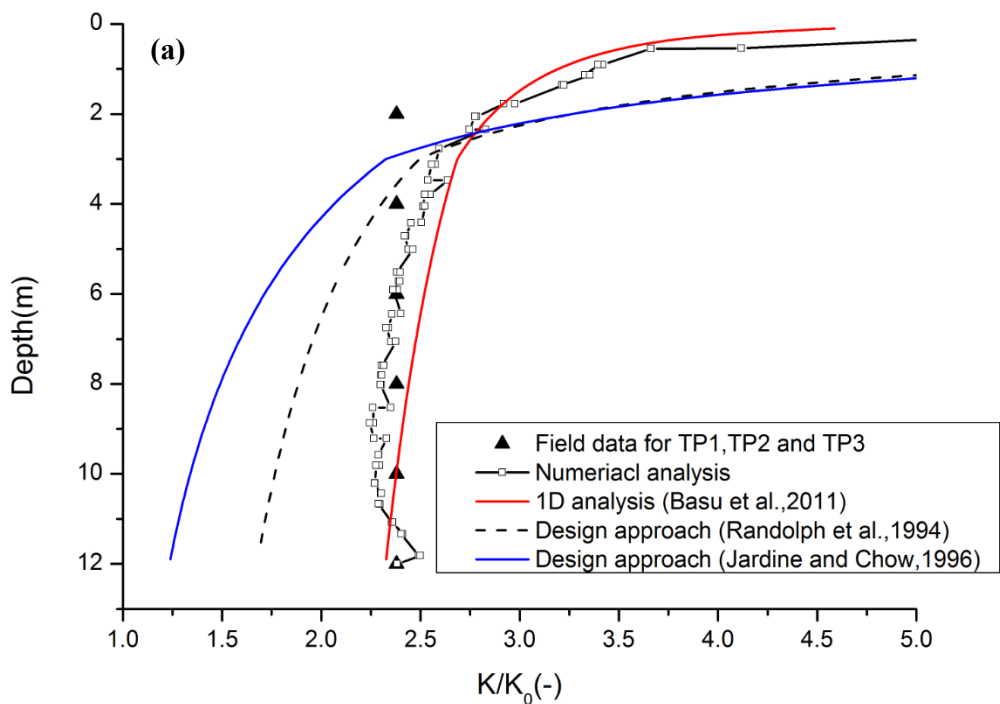
Figure 5-36 Comparison of K/K_o from the pile load tests on Jack-in piles with FEM predictions and other equations available in the literature (a) in sand layer (b) clayed layer.
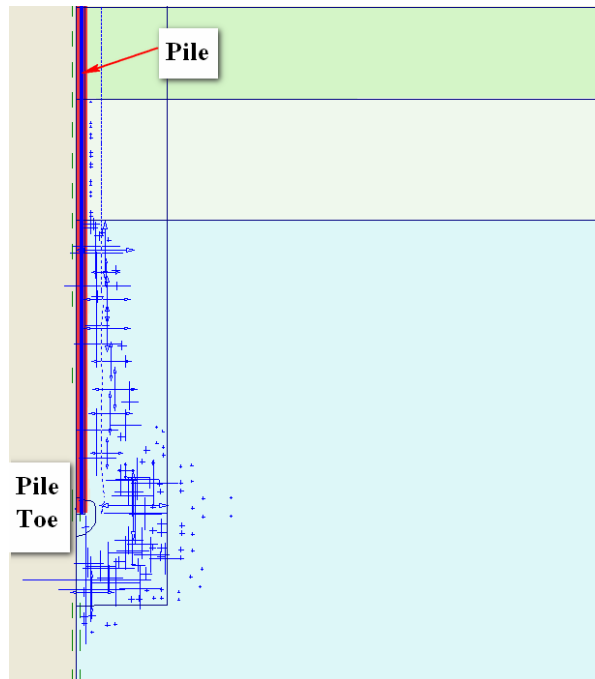
Figure 5-37 The FEM prediction of excess pore pressure distribution near the pile toe.
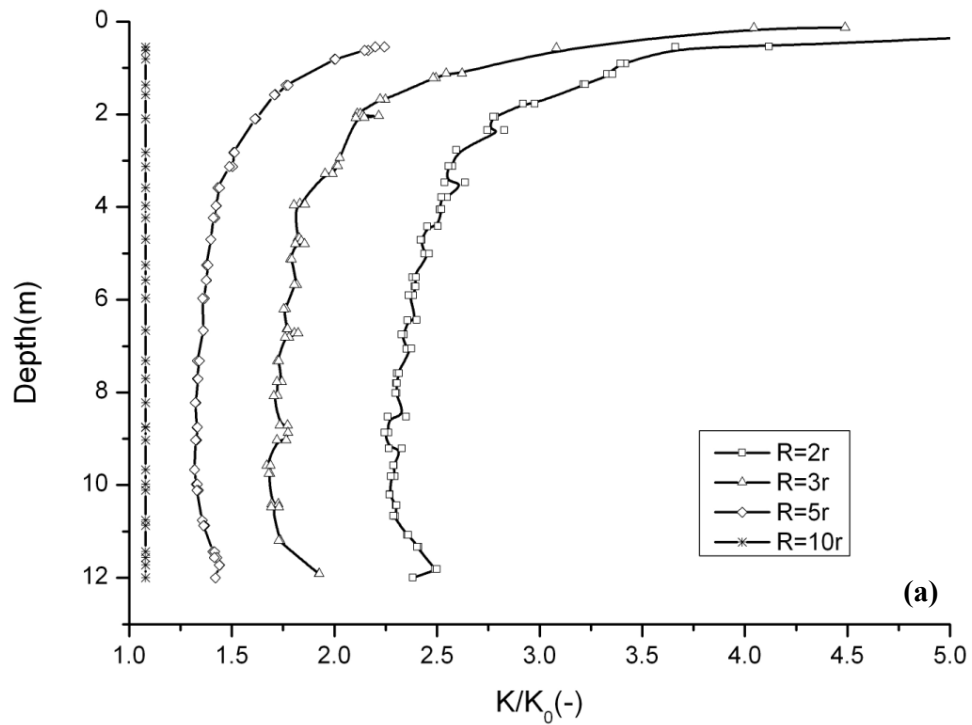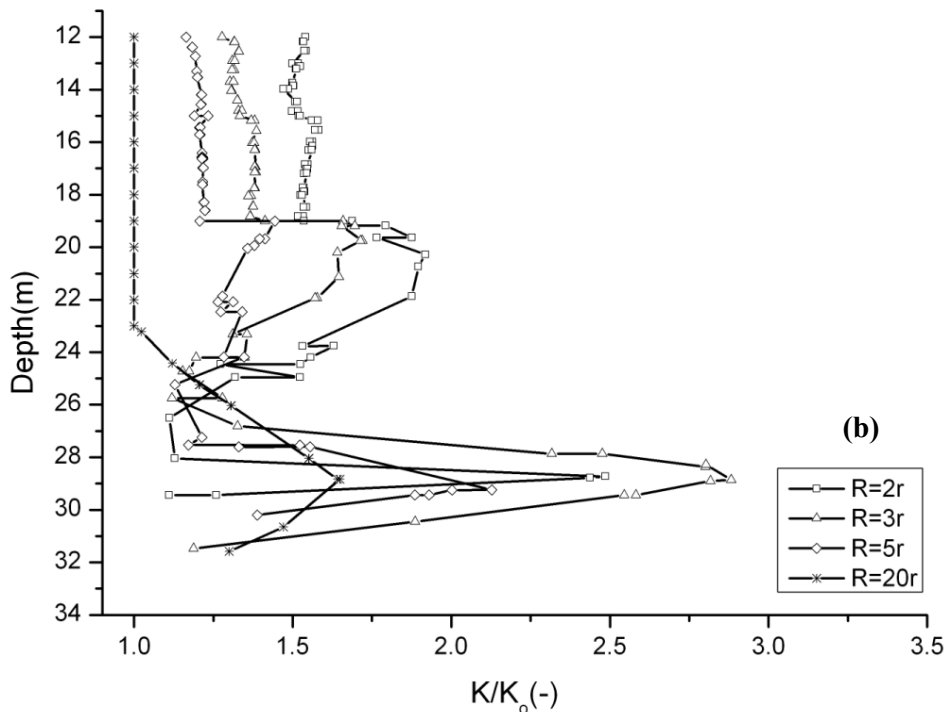
Figure 5-38 The FEM prediction of K/K$_o$ at different distance from the center of the pile (a) in sand layer (b) clayed layer.
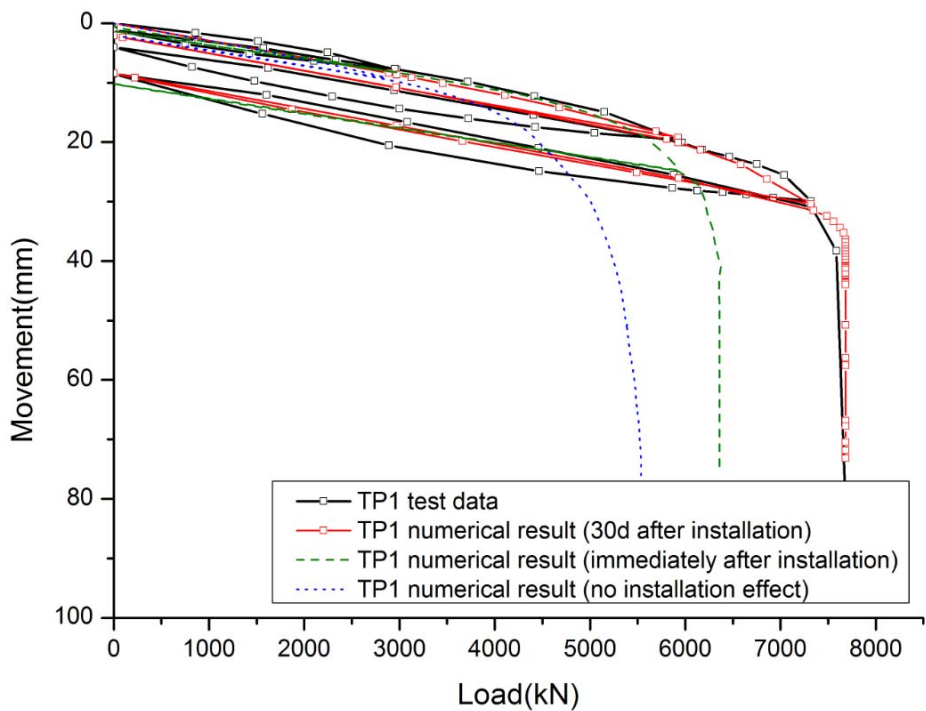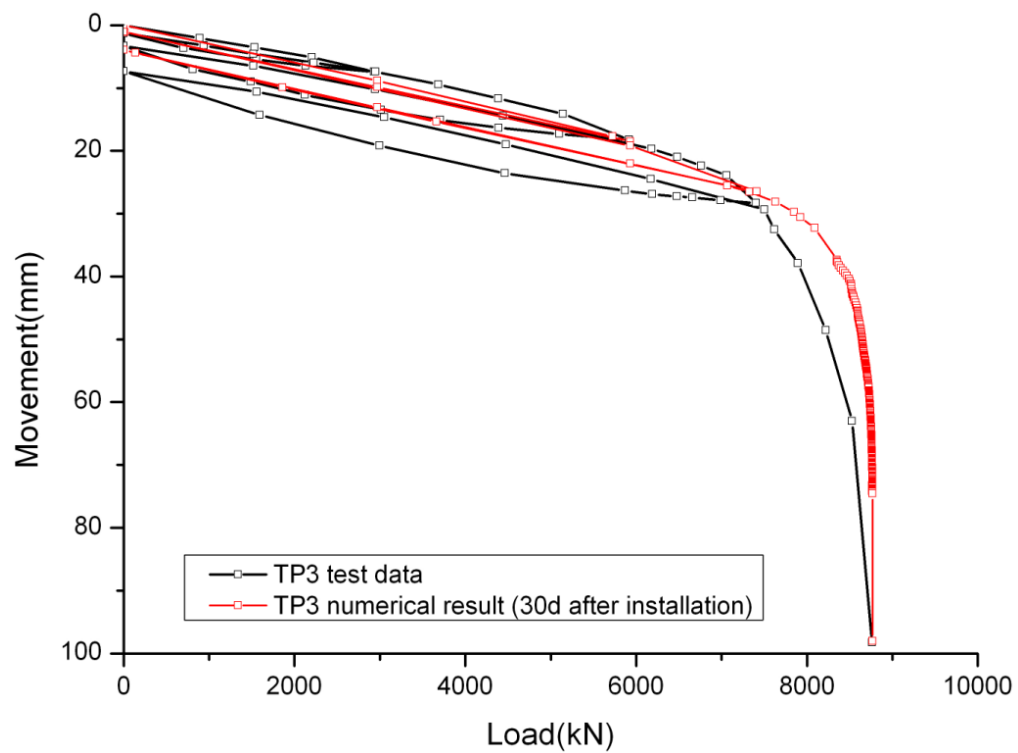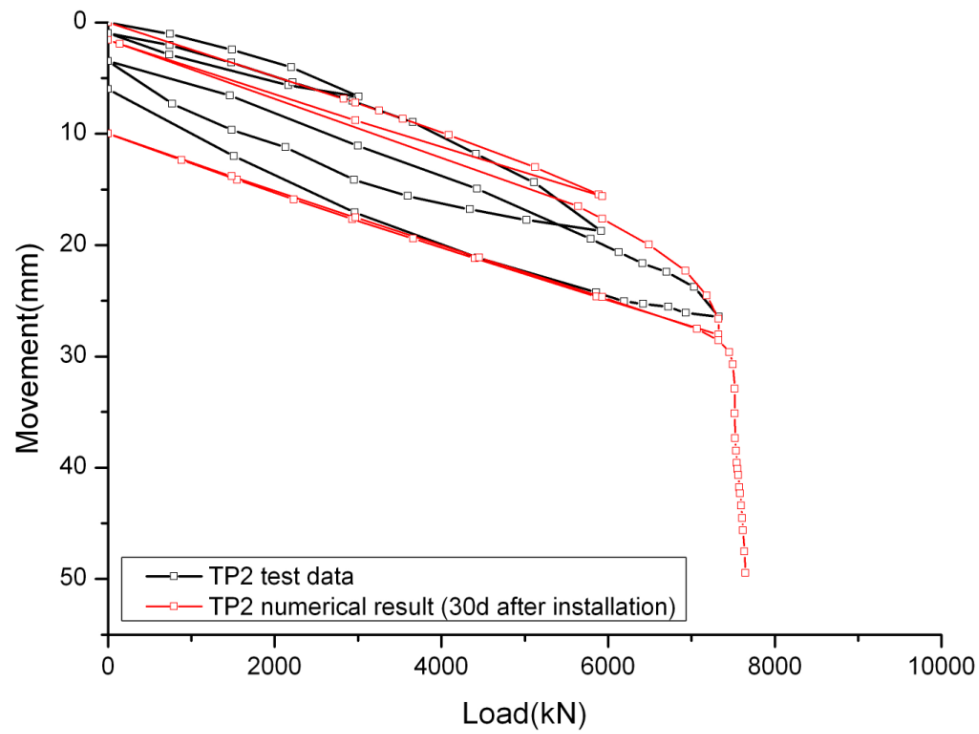
Figure 5-39 Comparison of Load-movement behavior from the pile load tests on Jack-in piles with FEM predictions.
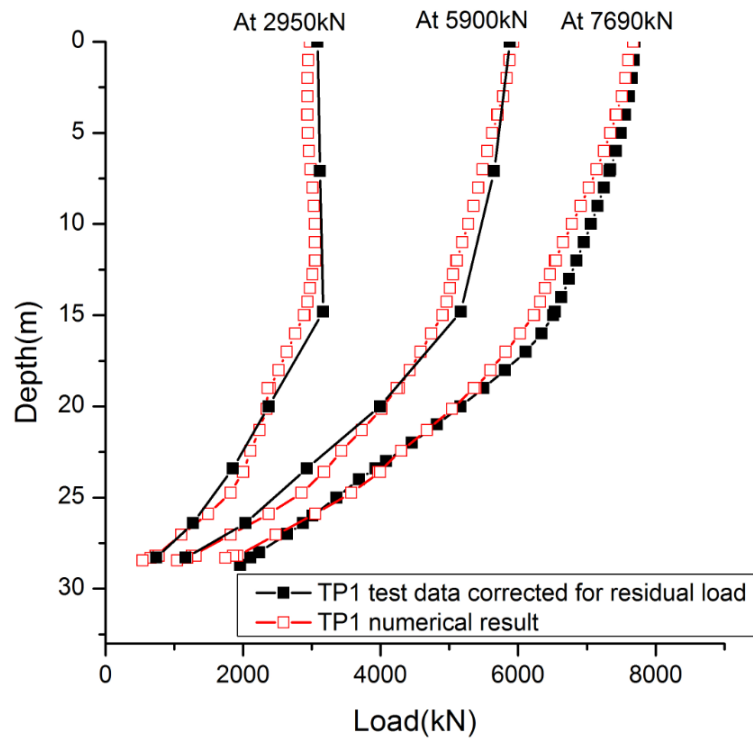
Figure 5-40 Comparison of load distribution profile at different loading level from the pile load tests with FEM predictions.

CHAPTER 6 NUMERICAL STUDY OF NSF IN UNIFIED PILE DESIGN METHOD

6.1 INTRODUCTION

As presented in the literature review, many engineers and some design codes still treat the negative skin friction (NSF) as an additional load on the pile, which makes for unnecessary costly pile design. The Unified Design Method (UDM) for piles, developed by Fellenius (1988; 1997; 2004) corrects this misconception and considers capacity, NSF and settlement together in the same analysis. However, the Unified Design Method was supported by limited field test cases and more studies need to be conducted to verify the applicability of the Unified Design Method. This Chapter presents further verification of the Unified Deign Method through numerical FEM study. Geotechnical FEM software package, PLAXIS 2D, was utilized for the numerical investigations.

In this Chapter, the numerical tool was first calibrated against the centrifuge test data, presented by Shen (2008). Then, the verification of the Unified Pile Deign Method is conducted through numerical analyses. Finally, parametric studies were conducted to investigate the factors which affect the size of transition zone from NSF to positive skin friction.

6.2 CALIBRATION OF THE FEM MODEL

6.2.1 Centrifuge model test (Shen, 2008)

Three centrifuge model tests were conducted by Shen (2008) to investigate the mechanism of NSF on the single pile under different conditions: end-bearing pile, floating pile and socketed pile. The model hollow cylindrical aluminum pile was jacked in using displacement control, representing an installation of 16m of 1.28m diameter pipe pile with a wall thickness of 100mm through top 2m thick sand layer and 14m underlying thick soft clay. In the end-bearing pile model test, the pile toe went through the soft clay and was in contact with the underlying solid acrylic block. For the floating model pile, the pile was installed until the pile conical tip barely touched the base sand layer. While, for the socketed pile, the model pile was installed with 0.5D socket length into the base sand layer. Negative skin friction (NSF) was induced by three causes, re-consolidation of soft clay layer after installation, ground water drawdown and imposed surface surcharge loading. The model piles were instrumented with strain-gages placed at 7 different levels of the piles to measure the dragload distribution along the pile shaft. The setups of three centrifuge model tests are shown in Figure 6.1.

6.2.2 FEM mesh and soil properties

The axisymmetric configurations for the back-analysis of centrifuge model tests using

PLAXIS 2D are shown in Figure 6.2. The FEM mesh features 15-noded triangular elements with 12 Gauss points for numerical integration. Fine meshes are deployed adjacent to the pile. The soil profile is determined based on the soil condition presented in Figure 6.1. The ground water level was set initially at ground level. The interface elements are deployed along the pile-soil interface to simulate the pile-soil interaction. Consolidation is prohibited along both right and left boundaries, while the top surface and bottom allow dissipation of the excess pore pressure in the case of consolidation analysis.

The HS model is used in the calculation. The parameters for the different soil layers were given in Table 6.1, based on the FEM studies by Shen (2008). The pipe pile was modeled by an equivalent circular solid pile in axi-symmetry. The axi-symmetric model maintains the same perimeter as the pipe pile (so that unit shaft resistance is correctly estimated) and the same axial stiffness, EA, as the pipe pile. The linear elastic model was used to model the aluminum pile material. The equivalent $E = 1.17 \times 10^7 kPa$ for test pile, the equivalent volumetric weight $\gamma = 4.5 kN/m^3$ and a Poisson's ratio $v = 0.2$. For the case of end-bearing model pile test, the acrylic block was modeled as linear elastic material with $E = 3.1 \times 10^6 kPa$ and $v = 0.2$.

Table 6-1 Soil parameters for FEM back-analysis of NSF on piles (after Shen, 2008)

Parameter	Unit	Symbol	1-Top sand	2-Soft clay	3-Base sand	3*-Ridge Base
Type of behavior			Drained	Undrained	Drained	Nonporous
Dry weight	kN/m^3	γ_{unsat}	14.2	15.5	19.2	24
Wet weight	kN/m^3	γ_{sat}	18.2	15.5	19.2	24
Young's modulus	kN/m^2	E_{50}^{ref}	1.00E+04	4500	2.00E+05	3.1E+06
Oedometer modulus	kN/m^2	E_{oed}	1.00E+04	4720	2.00E+05	-
Power	-	m	0.5	1	0.5	-
Unloading modulus	kN/m^2	E_{ur}^{ref}	3.00E+04	1.20E+04	6.00E+05	-
Poisson's ratio		ν	0.20	0.20	0.20	0.2
Reference stress	kN/m^2	p	100	100	100	-
Cohesion	kN/m^2	c	0	0	0	-
Friction angle	°	φ	30	17.3	38	-
Dilatancy angle	°	ψ	0	0	0	-
Interface strength reduction	-	R_{inter}	0.9	1	-	-

6.2.3 Numerical procedure and results

The typical simulation procedure was adopted for the three centrifuge model tests, shown in Table 6.2. Not all of the centrifuge procedure was simulated for calibration of the numerical model. The installation effect of model pile was simulated by the numerical procedure proposed in Chapter 4. Since the pile shaft friction dominates the magnitude of the dragload, only horizontal prescribed displacement of 2% of the pile radius is applied to the pile shaft. For the simulation of water level drawdown, a new water table was explicitly defined in PLAXIS, causing an increment of effective vertical stress of 11 kPa in the soft clay layer.

The comparisons of numerical results of the dragload distribution along the pile shaft at end of water drawdown stage with the centrifuge test data are shown in Figure 6.3.

As can be seen, the numerical results capture the approximately the same neutral plane of the three kinds of pile conditions and showed good agreement with the measured dragload as well.

Table 6-2 FEM analysis phases for three centrifuge model tests

Phase No.	Description	Calculation type	Duration (days)
1	Simulation of the pile installation	Plastic	-
2	Lower down the ground water level by 2m	Plastic	-
3	Consolidation of the soft clay for 337 days for the excess pore pressure generated due to phase 1 and phase 2.	Consolidation	337

6.3 VALIDATION OF THE UNIFIED DESIGN METHOD FOR PILES

6.3.1 Problem definition and numerical procedure

The subsoil was divided into three layers. These are reclaimed fill, soft clay and underlying stiff clay. The reclaimed fill starts from ground surface to 3m depth. Soft clay is below the fill layer. The thickness of this formation is 12m. The stiff clay is below the soft clay layer. The water level is assumed at ground level. The reclaimed fill causes long term settlement in the soft clay layer by slow consolidation. The negative skin friction (NSF) is developed along the pile shaft due to this long term settlement. It is assumed that there is negligible settlement in the stiff clay layer. The bored pile is assumed 20m long with 5m socket into the stiff clay layer. Pile radius is chosen as 0.565m so that the pile section area is equal to $1\,m^2$ for convenience to get

load in kPa same as in kN in Plaxis plot of load vs movement of pile. The

$E = 2.5 \times 10^7 kPa$ for the concrete pile, with volumetric weight $\gamma = 24 kN/m^3$ and a

Poisson's ratio $v = 0.2$. The axisymmetric configuration for the calculations using

PLAXIS-2D is shown in Figure 6.4. Pile and soil are modeled using 15-noded

triangular elements with 12 Gauss points for numerical integration. The interface

elements are deployed along the pile-soil interface to simulate the pile-soil interaction.

The Hardening Soil (HS) model is used in the calculations and the parameters for the

different soil layer are shown in Table 6.3.

Table 6-3 Soil parameters for calculation

Parameter	Unit	Symbol	1- Reclaimed fill	2-Soft clay	3-Hard clay
Type of behavior			Drained	Undrained	Undrained
Dry weight	kN/m^3	γ_{unsat}	20	20	20
Wet weight	kN/m^3	γ_{sat}	20	20	20
Young's modulus	kN/m^2	E_{50}^{ref}	1.00E+04	7000	1.3E+05
Oedometer modulus	kN/m^2	E_{oed}^{ref}	1.00E+04	6962.5	1.3E+05
Power	-	m	0.5	1	1
Unloading modulus	kN/m^2	E_{ur}^{ref}	3.00E+04	2.10E+04	3.9E+05
Poisson's ratio		v	0.20	0.20	0.20
Reference stress	kN/m^2	p	100	100	100
Cohesion	kN/m^2	c	0	0	100
Friction angle	°	φ	35	22	30
Dilatancy angle	°	ψ	0	0	0
Interface strength reduction	-	R_{inter}	1	1	1

In order to investigate the effect of NSF on the pile behavior and verify the Unified

Deign Method for a single pile, the same FEM models with different magnitude of

NSF are considered. It is stated by Shen (2008) that the NSF on pile from the drained

analysis is approximately the same as that from the fully consolidated analysis, and

this is verified in his FEM analysis. In general, drained analysis takes less

computational time than consolidation analysis. Therefore, drained analysis was

adopted to compute the different magnitudes of NSF induced by different ground

settlements for the parametric study in section 6.4. The different ground settlements

can be simulated by input of fictitious value of unit weight of 3m reclaimed fill above

the soft clay layer. The ground settlements varied from 40mm to 245mm in the

numerical analysis. The pile behavior under long term working load (W.L.) condition

is examined. The cases for the pile under 1×W.L. and 2×W.L. with different ground

settlements were considered. The simulation procedures are given in Table 6.4.

Table 6-4 FEM analysis phases for investigation the effect of NSF on the pile behavior

-	Phase No.	Description	Soil behavior
Case 1	1	Pile installation and reclaimed fill loading after full consolidation (Final ground settlement *so*=40mm)	Drained
	2	Simulation of the pile load test	Undrained
Case 2	1	Pile installation and reclaimed fill loading after full consolidation (Final ground settlement=145mm)	Drained
	2	Simulation of the pile load test	Undrained
Case 3	1	Pile installation and reclaimed fill loading after full consolidation (Final ground settlement=245mm)	Drained
	2	Simulation of the pile load test	Undrained
Case 4	1	Pile installation and application of 4000 kN axial load on top of pile	Drained
	2	Reclaimed fill loading after full consolidation (*so*=40mm)	Drained
Case 5	1	Pile installation and application of 4000 kN axial load on top of pile	Drained
	2	Reclaimed fill loading after full consolidation (*so*=245mm)	Drained
Case 6	1	Pile installation and application of 8000 kN axial load on top of pile	Drained
	2	Reclaimed fill loading after full consolidation (*so*=40mm)	Drained
Case 7	1	Pile installation and application of 8000 kN axial load on top of pile	Drained
	2	Reclaimed fill loading after full consolidation (*so*=245mm)	Drained

6.3.2 Results and discussion

The axial load in the pile before the pile load test and the load-movement behaviors

from the simulation of pile load test under different amount of NSF (Case1 to Case 3)

are shown in Figure 6.5. As observed, the dragload, produced by NSF, increases as the

final ground settlement increases. The maximum dragload increases from 300kN to

900kN when ground settlement increases from 40mm to 245mm. The neutral plane

does not vary much from case 1 to case 3, and is approximately located at the interface

between the soft soil layer and the stiff clay layer, since there is little settlement in the

stiff clay layer. Although the pile experience different amount of dragloads, the

ultimate pile bearing capacity obtained from the simulation of pile load test is not

affected by the dragload (NSF). This agrees with the design concept of the Unified

Deign Method that NSF or dragload is not an external imposed load, and does not

diminish geotechnical axial load capacity of the pile.

The effects of NSF on the long term pile behavior under different top load are shown

in Figure 6.6 for case 4 to case 7, and Table 6.5. For the same ground settlement, when

the top load increases from 4000kN to 8000kN, the NP goes up and dragload (NSF)

reduces. The pile toe moved further down relative to the soil and larger toe resistance

was mobilized. For the same top load, when the ground settlement increases, from

40mm to 245 mm, the NP moves down and dragload (NSF) increases significantly.

The pile toe moves further down relatively to the soil and larger toe resistance

mobilizes. The length of the zone of transition from negative shaft friction to positive

shaft friction is more influenced by the ground settlement. Small ground settlement

results in a long transition zone and large ground settlement results in short transition

zone. Moreover, the location of NP is where the force equilibrium is achieved as well

as where there is no relative movement between for the pile and the soil for all cases. These behaviors obtained from FEM analysis showed good agreement with the Unified Design Method's basic principle and concept which are summarized in Chapter 2.

The Unified Design Method for single pile was implemented to determine the neutral plane and dragload of the situation of case 7. As mentioned in Chapter 2, the shaft resistance distribution, toe-movement response and the distribution of soil settlement need to be calculated or obtained from measurement results before the neutral plane and dragload can be correctly determined by the Unified Design Method. In this hypothetical case study, all of these were obtained from FEM results and shown in Figure 6.7. The toe-movement response was calculated based on drained condition of the soil, according to the drained penetration of the pile toe in case 7. However, in practice, the toe-movement response would be obtained from the undrained calculation or the results of ultimate pile load test with instruments to measure actual pile toe movement response. The distribution of soil settlement was obtained from the calculation of phase 2 in case 7 and the shaft resistance distribution was obtained from the simulation of the ultimate pile load test. After these three curves were plotted, the Unified Design Analysis can be conducted in an iterative procedure suggested by Fellenius (2011). The NP is assumed firstly at depth of 15m. From the toe-movement response curve, the toe load can be determined (900kN) to fit the NP location as settlement equilibrium. However, this value is not consistent with toe load determined

from the load distribution curve, which is much larger than 900kN. Thus, the NP assumed at 15m is wrong. Repeat this step, with the NP assumed at depth of 10m. The toe load, fitted the NP location as settlement equilibrium, but is much larger than that which fits the force equilibrium from the load distribution curve. After several trial-and-error steps, the NP is found at depth of 13m and the toe load is 2500 kN which fits both the settlement equilibrium and the force equilibrium from the load distribution curve. The maximum dragload is 9350kN. The axial load distribution obtained by the Unified Design Method was compared with that from FEM analysis, shown in Figure 6.8. The Unified Design Method gave almost the same location of NP as that from FEM analysis. However, the maximum dragload determined from the Unified Pile Design Method is overestimated by 22%, compared to the FEM result. This is because fully mobilized skin friction is assumed in the Unified Design Method while the FEM analysis shows that skin friction is not fully mobilized in the transition zone. This overestimated dragload will not affect the pile design significantly in this particular case. However, in the case with small soil settlements and very deep settling layer, the overestimated dragload based on the assumption of fully mobilized skin friction will result in over-sized costly pile design. As a result, the factors which affect the size of the transition zone of the NSF are investigated in detail in section 6.4.

Table 6-5 FEM analysis results for investigation the effect of NSF on the pile behavior

-	So (mm)	Top Load (kN)	Location of NP (m)	Max. Dragload (kN)	Length of the zone of transition (m)	Toe relative movement (mm)	Toe resistance (kN)
Case 4	40	4000	8.6	159	15	3.5	920
Case 5	40	8000	5	100	15	12	1950
Case 6	245	4000	14.5	1252	7.5	5.8	1220
Case 7	245	8000	12.5	1090	7.5	15	2400

6.4 MOBILIZATION OF NSF

6.4.1 FEM and analysis program

The FEM analysis presented in section 6.3 has demonstrated that the NSF around neutral plane is not fully mobilized. As a result, the maximum dragload will be overestimated when the Unified Design Method is used. The same phenomena have been observed by Shen (2008) based on his centrifuge model tests and the numerical analysis. This partial mobilization of NSF has been studied by several researchers (Poulos and Davis, 1980; Matyas and Santamarina, 1994; Fellenius, 2006; Shen, 2008). Based on their filed measurements and numerical analysis, the following factors have been considered to affect the mobilization of NSF at the NP in the transition zone of NSF:

The factors to consider are: magnitude of ground movement (or surcharge), the relative stiffness of the pile and the settling soil, and the pile length-diameter ratio.

It is found that the transition zone of NSF is dependent on the magnitude of ground

movement by Fellenius (2006) and Shen (2008). Small ground settlement results in a

long transition zone and large ground settlement results in short transition zone. This is

consistent with the FEM analysis presented in section 6.3. The effect of the relative

stiffness of the pile and the settling soil, and the pile length-diameter ratio are not well

understood. Poulos and Davis (1980) found from their analysis that these factors

which effect on the mobilization of NSF were small. However, these findings are not

consistent with those proposed by Matyas and Santamarina (1994) and Shen (2008),

where the relative stiffness of the pile and the settling soil and the pile length-diameter

ratio substantially affects the mobilization of NSF and the transition zone of NSF.

Moreover, the relative stiffness of the soil below pile toe and around the pile shaft may

also affect the mobilization of NSF.

In order to get better understanding of the mobilization of NSF, an extensive

parametric study was carried out with various pile-soil conditions. The basic FEM

model is the same as that used in section 6.3, and shown in Figure 6.9. The boundary

of the mesh is up to 2 times the pile length to avoid the boundary effects. Four factors

are considered in the study. First, the different ground settlements or surcharges can be

simulated by input of a fictitious value of unit weight of the 3m reclaimed fill above

the soft clay layer. The surcharges used are from 15kPa to 60kPa, resulting in ground

settlements from 250mm and 1000 mm. Second, the relative stiffness of the pile and

the settling soil is used as that proposed by Poulos and Davis (1980),

$$K = \frac{E_p R_A}{E_{s1}}$$ (6.1)

where E_p is the Young's modulus of the pile, E_{s1} is the Young's modulus of the soil

around pile shaft, R_A is the pile section ratio which is unity for solid pile.

Since the NSF problem applies in soft soils which possess relatively low stiffness, the

modulus of the soft soil used a typical low value of 2000 kPa. The modulus of the

concrete pile, E_p, would be in the range 1.5E+7< E_p<3.0E+7 kPa. To simplify the

problem, only solid pile is considered in the study. As a result, the pile-soil stiffness

ratio K as defined as Eq.6.1 would to be in the range 7500<K<15000. Third, pile

length-diameter ratio is defined as L/d, where L and d are the pile length and the pile

diameter respectively. A short pile is assumed 20m long with 5m socket into the stiff

clay layer. The diameter is chosen as same as that in the section 6.3, 1.13m, resulting

in the pile length-diameter ratio of 17. A relatively long pile has L=35 m with 5m

socket into the stiff clay layer and d=1.13m, resulting in L/d ratio of 31. The last factor

is the relative stiffness of the soil below pile toe and around the pile shaft. It is defined

as E_{s2}/E_{s1}, where E_{s2} and E_{s1} are the Young's modulus of the soil below pile toe and

around pile shaft respectively. E_{s2}/E_{s1} ratio is varied from 5 to 100 which represents

floating pile to end bearing pile. For given L/d and surcharge, 12 cases were analyzed

for cases involving these ranges, as presented in Table 6.6. The same analysis program

was conducted with the L/d varying from 17 to 60, while the ground settlements vary

from 250mm and 1080 mm.

Table 6-6 FEM analysis program for given L/d and surcharge

Group	No	E_p (kPa)	E_{s1} (kPa)	E_{s2} (kPa)	K	E_{s2}/E_{s1}
	1			10000		5
Group 1	2	3e7		2e4	15000	10
	3			2e5		100
	4			10000		5
Group 2	5	2.5e7		2e4	12500	10
	6		2000	2e5		100
	7			10000		5
Group 3	8	2e7		2e4	10000	10
	9			2e5		100
	10			10000		5
Group 4	11	1.5e7		2e4	7500	10
	12			2e5		100

6.4.2 Results and discussion

The factor, η, the degree of mobilization of NSF, is introduced to evaluate the mobilization of NSF. η is defined as,

$$\eta = \frac{P_{n,mob}}{P_{n,\beta}} \tag{6.2}$$

where $P_{n,mob}$ is the mobilized maximum dragload at the neutral point (NP). $P_{n,\beta}$ is the calculated maximum dragload at the neutral plane based on the β method. As mentioned in Chapter 2,

$$P_{n,\beta} = \int_0^{Zn} \beta\sigma'_v dz \tag{6.3}$$

where Z_n is the depth of NP, $\beta = K_s \tan\delta$, K_s =lateral stress coefficient; δ =pile-soil friction angle. For the present numerical analysis, $\beta = 0.3$.

The axial load distribution along the pile shaft under various pile-soil conditions are

shown in Figure 6.10. Only the results of pile-soil stiffness ratio K=15000 (Group 1) are presented in Figure 6.10 for clarity of presentation. It should also be noted that the axial load (dragload) along the pile shaft was normalized by the maximum dragload at the intersection of soft clay layer and stiff clay layer, $P_{\beta\max}$, calculated by the β method and the depth z was normalized by the length of the soft clay layer. The normalized axial load distribution calculated by the β method was also plotted in Figure 6.10. As can be seen, for all the cases, the normalized dragload is less than that calculated by the β method near the NP. For the short pile (L/d=17), the magnitude of ground settlement has a dominant effect on the mobilization of NSF, compared with the E_{s2}/E_{s1} ratio. This is because the pile penetration due to the dragload does not change significantly with the E_{s2}/E_{s1} ratio under same surcharge. The NP is approximately the same for all the cases of the short pile (L/d=17) at the interface of the soft clay layer and the stiff clay layer. For the relatively long pile (L/d=31), the maximum dragload increases with the magnitude of ground settlement under the same E_{s2}/E_{s1} ratio. This is the same trend as the short pile. However, the substantial reduction of the maximum dragload was observed when the E_{s2}/E_{s1} ratio decreases (Figure 6.10 (b)). The reason for this phenomenon is that the pile penetration due to the dragload tends to substantially increase as the E_{s2}/E_{s1} ratio decreases, resulting in the NP moving upwards and a decrease in dragload. The NP is approximate at 30 m, which is the interface of the soft clay layer and the stiff clay layer, for the cases with $E_{s2}/E_{s1} \cong 50$. When the E_{s2}/E_{s1} reduces to 5, the NP moves up to approximate 24 m. The location of NP tends to depend only on the E_{s2}/E_{s1} ratio and is not much affected

by the magnitude of ground settlements as shown in Figure 6.10 (b).

The results of all the analyses on values of η, the degree of mobilization of NSF, and the location of NP, for various magnitude of ground settlements, pile-soil stiffness ratio K, L/d and E_{s2}/E_{s1}, the relative stiffness of the soil below pile toe and around the pile shaft are summarized in Figures 6.11 to 6.12. The general findings based on the numerical analysis are:

(1) For the same magnitude of ground settlement, for short pile, the degree of mobilization of NSF (η) is not affected by the pile-soil stiffness ratio K, as shown in Figure 6.11 (a) and (b). This is consistent with findings from Poulos and Davis (1980). However, for long piles as in Figure 6.11 (c), the degree of mobilization of NSF (η) slightly increases with pile-soil stiffness ratio K, which is consistent with the finding from Shen's numerical analysis (Shen, 2008). For the same ground settlement, the effect of E_{s2}/E_{s1} ratio on the degree of mobilization of NSF (η) also seems to be generally small, as shown in Figures 6.11 (a) to (c). However, there is a discernible trend of decreasing (η) with increase of E_{s2}/E_{s1} ratio for long piles.

(2) The location of NP is above or at the interface of soft clay layer and stiff clay layer for all cases. The E_{s2}/E_{s1} ratio dominates the location of the NP, and it is not sensitive to the pile-soil stiffness K ratio. The NP moves down to the interface of soft clay layer and stiff clay layer when the E_{s2}/E_{s1} ratio increases. This is more obvious for long piles than short piles (comparing Figure 6.12 (a) to Figure 6.12 (c)).

227

Generally speaking, the degree of mobilization of NSF (η) increases with decrease in L/d ratio, that is larger (η) for shorter piles. The effect of the pile-soil stiffness ratio K on (η) is small, but is more obvious for long piles than short piles. The E_{s2}/E_{s1} ratio has minor influence on the degree of mobilization of NSF (η), but influences the location of NP. The degree of mobilization of NSF (η) varies over wide ranges from 0.3 to 0.82 under different pile soil conditions and ground settlement. Moreover, the degree of mobilization of NSF (η) increases with time since the magnitude of ground settlement has the most dominant effect on it. As full consolidation is assumed for all cases studied, the degree of mobilization of NSF obtained from the current analysis is the final value. For those pile in very thick soft layer, the consolidation usually takes a very long time to complete due to low permeability of the clay and long drainage path. As a result, the degree of mobilization of NSF may not achieve the final value in its working life. Thus, the partial mobilization of NSF on the maximum dragload needs to be considered properly, especially for those cases with large L/d ratio and very thick soft clay layer, with small magnitude of ground settlements.

In order to capture the partial mobilization of NSF in design, a simple approach is desirable. The magnitude of ground settlement (S_0) has the dominated effect on the degree of mobilization of NSF (η). For the same L/d ratio, the degree of mobilization of NSF (η) increases with the magnitude of ground settlement (S_0). However, this is not consistent in the cases with different L/d ratio. For example, the degree of

mobilization of NSF (η) in case of the smaller magnitude of ground settlement (S_0) in

L/d=17 is larger than that in case of larger magnitude of ground settlement (S_0) in

L/d=60. This is because that when L/d ratio increases the thickness of soft clay layer

also increases. When the degree of mobilization of NSF (η) is plotted against the

magnitude of ground settlement (S_0) normalized by the soft clay thickness (H_s) in

Figure 6.13, a consistent trend is observed. A simple correlation involving normalized

ground settlement (S_0/H_s) provides an approximately hyperbolic (Eq 6.4) fit to the

degree of mobilization of NSF (η) calculated in all 192 cases studied (Figure 6.13).

$$\eta = \frac{s_0/H_S}{0.015 + s_0/H_S} \qquad\qquad (6.4)$$

6.5 CONCLUSION

Numerical analyses have been conducted to validate the Unified Deign Method on

determination of NSF on single pile using FEM geotechnical software package,

PLAXIS 2D.

Firstly, FEM model is properly well calibrated against a good set of centrifuge model

test data. Based on this FEM model, the verification of the Unified Deign Method is

conducted through numerical analyses. From the results of numerical analysis, it is

found that the ultimate pile bearing capacity obtained from the simulation of pile load

test is not affected by the dragload (NSF). The neutral plane (NP) location is the

position where the force equilibrium is attained, as well as where there is no relative movement between the pile and soil. The NP will always develop in piles with NSF. The NP goes up when the top load on the pile head increases and goes down when the ground settlement (or surcharge) increases. These behaviors obtained from FEM analysis showed agreement with the Unified Design Method's principles and concept.

Secondly, the Unified Design Method was implemented to determine the neutral plane and the dragload. The Unified Design Method gave almost the same location of NP as that from FEM analysis for soft clay layer on a stiff soil. However, the maximum dragload determined from the Unified Design Method is always overestimated, compared to the FEM result.

Finally, the FEM analysis shows that skin friction is not fully mobilized near the NP and the extensive parametric study was carried out to study the partial mobilization of NSF (η) under various pile-soil conditions. The design charts are proposed for preliminary evaluation of the degree of mobilization of NSF (η). The Unified Design Method with consideration of such degree of mobilization of NSF (η) near the NP will give more economical design of piles subjected to NSF, especially for those cases with large L/d ratio and small magnitude of ground settlements.
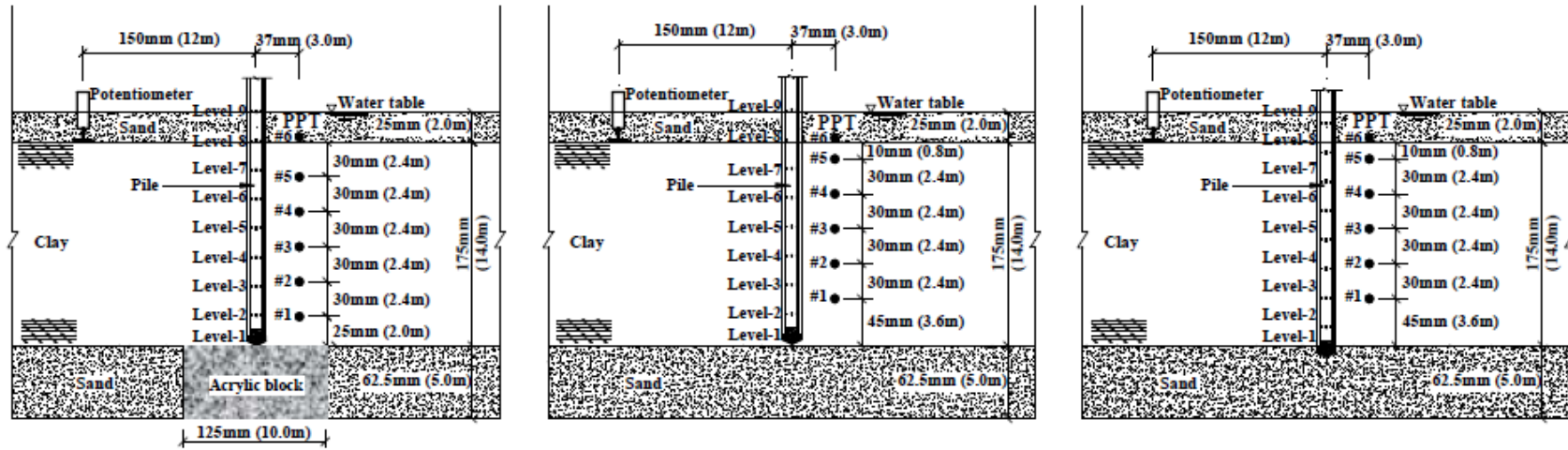
(a) Test ES: end-bearing single pile   (b) Test FS: floating single pile   (c) Test SS: socketed single pile

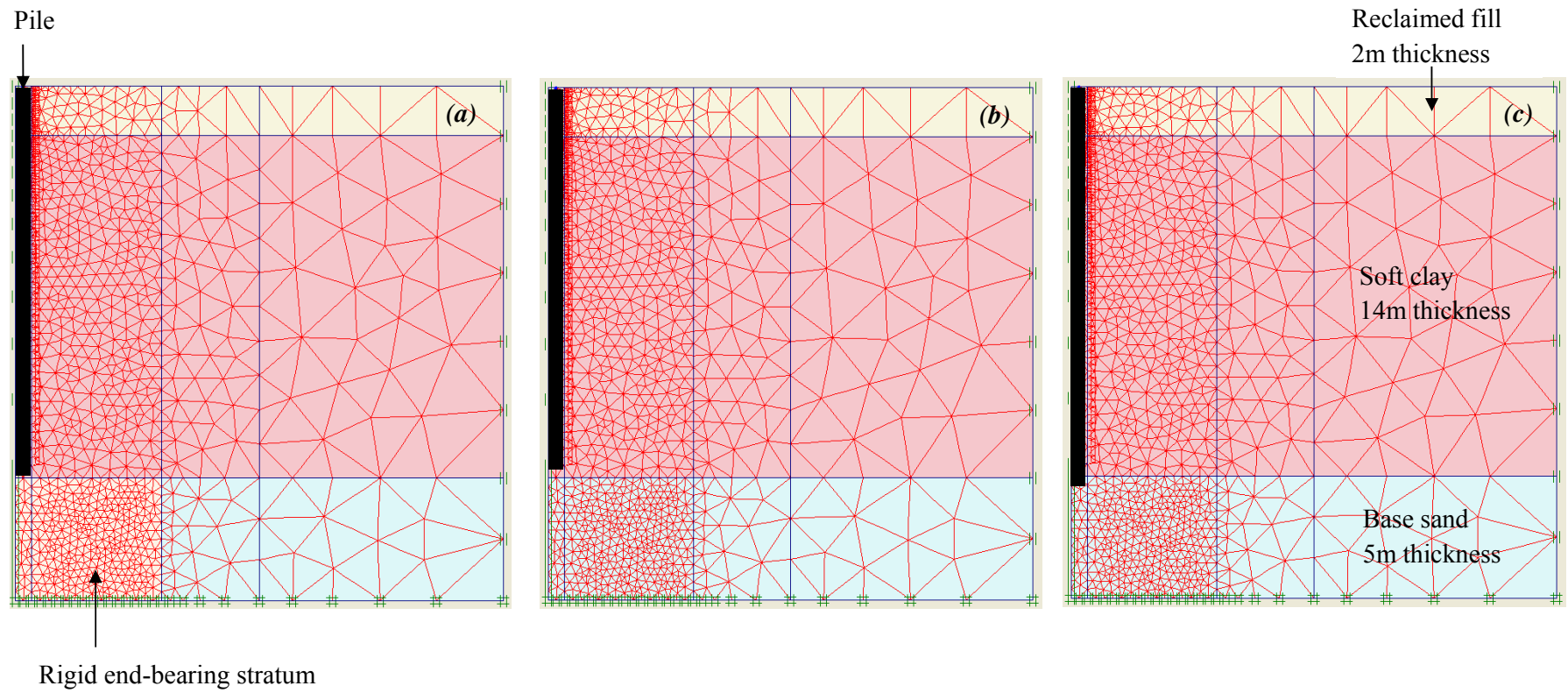Figure 6-1 Model test configurations for three centrifuge tests (Shen, 2008).

Pile

Reclaimed fill
2m thickness

(a)

(b)

(c)

Soft clay
14m thickness

Base sand
5m thickness

Rigid end-bearing stratum

Figure 6-2 FEM mesh for simulations of NSF on different pile conditions (a) End-bearing pile (b) Floating pile and (c) Socketed pile.
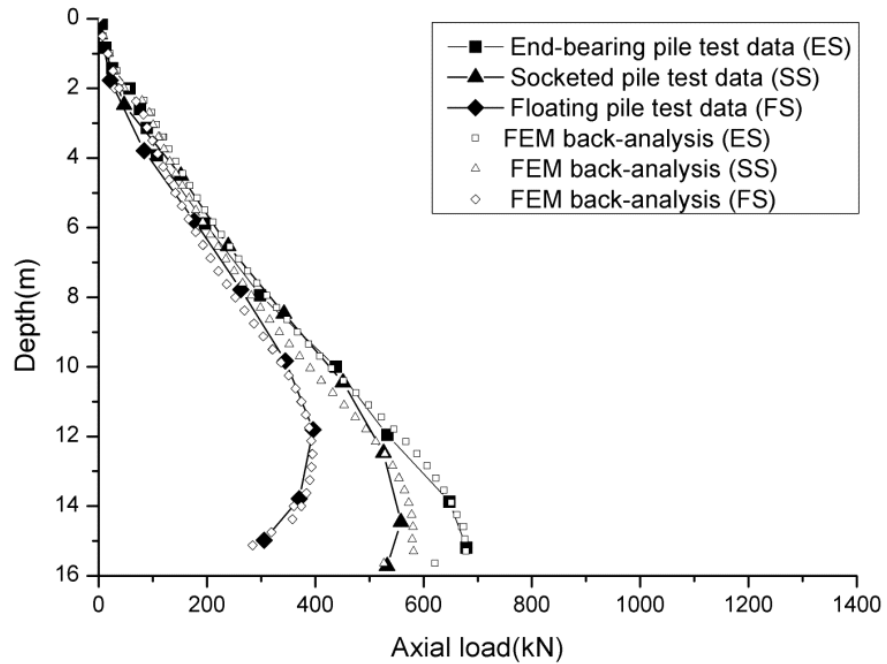
Figure 6-3 Comparison of the measured dragload distribution along the pile shaft at end of water level drawdown with FEM results.
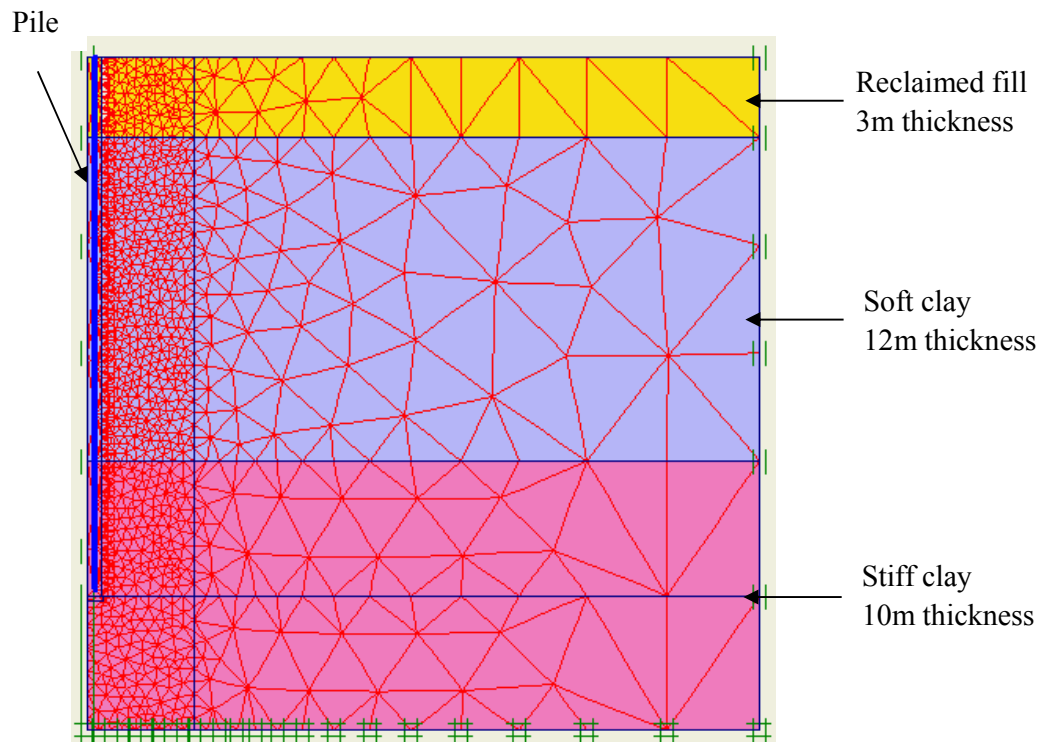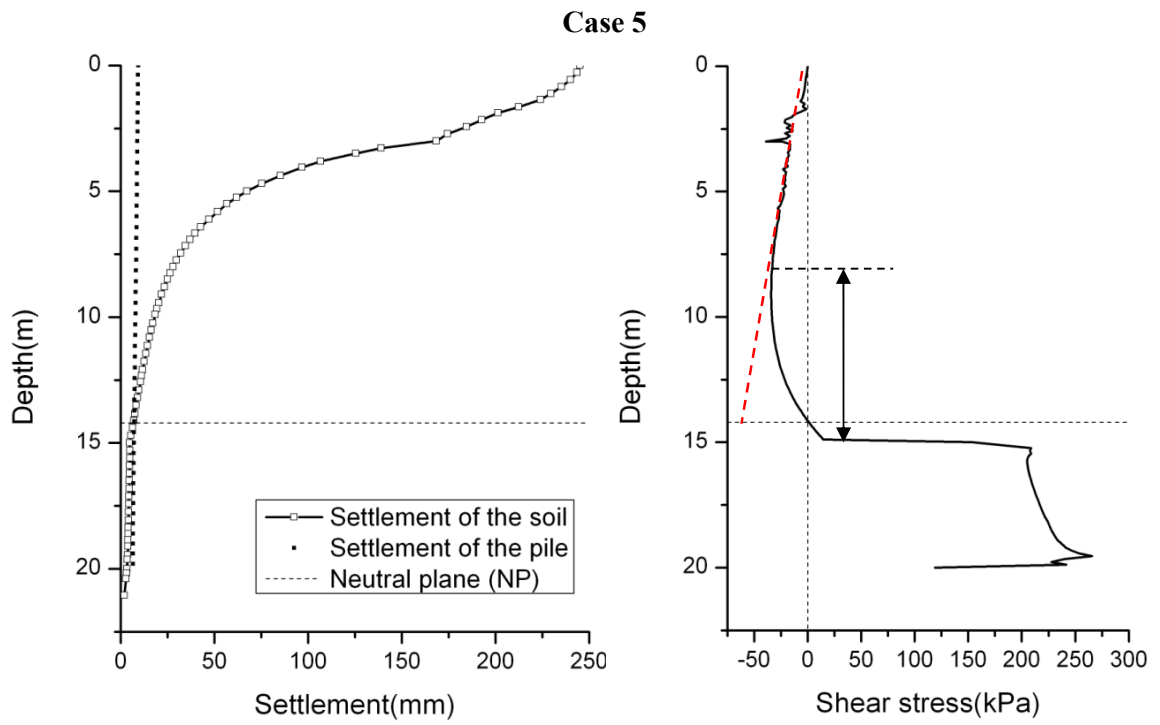

Figure 6-4 FEM mesh for the validation of the Unified Design method.
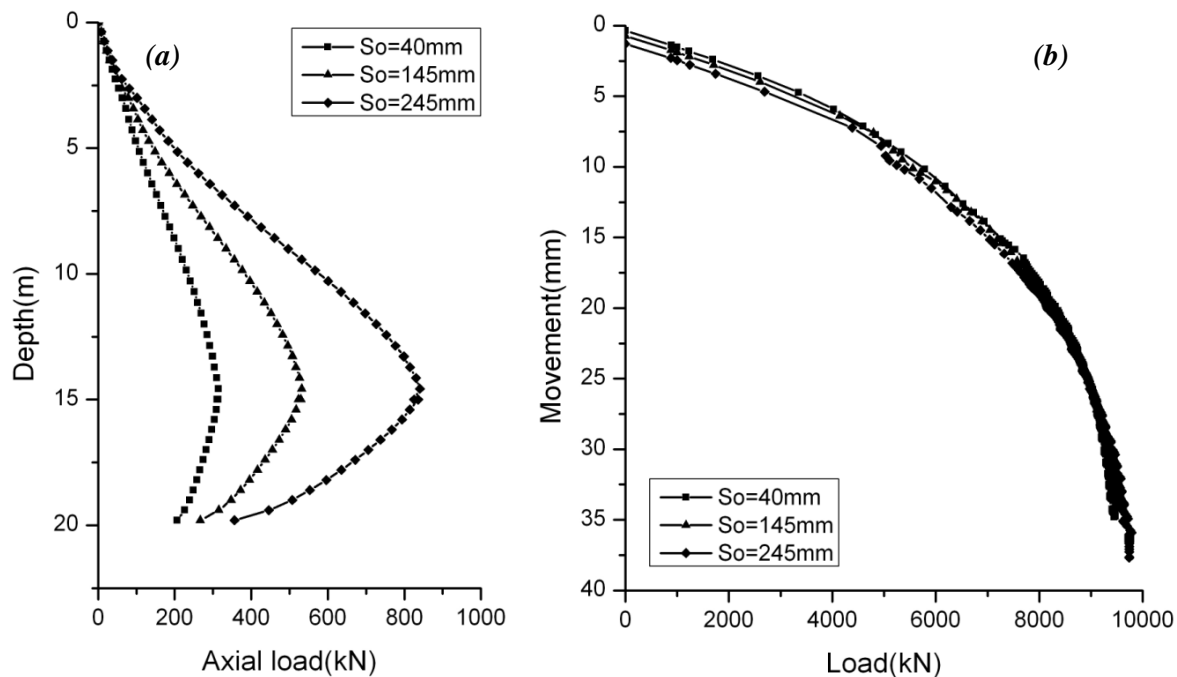
Figure 6-5 FEM results from Case 1 to Case 3 (a) the distribution of dragload and (b) the load-movement curve for simulation of pile load test.

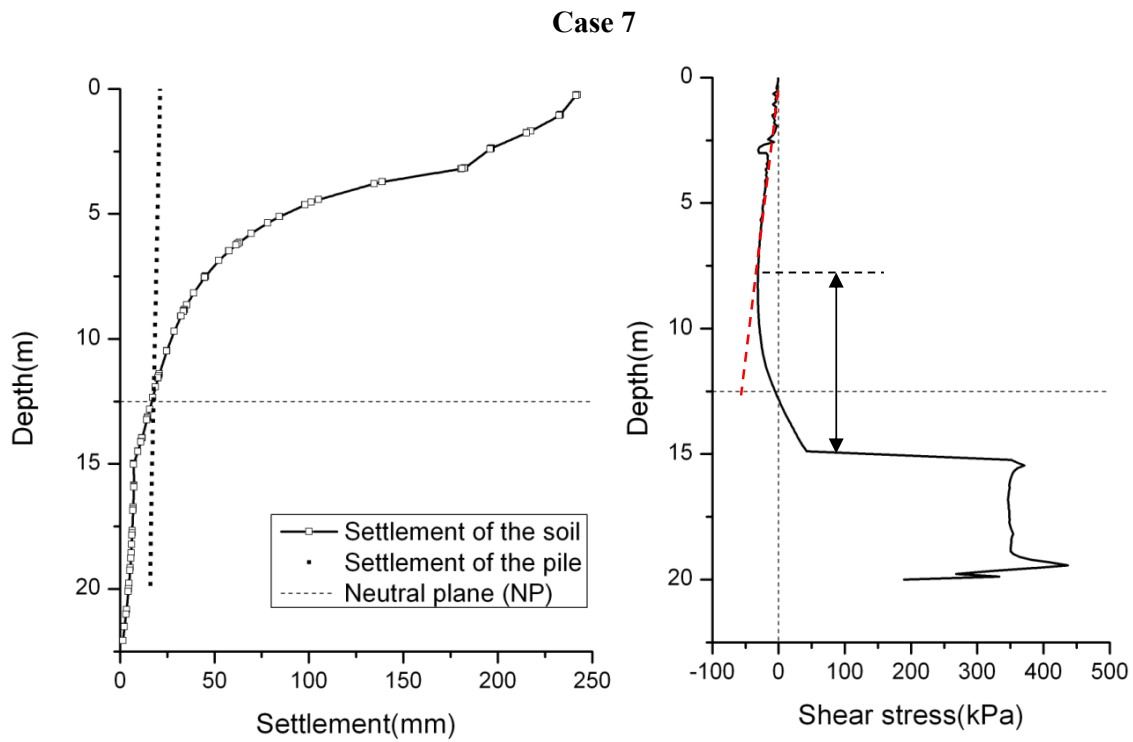**Case 4**

Case 5

Case 6
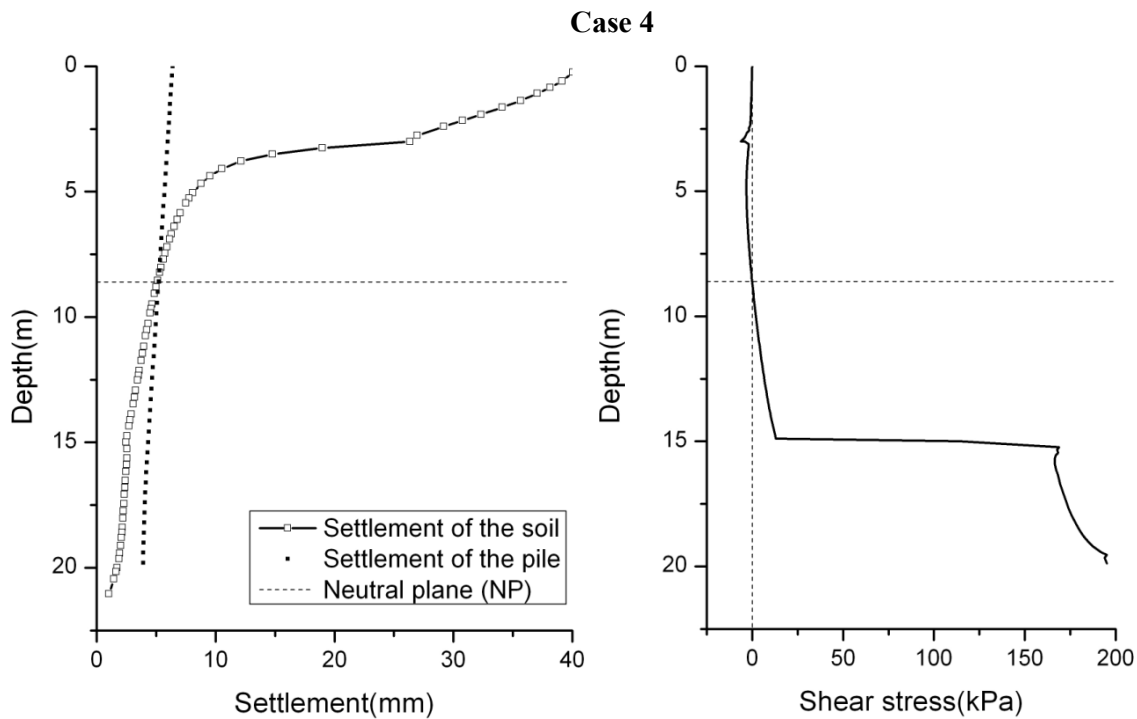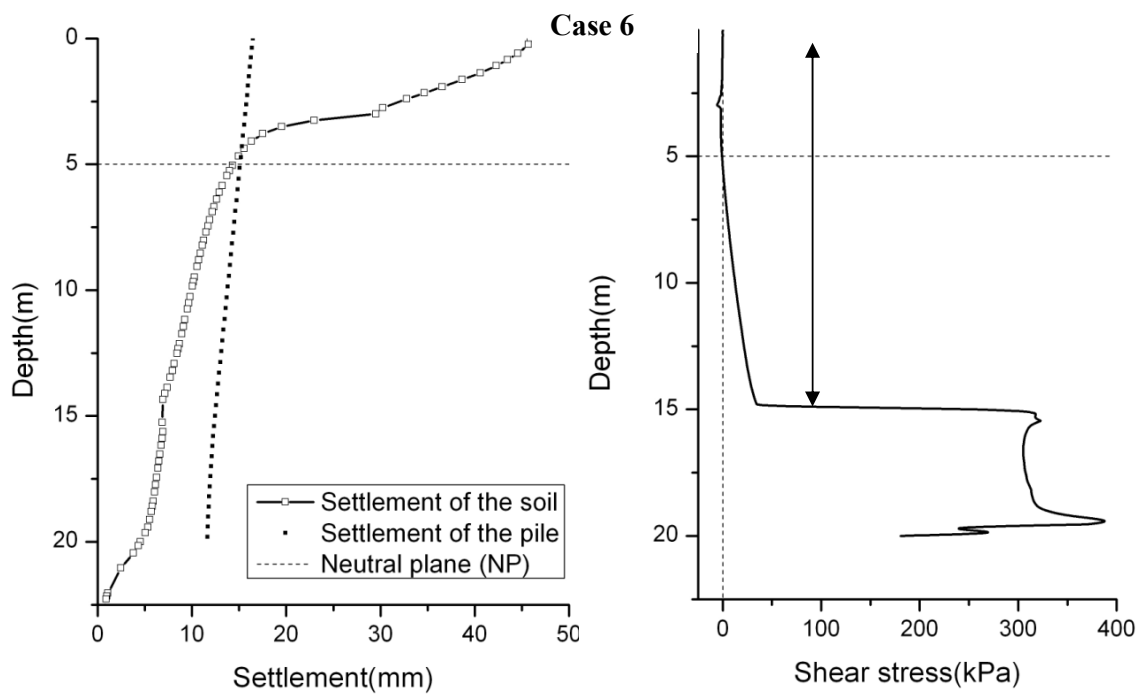
Case 7

Figure 6-6 Distribution of soil and pile settlement and distribution of shear stress along the pile shaft for Case 4 to Case 7.
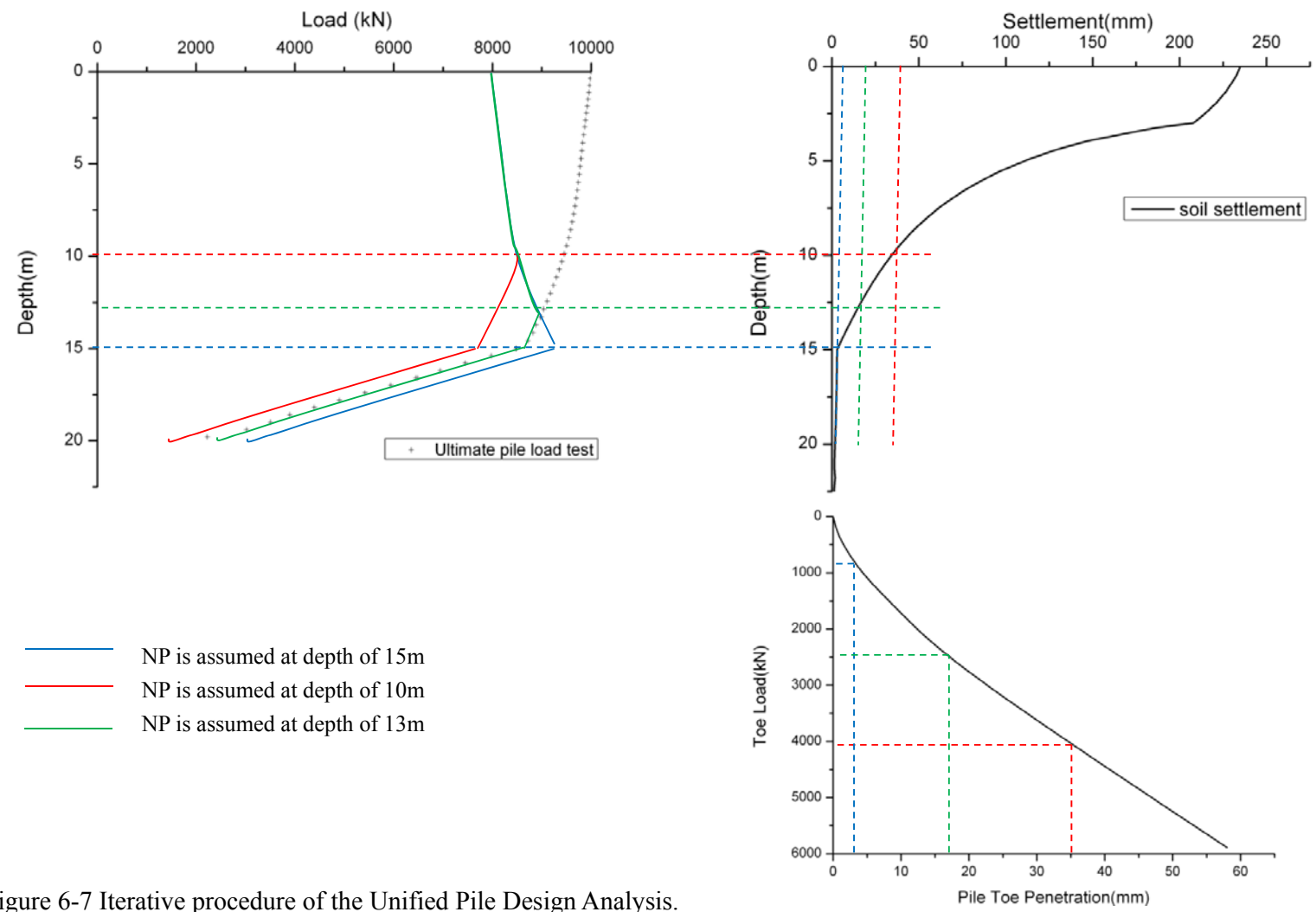
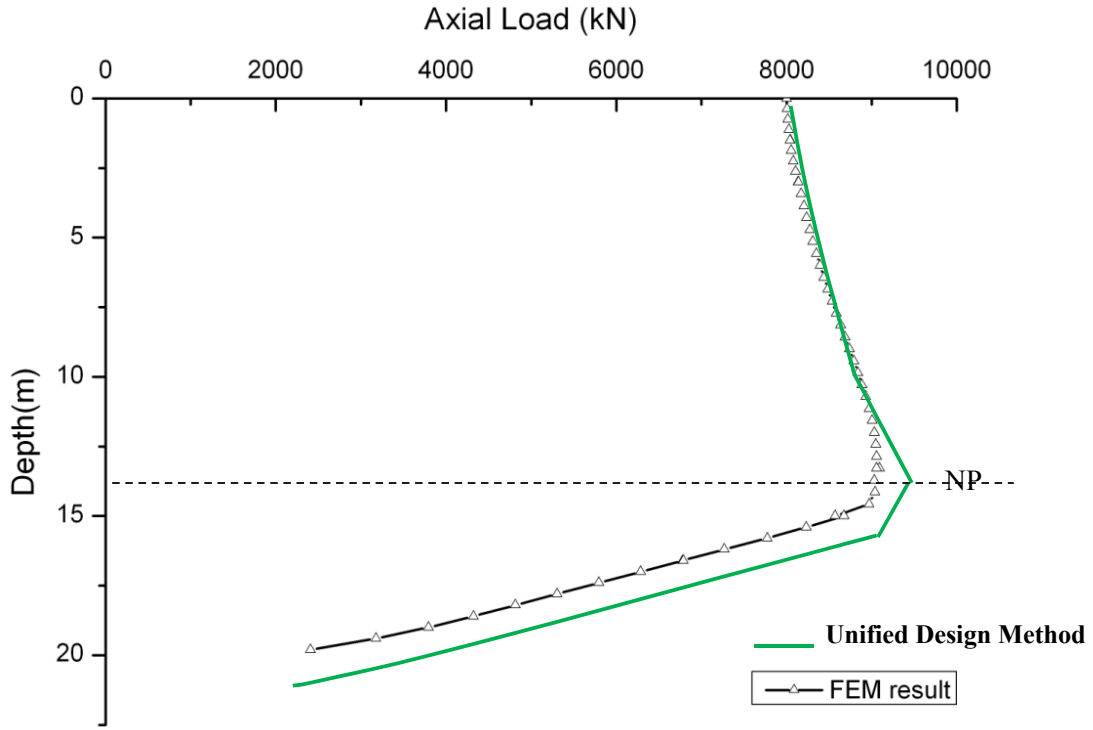Figure 6-7 Iterative procedure of the Unified Pile Design Analysis.

Figure 6-8 Axial load distribution obtained by the Unified Design method, compared with FEM results.
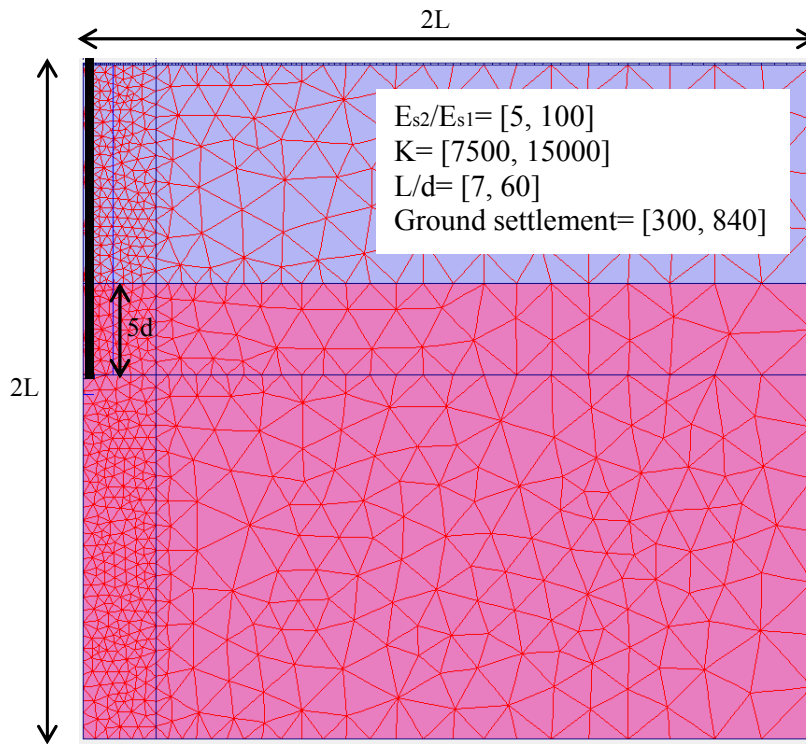

Figure 6-9 FEM mesh for simulations of NSF under various pile-soil conditions.
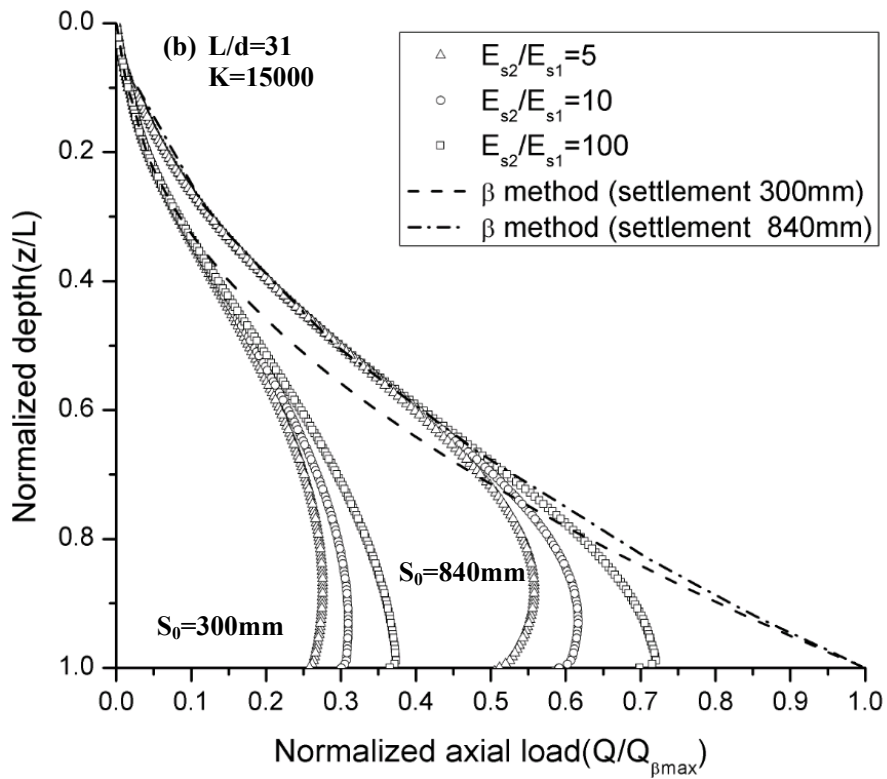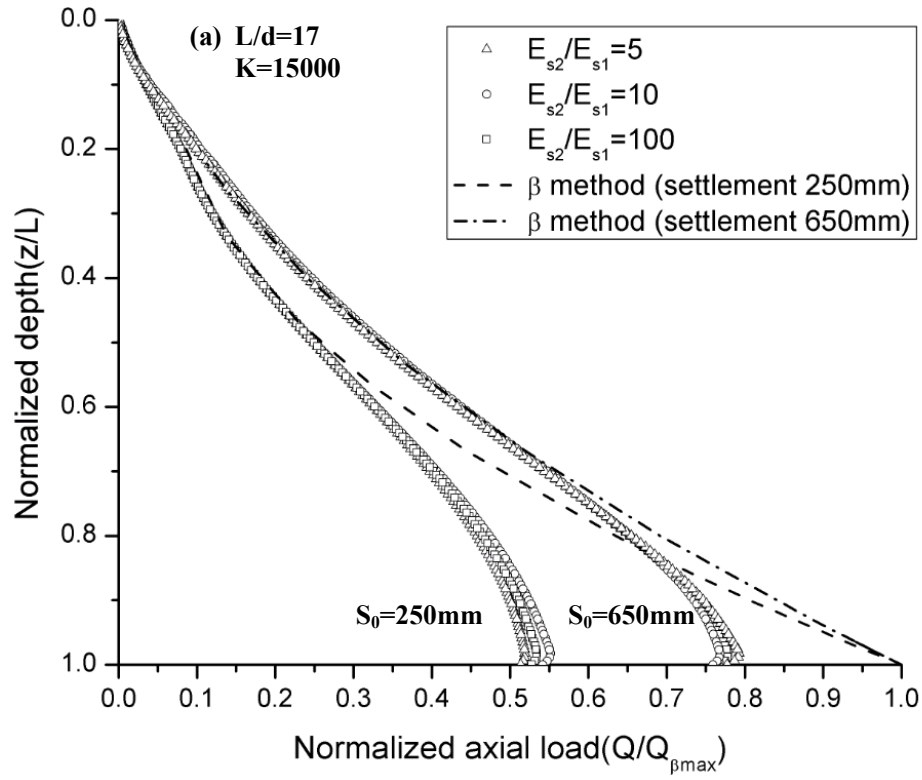
Figure 6-10 Normalized dragload distributions for (a) short and (b) relative long pile under various ground settlements.
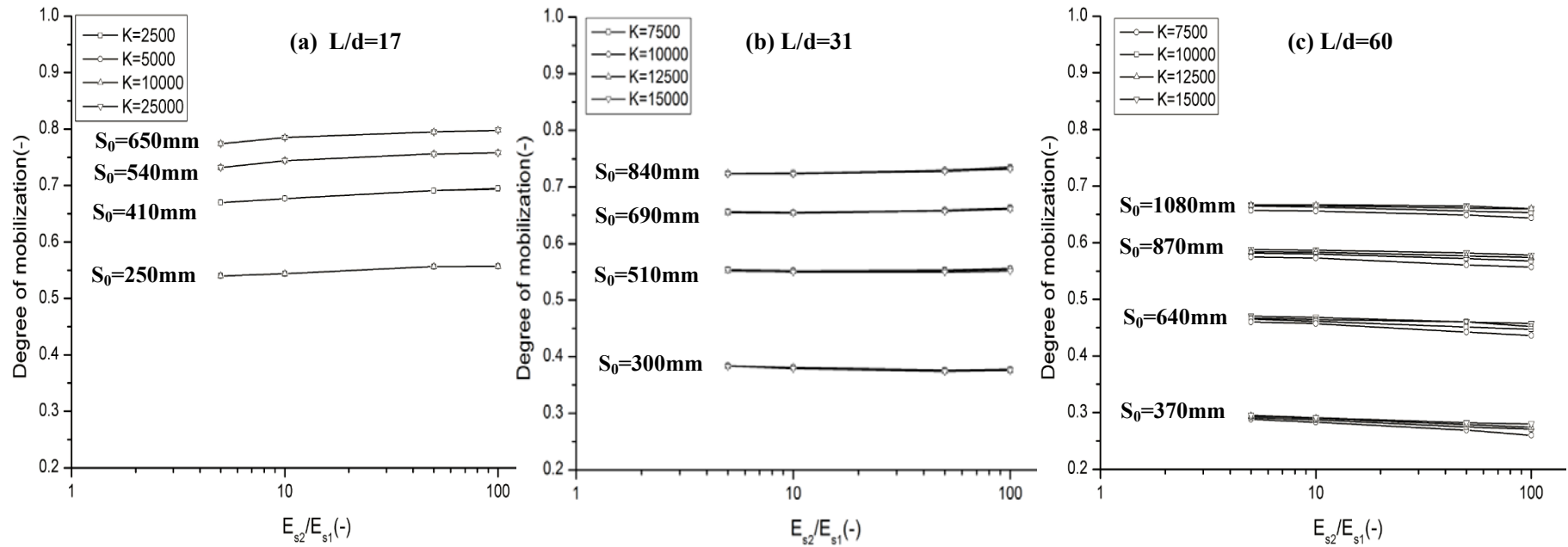
Figure 6-11 Variation on NSF degree of mobilization with L/d, K, E_{s2}/E_{s1} and ground settlement,S_o.

(b) L/d=31

(a) L/d=17

(b) L/d=31
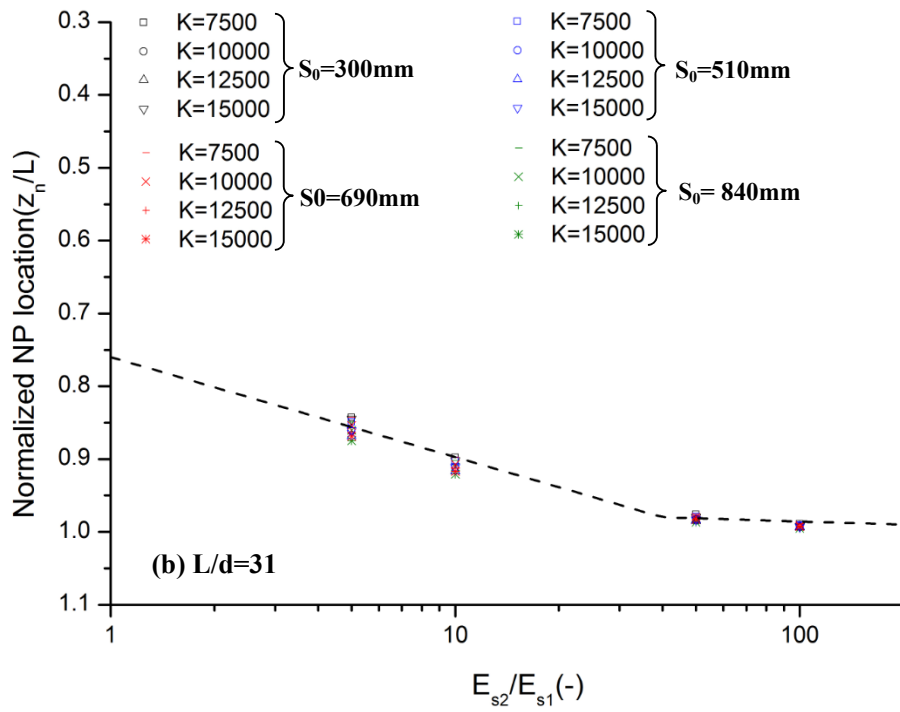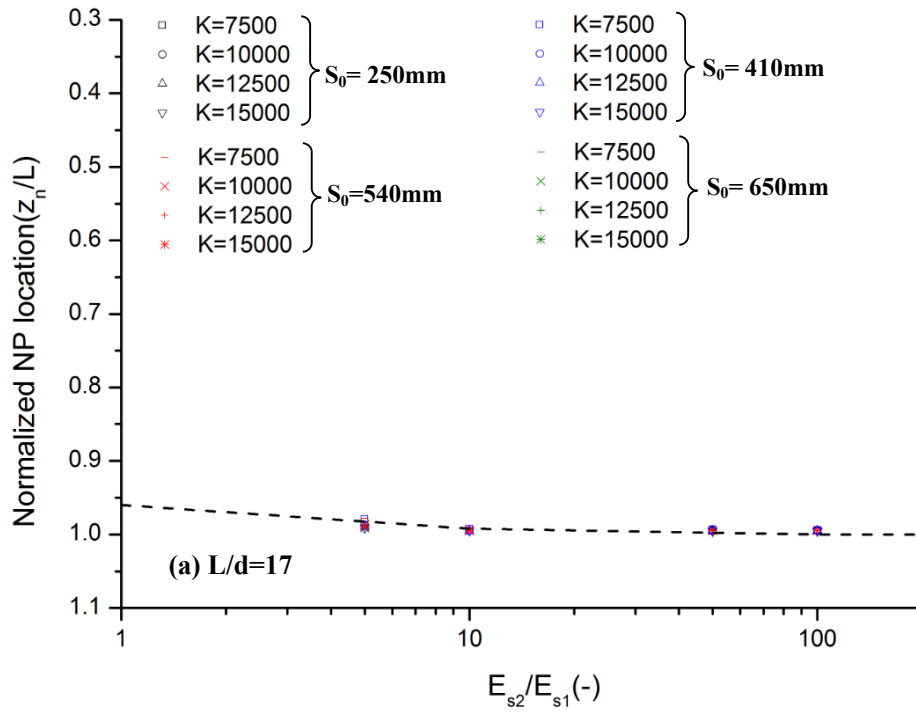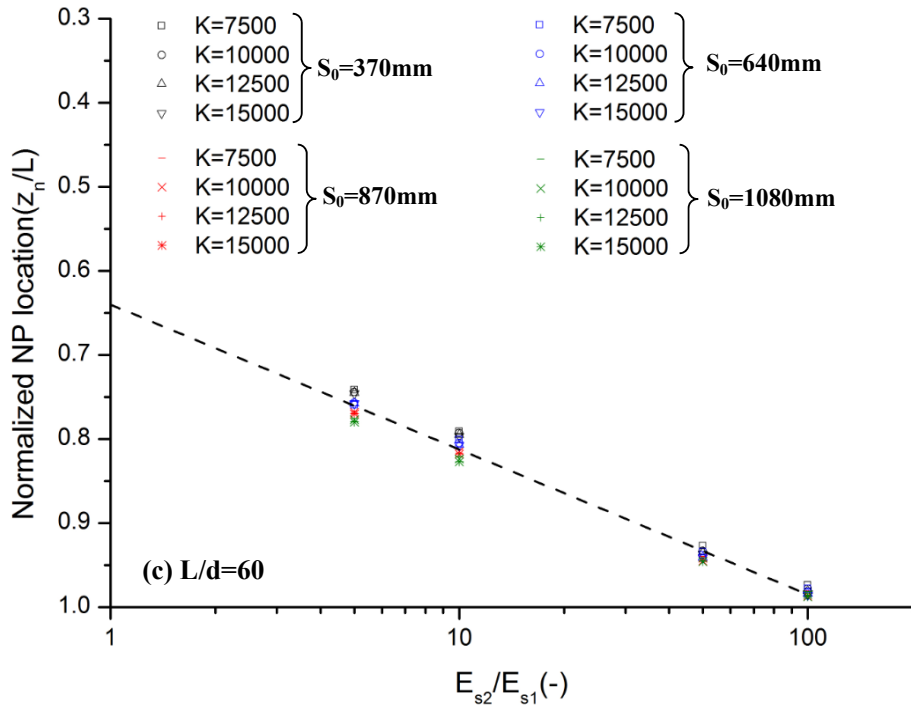
Figure 6-12 Variation on NP location with L/d, K, E_{s2}/E_{s1} and ground settlement.
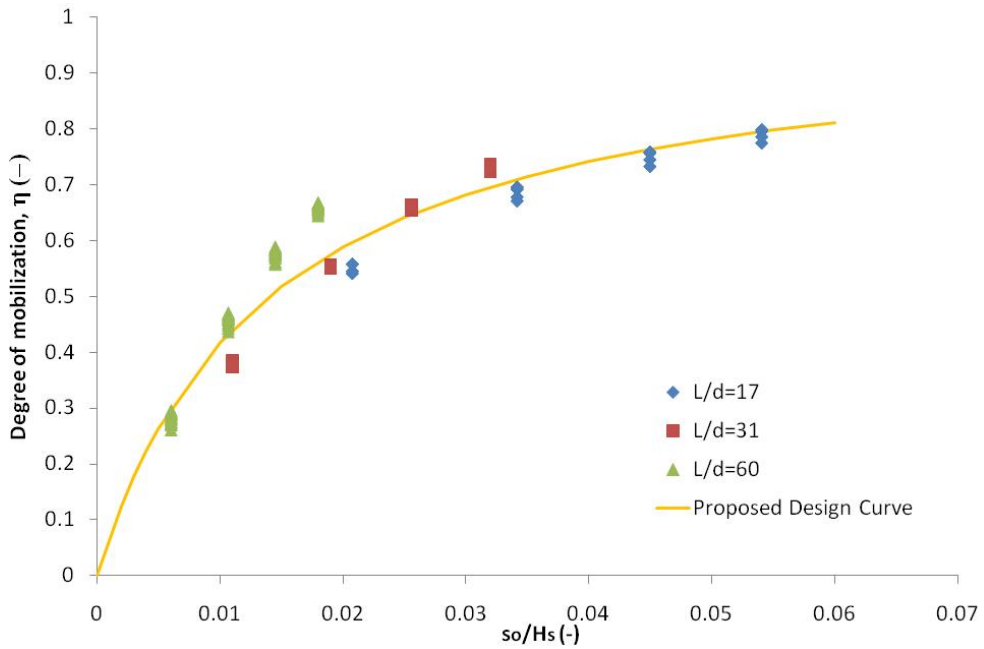

Figure 6-13 Tentative correlation for degree of mobilization.

CHAPTER 7 CONCLUSION AND RECOMMENDATION

7.1 INTRODUCTION

These main conclusions from each phase of research are presented. These conclusions are followed by some recommendations for future research.

7.2 CONCLUSION

This thesis provides an investigation of numerical modeling of a single pile behavior. Factors affecting the behavior of axially loaded pile, including constitutive soil models, installation method (particular attention is given to Jack-in method only), negative skin friction and interface, are investigated by using FEM and the FEM results together with full scale pile load tests performed in Tuas View have shown the following:

a) Compared to the MC model, more advanced features of HS model (including the cap type yield surface and a cone type yield surface; stiffness is stress-dependent and distinguishes between 'primary loading' and 'unloading'/'reloading) allow the HS model to simulate more realistic soil behavior and the HS model is superior to the MC model for modeling displacement pile.

b) The enhanced hypoplastic model for incorporating the structure effects into hypoplasticity opens a way to model the strain softening behavior of pile-soil interface. This behavior is important to simulate strain softening response in shaft friction produced by piles in structure sensitive soils

c) An improved numerical procedure was proposed to model the installation effect of Jack-in pile. The numerical study shows that applying horizontal

prescribed displacement to the pile shaft gives a reasonable distribution of the normal effective stress around the pile shaft at end of installation, while applying the simple vertical prescribed displacement to the pile tip to simulate the installation effect gives unreasonable behavior of shaft friction near the pile tip. Therefore, the spherical cavity volumetric expansion is applied to the soil cluster below the pile tip instead of the vertical prescribed displacement; and the horizontal prescribed displacement is applied at the interface between pile and soil along the pile shaft similar to Broere & van Tol's procedure. This approach produced a more correct distribution of shaft resistance all way to the toe of the pile, unlike the incorrect response of much reduced shaft friction near the pile toe produced by the vertical prescribed displacement method.

d) A series of full scale Jack-in pile tests was conducted at Tuas View. The soil condition around the test piles is very similar as shown in detailed insitu site measurements. A significant increase in the cone resistance was observed in the sand fill layer after piles installation. The magnitude of the increase of the cone resistance reduces for soil further away from the center of the piles. However, the cone resistance did not change significantly in the soft marine clay layer and the sandy silt layer after installation, due to generation of excess pore pressures in undrained loading.

e) The pile load tests indicated that the ultimate bearing capacity of Jack-in pile increases as the Jack-in force increases. Generally, the pile developed larger stiffness response in the load-movement curve when it is installed by larger jack-in force. However, the test piles showed approximately the same load-movement curve under 2 times working load for all three test piles. The difference in behaviors between test piles is caused by the difference in the toe

stiffness response of each test pile. Due to the Jack-in construction method, at start of the static load test, the toe was already subjected to residual loads and the load-movement curve displays an initial steep reloading portion when pile is loaded after installation. The larger the Jack-in force, the larger the volumetric compression of the bulb of soil below the toe of the piles. As a result, the larger reloading portion around pile toe causes the larger stiffening effect in pile response.

f) The independent data obtained from pile load test provided the validation of the general applicability of the proposed numerical procedure for simulation of installation effects. The results show that amount of cylindrical cavity expansion by prescribed outward radial displacement at pile shaft to induce approximately correct soil setup is about 2% to 4% of pile radius in sand layer. The soil setup is dependent on the elapsed time after installation in clayey soils due to radial reconsolidation around pile shaft. The setup of end bearing is correctly modeled by spherical cavity volume expansion. The spherical cavity volume maybe defined by the limit pressure of the spherical zone proposed by Randolph (1994). The approximate amount of volumetric strain to apply is dependent upon jack-in force used in pile installation. From the field trials, it appears to be about 70% to 150% for 1.5 W.L. to 2.25 W.L. as the applied jack-in force of the test piles.

g) The ultimate pile bearing capacity is not affected by the dragload (NSF). The NP goes up when the top load on the pile head increases and goes down when the ground settlement (or surcharge) increases. These behaviors obtained from FEM analysis showed agreement with the Unified Design Method's principle and concept.

h) The Unified Design Method was implemented to determine the neutral plane and the dragload. The Unified Pile Design Method gave almost the same location of NP as that from FEM analysis for soft clay on stiff soils. However, the maximum dragload determined from the Unified Pile Design Method is always overestimated, compared to the FEM result.

i) The extensive parametric FEM study of revealed that skin friction is not fully mobilized near the NP. The Unified Pile Design Method with consideration of such degree of mobilization of NSF near the NP will give more economical design of piles subjected to NSF, especially for those cases with large L/d ratio and small magnitude of ground settlement.

7.3 RECOMMENDATION FOR FUTURE WORK

a) Present numerical study shows pile setup is dependent on the elapsed time after installation in clayey soil due to radial reconsolidation around pile shaft. Unfortunately, the pile load test was not conducted repeatedly at different times after installation owing to limited time and cost in field work. A confirmation of such numerical inferences using field test data of good quality is needed.

b) Although an improved numerical procedure has been proposed to consider the installation effects based on available centrifuge test data and field data, there is still a lack of data for its universal applicability. Further research therefore is needed to perform more tests with different piles, different installation methods and different soil conditions.

c) Since the goal of this thesis is to improve the accuracy of the design of single axially load pile, only single pile case is considered here. However, it is

interesting to study whether the proposed improved numerical procedure could be used to simulate installation effect of pile group. Further research could be done to test the applicability of the procedure in pile groups.

d) As shown in Chapter 5, the amount volumetric strain applied to simulate the installation effect to the pile toe is dependent upon jack-in force. It requires further investigation to define the nature of this relationship.

e) The design chart proposed for evaluation of the degree of mobilization of NSF was based on numerical study in Chapter 6. Therefore, to verify the predictive performance, good quality field test data are required to test the universal applicability of the design chart.

APPENDIX A
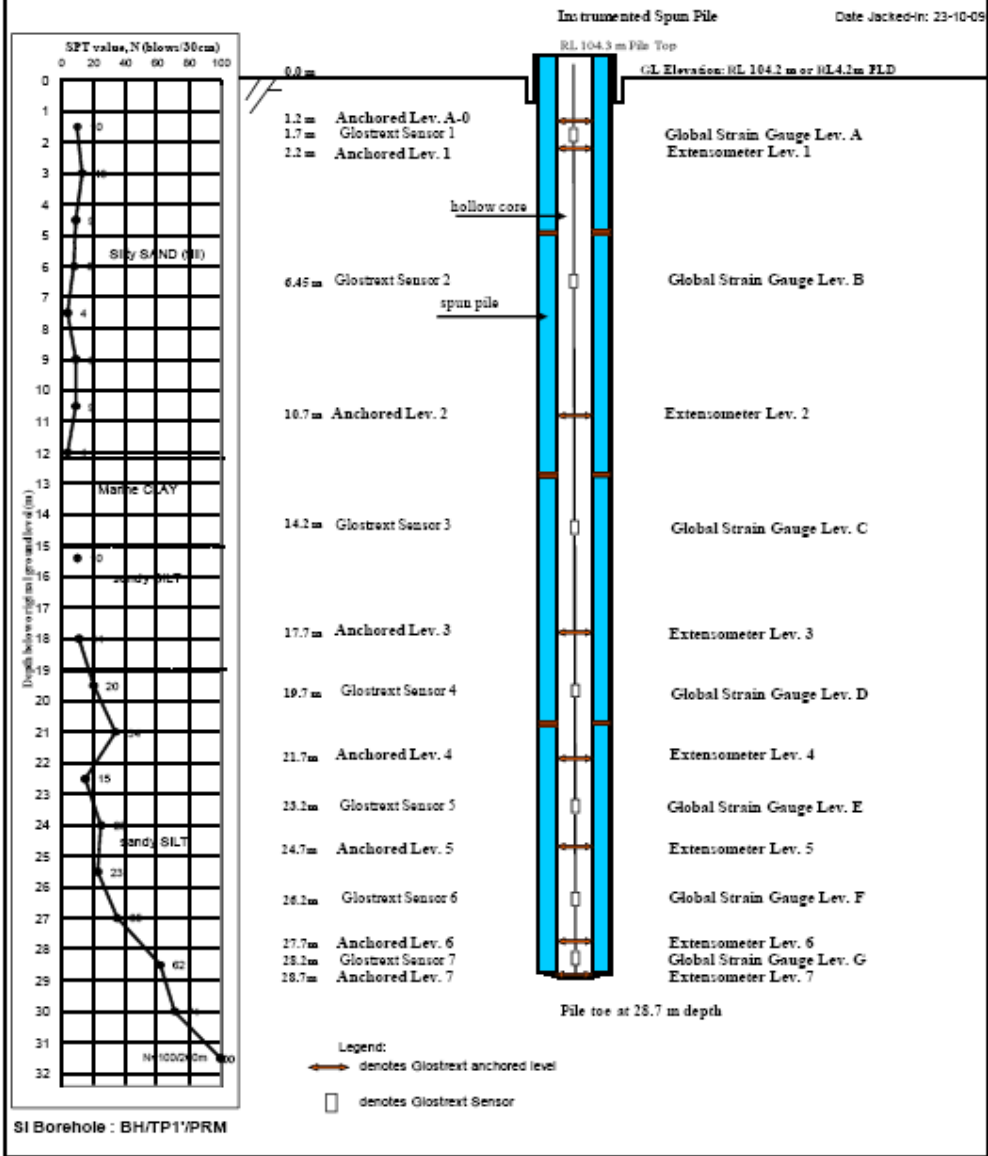
Instrumentation levels for Instrumented Test Pile

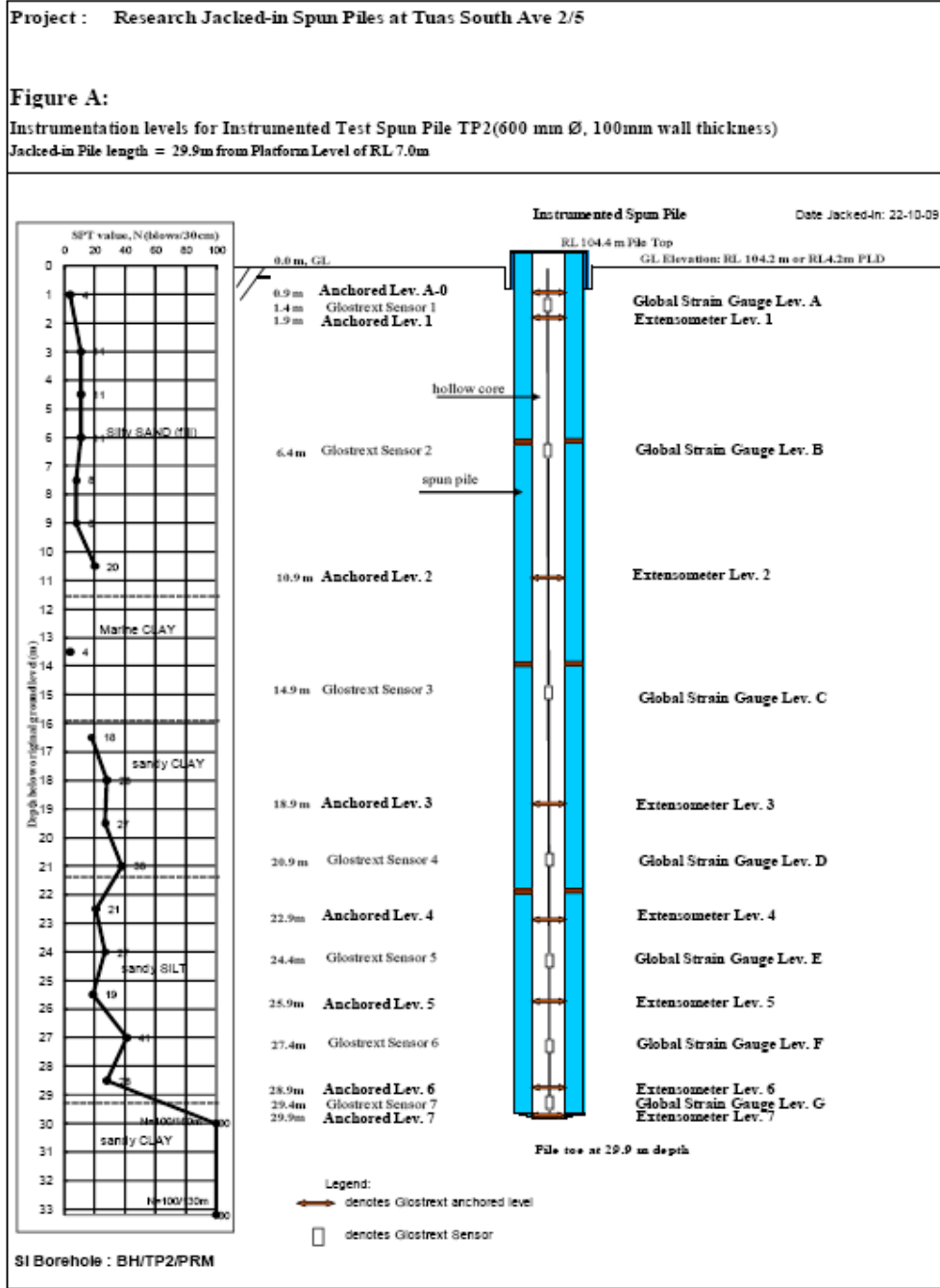Figure A-1 Instrumentation levels for Instrumented Test Pile TP1

Figure A-2 Instrumentation levels for Instrumented Test Pile TP2
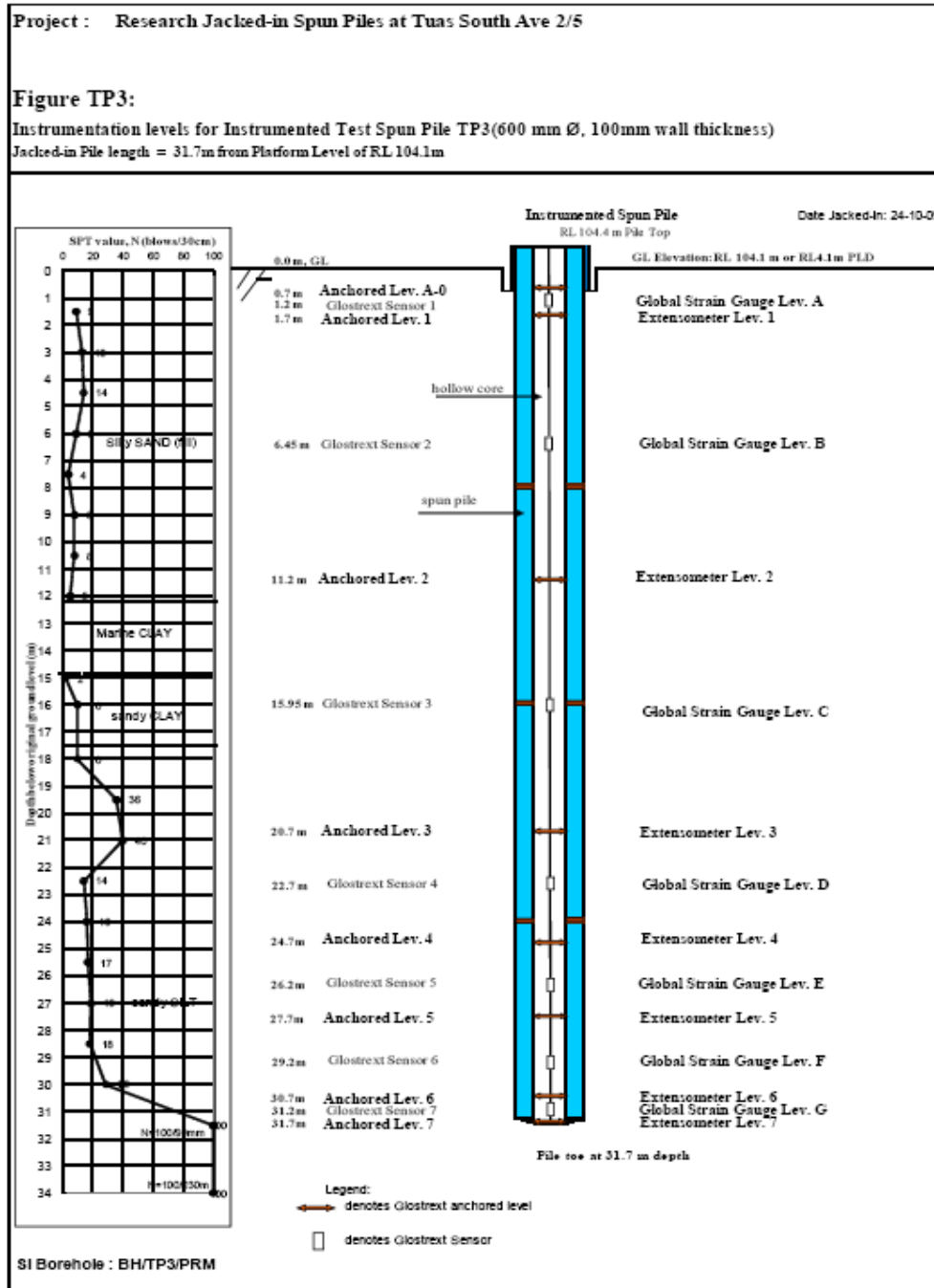
Figure A-3 Instrumentation levels for Instrumented Test Pile TP3

APPENDIX B

Load-strain curves for each gage level

1st cycle

2nd cycle
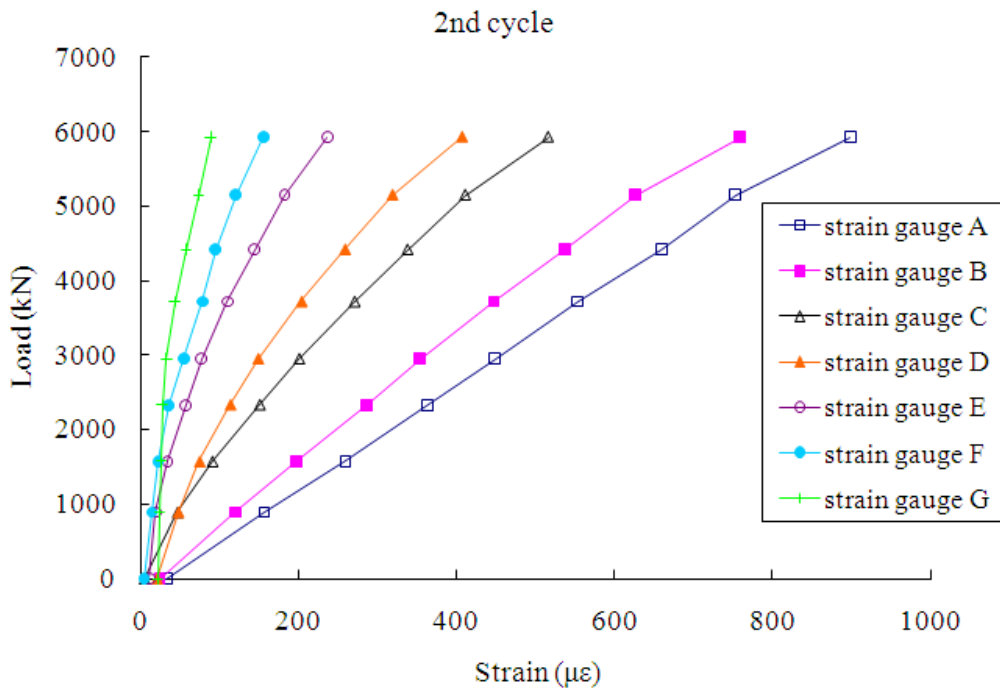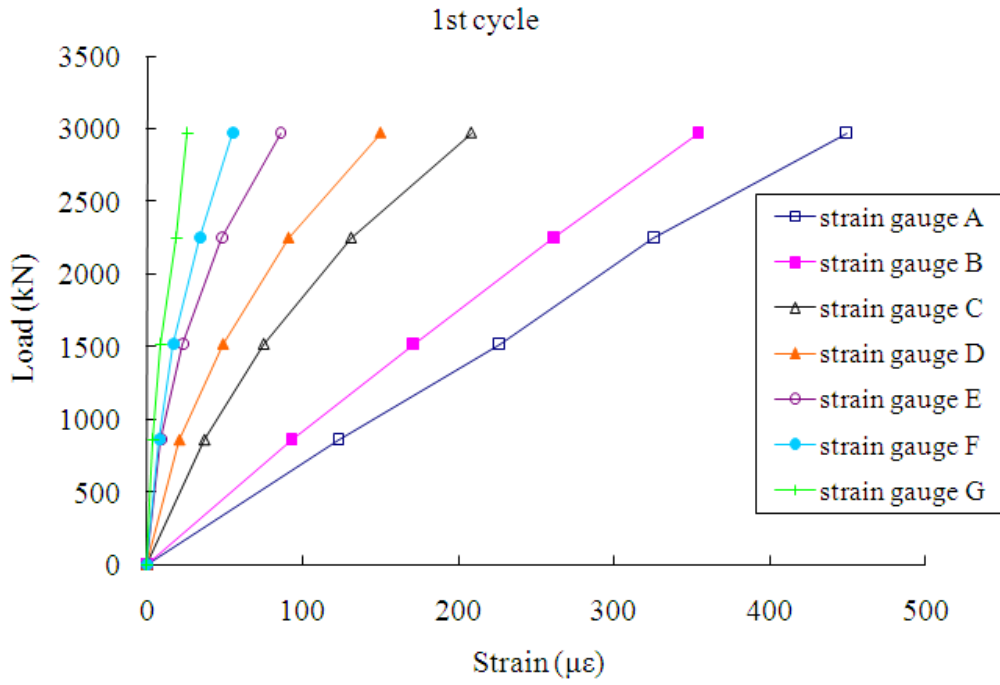
Figure B-1 Load-strain curves for each gage level as measured for TP1.

1st cycle

2nd cycle

3rd cycle

Figure B-2 Load-strain curves for each gage level as measured for TP2.

1st cycle

2nd cycle

3rd cycle

Figure B-3 Load-strain curves for each gage level as measured for TP3.

APPENDIX C

Pressremeter Test and numerical simulation

Figure C-1 Pressuremeter test result and numerical simulation for PMT at BH1(33.0m).
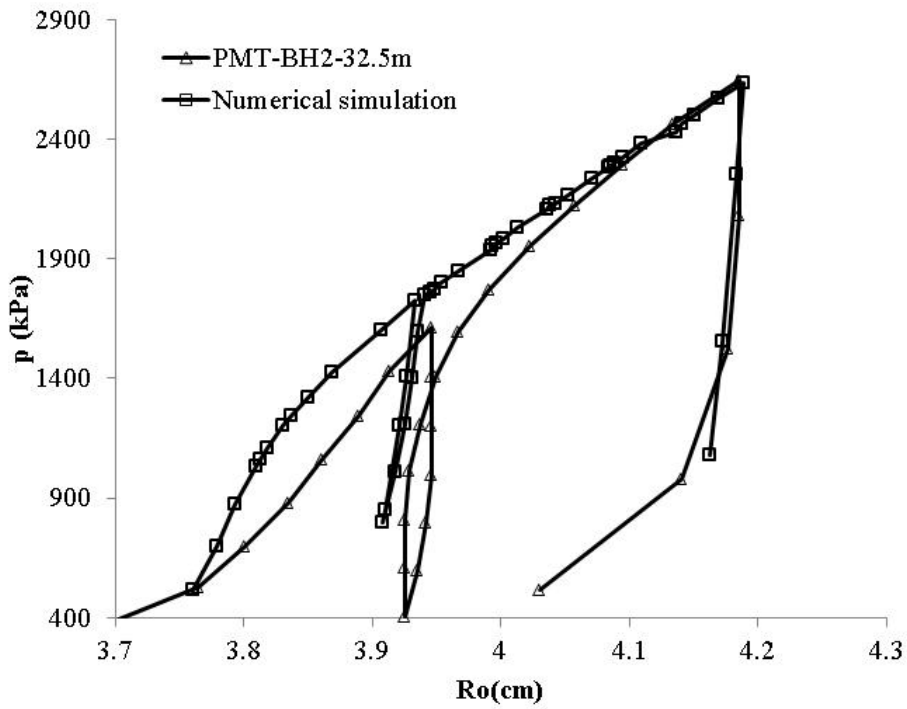
Figure C-2 Pressuremeter test result and numerical simulation for PMT at BH2(32.5m).
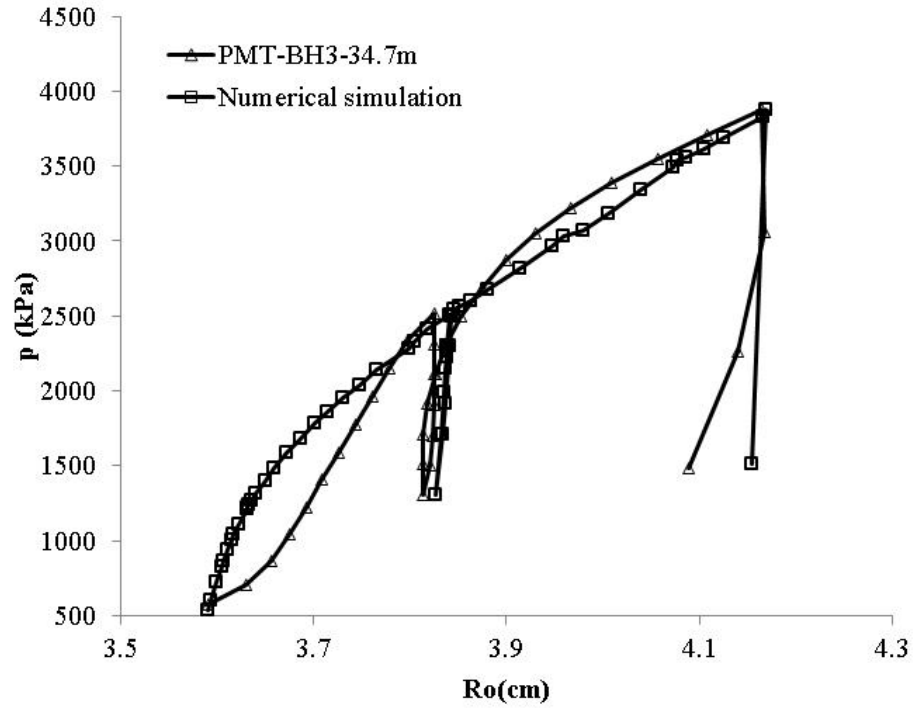
 Figure C-3 Pressuremeter test result and numerical simulation for PMT at BH3(34.7m).

REFERNCE
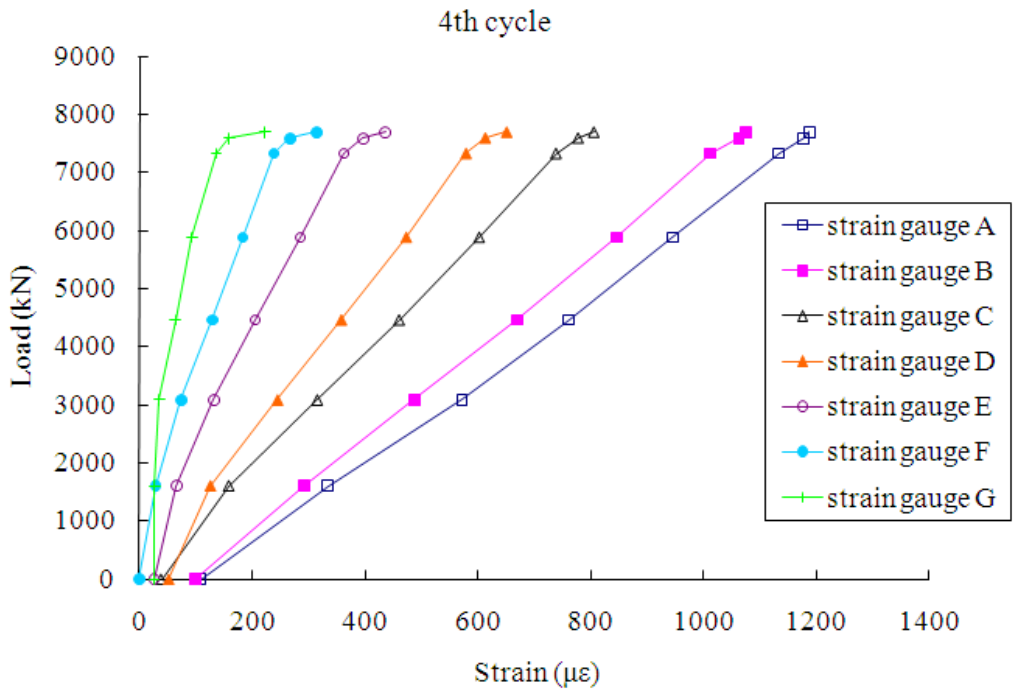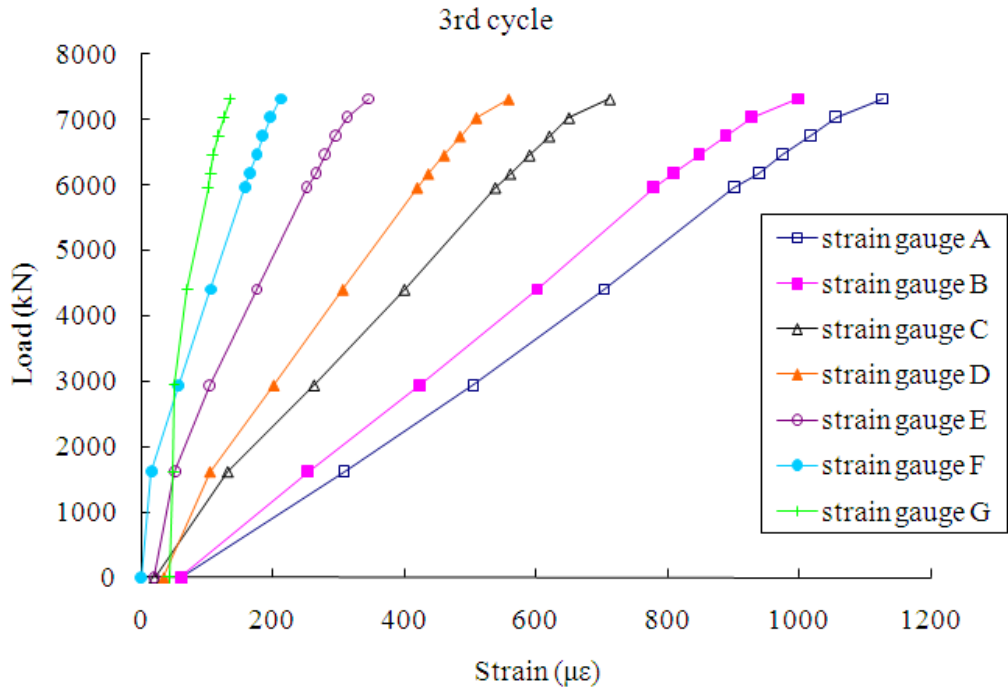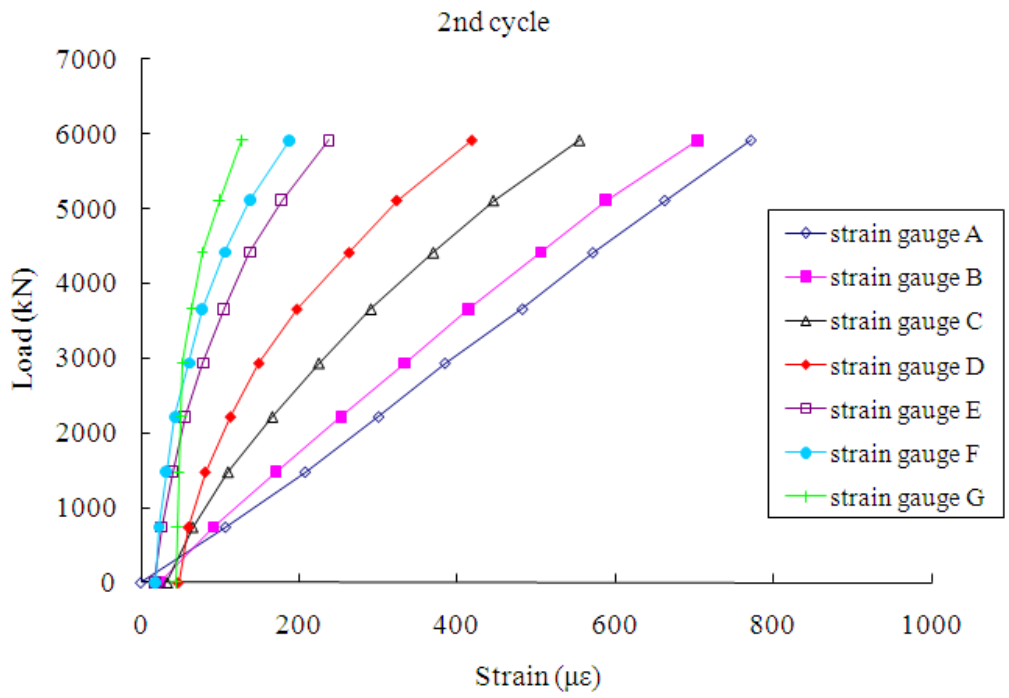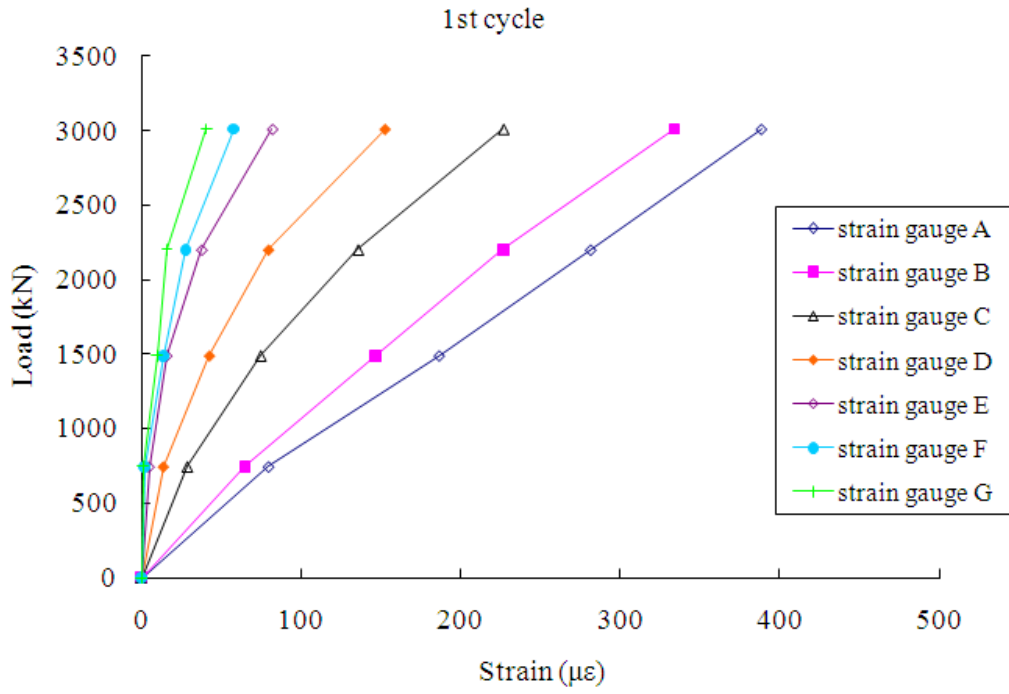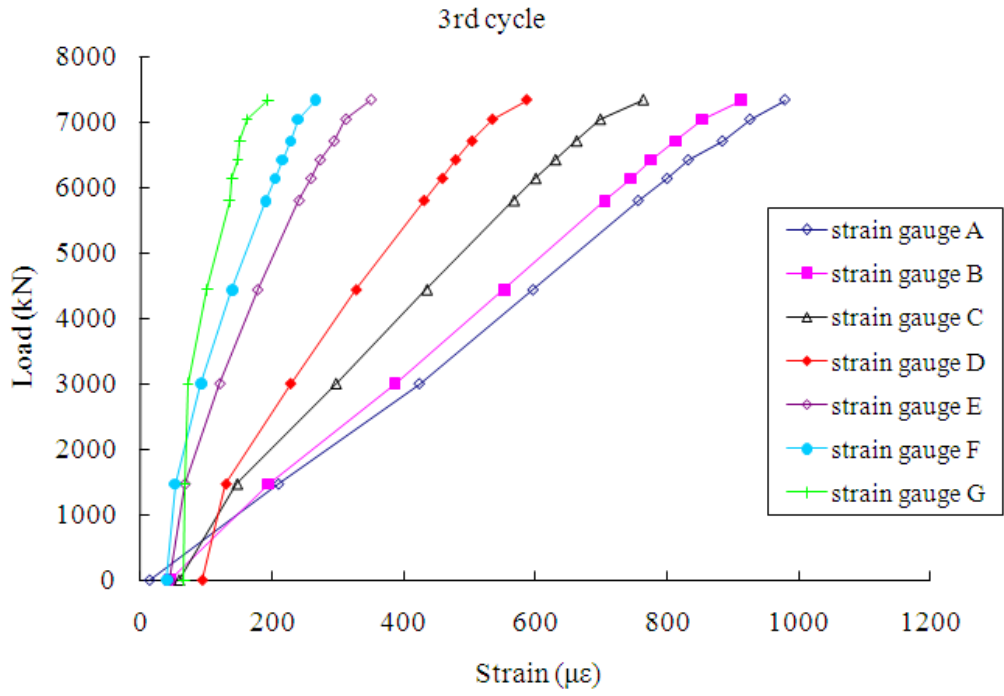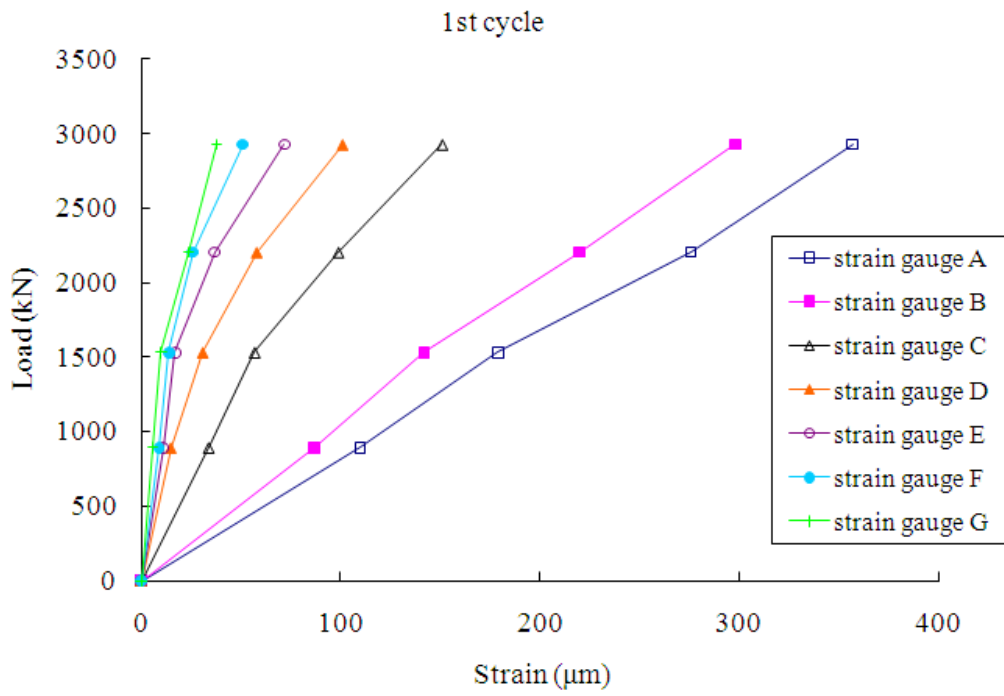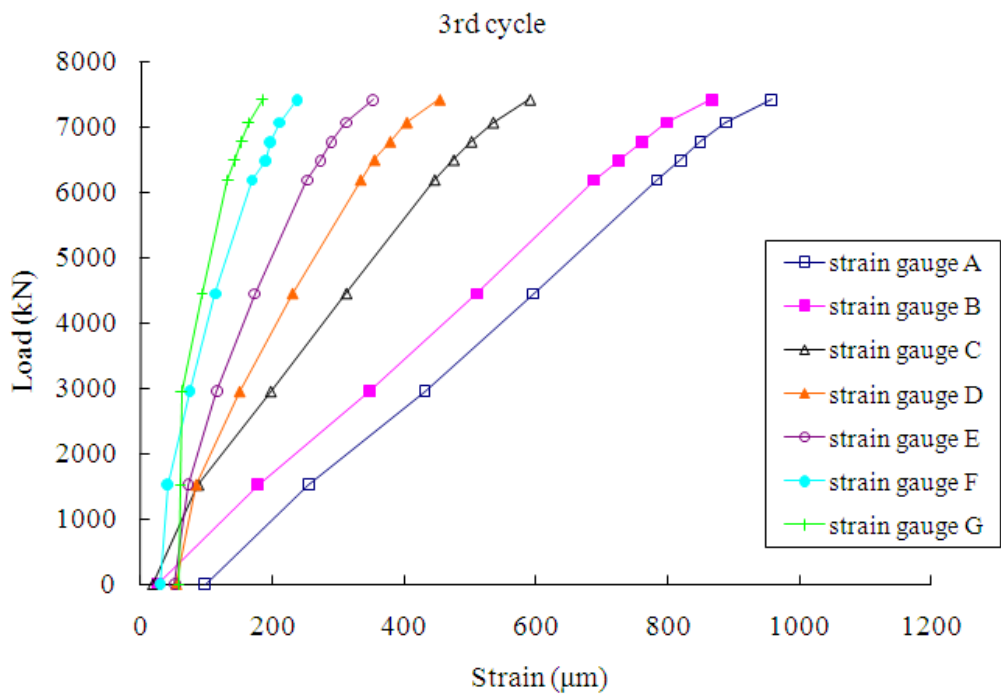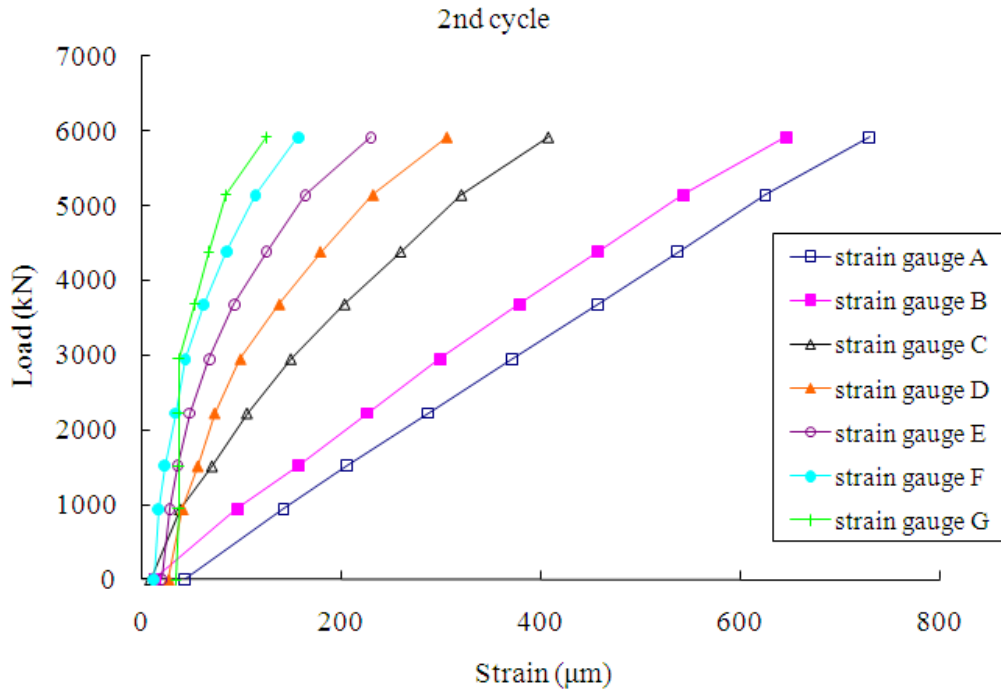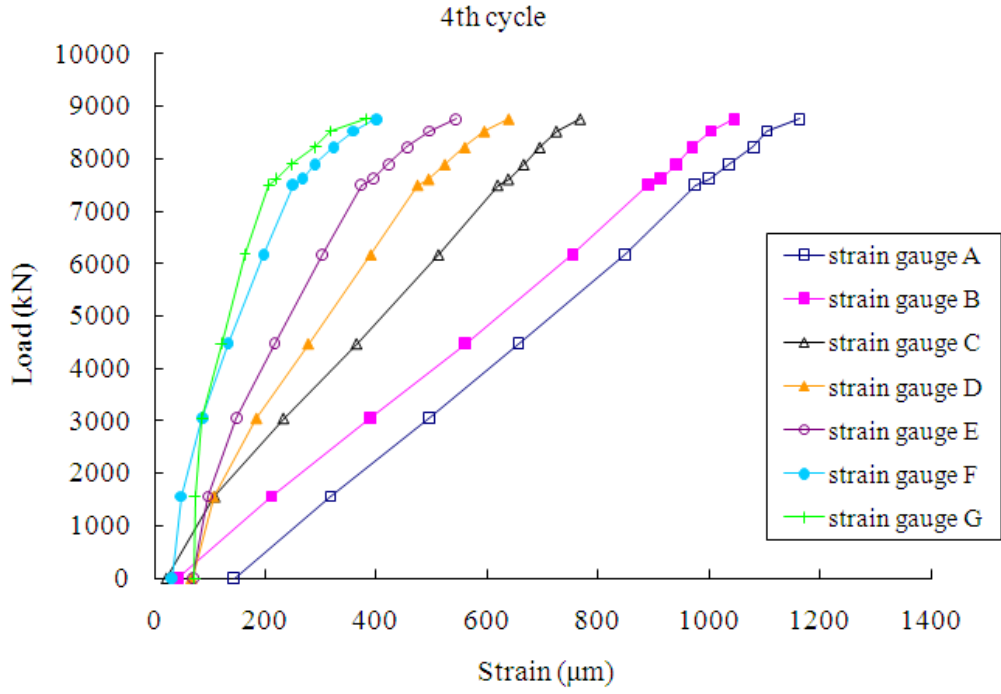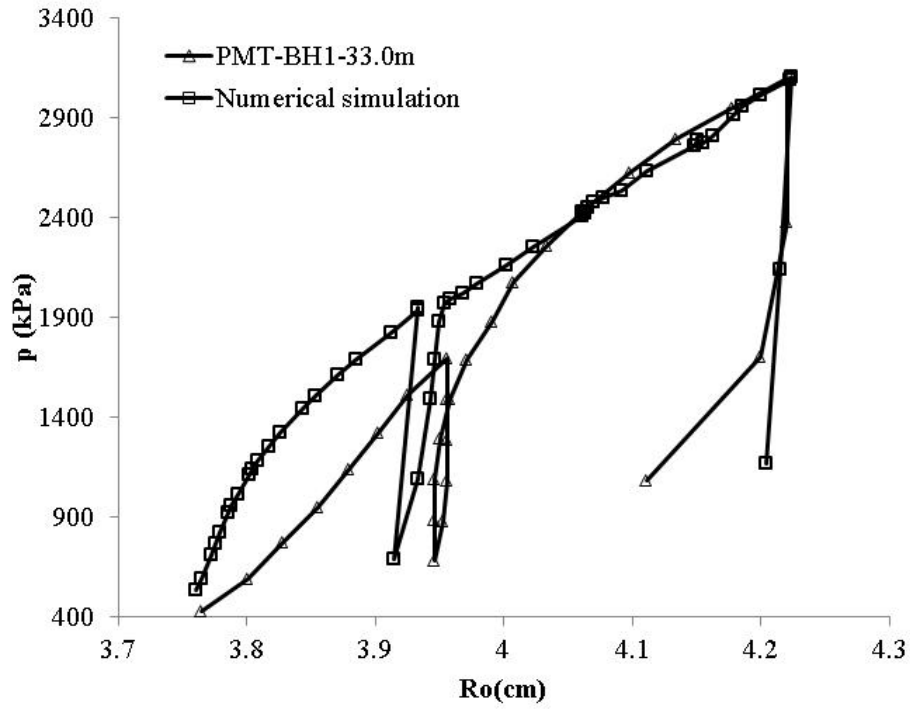
Ali, F. H. and S. K. Lee (2008). A New Instrumentation Method for Driven Prestressed Spun Concrete Piles. Electronic Journal of Geotechnical Engineering **13**.

Allard, M. A. G. (1996). Centrifuge tests on Tesion piles, GeoDeflt.

American Petroleum Institute (1993). Recommended Practice for Planning and Constructing Fixed Offshore Platforms-Working Stress Design.

Anaraki, K. E. (2008). Hypoplasticity Investigated:Parameter Determination and Numerical Simulation. Master of Science, Delft University of Technology.

Azzouz, A., M. Baligh and A.J. Whittle. (1990). Shaft resistance of piles in clay. Journal of Geotechnical Engineering **116**(2): 205-221.

Baars, S. and W. Niekerk (1999). Numerical modelling of tension piles. International symposium on beyond 2000 in computational geotechnics**:** 237-246.

Basu, P., D. Loukidis and M. Prezzi. (2011). Analysis of shaft resistance of jacked piles in sands. International Journal for Numerical and Analyticl Methos in Geomechanics.

Berg, V. d. (1994). Analysis of Soil Penetration, Delft Univercity of Technology. Doctor of Philosophy.

Johannessen, I. and Bjerrum, L. (1965). Measurements of the compression of a steel pile to rock due to the settlement of the surrouding clay. Proccedings 6th International Conference on Soil Mechanics and Foundation Engineering Montreal.

Bjerrum, L. , I. Johannessen and Eide, O. (1969). Reduction of negative skin friciton of steel piles to rock. Proccedings 7th International Conference on Soil Mechanics and Foundation Engineering Mexico.

Bond, A. J. and R. J. Jardine (1991). Effects of installing displacement piles in a high OCR clay. Geotechnique **41**(3): 341-363.

Bond, A. J. and R. J. Jardine (1995). Shaft capacity of displacement piles in a high OCR clay. Geotechnique **45**(1): 3-23.

Bozouk, M. (1972). Downdrag measurements on a 160-ft floating pipe pile in marine clay. Canadian Geotechnical Journal **9**(4): 127-136.

Bozouk, M. (1981). Bearing capacity of pile preloaded by downdarg. Proccedings

10th International Conference on Soil Mechanics and Foundation Engineering, Stockholm.

Brinkgreve, R. B. J. (2005). Selection of Soil Models and Parameters for Geotechnical Engineering Application. Soil Constitutive Models: Evaluation, Selection, and Calibration (GSP 128) Proceedings of the Sessions of the Geo Frontiers 2005 Congress

Brinkgreve, R. B. J., editor (2009). PLAXIS, 2D Version 9, AA,Balkema.

Broere, W. and A. F. van Tol (2006). Modelling the bearing capacity of displacement piles in sand. Proceedings of the Institution of Civil Engineers: Geotechnical Engineering **159**(3): 195-206.

Burland, J. B. (1973). Shaft friction of piles in clay. Ground Engineering **6**(3): 30-42

Bustamante, M. and L. Gianeselli (1982). Pile Bearing Capacity Prediction By Means Of Static Penetrometer CPT, Amsterdam, Neth, A. A. Balkema.

Callisto, L. and S. Rampello (2004). An Interpretation of Structural Degradation for Three Natural Clays. Canadian Geotechnical Journal **41**: 392-407.

Canadian Building Code and Highway Design Code. (1992). Canadian Geotechnical Society.

Carter, J. P., J. R. Booker and S.K. Yeung. (1986). Cavity expansion in cohesive-frictional soils. Geotechnique **36**: 349-358.

Castro, J. and M. Karstunen (2010). Numerical simulations of stone column instalation. Canadian Geotechnical Journal **47**: 1127-1138.

Chow, F. C. (1997). Investigations into the behaviour of displacement piles for offshore foundations. London, University of London. PhD.

Chong, P. T. (2002). Characterization of Singapore Lower Marine clay. Ph.D, National University of Singapore.

Civil Design Criteria for Road and Rail Transit Systerm. Land Transport Authority, Singapore, Rev. A4, Septermber, 2002.

Clemente, F. M. (1981). Downdrag on bitumen coated piles in a warm climate. Proccedings 10th International Conference on Soil Mechanics and Foundation Engineering, Stockholm.

Code of Practice for Foundation. Building and Construction Standards Committee of Singapore, 2003.

Collins, I. F. and H. S. Yu (1996). Undrained Cavity Expansions In Critical State Soils. International Journal for Numerical and Analytical Methods in Geomechanics **20**(7): 489-516

Cotecchia, F. and J. Chandler (2000). A General Framework for The Mechanical Behaviour of Clays. Geotechnique **50**(4): 431-447.

De Nicola, A. (1996). The performance of pipe piles in sand. Ph.D., University of Western Australia.

De Nicola, A. and M. F. Randolph (1999). Centrifuge modelling of pipe piles in sand under axial loads. Geotechnique **49**(3): 295-318.

Demers, D. and S. Leroueil (2002). Evaluation of preconsolidation pressure and over-consolidation ratio from piezocone tests of clay deposits in Quebec. Canadian Geotechnical Journal **39**(1): 174-192.

Dijkstra, J., W. Broere and A.F. van Tol. (2006). Numerical investigation into stress and strain development around a displacement pile in sand. The 6th European Conference on Numerical Methods in Geotechnical Engineering, Graz.

Dijkstra, J., W. Broere and A.F. van Tol. (2011). Numerical simulation of pile installation. Computers and Geotechnics **38**(5): 612-622.

Duncan, J. M. and C. Y. Chang (1970). Nonlinear analysis of stress and strain in soils. Journal of the Soil Mechanics and Foundations Division, **96**(5): 1629-1653

Endo, M., A. Minou, I. Kawasaki and T. Shibata. (1969). Negative skin fricition acting on steel pipe pile in clay. Proceedings of the 7th International Conference on Soil Mechanics and Foundation Engineering, Mexico.

Eslami and B. H. Fellenius (1997). Pile capacity by direct CPT and CPTU methods applied to 102 case histories. Canadian Geotechnical Journal **34**(6): 888-904.

Fellenius, B. H. (1988). Unified design of piles and pile groups. Transportation Research Record **1169**: 75-82.

Fellenius, B. H. (1989). Tangent modulus of piles determined from strain data. 1989 Foundation Congress.

Fellenius, B. H. (1997). Design piles and pile groups considering capacity, settlement and negative skin friciton, User manuak for Unipile program.

Fellenius, B. H. (2002). Determining the Resistance Distribution in Piles. Geotechnical News Magazine **20**(3): 25-29.

Fellenius, B. H. (2004). Unified desgin of piled foundations with emphasis on settlement analysis. ASCE Geotechnical Special Publication(GSP 125). Los Angeles.

Fellenius, B. H. (2006). Restuls from long-term measurement in piles of drag load and downdrag. Canadian Geotechnical Journal **43**(4): 409-430.

Fellenius, B. H. (2008). Effective stress analysis and set-up for shaft capacity of piles in clay. Honoring John Schmertmann "From research to practice in geotechnical Engineering", The Geo-Institute of the American Society of Civil Engineers**: 384-406.

Fellenius, B. H. (2009). Basics of foundation design, www.Geoforum.com.

Fellenius, B. H., M. Hussein, P. Mayne and R.T McGillivray. (2004). Murphy's law and the pile prediction event at the 2002 ASCE GeoInstitute's Deep Foundation Conference. Proceedings DFI 29th Annual Conference on Deep Foundations, Vancouver.

Fellenius, B. H., J. A. Santos and A.V. da Fonseca. (2007). Analysis of piles in residual soil-The ISC'2 prediction. Canadian Geotechnical Journal **44**: 201-220.

Fellenius, B. H. and S. A. Tan (2010). Combination of O-cell test and conventional head down test. Art of Foundation Engineering Practice-Geotechnical Special Publications (GSP) 198 Geo-Institute of ASCE**: 240-260.

Fioravante, V., M. Jamiolkowski and S. Pedroni. (1994). Modelling the behaviour of piles in sand subjected to axial load. Proceedings of Centrifuge' 94, Singapore, Singapore.

Fleming, W. G. K. (1992). New method for single pile settlement prediction and analysis. Geotechnique **42**(3): 411-425.

Foray, P., J. M. Genevois, S. Labanieh and A. Goulois. (1989). Effet de la mise en place sur lacapacite pieux des pieux dans les sables. Proceeings 12th International Conference on Soil Mechanics and Foundation Engineering.

Gajo, A. and D. Muir Wood (2001). A New Approach to Anisotropic Bounding Surface Plasicity: General Formulation and Simulations of Natural and Resconstituted Clay Behaviour. International Journal for Numerical and Analyticl Methos in Geomechanics **25**: 207-241.

Gibson, R. E. (1950). "Correspondence." Journal of Institution of Civil Engineers **34**: 382-383.

Gibson, R. E. and W. F. Anderson (1961). In situ measurement of soil properties with the pressuremeter. Civil Engineering and Public Works Review 56: 615-618.

Gudehus, G. and D. Kolymbas (1979). A constitutive law of rate-type for soils. Proceeings of 3rd International Conference on Numerical Method in Geomechanics, Aachen, 319-329.

Gudehus, G. (1996). A Comprehensive Constitutive Equation for Granular Materials. Soils and Foundations **36**(1): 1-12.

Gupta, R. C. (2002). Estimating bearing capacity factors and cone tip resistance. Soils

and Foundations **42**(6): 117-127.

Heerema, E. P. (1980). Predicting pile driveability: Heather as an illustration of the "friction fatigue" theory. Ground Engineering **13**(7): 15-20.

Herle, I. and D. Kolymbas (2004). Hypoplasticity for Soils with Low Friction Angles. Computers abd Geotechnics **31**: 365-373.

Hill (1950). The Mathematical Theory of Plasticity. London,U.K., Oxford University Press.

Indrarata, B., A. S. Balusubramanimam, P. Phamvan and Y.K. Wong. (1992). Development of negative skin friction on Driven piles in Bangkok clay. Canadian Geotechnical Journal **29**(3): 393-404.

Ingram, P. J. (2000). The application of numerical models to natural stiff soil. Ph.D., City University.

Jardine, R., F. Chow, R. Overy and J. Standing.. (1996). New design methods for offshore Piles MTD Publication 96/103, Thomas Telford Marine Technology Directorate, London.

Jardine, R., F. Chow, R. Overy and J. Standing. (2005). ICP design methods for Driven Piles in Sands and Clays, Thomas Telford .

Karlsrud, K., C. J. F. Clausen and P.M. Aas. (2005). Bearing capacity of driven piles in clay, the NGI approach. International Symposium. on Frontiers in Offshore Geotechnics 775-781.

Karlsrud, K., B. Kalsnes and F. Nowacki. (1992). Response of piles in soft clay and silt deposits to static and cyclic axial loading based on recent instrumented pile load tests. Publikasjon - Norges Geotekniske Institutt(188).

Katzenbach, R., U. Arslan and O. Reul. (1995). Geotechnische Meßüberwachung des 300 m hohen Commerzbank-Hochhauses in Frankfurt am Main. Proceedings Pfahl-Symposium '95.

Komurka, V. E. (2004). Incorporating set-up and support cost distributions into driven pile design, Los Angeles, CA, United states, American Society of Civil Engineers.

Komurka, V. E. and A. B. Wagner (2003). Estimating Soil/Pile Set-Up. United States: one CD-ROM containing 58 page document.

Konrad, J. M. and M. Roy (1987). Bearing capacity of fricition piles in marine clay. Geotechnique **37**(2): 163-175.

Kullhawy, F. H. and P. W. Mayne (1990). Manual on Estimating Soil Properties for Foundation Design. Report EPRI EL-6800. Palo Alto, Electric Power Research Institute**:** 306.

Kulhaney, F. H. (1984). Limiting Tip And Side Resistance: Fact Or Fallacy?, San Francisco, CA, USA, ASCE.

Ladanyi, M. B. (1961). Discussion. In Proceedings of the 5th International Conference on Soils Mechanics and Foundation Engineering: 270-271.

Lee, J. H. and R. Salgado (1999). Determination of pile base resistance in sands. Journal of Geotechnical and Geoenvironmental Engineering **125**(8): 673-683.

Lehane, B. M. and R. J. Jardine (1994 a). Displacement-pile behaviour in a soft marine clay. Canadian Geotechnical Journal **31**(2): 181-191.

Lehane, B. M. and R. J. Jardine (1994 b). Displacement pile behaviour in glacial clay. Canadian Geotechnical Journal **31**(1): 79-90.

Lehane, B. M., R. J. Jardine and AJ. Bond. (1993). Mechanisms of shaft friction in sand from instrumented pile tests. Journal of geotechnical engineering **119**(1): 19-35.

Lehane, B. M., J. A. Schneider and X. Xu. (2005). CPT based design of driven piles in sand for offshore structures. Perth, The University of Western Australia.

Leung, C. F., R. Radharkrishnan and T.A. Tan. (1991). Performance of precast driven piles in marine clay. Journal of Geotechnical l Engineering **117**(4): 637-657.

Li, Y. (2004). Finite element study on static pile load testing. Master of Engineering, National University of Singapore.

Mahutka, K.-P., F. Konig and J. Grabe. (2006). Numerical modelling of pile jacking, driving and vibratory driving. Proc. Int. Conf. Numerical Simulation of Construction Processes in Geotechnical Eng. for Urban Environment Bochum, Germany.

Mair, R. J. (1993). Developments in geotechnical engineering research: applications to tunnels and deep excavations. Proceedings of the Institution of Civil Engineers **97**(1): 27-41.

Masin, D. (2005). A Hypoplastic Constitutive Model for Clays. International Journal for Numerical and Analyticl Methos in Geomechanics **29**: 311-336.

Masin, D. (2005). TRIAX-Single element program for soil mechanics.

Masin, D. (2007). A Hypoplstic Constitutive Model for Clays with Meta-stable Structure. Canadian Geotechnical Journal **44**: 363-375.

Masin, D. and I. Herle (2005). State boundary surface of a hypoplastic model for clays. Computers abd Geotechnics **32**(6): 400-410.

Matyas, E. L. and J. C. Santanmarina (1994). Negative skin friction the neutral plane.

Canadian Geotechnical Journal **31**: 591-597.

Mayne, P. W. (1995).Profiling yield stresses in clays by in-situ tests. Transportation Research Record **1479**: 43-50.

Mayne, P. W. (2005). Integrated Ground Behavior: In-Situ and Lab Tests. Deformation Characteristics of Geomaterials **2**: 155-177.

Mayne, P. W. and R. G. Campanella (2005). Versatile site characterization by seismic piezocone. Proceeings 16th International Conference on Soil Mechanics and Geotechnical Engineering **2**:721-724.

Monnet, J. (2007). Numerical analysis for an interpretation of the pressuremeter test in granular soil. 18ème Congrès Français de Mécanique. Grenoble**:** 1-8.

Ng, N., P. Berner, et al. (1998). The ageing effects of sands. Ground Engineering **21**(10).

Niemunis, A. and I. Herle (1997). Hypoplastic model for cohesionless soils with elastic strain range. Mechanics of Cohesive-Frictional Material **2**: 279–299.

Niemunis, A. (2002). Extended Hypolastic Model for Soils. Habilitation, Ruhr Unviersity.

Pile Design and Construction. Geotechnical Engineering Office of Hong Kong, 2006.

Potts, D., K. Axelsson, et al. (2002). Guidelines for the use of advanced numerical analysis, Co-operation in Science and Technology (COST) Action C7.

Poulos, H. G. (1997). Piles subjected to negative friction: A procedure for desgin. Geotechnical Engineering **28**(1): 23-44.

Poulos, H. G. and E. H. Davis (1980). Pile foundation analysis and design. John Wiley and sons, New York.

Prandtl, L. (1921). Harte plashercher Korper. Nachrichten Ges.

Randolph, and C. P. Wroth (1979). Analytical solution for the consolidation around a driven pile. International Journal for Numerical and Analytical Methods in Geomechanics **3**(3): 217-229.

Randolph, M. F., J. Dolwin and R. Beck. (1994). Design of driven piles in sand. Geotechnique **44**(3): 427-448.

Randolph, M. F. (2003). Science and empiricism in pile foundation design. Geotechnique **53**(10): 847-875.

Rouainia, M. and D. Muir Wood (2000). A Kinematic Hardening Constiutive Model for Natural Clays with Loss of Structure. Geotechnique **42**(2): 257-274.

Said, I., V. De Gennaro and R. Frank. (2008). Axisymmetric finite element analysis of pile loading tests. Computers abd Geotechnics **36**: 6-19.

Santos, J.A., R. J. L. Duarte, A.V. da Fonseca and E.F.M. da Costa Esteves. (2005). ISC'2 experimental site-Prediction and performance of instrumented axially loaded piles. Proceedings of the 16th International Conference of Soil Mechanics and Geotechnical Engineering, Osaka.

Schanz, T. (1998). Zur Modellierung des Mechanischen Verhaltens van Reibungsmaterialen. Ph.D, Stuttgart University.

Schanz, T., P. A. Vermeer and PG. Bonnier. (1999). The hardening soil model: formulation and verification. In Beyond 2000 in Computational Geotechnics - 10 Years of Plaxis. Rotterdam.

Schweiger, H. F., C. Kummerer and R. Otterbein. (2004). Numerical modelling of settlement compensation by means of fracture grouting. Soils and Foundations **44**(1): 71-86.

Shen, R. F. (2008). Negative skin fricton on single piles and pile groups. Ph.D, National University of Singapore.

Sheng, D., Dieter Eigenbrod., K., Wriggers, P. (2005). Fintie element analysis of pile installation using large-slip friction contact. Computers and Geotechnics **32**(1): 17-26.

Susila, E., and Hryciw, R. (2003). Large displacement FEM modelling of cone penetration in layered soil. International Journal for Numerical and Analytical Methods in Geomechanics **27**(7): 585-602.

Tanchaisawat, T., P. Suriyavanagul and P.Jamsawang. (2006). Stiffened Deep Cement Mixing (SDCM) Pile: Laboratory Investigation, Kasetsart University.

Tan, S. A. and Fellenius, B. H. (2012). Failure of a barrette as revealed in O-cell test. ASCE Geotechnical Special Pubilcation (GSP 227): 307-321

Teh, C. I. and G. T. Houlsby (1991). Analytical study of the cone penetration test in clay. Geotechnique **41**(1): 17-34.

Tomlinson, M. J. (2001). Foundation design and construction. England.

Tomlionson, M. and J. Woodward (2008). Pile Design and Construction Practice. London and New York, Taylor&Francis.

Townsend, F. C., J. B. Anderson and L. Rahelison. (2001). Evaluation of FEM Engineering Parameters from Insitu Tests. Florida, Florida Department of Transportation.

Vermeer, P. A. (1978). A Double Hardening Soil Model for Sand. Geotechnique **28**(4): 413-433.

Vesic, A. S. (1970). Tests on instrumented piles, Ogeechee River site. Journal of the Soil Mechanics and Foundations Division **96**(2): 561-584.

Vesic, A. S. (1977). Design of pile foundation. National Cooperative Highway Research Program, Synthesis of Highway Practice(42).

Wehnert, M. (2006). A contribution to the drained and undrained analysis in the Geotechnical Engineering. PhD, Unviersity Stuttgart.

Wehnert, M. and P. A. Vermeer (2004). Numerical analyses of load tests on bored piles. Proceedings of the 9th International Sympsium on Numerical Methods in Geomechnics. Ottawa, Canada**:** 505-511.

White, D. J. and M. D. Bolton (2005). Comparing CPT and pile base resistance in sand. Proceedings of the Institution of Civil Engineers: Geotechnical Engineering 158(1): 3-14.

White, D. J. and B. M. Lehane (2004). Friction fatigue on displacement piles in sand. Geotechnique **54**(10): 645-658.

White, D.J. (2002). An investigation into the behaviour of pressed-in piles. Churchill College, University of Cambrige. Doctor of Philosophy.

Xiao, H. W. (2009). Yielding and failure of cement treated soil. Ph.D, National University of Singapore.

Xu, X. (2007). Investigation of the bearing performance of displacment piles in sand, The University of Western Australia. PhD.

Xu, X. and B. M. Lehane (2005). Evaluation of end-bearing capacity of closed ended piles in sand from cone penetration data. International Symposium on Frontiers in Offshore Geotechnics. Perth: 733-740.

Xu, X. and B. M. Lehane (2008). Pile and penetrometer end bearing resistance in two-layered soil profiles. Geotechnique **58**(3): 187-197.

Yasufuku, N. and A. F. L. Hyde (1995). Pile end-bearing capacity in crushable sands. Geotechnique **45**(4): 663-676.

Yasufuku, N., H. Ochiai and S. Ohno. (2001). Pile end-bearing capacity of sand related to soil compressibility. Soils and Foundations **41**(4): 59-71.

Yu, H. S. and G. T. Houlsby (1991). Finite cavity expansion in dilatant soils: loading analysis. Geotechnique **41**(2): 173-183.

Yu, H. S. and J. K. Mitchell (1998). Analysis of cone resistance: Review of methods. Journal of Geotechnical and Geoenvironmental Engineering **124**(2): 140-147.

Yu, H. S. (2000). Cavity expansion Method in Geomechanics. Kluwer Academic Publishers, The Netherlands.